UNIVERSITÀ DI PARMA

UNIVERSITÀ DEGLI STUDI DI PARMA

DOTTORATO DI RICERCA IN

"*SCIENZE CHIMICHE*"

CICLO XXXVI

Metals in medicine: bioinorganic chemistry to fight infectious diseases and cancer

Coordinatore:

Chiar.ma Prof.ssa Alessia Bacchi

Tutore:

Chiar.mo Prof. Giorgio Pelosi

Dottorando: Dott. Mirco Scaccaglia

Anni Accademici 2020/2021 – 2022/2023

Table of Contents

Abstract **7**

Introduction **9**

Medicinal inorganic chemistry: the role of metals in biology and medicine 9
From penicillin to metalloantibiotics: addressing the evolving threat of antimicrobial resistance 11
Thiosemicarbazones: from synthesis to antibacterial and anticancer applications 12
Aim of the thesis: exploring medicinal inorganic chemistry for novel metal-based therapies 15

1. Bismuth complexes as an adjuvant approach for infections by superbugs **17**

Abstract 18
Beta-lactam antibiotics: key players in combating bacterial infection 19
Beta-lactamases in the global spread of antibiotic resistance 19
Thiosemicarbazones and their bismuth(III) complexes as promising antibiotic enhancers for MBL-positive bacteria 21
Synthesis 23
Stability assessment of bismuth(III) complexes 23
Metal exchange studies between bismuth(III) and zinc(II) complexes 25
Crystallographic structural analysis of bismuth(III) complexes 26
Antibacterial effects of compounds on carbapenem-resistant *Klebsiella pneumoniae* NDM-1 27
Synergic studies with meropenem against *Klebsiella pneumoniae* NDM-1 28
Cytotoxicity assessment in eukaryotic cells 31
Conclusions 32
Experimental section 33

2. Chemical space exploration of a second-generation Bi(III), Ga(III), and Sb(III) compounds in the fight against superbugs 43

Abstract 44
Chemical space in drug development 45
Metallodrug chemical space 45
Exploration of the chemical space around a lead compound 46
Synthesis 47
Antimicrobial activity of Bi(III), Sb(III), Ga(III) compounds 48
Synergic studies against *Klebsiella pneumoniae* NDM-1 and *Klebsiella pneumoniae ESβL* 50
Cytotoxicity assessment in eukaryotic cells 52
In vivo toxicity evaluation using *Galleria mellonella* larvae 52
Conclusion 54
Experimental section 55

3. Gallium complexes as growth inhibitors of gram-negative bacteria 61

Abstract 62
Diverse mechanisms of antibiotic resistance: beyond β-lactamases 63
The antimicrobial potential of gallium(III) salts 64
Exploring gallium(III)-complexes with a pyridoxal moiety: insights into their antimicrobial potential 64
Synthesis 65
Exploring pH-dependent species distribution in gallium(III) complexes 66
Complex interactions between gallium(III) and ligands enhance antibacterial properties 70
Enhancing carbapenem sensitivity in *Klebsiella pneumoniae* NDM-1 with gallium(III) complexes 71
Bacterial selectivity: no toxicity in healthy eukaryotic cells 73
Conclusion 74
Experimental section 75

4. Mn(I) tricarbonyl libraries for the discovery of new metalloantibiotics . 81

Abstract 82
Exploring new metalloantibiotics: the power of combinatorial chemistry 83
Tricarbonyl moieties as a scaffold for antibacterial drug development 84
Antimicrobial insights into manganese tricarbonyl complexes 85
Optimization of $Mn(CO_3)$ combinatorial synthesis and preparation of compound library 85
Antimicrobial activity of combinatorial $Mn(CO)_3$ library 89
Re-synthesis, purification and characterization of lead compounds 91
Stability of manganese tricarbonyl complexes 93
Biological evaluation of lead manganese compounds 94
Analyzing the CO-mediated antibacterial activity 96
Bacterial cytological profiling 97
Influence on bacterial membranes and respiratory chain inhibition 100
In vivo toxicity evaluation using *Galleria mellonella* larvae 101
In vivo efficacy test in a *Galleria mellonella* systemic infection 102
In vivo efficacy test in a *Galleria mellonella* burn wound infection model 103
Conclusion 104
Experimental section 106

5. Targeting lung cancer cells with gold(III) complexes 117

Abstract 118
Cancer as a global challenge 119
“Golden” innovations in cancer therapy: the potential of gold-based compounds 119
Gold(III)-thiosemicarbazone complexes as cytotoxic agents against lung cancer 120
Synthesis 120
Crystallographic structural analysis of gold(III) complexes 121
Stability assessment of gold(III) complexes 122
Gold(III) stability through cyclic voltammetry 122

Computational electronic potential surface calculation 123
DNA interaction studies 124
Serum protein interaction studies 128
Cytotoxicity evaluation of gold(III) complexes on lung cancer cells 130
Morphological analysis 131
Cell cycle progression and apoptosis 133
Compounds' influence on cyclins and cyclin-dependent kinases 134
Oxidative stress evaluation 135
Interleukin-6 as a biomarker of inflammation 137
In vivo toxicity evaluation using *Galleria mellonella* larvae 137
Conclusion 139
Experimental section 140

6. Targeting *Toxoplasma gondii* infections with gold(III) complexes 149

Abstract 150
Toxoplasma gondii and toxoplasmosis: insights into its life cycle and impact on human health 151
Gold complexes from thiosemicarbazone ligands against *Toxoplasma* 152
In vitro screening 153
Mode of action: parasitostatic versus parasiticidal effect 154
In vitro interaction with the immune system: viability of splenocytes 155
In vivo toxicity in zebrafish model 156
In vivo efficacy on infection in murine cerebral toxoplasmosis model 159
In vivo interaction with the immune system 160
Conclusion 161
Experimental section 163

Conclusions 165

List of publications 167

Poster contributions 168

Bibliography 170

Abstract

Metals have played a vital role in the field of medicine, underscoring the enduring connection between inorganic chemistry and healthcare. This thesis embarks on an exciting journey, harnessing the tools of bioinorganic chemistry, to address pressing biomedical healthcare challenges. With a primary aim to develop innovative metal-based compounds for diverse applications, the research explores antimicrobial resistance, antibacterial drug discovery, cancer therapeutics, and antiparasitic agents. Along this journey, novel bismuth(III), gallium(III), antimony(III), manganese(I), and gold(III) complexes have been synthesized and rigorously studied, providing valuable insights for future advancements. This thesis represents a significant stride towards simplifying the underlying chemistry, enhancing the assessment of biological activity, and fostering hope for pioneering therapeutic solutions in the ever-evolving healthcare landscape.

Introduction

Medicinal inorganic chemistry: the role of metals in biology and medicine

Metals play a fundamental role in the intricate chemistry of living systems. Their unique reactivity stems from their ability to easily lose electrons, transitioning from the metallic state to positively charged ions when they interact with biological fluids. In this cationic form, metals become soluble and have the possibility to interact with various biological molecules. This interplay between positively charged metal ions and electron-rich biological molecules, such as proteins and DNA, underlies the critical role of metals in biology.[1,2] The use of metals in medicine dates back to ancient civilizations. Already in 3000 BC the Egyptians were known to utilize copper salts to sterilize water and historical records indicate that as early as in 2500 BC, the Chinese employed gold to treat smallpox and lung diseases. From the 16th century, mercury-containing formulations were also applied to combat syphilis.[3,4]

Today, metals continue to play a crucial role in modern medicine. Lithium carbonate, for instance, is used to stabilize the moods of individuals with manic-depressive disorders, and bismuth subsalicylate serves as an effective antidiarrheal agent, iron-based compounds are used to address anaemia, vanadium-based compounds are utilized for diabetes management, and gold-based agents like Auranofin® combat rheumatoid arthritis (Figure 1). Additionally, bismuth-based compounds have proven valuable in the treatment of ulcers.[5,6] However, the turning point in the history of metal-based medicine arrived with the discovery of cisplatin, a platinum-based complex (cis-diammine-dichloro-platinum(II), Figure 1). Cisplatin's remarkable anti-cancer activity against solid tumors, achieved by binding to the DNA of cancerous cells and inhibiting their proliferation, revolutionized cancer treatment.[7] Nevertheless, these platinum-based compounds come with severe side effects and can lead to resistance when used repeatedly, driving the research into the exploration of other metals' anticancer properties. Gold and ruthenium currently stand as the most extensively studied alternatives, with various other metals, including osmium, silver, copper, zinc, and also nickel, are under investigation.[8,9]

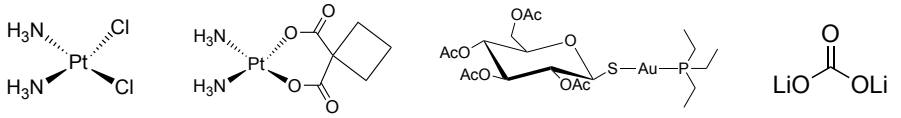

Cisplatin
Treatment of various type of cancers

Carboplatin
Treatment of advanced ovarian carcinoma

Auranofin
Antirheumatic

Lithium carbonate
Treatment of manic episodes of bipolar disorder.

Figure 1. Chemical structures of representative metallodrugs approved for clinical use.

In addition to their role in cancer treatment, metals have demonstrated antibacterial properties. For instance, metallic copper and silver have long been recognized for their antibacterial properties and were employed in medieval times as vessels for handling liquids and food.[10] In the early 20th century, in addition to mercury-based antisyphilis drugs, mercury-containing antiseptics like thimerosal and merbromin found wide use in disinfecting solutions (Figure 2).[11] In more recent times, colloidal bismuth(III) subcitrate was utilized in the treatment of gastric ulcers caused by *H. pylori*.[12]

Figure 2. Mercurochrome: a mercury-containing general antiseptic.

Metal complexes, with their unique geometries and the potential for various mechanisms of action, offer a distinctive advantage in medicinal chemistry. Unlike purely organic drug candidates, metal complexes provide a rich and diverse range of structural possibilities, making them intriguing starting points for challenging biological targets. Their capacity to explore three-dimensional space and the potential to enhance target selectivity make metal complexes a valuable tool in the search for new and innovative medical treatments.

From penicillin to metalloantibiotics: addressing the evolving threat of antimicrobial resistance

Around a century ago, the era of antibiotics in modern medicine began. Paul Ehrlich's arsenic compounds and subsequent discoveries like sulfonamides paved the way. However, Sir Alexander Fleming's accidental find of penicillin in 1928 marked a turning point, ushering in a Golden Age of antibiotic research (Figure 3). During this period, scientists uncovered antibiotics, revolutionizing medicine, and saving countless lives. These breakthroughs established antibiotics as essential drugs in modern healthcare.[13–15]

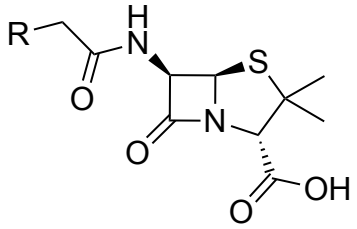

Figure 3. Penicillin core structure.

However, over the decades, a pressing concern emerged: the rise of antimicrobial resistance (AMR). Despite the tremendous success of antibiotics, the inappropriate and excessive use of these drugs has led to a steady increase in the number of bacteria strains exhibiting resistance. What makes this situation even more alarming is the speed at which resistance can develop following the discovery of a new antibiotic (Figure 4). This ongoing challenge is exacerbated by the fact that the majority of current antibiotics share similar mechanisms of action, making it difficult to combat these evolving mechanisms of resistance.[16]

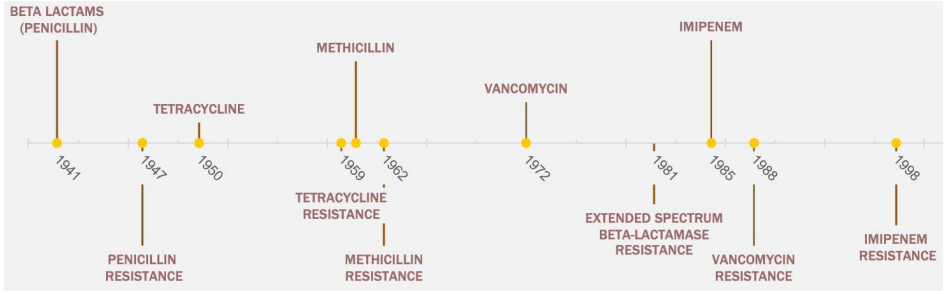

Figure 4. Timelines detailing the discovery of specific antibiotics and their corresponding resistance.

In response to the urgent need for innovative solutions, a promising avenue has emerged: metalloantibiotics. Metal complexes are now at the forefront in the search for new antimicrobial agents. These complexes offer a rational approach to drug design, harnessing the unique chemical properties of metal centres. Notably, their variable oxidation states enable them to mediate chemical reactions, particularly those involving redox chemistry, that are often inaccessible to organic structures. By controlling the inner coordination sphere of these complexes, their redox properties can be finely tuned. Additionally, multivalent transition metal complexes offer greater structural and stereochemical diversity compared to pure organic moieties.[17,18]

This approach to antibiotic development is vital, given the urgency of addressing the growing public health crisis posed by AMR. As bacteria continue to evolve and develop resistance to existing antibiotics, metalloantibiotics represent a promising solution to diversify the chemical space of antimicrobial agents and broaden the scope of potential candidates.

Thiosemicarbazones: from synthesis to antibacterial and anticancer applications

Thiosemicarbazones (TSs) constitute a versatile class of compounds characterized by a chemical structure in which a thione group coexists with a hydrazine part. This structure exhibits extensive electronic delocalization in the presence of a thione-thiol tautomerism (Scheme 1).

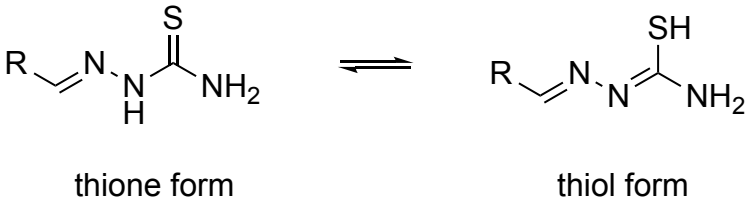

Scheme 1. Thione-thiol tautomerism.

TSs are synthesized through a straightforward condensation reaction between the hydrazine part of thiosemicarbazide and the carbonyl group of an aldehyde or a ketone, typically in protic solvents like ethanol or methanol (Scheme 2). While most reactions proceed rapidly, certain instances may require mild acidic

catalysis, particularly when steric hindrance is a determining factor. What characterises TSs is their remarkable structural adaptability; their structure can in fact be readily modified by employing various aldehydes or ketones, offering a wide versatility in the chemical design.

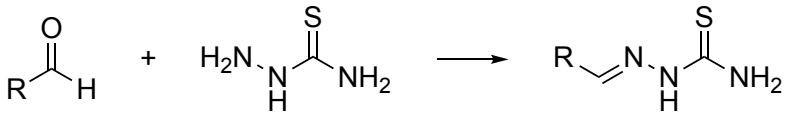

Scheme 2. General synthetic way to obtain a TS.

TSs basically possess a bidentate ligand character, utilizing both the sulfur and the iminic nitrogen atoms to form five-term coordination rings when they bind to metal ions (Figure 5). The mixed hard-soft nature of the N-S donor atoms in TSs enhances their affinity for a wide range of metal ions, making them effective chelators for transition elements and metals of the p-block.

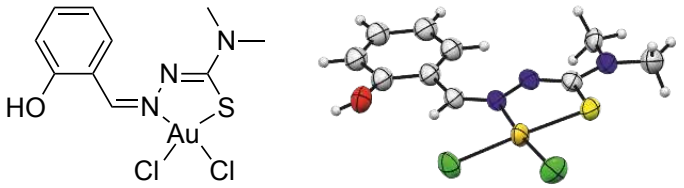

Figure 5. Example of a TS coordinating a transition metal complex, and its corresponding crystal structure (CCDC No 2193028).

TSs, particularly their metal complexes, have garnered significant attention for their diverse biological activities. Among these, their potential in anticancer applications has been extensively studied and holds great promise for future developments. The efficacy of TSs in combating tumors varies depending on factors like the specific TS's chemical structure, the metal ions involved in complexation, and the nature of the targeted tumor cells. Their mechanisms of action against cancer are multifaceted and include inhibition of ribonucleotide reductase, generation of reactive oxygen species (ROS), interference with topoisomerase II, disruption of the mitochondrial membrane, and direct interactions with DNA.[19] Notably, Triapine® (3-aminopyridine-2-carboxaldehyde thiosemicarbazone, Figure 6) has emerged as a patented drug that has progressed to Phase II clinical trials for cancer treatment, highlighting the substantial potential of TS-based compounds in the pharmaceutical industry.

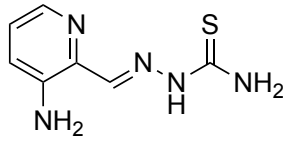

Figure 6. Triapine.®

The exploration of thiosemicarbazones (TSs) in the realm of infectious diseases is an attracting field with emerging evidence of their efficacy. One of the notable areas of interest lies in their antibacterial properties, making them potentially valuable in the battle against antimicrobial resistance.[20] TSs have demonstrated the ability to inhibit beta-lactamases, enzymes responsible for conferring resistance to beta-lactam antibiotics, thus offering a promising avenue for combating drug-resistant bacterial infections.[21] Furthermore, TSs and their metal complexes have exhibited significant potential against protozoal diseases, including trypanosomiasis and malaria.[22]

Aim of the thesis: exploring medicinal inorganic chemistry for novel metal-based therapies

In the field of medicinal inorganic chemistry, exploring new metal-based drugs is a promising approach to tackle urgent healthcare issues. This field offers a unique toolkit for the rapid discovery and development of innovative therapeutic agents with diverse applications.

The primary aim of this thesis was to create a series of metal-based compounds using an easy synthetic approach, with a focus on ligands like Schiff bases and thiosemicarbazones. My research aimed to streamline the synthesis process, reducing the number of steps or complicated separations to facilitate the translation of these molecules into potential industrial applications. The focus was then to simplify the process for quickly testing the biological activity of these compounds.

The thesis is organized into distinct projects, each with its own set of goals and outcomes.

The initial phase of my work was dedicated to addressing the pressing issue of antimicrobial resistance. In the first chapter, I focused on the use of metal-based compounds as adjuvants of antibiotics to reinstate antibiotic sensitivity in bacterial strains that had developed resistance. Following the identification of promising lead compound, my work, presented in the second chapter, involved an exploration of the chemical space surrounding it in order to discover novel compounds that exhibit enhanced safety and efficacy.

In the third chapter, I delved deeper into the water solubility and species distribution characteristics of a set of compounds exhibiting antibacterial activity, particularly against the more challenging Gram-negative pathogens.

In the fourth chapter, I used the tools of combinatorial chemistry, an approach that broadened the spectrum of ligands to construct compound libraries. This allowed me to generate a large number of compounds to identify novel antibacterial agents with promising activity.

In the fifth chapter, I marked a shift towards the development of compounds as potential treatments for various forms of lung tumors.

Finally, in chapter six, I delved into the evaluation of some promising compounds for their efficacy in combating toxoplasmosis, a parasitic infection.

The work presented in my thesis gave me the opportunity to “traverse” the periodic table, starting with metals from the p-block, such as bismuth, gallium and antimony. I then ventured into the more established d-block, featuring elements like manganese, and concluded by exploring the potential of precious metals such as gold.

Through these three years of research, I aimed to contribute to the fields of antimicrobial resistance, antibacterial drug discovery, cancer therapeutics and antiparasitic agents with a focus on simplifying the underlying chemistry to facilitate rapid assessments of their biological activity.

1. Bismuth complexes as an adjuvant approach for infections by superbugs

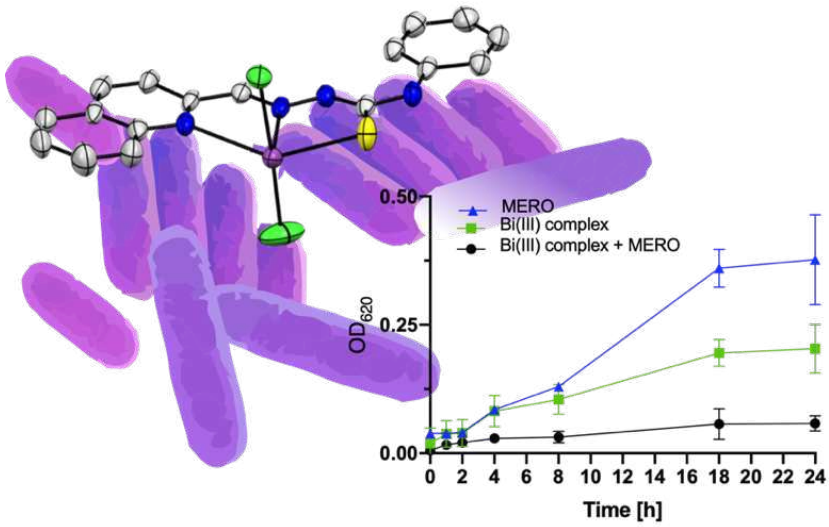

This chapter's research involved a collaborative work with Dr. Martina Rega from the Department of Veterinary Medicine (Food Inspection Unit) of the University of Parma. The project was co-supervised by Prof Franco Bisceglie and Prof Cristina Bacci.

Abstract

In this chapter I focus the attention on the synthesis and characterization of six bismuth complexes, adhering to the general formula $BiLCl_2$, wherein L denotes a thiosemicarbazone featuring a quinoline moiety. These complexes, along with their X-ray crystal structures, were investigated in the context of *carbapenem-resistant Klebsiella pneumoniae* (NTCT14331) harboring the NDM-1 gene.

I conducted the vitro experiments to explore the synergistic interaction between these compounds and meropenem. Notably, the bismuth complex known as quinoline-2-carboxaldehyde-N^4-phenyl-3-thiosemicarbazone bismuth dichloride exhibited synergy with carbapenem, effectively restoring antibiotic susceptibility in the NDM-1 enzyme-producing strain. This synergistic effect led to a remarkable 128-fold reduction in the minimum inhibitory concentration (MIC) of meropenem.

Beta-lactam antibiotics: key players in combating bacterial infection

Diseases and infections originating from drug-resistant pathogens are increasingly recognized as a significant threat to the well-being of both humans and animals. Pharmaceutical and medical research communities express profound concern regarding the widespread phenomenon known as antimicrobial resistance (AMR), which represents the adaptive response of certain microorganisms as a survival defense mechanism. This phenomenon primarily arises from the improper or excessive utilization of antibiotics. Consequently, the arsenal of effective antibiotics available for treating these infections is steadily dwindling. Furthermore, the development of new antibiotics is experiencing a dearth of interest from private companies because of the connected low profit.[23,24]

The most successful and effective group of antibiotics currently in use belongs to the class of beta-lactams. They are distinguished by their broad-spectrum activity against various bacterial families, encompassing both Gram-positive and Gram-negative bacteria. This class of molecules is characterized by a shared functional group known as the beta-lactam ring, and it can be further categorized into four distinct subclasses: penicillins, cephalosporins, carbapenems, and monobactams, each displaying considerable structural diversity (Figure 7).[25]

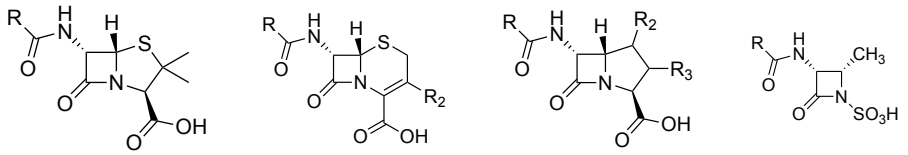

Figure 7. Chemical structures of beta-lactam and monobactam antibiotics.

Beta-lactamases in the global spread of antibiotic resistance

In Gram-negative bacteria, beta-lactamase enzymes play a crucial role by breaking down the amide bond found in the four-membered beta-lactam ring of beta-lactam antibiotics (Figure 8). According to the Ambler classification system, beta-lactamases are categorized into four classes. Three of these classes

(designated as classes A, C, and D) employ an active serine residue in their enzymatic activity, while the fourth class relies on zinc ions for its catalytic function and is known as metallo beta-lactamases (MBLs, class B).[26] The class B metallo beta-lactamases (MBLs) are of significant concern because they possess the capability to hydrolyze carbapenems, which are the last line of defense against multidrug-resistant pathogens. Furthermore, these enzymes can also break down most beta-lactam antibiotics, with the exception of monobactams. This versatility in antibiotic resistance makes MBLs particularly worrisome in the context of antimicrobial resistance.[27]

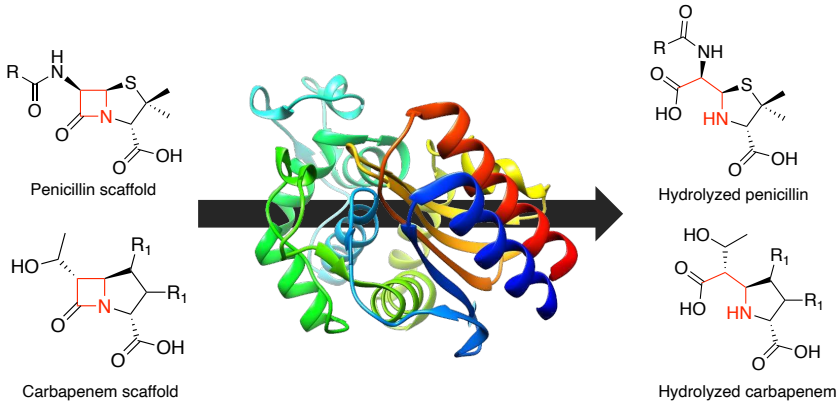

Figure 8. Beta-lactam antibiotics (the beta-lactam ring is depicted in red) can undergo hydrolysis by beta-lactamases, rendering the antibiotic inactive.

The study of metallo beta-lactamases (MBLs) gained significant attention following the discovery of NDM-1 (New Delhi Metallo beta-lactamases, Figure 9) in 2009. NDM-1 is a carbapenemase enzyme that contains zinc and was initially identified in an isolate from India. What makes this concerning is that the gene, blaNDM, responsible for encoding NDM-1, can be transmitted via plasmids, which are small pieces of genetic material. This plasmid-mediated transmission has the potential to rapidly spread the blaNDM gene worldwide. This phenomenon is especially common among Gram-negative bacteria and is often associated with the transmission of genes conferring resistance to other classes of antibiotics.[28] *Enterobacteriaceae* are frequently implicated in this phenomenon, referred to as carbapenem-resistant *Enterobacteriaceae* (CRE), earning them the classification of "superbug bacteria". CRE infections can give rise to various serious medical

conditions, including pneumonia, urinary tract infections, endocarditis, meningitis, septicaemia, and intra-abdominal infections. These infections are particularly challenging to treat due to the resistance exhibited by CRE to many antibiotic.[29]

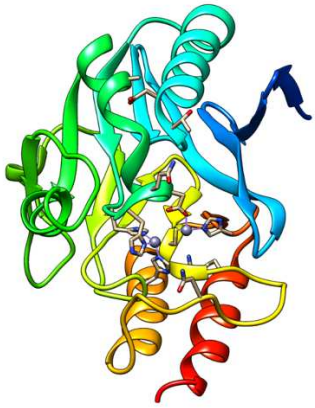

Figure 9. Crystal structure of the native NDM-1 (PDB 5XP6)

Thiosemicarbazones and their bismuth(III) complexes as promising antibiotic enhancers for MBL-positive bacteria

An established strategy for addressing beta-lactamase-mediated resistance involves employing combination therapy, which combines a beta-lactam drug with a beta-lactamase inhibitor (Figure 10). As of now, only one inhibitor specifically designed for metallo beta-lactamases (MBLs), known as a cyclic boronate, has progressed to the clinical development phase.[30] A common strategy for inhibiting metalloenzymes is to utilize ligands and coordinating groups with robust zinc-binding properties.[31] Nevertheless, this approach poses a potential risk to other critical metalloenzymes due to its lack of selectivity.

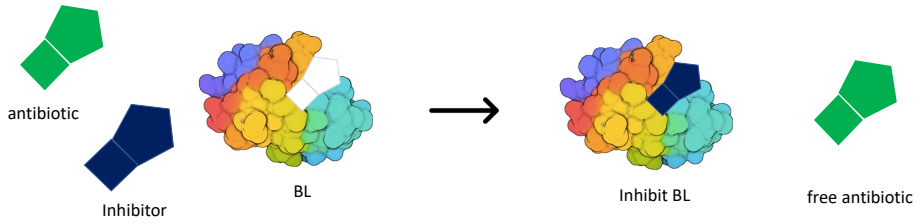

Figure 10. Strategy to restore antibiotic efficacy: inhibiting the beta-lactamase (BL).

My approach involved developing inhibitors based on thiosemicarbazones (TSC), as compounds containing a sulfur atom have shown the lowest bacterial inhibition

constant values. More recently, researchers have examined thiosemicarbazone derivatives in clinical isolates positive for NDM, exploring their potential in combination with meropenem, and these investigations have yielded encouraging outcomes.[32–35] The selection of bismuth(III) as the metal of choice stemmed from its association with another form, colloidal bismuth subcitrate (CBS), currently employed in clinical settings alongside antibiotics to combat bacterial gastritis induced by *Helicobacter pylori.*[36–40] Furthermore, CBS has recently demonstrated its ability to irreversibly inhibit MBLs by displacing the two active zinc(II) ions with bismuth(III) ions (Figure 11). This renders CBS a promising scaffold for the development of broad-spectrum MBL inhibitors.[41]

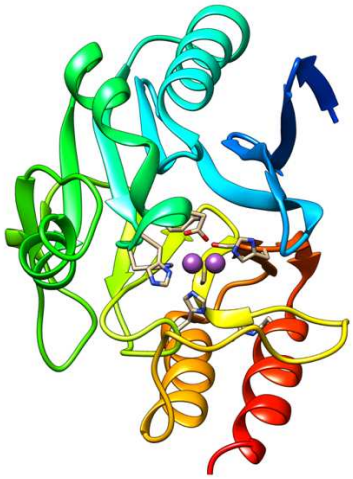

Figure 11. Crystal structure of the Bi(III)- bound NDM-1 (PDB 5XP9).

I chose a ligand derived from quinoline thiosemicarbazone for coordinating Bi(III) (Figure 12). Indeed, quinoline derivatives, exemplified by 2-carboxy-8-hydroxyquinoline, possess a well-documented efficacy in the inhibition of MBLs.[42] This compound has been derivatized to include the coordinating moiety of the thiosemicarbazone (**L1-4**), which presents a tetradentate structure. Additionally, I synthesized the corresponding ligands without the hydroxyl group in the 8-position (**L5-8**) to investigate their different coordination behaviour with Bi(III). Bismuth is a highly promising metal; however, bismuth salts suffer from low solubility and a tendency to form colloids in water.[43] Consequently, the metal

complexes I intend to use serve as a valuable scaffold to enhance the solubility of Bi(III).

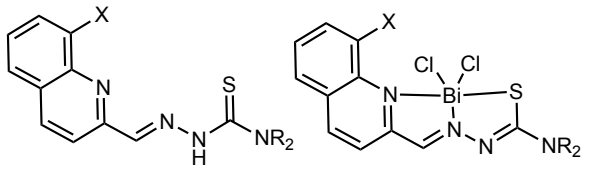

*Figure 12. Structure of the ligands (on the left), denoted as **L1-8**, and the corresponding complexes (on the right), labeled as **Bi1-8**.*

Synthesis

The ligands were produced by condensing the respective aldehyde with different N^4-substituted thiosemicarbazides (Scheme 3). The reaction was conducted in methanol with acetic acid serving as the catalyst. The complexes were formed by dissolving the ligands in a heated mixture of ethanol and methanol in a 2:1 ratio and introducing bismuth trichloride dissolved in the smallest feasible quantity of acetic acid.

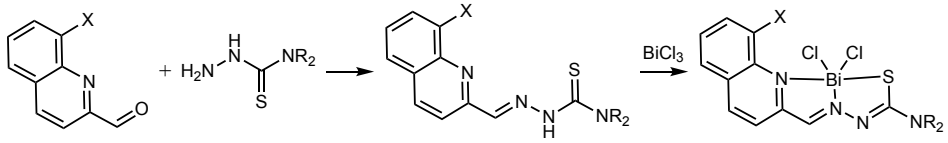

*Scheme 3. Synthetic route of Bi(III) complexes **Bi1-8.***

Stability assessment of bismuth(III) complexes

The stability of bismuth(III) complexes was assessed by analyzing their behaviour over 24 hours at 37°C in a phosphate buffer solution (PBS). As depicted in Figure 13, there were no significant differences in the absorption profiles observed for complexes **Bi3-8**. These complexes all exhibited an absorption band attributed to the ligand-to-metal charge transfer, which is characteristic of the Bi-S bond.

In contrast, complexes **Bi1-2** displayed spectra with no notable distinctions compared to the pure free ligand. Further confirmation of their instability was found in pure DMSO, as evidenced by NMR data. The NMR spectra of **Bi1-2**

closely resembled those of the corresponding free ligand. Several attempts were made to characterize the complexes in different solvents, but they were unsuccessful due to their limited solubility. Consequently, complexes **Bi1-2** were deemed unstable under these conditions and were not subjected to further investigation.

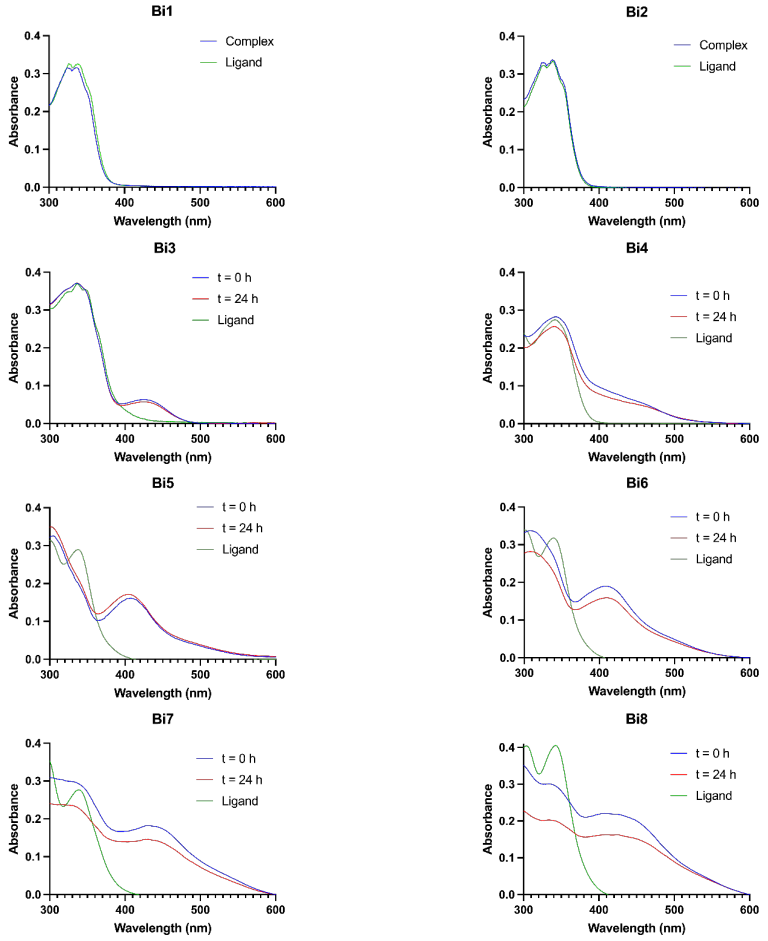

*Figure 13. UV-Vis spectra of the Bi(III) complexes stability (**Bi1-8**) at 20 μM in 5%DMSO/PBS freshly made (t=0 h) and after incubation at 37°C for 24 hours (t=24 h) plus comparison with the free ligand at 20 μM in 5% DMSO/PBS.*

Metal exchange studies between bismuth(III) and zinc(II) complexes

$ZnCl_2$ was subjected to titration with bismuth complex solutions in a physiological solution (PBS, pH 7.4) to investigate the stability of the complexes in the presence of zinc(II) ions. The hydroxyl derivatives **Bi5-8** maintained their absorbance characteristics, while **Bi3-4** displayed a novel band in the 400-500 nm range, indicating an interaction with Zn(II) ions. (Figure 14). This experiment indicates that ligands **L3-4** exhibit a greater affinity for zinc(II) over bismuth(III) ions, consistent with prior reports on quinoline thiosemicarbazone derivatives.[44] No further alterations in the UV-Vis spectra were observed following the introduction of 0.5 equivalents of $ZnCl_2$, indicating a preference for a 2:1 stoichiometry in the creation of zinc(II) complexes. To assess the affinity of zinc(II) for the ligands, a parallel experiment was conducted using pure dimethylsulfoxide (DMSO). (Figure 14). In physiological solutions the quantification was not possible because upon the addition of the Zn(II), an increased turbidity of the mixture was observed. The logβ were calculated from a model that considers the BiL^{2+}, ZnL_2^{+}, Bi^{3+}, Zn^{2+} and HL species (Table 1). The logβ values for the zinc complexes exceed those of the corresponding bismuth complexes, demonstrating a stronger affinity of **L3-4** for zinc(II) ions. Furthermore, the logβ value for **Bi3** is higher, signifying a more effective binding of **L3** to the metal.

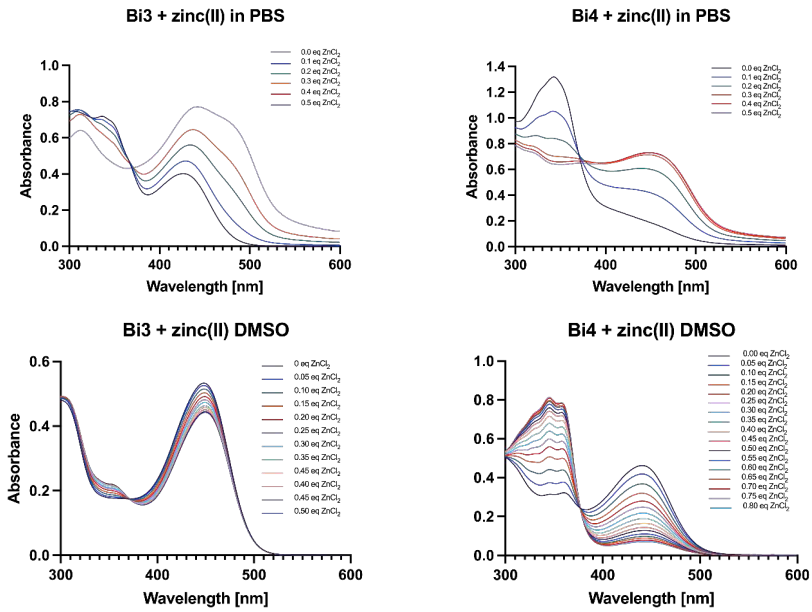

*Figure 14. Titration UV-Vis spectra of the Bi(III) complexes (**Bi3**-**4**) at 20 μM in 5% DMSO/PBS or pure DMSO with $ZnCl_2$.*

Table 1. Calculated logβ in DMSO.

	C3	C4
Logβ of BiL^{2+}	6.76(3)	4.8(1)
Logβ of ZnL^{2+}	14.74(7)	11.7(1)

Crystallographic structural analysis of bismuth(III) complexes

Bi4 crystals have a monoclinic structure (space group C2/c) with a single molecule of the Bi(III) complex in the asymmetric unit. The Bi(III) ion exhibits hexacoordination, involving the quinoline nitrogen, hydrazine nitrogen, sulfur, two apical chlorides, and an oxygen from a disordered DMSO molecule.

The bismuth complexes **Bi5**, **Bi6**, **Bi7**, and **Bi8** exhibit diverse crystal structures and coordination geometries. **Bi5** adopts a tetragonal structure, forming dimers with heptacoordinated Bi(III) complexes and bridging chlorides. In contrast, **Bi6** crystallizes in a triclinic space, displaying pentagonal bipyramidal coordination in dimeric structures. **Bi7**, found in monoclinic crystals, exhibits heptacoordination and features a hydrogen bond with DMSO. Lastly, **Bi8**, also in monoclinic

crystals, showcases heptacoordination with a disordered sulfur atom and hydrogen bonding with DMSO (Figure 15).

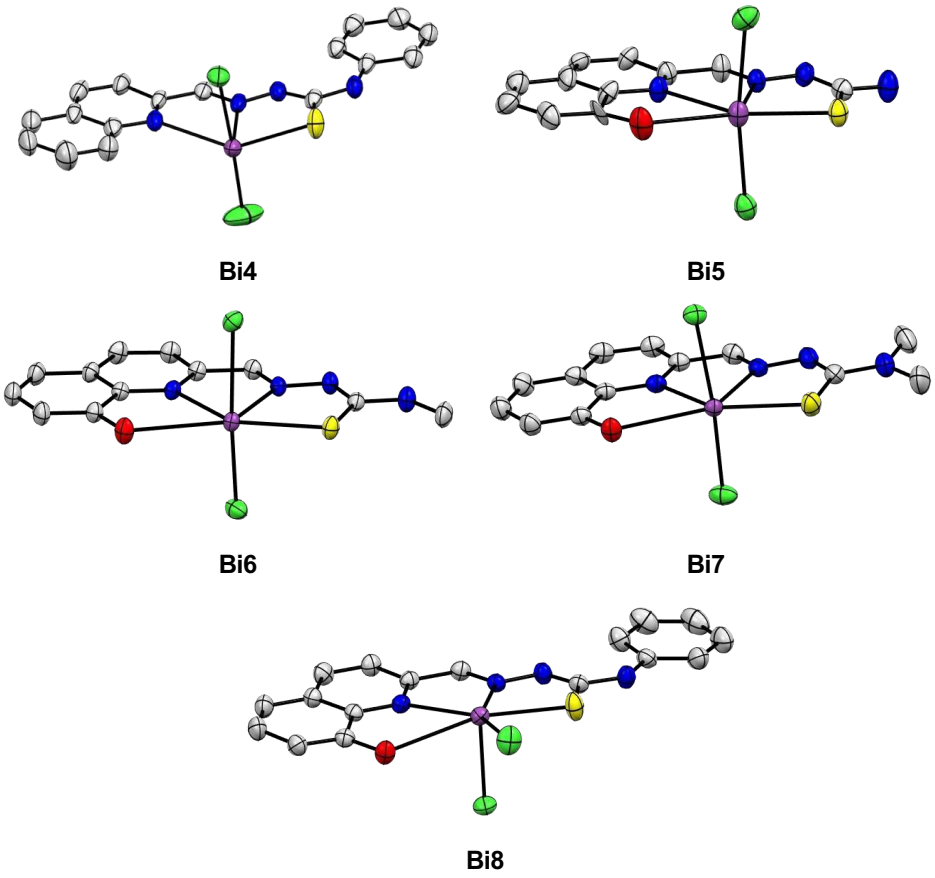

Figure 15. X-ray crystallographic structures of the Bi(III) complex moieties. Hydrogens are omitted for clarity. CCDC No 2152012-2152016 contain all the supplementary crystallographic data.

Antibacterial effects of compounds on carbapenem-resistant *Klebsiella pneumoniae* NDM-1

Compounds **L3-8** and **Bi3-8** were initially subjected to in vitro antibacterial testing *against Klebsiella pneumoniae* NDM-1 (NTCT14331), an isolate obtained from a human blood infection. This strain harbors the *bla*$_{\text{NMD-1}}$ gene, which encodes the corresponding metallo beta-lactamase capable of hydrolyzing the beta-lactam ring of carbapenems, rendering them ineffective. This particular strain exhibited resistance to meropenem, with a minimum inhibitory concentration (MIC) of 256

μg/mL, which is 128 times higher than the sensitivity threshold.[45] The strain was also subjected to testing with DMSO, and it was confirmed that a concentration of 5% DMSO had no impact on bacterial growth. The compounds were tested starting from the higher possible concentrations, which were 250 μM for the complexes and 125 μM for the ligands due to solubility constraints. A real-time growth dynamics assay was conducted, measuring OD_{620} over 24 h time. Notably, only complex **Bi3** exhibited growth inhibition, with a MIC value of 62.5 μM (Table 6) and a Minimum Bactericidal Concentration (MBC) value of 125 μM. In the case of the other compounds, only a reduction in bacterial growth rate was observed compared to the control treated with DMSO alone.

Synergic studies with meropenem against *Klebsiella pneumoniae* NDM-1

An initial screening to assess the synergistic effects of meropenem and the compounds involved both MIC evaluation and real-time growth dynamics assays for **L3-8** and **Bi3-8**, in the presence of different antibiotic concentrations (8 μg/mL and 16 μg/mL). In the case of **L3**, the MIC value was notably reduced to 62.5 μM under both antibiotic concentrations tested (Table 6). However, the MBC value remained above 125 μM, indicative of a bacteriostatic activity. Complex **Bi3** exhibited a decrease in MIC value, from 62.5 μM to 31.25 μM, when combined with 16 μg/mL of meropenem (Table 6). The MBC value of **Bi3** with 16 μg/mL of meropenem was determined to be 62.5 μM. While **Bi4**, when used as monotherapy, failed to inhibit bacterial growth, it did induce growth inhibition when combined with 8 μg/mL and 16 μg/mL of meropenem, effective up to a concentration of 125 μM (Figure 16). Furthermore, MIC values and growth curves were assessed for the resistant strain in the context of a combination therapy involving CBS and meropenem, revealing no significant activity.

*Table 2. MIC values of the tested compounds in monotherapy and in combination therapy with different concentration of meropenem. MIC values of colloidal bismuth subcitrate (CBS) and meropenem (MERO) are reported for comparison. *µg/mL*

Compounds	MIC [µM]	MIC[µM] with MERO 8 µg/mL	MIC[µM] with MERO 16 µg/mL
L3	>125	62.5	62.5
L4	>125	>125	>125
L5	>125	>125	>125
L6	>125	>125	>125
L7	>125	>125	>125
L8	>125	>125	>125
C3	62.5	62.5	31.25
C4	>250	125	125
C5	>250	>250	>250
C6	>250	>250	>250
C7	>250	>250	>250
C8	>250	>250	>250
MERO	256*	-	-
CBS	>250	>250	>250

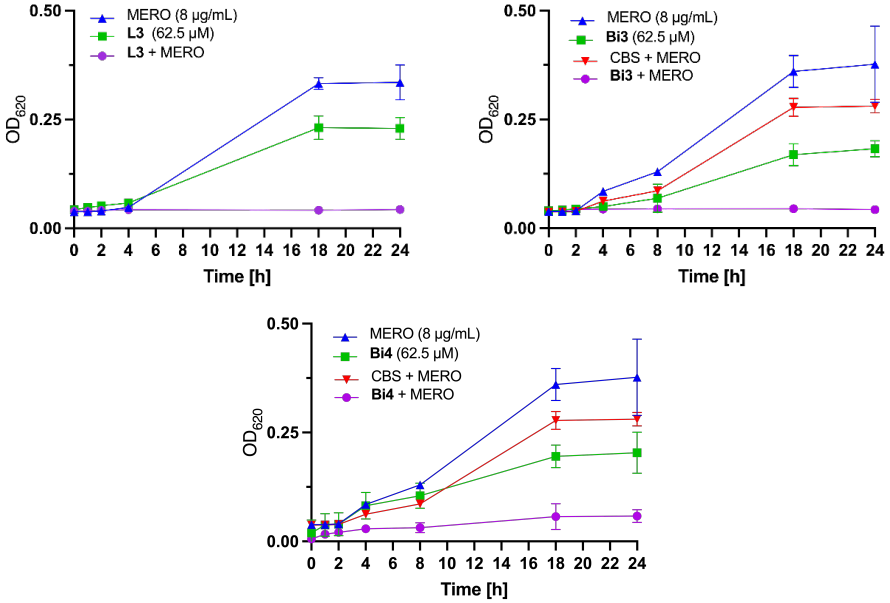

*Figure 16. Time growth curves of MERO and **L3, Bi3** and **Bi4** in monotherapy and in combination therapy against K. pneumoniae NDM-1 during 24h incubation. The concentration of MERO and **L3, L3, Bi3** and **Bi4** are displayed in the corresponding graph while the concentration used in the combination therapy are the same used in the monotherapy.*

The MIC of meropenem was assessed in the presence of different concentrations of complexes for **L3**, **Bi3**, and **Bi4**. Initially, the resistant *K. pneumoniae* strain exhibited a meropenem MIC of 256 µg/mL, which significantly decreased to 8 µg/mL in combination with 62.5 µM of **L3**, to 16 µg/mL with 31.25 µM of **Bi3**, and to 2 µg/mL with 250 µM of **Bi4**. Heat plots illustrating the OD values of the checkboard assay for **L3**, **Bi3** and **Bi4** can be found in Figure 17. The determination of MBC values revealed that **L3** had only a bacteriostatic effect, while **Bi3** and **Bi4** displayed bactericidal activity.

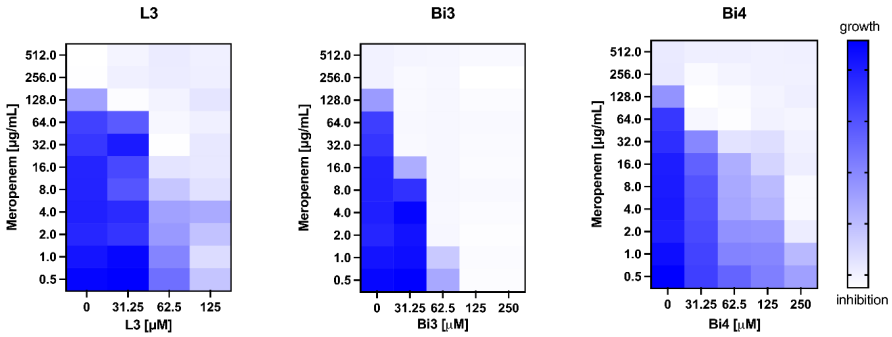

*Figure 17. Representative heat plots of microdilution checkboard assay by for the combination of **L3, Bi3, Bi4** and meropenem against K. pneumoniae NDM-1.*

The antimicrobial efficacy of the **L3**-**Bi4** and meropenem combination was further substantiated by calculating the fractional inhibitory concentration index (FICI). FICI values were determined using the formula: $FICI = FIC_A + FIC_B = C_A/MIC_A + C_B/MIC_B$, where MIC_A and MIC_B represent the MIC values of compounds A and B individually, and C_A and C_B are the effective concentrations of A and B when administered. A FICI index of 0.5 or less suggests a synergistic effect, while values between 0.5 and 4 indicate an additive effect.[46,47] The FICI values for **L3** at a concentration of 62.5 µM and for **Bi4** ranging from 31.25 µM to 250 µM are consistently below 0.5, signifying a synergistic interaction. Conversely, the FICI index for **Bi3** consistently exceeds 0.5, indicating the absence of synergistic activity. These results are graphically depicted in the isobolograms presented in Figure 18.

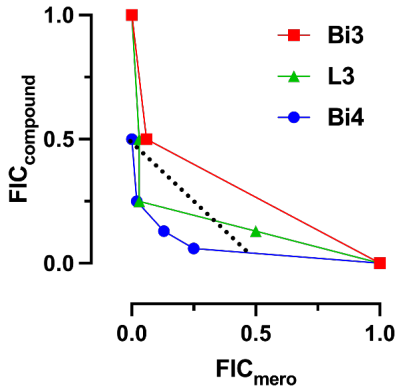

*Figure 18. Isobolograms of the combination of meropenem and **L3**, **Bi3**, **Bi4** against K. pneumoniae NDM-1. The dashed black line represents the ideal isobole, where drugs act additively and independently. Data below this line indicate a synergistic effect.*

Cytotoxicity assessment in eukaryotic cells

To evaluate the cytotoxicity of **Bi3-4** on eukaryotic cells, we utilized HuDe human epithelial cells and A549 lung carcinoma cells as the experimental models. The complexes displayed a moderate level of cytotoxicity. Notably, **Bi3** exhibited higher cytotoxicity towards lung carcinoma cells (IC_{50} = 5 ± 2 μM) compared to human epithelial cells (IC_{50} = 106 ± 16 μM), where the IC_{50} exceeded the MIC value. In contrast, **Bi4** did not exhibit selectivity for tumor tissue (A549: IC_{50} = 47 ± 17 μM, HuDe: IC_{50} = 54 ± 10 μM). However, it is worth noting that the IC_{50} values recorded were higher than the effective concentrations required for synergistic activity with the antibiotic.

Conclusions

In this study, a series of bismuth complexes with the general formula $BiLCl_2$, where L represents a quinoline thiosemicarbazone ligand, were comprehensively characterized, including their structural elucidation via X-ray analysis.

To assess their potential as antibacterial agents, we conducted a phenotypic cell-based screening using *Klebsiella pneumoniae* NDM-1 (NTCT 14331), which harbors the bla_{NDM-1} metallo-carbapenemase gene. Among the tested complexes, **Bi3** exhibited bactericidal properties on its own. Complex **Bi4** demonstrated synergistic activity with meropenem (FICI < 0.5), while showing negligible antibacterial activity as a monotherapy (MIC > 250 µM). Interestingly, **Bi4** displayed activity against the bacterial strain that was resistant to bismuth subcitrate, previously tested for antibacterial effects. Notably, complexes containing a hydroxyl group involved in bismuth coordination displayed no significant antimicrobial activity.

Solution studies unveiled **Bi4**'s enhanced affinity for zinc(II) ions, indicating that more labile complexes have an increased antibacterial activity. This suggests a potential mode of action for **Bi4** as a zinc ejector.

L3 exhibited synergism with meropenem but demonstrated only bacteriostatic activity. In contrast, bismuth(III) complex **Bi4** not only restored carbapenem sensitivity but also displayed bactericidal effects.

Cytotoxicity assessments against human cancer and healthy cells revealed moderate cytotoxicity, suggesting the potential for structural optimization in future development. Given the selective toxicity of Bi(III) compounds toward pathogens and their existing clinical use, we expect that this class of compounds can be used to lead further development of clinically relevant antibacterial agents.

Materials

Thiosemicarbazide, 99% (Fluka), 4-methyl-3-thiosemicarbazide, 97% (Aldrich), 4,4-dimethyl-3-thiosemicarbazide, 98% (TCI), 4-phenyl-3-thio-semicarbazide, 98% (Janssen), quinoline-2-carboxaldehyde, 97% (Aldrich), 8-hydroxy quinoline-2-carboxaldehyde, 99% (Aldrich), $BiCl_3$, 98% (Aldrich), bismuth(III) citrate (Aldrich), ethylenediaminetetraacetic acid disodium salt dihydrate (EDTA), 98% (Riedel-de Haën), Meropenem (Aldrich) were commercially available and they were used without any further purification. Colloidal bismuth subcitrate was prepared accordingly to previous published procedures[48]. Triptic Soy Agar (TSA; Biolife Italiana, Milan, Italy) and Buffered Peptone Water (BPW; Biolife Italiana, Milan, Italy) were commercially available.

NMR were recorded on a Bruker Anova spectrometer at 400 MHz, with chemical shift reported in δ units (ppm). NMR spectra were referenced relative to residual NMR solvent peaks. Coupling constants (J) are reported in hertz (Hz). Solvent used in the spectra's acquisitions is DMSO-d_6.

The FT-IR measurements were recorded on Perkin Elmer's Spectrum Two in the 4000-400 cm^{-1} range, equipped with the UATR accessory.

Elemental analyses were performed using Flashsmart CHNS Elemental Analyzer (Thermofisher Scientific).

Mass analyses were carried out using a Waters Acquity Ultraperformance ESI-MS spectrometer with Single Quadrupole Detector (Mode used: Flow Injection; Source temperature (°C) 150; Desolvation Temperature (°C) 300; Cone Gas Flow (L/Hr) 100; Desolvation Gas Flow (L/Hr) 480; Solvent Flow (mL/min) 0.2; Capillary voltage (kV) 3, Cone voltage (V) 50). The compounds were dissolved in MeOH.

UV-Vis spectrum were collected using Thermofisher Scientific's Evolution 260 Bio Spectrophotometer in a quartz cuvette. Stock solution of the compounds (10 mM) were made in DMSO and stored at -18 °C. Stock solution of meropenem (2048 μgmL^{-1}) was dissolved in sterile water and stored at -18 °C.

The 96-wells plates optical density was recorded at 620 nm by Multiskan FC Version 1.00.75 by Thermofisher Scientific.

The plates containing Klebsiella pneumoniae were incubated in ICN200 Super ArgoLab at 37 °C.

Preparation of the ligands.

The desired thiosemicarbazones were synthetized by mixing an equimolar amount of thiosemicarbazide with the proper aldehyde in methanol with acetic acid as a catalyst. The mixture was refluxed under stirring for 8 hours and left overnight at 0°C. The precipitate was filtered out, washed with cold ethanol and diethyl ether and dried under vacuum.

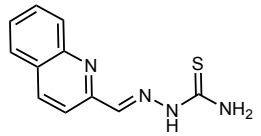

L1. Thiosemicarbazide (200mg, 2.2 mmol), quinoline-2-carboxaldehyde (344 mg, 2.2 mmol), MeOH (20 mL). White powder. Yield: 82.9%. CHNS analysis: $C_{11}H_{10}N_4S$ Calc: C 57.37%, H 4.38%, N 24.33%, S 13.92% Exp: C 57.63%, H 4.17%, N 24.12%, S 13.81%. ^{1}H NMR (400 MHz, DMSO-d_6):11.80 ppm (s, 1H, -NH=N); 8.46 ppm (d, 1H, H arom., J=8.4 Hz); 8.40 ppm (d, 1H, CH arom., J=8.4 Hz); 8.38 ppm (d, 2H, -NH2; J=42.5 Hz); 8.24 ppm (s, 1H, CH=N); 8.00 ppm (m, 2H, CH arom.); 7.62 ppm (dd, 1H, CH arom.,); 7.78 ppm (dd, 1H, CH arom.). ^{13}C NMR (101 MHz, DMSO) δ 178.94, 154.39, 147.80, 143.00, 136.75, 130.40, 129.25, 128.39, 128.31, 127.61, 118.59. ESI-MS (+, m/z, MeOH): 253.4 $[M+Na]^+$; 231.4 $[M+H]^+$. IR (ATR): 3393 cm^{-1} and 3261 cm^{-1} ν N-H, 3143 cm^{-1} ν C-H arom., 2978 cm^{-1} ν C-H aliph., 1612 cm^{-1} ν C=N, 1524 cm^{-1} and 1497 cm^{-1} ν C=C, 1109 cm^{-1} and 835 cm^{-1} ν C=S.

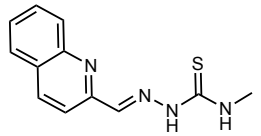

L2. N^4-methyl-3-thiosemicarbazide (101 mg, 1.0 mmol), quinoline-2-carboxaldehyde (150 mg, 1.0 mmol), MeOH (8 mL). White-pinkish powder. Yield: 62%. CHNS analysis: $C_{12}H_{12}N_4S$ Calc: C 58.99%, H 4.95%, N 22.93%, S 13.12% Exp: C 59.15%, H 4.70%, N 22.64%, S 12.87%. ^{1}H NMR (400 MHz, DMSO-d_6): 11.87 ppm (s, 1H, -NH=N); 8.81 ppm (m, 1H, -NHMe); 8.44 ppm (d, 1H, CH arom., J=8 Hz); 8.39 ppm (d, 1H, CH arom., J=8 Hz); 8.23 ppm (s, 1H, -CH=N); 8.00 ppm (m, 2H, CH arom., J=8 Hz); 7.78 ppm (m, 1H, CH arom., J=8 Hz); 7.63 ppm (m, 1H, CH arom., J=8 Hz); 3.07 ppm (d, 3H, -N(CH_3), J=8 Hz). ^{13}C NMR (101 MHz, DMSO) δ 178.45, 154.43, 147.83, 142.44, 136.71, 130.43, 129.24, 128.40, 128.27, 127.60, 118.47, 31.44. ESI-MS (+, m/z, MeOH): 267.3 $[M+Na]^+$; 244.8 $[M+H]^+$; IR (ATR): 3314 cm^{-1} and 3122 cm^{-1} ν N-H, 3058 cm^{-1} ν C-H arom., 2931 cm^{-1} ν C-H aliph., 1598 cm^{-1} ν C=N, 1524 cm^{-1} and 1503 cm^{-1} ν C=C arom., 1456 cm^{-1} ν C-N arom., 1109 cm^{-1} and 829 cm^{-1} ν C=S.

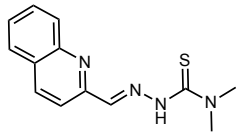

L3. N^4,N^4-dimethyl-thiosemicarbazide (105 mg, 0.7 mmol), quinoline-2-carboxaldehyde (80mg, 0.7 mmol), MeOH (20 mL). Yellow powder. Yield: 46%. CHNS analysis $C_{13}H_{14}N_4S$ Calc: C 60.44%, N 21.69%, H 5.46%, S 12.41% Exp: C 60.64%, N 22.07%, H 5.71 %, S 12.87%; ^{1}H NMR (400 MHz, DMSO-d_6): 11.37 ppm (s, 1H, NH); 8.37 ppm (m, 2H, CH=N and CH arom.); 8.02 ppm (m, 3H, CH arom.); 7.78 ppm (t, 1H, CH arom.); 7.62 ppm (t, 1H, CH arom.) methyl peaks rely under water peak. ^{13}C NMR (101 MHz, DMSO-d_6): δ 181.07, 154.57, 147.83, 144.17, 137.06, 130.50, 129.23, 128.47, 128.19, 127.55, 117.85, 42.89. ESI-MS (+, m/z, MeOH): 259.2 $[M+H]^+$, 281.2 $[M+Na]^+$. IR (ATR): 3065 cm^{-1} ν N-H, 2999 cm^{-1} and 2912 cm^{-1} ν C-H arom., 1618 cm^{-1} ν C=N, 1575 cm^{-1}, 1540 cm^{-1} and 1496 cm^{-1} ν C=C, 1102 cm^{-1} and 820 cm^{-1} ν C=S.

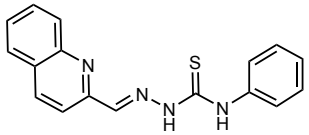

L4. N^4-phenyl-3-thiosemicarbazide (150 mg, 0.9 mmol), quinoline-2-carboxaldehyde (141 mg, 0.9 mmol), MeOH (10 mL). White powder. Yield: 72%. CHNS analysis $C_{17}H_{14}N_4S$ Calc: C 66.64%, H 4.61%, N 18.29%, S 10.47% Exp: C 66.38%, H 4.53%, N 18.58%, S 10.37%. ^{1}H NMR (400 MHz, DMSO-d_6): 12.20 ppm (s, 1H, C=N-NH); 10.40 ppm (s, 1H, S=C-NHPh); 8.62 ppm (d, 1H, J=8.8 Hz, CH arom,quin); 8.40 ppm (d, 1H, J=8.8 Hz, CH arom,quin); 8.35 ppm (s, 1H, CH=N); 8.02 ppm (m, 2H, CH arom,quin); 7.79 ppm (t, 1H, J=8.4 Hz, CH arom,quin); 7.64 ppm (t, 1H, J=7.6 Hz, CH arom,quin); 7.57 ppm (d, 2H, J=7.6 Hz, CH arom,phe); 7.42 ppm (t, 2H, J=7.6 Hz, CH arom,phe); 7.26 ppm (t, 1H, J=7.6 Hz, CH arom,phe). ^{13}C NMR (101 MHz, DMSO-d_6): δ 177.05, 154.26, 147.85, 143.56, 139.44, 136.72, 130.45, 129.57, 129.31, 128.63, 128.41, 127.72, 126.84, 126.17, 118.93. ESI-MS (+, m/z, MeOH): 328.7 $[M+Na]^+$, 307.3 $[M+H]^+$. IR (ATR): 3311 cm^{-1} and 3108 cm^{-1} ν N-H, 2934 cm^{-1} ν C-H aliph., 1592 cm^{-1} ν C=N, 1539 cm^{-1} and 1500 cm^{-1} ν C=C arom, 1115 cm^{-1} and 820 cm^{-1} ν C=S.

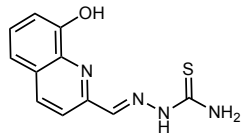

L5. 8-hydroxyquinoline-2-carboxaldehyde thiosemicarbazone. Thiosemicarbzide (104 mg 1.14 mmol), 8-hydroxyquinoline- 2-carboxaldehyde (192 mg, 1.11 mmol), MeOH (20 mL). White powder. Yield: 89%. CHNS analysis $C_{11}H_{10}N_4OS$ Calc: C 53.64%, H 4.09%, N 22.75%, S 13.02% Exp: C 53.49%, H 4.23%, N 23.02%, S 12.67%. ^{1}H NMR (400 MHz, DMSO-d_6): 11.85 ppm (s, 1H, C=N-NH); 9.84 ppm (s, 1H, -OH); 8.43 ppm (m, 2H, CH arom and -NH_2); 8.31 ppm (s, 1H, -NH_2); 8.28 ppm (m, 2H, CH arom. + CH=N); 7.44 ppm (t, 1H, J=8.8 Hz, CH arom.); 7.39 ppm (dd, 1H, J_o=8 Hz and J_m=1.3 Hz, CH arom.); 7.10 ppm (dd, 1H, J_o=8 Hz and J_m=1.3 Hz, CH arom.). ^{13}C NMR (101 MHz, DMSO-d_6): δ 178.90, 153.90, 152.32, 142.84, 138.62, 136.61, 129.26, 128.55, 118.91, 118.22, 112.58. ESI-MS (+, m/z, MeOH): 269.2 $[M+Na]^+$, 246.9 $[M+H]^+$. IR (ATR): 3378 cm^{-1}, 3238 cm^{-1} and 3146 cm^{-1} ν O-H and ν N-H, 3119 cm^{-1} ν C-H arom., 2984 cm-1 ν C-H aliph., 1601 cm-^{1} ν C=N, 1536 cm^{-1} and 1501 cm^{-1} ν C=C, 1078 cm^{-1} and 830 cm^{-1} ν C=S.

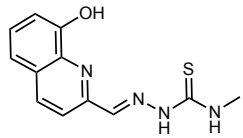

L6. 8-hydroxyquinoline-2-carboxaldehyde N^4-methyl-3-thiosemicarbazone. N^4-methyl-3-thiosemicarbazide (100 mg, 0.9 mmol), 8-hydroxy-2-quinolinecarboxaldehyde (165mg, 0.9 s mmol), MeOH (10 mL). White powder. Yield: 87%. CHNS analysis $C_{12}H_{12}N_4OS$: Calc: C 55.37%, H 4.65%, N 21.52%, S 12.32%. Exp: C 55.46%, H 4.66%, N 21.45%, S 12.14%. ^{1}H NMR (400 MHz, DMSO-d_6): 11.92 ppm (s, 1H, C=N-NH); 9.84 ppm (s, 1H, OH); 8.80 ppm (m, 1H, NH-C); 8.42 ppm (d, 1H, J=8.8 Hz, CH arom.); 8.31 ppm (d, 1H, J=8.8 Hz, CH arom.); 8.27 ppm (s, 1H, CH=N); 7.44 ppm (t, 1H, J=8 Hz, CH arom.); 7.39 ppm (dd, 1H, J_o=8 Hz and J_m=1.6 Hz, CH arom.); 7.11 ppm (dd, 1H, J_o=8 Hz and J_m=1.6 Hz, CH arom.); 3.07 ppm (d, 3H, J=4.4 Hz, N-CH_3). ^{13}C NMR (101 MHz, DMSO-d_6): δ 178.43, 153.89, 152.37, 142.31, 138.63, 136.56, 129.23, 128.53, 118.75, 118.23, 112.61, 31.43. ESI-MS (+, m/z, MeOH): 283.5 $[M+Na]^+$, 261.3 $[M+H]^+$. IR (ATR): 3385 cm^{-1}, 3349 cm^{-1} and 3143 cm^{-1} ν O-H and ν N-H, 3005 cm-1 ν C-H arom., 2958 cm^{-1} ν C-H aliph., 1630 cm-1 ν C=N, 1551 cm^{-1}, 1530 cm^{-1} and 1501 cm^{-1} ν C=C, 1101 cm^{-1} and 842 cm^{-1} ν C=S.

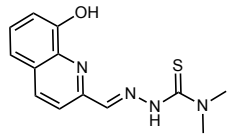

L7. 8-hydroxyquinoline-2-carboxaldehyde N^4,N^4-dimethyl-3-thiosemicarbazone. 8-Hydroxyquinoline-2-carboxaldehyde (147 mg, 0.849 mmol), N^4,N^4-dimethyl-3-thiosemicarbazide (99 mg, 0.831 mmol), MeOH (10 mL). Pale yellow powder. Yield: 50%. CHNS analysis $C_{13}H_{14}N_4SO$: Calc: C 56.92%, N 20.42%, H 5.14%, S 11.69%. Exp: C 56.74%, N 20.38%, H 5.16%, S 11.51%. ^{1}H NMR (400 MHz, DMSO-d_6): 11.40 ppm (s, 1H, C=N-NH); 9.78 ppm (s, 1H, OH); 8.39 ppm (s, 1H, CH=N); 8.30 ppm(d, 1H, J=8.8 Hz, CH arom.); 8.03 ppm (d, 1H, J=8.8 Hz, CH arom.); 7.44 ppm (t, 1H, J=8 Hz, CH arom.); 7.39 ppm (d, 1H, J=8 Hz, CH arom.); 7.12 ppm (dd, 1H, J_o=7.2 Hz and J_m=1.2 Hz, CH arom.); methyl peaks rely under water peak. ^{13}C NMR (101 MHz, DMSO-d_6): δ 181.12, 153.78, 152.53, 144.07, 138.58, 136.88, 129.11, 128.47, 118.30, 118.07, 112.60, 42.92.ESI-MS (+, m/z, MeOH): 297.4 $[M+Na]^+$, 275.4 $[M+H]^+$. IR (ATR): 3196 cm^{-1} ν O-H and ν N-H, 2940 cm^{-1} ν C-H aliph., 1613 cm^{-1} ν C=N, 1548 cm^{-1}, 1533 cm^{-1} and 1507 cm^{-1} ν C=C arom., 1424 cm^{-1} ν C-N arom., 1101 cm^{-1} and 827 cm^{-1} ν C=S.

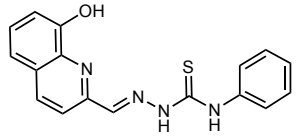

L8. hydroxyquinoline-2-carboxaldehyde N^4-phenyl-3-thiosemicarbazone. 8-hydroxyquinoline-2-carboxaldehyde (100 mg, 0.577 mmol), N^4-phenyl-3-thiosemicarbazide (97 mg, 0.577 mmol), MeOH (15 mL). Pale yellow powder. Yield 66%. CHNS analysis $C_{13}H_{14}N_4SO$: Calc: C 63.34%, N 17.38%, H 4.38%, S 9.94%. Exp: C 62.25%, N 17.39%, H 4.36%, S 10.05%.^{1}H NMR (400 MHz, DMSO-d_6): 12.25 ppm (s, 1H, C=N-NH); 10.38 ppm (s, 1H, S=C-NH-Ph); 9.91 ppm (s, 1H, OH); 8.60 ppm (d, 1H, J=8.8 Hz, CH arom,quin); 8.38 ppm (s, 1H, CH=N); 8.31 ppm (d, 1H, J=8.8 Hz, CH arom,quin); 7.56 ppm (d, 2H, J=7.6 Hz, CH arom,quin); 7.44 ppm (m, 4H, CH arom,quin and CH arom,phe); 7.26 ppm (t, 1H, J=7.6 Hz, CH arom.quin); 7.12 ppm (d, 1H, J=7.2 Hz, CH arom,phe). ^{13}C NMR (101 MHz, DMSO-d_6): δ 177.03, 153.95, 152.18, 143.42, 139.47, 138.70, 136.56, 129.35, 128.66, 128.62, 126.86, 126.15, 119.21, 118.24, 112.61. ESI-MS (+, m/z, MeOH): 345.5 $[M+Na]^+$, 322.8 $[M+H]^+$. IR (ATR): 3549 cm^{-1} ν O-H, 3347 cm^{-1} and 3126 cm^{-1} ν N-H, 2961 cm-^{1} ν C-H aliph., 1586 cm^{-1} ν C=N, 1524 cm-^{1} and 1504 cm^{-1} ν C=C arom., 1101 cm^{-1} and 836 cm^{-1} ν C=S.

Preparation of the complexes.
The complexes were synthesised dissolving the ligand in a hot solution of MeOH:EtOH 2:1. The metal was dissolved in an adjusted volume of glacial acetic acid and then added dropwise to the solution of the ligand. The reactions were quick, with a sudden change in colour (typically from colourless to orange red) and the formation of a coloured solid. The reactions were stirred for 24 h then filtered via filter paper and analysed. **Bi1-2** demonstrated to be not stable in DMSO solution. **Bi3-8** were also isolated as crystals and characterized by means of X-ray diffraction. **Bi3** crystals were badly twinned and therefore its refinement could not be carried out properly. The last refinement of **C3**.

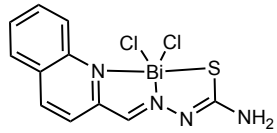

Bi1. L1 (100 mg, 0.4 mmol), $BiCl_3$ (137 mg, 0.4 mmol), MeOH:EtOH 2:1 (15 mL). Orange powder. Yield 62%. CHNS analysis $C_{11}H_9BiCl_2N_4S$: Calc: C 25.95%, N 11.00%, H 1.78%, S 6.30%. Exp: C 25.64%, N 10.82%, H 1.96%, S 5.98%. ESI-MS (+, m/z, MeOH): 473.7 $[M\text{-}Cl]^+$. IR (ATR): 3352 cm^{-1}, 3270 cm^{-1}, 3214 cm^{-1} and 3182 cm^{-1} ν N-H, 2940 cm^{-1} ν C-H arom., 1636 cm^{-1} ν C=N, 1115 cm^{-1} and 820 cm^{-1} ν C=S.

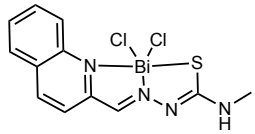

Bi2. L2 (50 mg, 0.205 mmol), $BiCl_3$ (65 mg, 0.205 mmol) , MeOH:EtOH 2:1 (7 mL). Bright yellow powder. Yield 78%. CHNS analysis $C_{12}H_{11}BiCl_2N_4S$ Calc: C 27.55%, N 10.71%, H 2.12%, S 6.13%. Exp: C 27.44%, N 10.33%, H 1.98%, S 5.84%. ESI-MS (+, m/z, MeOH): 486.7 $[M\text{-}Cl]^+$. ESI-MS (+, m/z, MeOH): 486.7 $[M\text{-}Cl]^+$. IR (ATR): 3308 cm^{-1}, 3229 and 3202 cm^{-1} ν N-H, 3043 cm^{-1} ν C-H arom., 2961 cm^{-1} ν C-H aliph., 1580 cm^{-1} ν C=N, 1100 cm_{-1} and 836 cm^{-1} ν C=S.

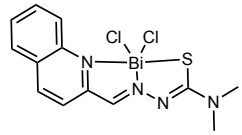

Bi3. L3 (50 mg, 0.194 mmol), $BiCl_3$ (61 mg, 0.194 mmol), MeOH:EtOH 2:1 (7 mL). Dark orange powder. Yield 72 %. CHNS analysis $C_{13}H_{13}BiCl_2N_4S$. Calc: C 29.07%, N 10.43%, H 2.44%, S 5.95%.Exp: C 29.23%, N 10.25%, H 2.48%, S 6.00%. ^{1}H NMR (400 MHz, DMSO-d_6): 9.16 (s, 1H, CH=N) 8.71 ppm (dd, 1H, J1=8.5 Hz, J2=0.9 Hz, CH arom); 8.30 ppm (dd, 1H, J_o=8.5 Hz and J_m=1.0 Hz ,CH arom.); 8.12 ppm (dd, 1H, J_o=8.3 Hz and J_m=1.4 Hz, CH arom); 7.96 ppm (m, 2H, CH arom.), 7.74 ppm (td, 1H, J_o=7 Hz and J_m=1.2 Hz, CH arom.); 3.33 (s, 6H, $N(CH_3)_2$). ^{13}C NMR (101 MHz, DMSO-d_6): δ 176.24, 150.69, 150.41, 146.09, 139.97, 132.13, 128.89, 128.54, 128.46, 127.56, 124.11, 41.32. ESI-MS (+, m/z, MeOH)): 501.5 $[M\text{-}Cl]^+$. IR (ATR):1639 cm-^{1} v C=N, 1142 cm^{-1} and 868 cm^{-1} v C=S.

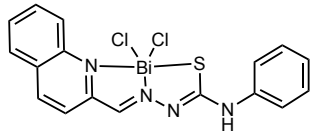

Bi4. L4 (50mg, 0.163 mmol), $BiCl_3$ (51 mg, 0.163 mmol), MeOH:EtOH 2:1 (7 mL). Yield 53%. CHNS analysis $C_{17}H_{13}BiCl_2N_4S$ Calc: C 34.89%, N 9.58%, H 2.24%, S 5.48%. Exp: C 34.70%, N 9.98%, H 2.21%, S 5.63%. ^{1}H NMR (400 MHz, DMSO-d_6): 10.17 ppm (s, 1H, NH), 9.27 ppm (s, 1H, CH=N), 8.74 ppm (d, 1H, J=7.8 Hz, CH arom,quin); 8.42 ppm (d, 1H, 8.7 Hz, CH arom,quin); 8.13 ppm (m, 2H, CH arom,quin); 8.05 ppm (d, 1H, J=8.6 Hz, CH arom,quin); 7.97 ppm (t, 1H, J=7.8 Hz, CH arom,quin); 7.75 ppm (m, 2H, CH arom,phen); 7.36 ppm (d, 2H, J=7.4 Hz, CH arom,phen); 7.08 (t, 1H, J=7.4 Hz, CH arom,phen). ^{13}C NMR (101 MHz, DMSO-d_6): δ 177.09, 154.25, 147.84, 143.54, 140.07, 136.76, 130.47, 129.29, 129.10, 128.64, 128.43, 127.74, 126.81, 121.46, 118.95. ESI-MS (+, m/z, MeOH): 548.8 $[M\text{-}Cl]^+$. IR (ATR): 3279 cm^{-1} v N-H, 3052 cm^{-1} v C-H arom., 1598 cm^{-1} v C=N, 1109 cm^{-1} and 744 cm^{-1} v C=S.

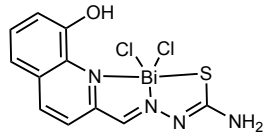

Bi5. L5 (50mg, 0.202 mmol), $BiCl_3$ (64mg, 0.202 mmol), MeOH:EtOH 2:1 (7 mL). Light brown powder. Yield 83%. CHNS analysis $C_{11}H_9BiCl_2N_4OS$ Calc.: C 25.16%, N 10.67%, H 1.73%, S 6.10%. Exp.: C 25.23%, N 10.44%, H 1.98%, S 6.46%. ^{1}H NMR (400 MHz, DMSO-d_6): 11.87 ppm (s, 1H, N-NH); 8.44 ppm (d, 2H, CH arom. and NH); 8.33 ppm (s, 1H, NH); 8.30 ppm (d, 1H, CH arom.), 8.28 ppm (s, 1H, CH=N); 7.45 ppm (t, 1H, CH arom., J_o=8.4 Hz and $J_{o'}$=7.6 Hz); 7.39 ppm (dd, 1H, CH arom., J_o=8.4 Hz and J_m=1.6 Hz); 7.11 ppm (dd, 1H, CH arom., J_o=7.6 Hz and J_m=1.6 Hz). ^{13}C NMR (101 MHz, DMSO-d_6): δ 178.93, 153.71, 152.23, 142.48, 138.22, 136.96, 129.29, 128.65, 118.95, 118.27, 112.75. ESI-MS (+, m/z, MeOH): 453.1 $[Bi^{3+}+L^{2-}]^+$. IR (ATR): 3482 cm^{-1}, 3282 cm^{-1} and 3173 cm^{-1} ν N-H, 2982 cm^{-1} ν C-H arom., 1618 cm^{-1} ν C=N, 1086 cm^{-1} and 842 cm^{-1} ν C=S.

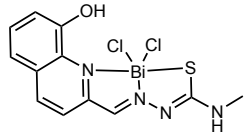

Bi6. L6 (50mg, 0.192 mmol), $BiCl_3$ (60mg, 0.192 mmol), MeOH:EtOH 2:1 (7 mL). Bright yellow powder. Yield 82%. CHNS analysis $C_{12}H_{12}BiCl_2N_4OS$ Calc.: C 26.68%, N 10.37%, H 2.24%, S 5.93%. Exp.: C 26.48%, N 10.67%, H 2.15%, S 6.19%. ^{1}H NMR (400 MHz, DMSO-d_6): 11.98 ppm (s, 1H, N-NH); 8.83 ppm (m, 1H, NH(CH3)); 8.45 ppm (d, 1H, CH arom., J=8.4 Hz); 8.37 ppm (d, 1H, CH arom., J=8.4 Hz); 8.29 ppm (s, 1H, CH=N); 7.45 ppm (m, 2H, CH arom.); 7.13 ppm (d, 1H, CH arom., J=8.4 Hz); 3.07 ppm (d, 3H, NH(CH_3)). ^{13}C NMR (101 MHz, DMSO-d_6): δ 178.43, 153.74, 152.30, 142.04, 138.36, 136.79, 129.24, 128.59, 118.77, 118.25, 112.73, 31.43. ESI-MS (+, m/z, MeOH): 467.2 $[Bi^{3+}+L^{2-}]^+$. IR (ATR): 3246 cm^{-1} and 3108 cm^{-1} ν N-H and ν O-H, 3058 cm^{-1}, 2982 cm^{-1}, 2929 cm^{-1} and 2867 cm^{-1} ν C-H, 1595 cm^{-1} ν C=N, 1350 cm^{-1} ν C-N arom., 1142 cm^{-1} and 847 cm^{-1} ν C=S.

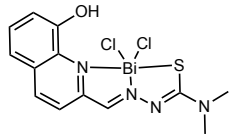

Bi7. L7 (50mg, 0.182 mmol), $BiCl_3$ (57mg, 0.182 mmol), MeOH:EtOH 2:1 (7 mL). Dark yellow powder. Yield 71%. CHNS analysis $C_{13}H_{13}BiCl_2N_4SO$ Calc.: C 28.22%, N 10.13%, H 2.37%, S 5.80%. Exp.: C 28.28%, N 9.79%, H 2.51%, S 5.45%. ^{1}H NMR (400 MHz, DMSO-d_6): 9.08 ppm (br, 1H, Ar-OH); 8.65 ppm (br, 1H, CH arom); 7.96 ppm (br, 1H, CH arom); 7.52 ppm (br, 3H, CH arom and CH=N) 7.29 ppm (br, 1H, CH arom); 3.46 ppm (br, 6H, $N(CH_3)_2$). ^{13}C NMR (101 MHz MHz, DMSO-d_6): δ 177.40, 165.35, 152.46, 148.96, 148.57, 139.76, 137.73, 129.17, 124.17, 119.02, 114.43, 25.60. ESI-MS (+, m/z, MeOH): 481.1 $[Bi^{3+}+L^{2-}]^+$. IR (ATR): 3043 cm-^{1} ν N-H, 2926 cm^{-1} and 2852 cm-^{1} ν C-H arom., 1574 cm^{-1} ν C=N, 1142 cm^{-1} and 849 cm-^{1} ν C=S.

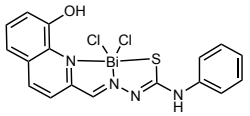

Bi8. L8 (50mg, 0.155 mmol), $BiCl_3$ (49 mg, 0.155 mmol), MeOH:EtOH 2:1 (7 mL). Bright red powder. Yield 57%. CHNS analysis $C_{17}H_{13}BiCl_2N_4OS$ Calc.: C 33.96%, N 9.32%, H 2.18%, S 5.33%. Exp.: C 33.71%, N 8.99%, H 2.26%, S 4.97%. ^{1}H NMR (400 MHz, DMSO-d_6): 10.09 ppm (s, 1H, Ar-OH); 9.45 ppm (s, 1H, CH=N); 8.72 ppm (d, 1H, CH arom,quin); 8.06 ppm (d, 1H, CH arom,quin); 7.76 ppm (d, 2H, CH arom,phe); 7.58 ppm (m, 2H, CH arom,quin and CH arom,phe); 7.35 ppm (m, 2H, CH arom,quin); 7.07 ppm (t, 1H, CH arom,phe). ^{13}C NMR (101 MHz MHz, DMSO-d_6): δ 171.28, 159.88, 149.17, 148.17, 141.49, 141.21, 140.23, 138.60, 137.01, 136.59, 129.02, 128.61, 123.69, 121.49, 112.65. ESI-MS (+, m/z, MeOH): 529.5 $[Bi^{3+}+L^{2-}]^+$. IR (ATR): 3329 cm^{-1} ν N-H, 2999 cm^{-1} ν C-H arom., 1598 cm-1 ν C=N, 1477 cm^{-1}, 1460 cm^{-1} and 1427 cm^{-1} ν C=C, 1115 cm^{-1} and 750 cm^{-1} ν C=S.

Crystallographic data collection and crystal structure determination

Single crystal X-ray diffraction analyses were carried out with a Bruker D8Venture diffractometer equipped with a kappa goniometer and an Oxford cryosystem. Microfocused MoKα radiation (λ = 0.71073) was used and Lorentz polarization and absorption correction were applied by the SADABS[49] procedure. The phase problem was solved by direct methods and the structures were refined by full-matrix least-squares on all F2 using SHELXL[50,51], as implemented in the OLEX2 suite of programs. Analytical expressions of neutral atom scattering factors were taken from the International Tables for X-Ray Crystallography[52]. The structure drawings were obtained using ORTEPIII[53] and Mercury[54]. CCDC 2152012-2152016 contain the crystallographic data. X-Ray structure determination analysis were performed on crystals grown by recrystallization from the solvent (DMSO, DMF).

Microdilution MIC, MBC and time growth assay

Klebsiella pneumoniae NDM-1 (NTCT14331) carrying the bla_{NMD-1} metallo-carapenemase gene was chosen to test the compounds. MIC (Minimum Inhibitory Concentration) and MBC (Minimum Bactericidal Concentration) values were determined by standard broth micro-dilution method following ISO 20776-1 (2019). Briefly, frozen stock bacteria were put into 5 mL of Buffered Peptone Water (BPW) and incubated for 2 h at 37 °C or until 0.5 McFarland. The bacterial density was adjusted to reach a final concentration of 5×10^5 $CFUmL^{-1}$. Tested antimicrobials or Bi(III) compounds were added in triplicate into 96-microwells plates, performing 2-fold serial dilution, followed by the addition of water (for antibacterial screening) or antibiotic (for combination therapy screening) and the prepared bacterial inocula. Time growth assay were performed by recording the optical density of the plates at 620 nm every 0, 1, 2, 4, 8, 18, 24h. Wells with only DMSO at the tested concentration (5%) were used as background control. The plates were incubated at 37 °C for 18-24h. The MIC values were determined by both visual reading and OD reading at 620 nm using a spectrophotometer plate reader. MIC is the lowest concentration of a drug/broth dilution of antimicrobials that results in inhibition of the growth of the tested bacteria[55]. The MBC values were determined by transferring 100 µL of broth microdiluition to a Triptic Soy Agar plate, a solid nonselective medium, and incubated at 37 °C for 18-24h. The MBC values were chosen as the lowest concentration of a drug/broth dilution of antimicrobials that results in killing 99.9% of the tested bacteria[55]. The FICI values were determined as follows: $FICI=FIC_A+FIC_B=C_A/MIC_A+C_B/MIC_B$, where MIC_A and MIC_B are the MIC values of compounds A and B alone, and C_A and C_B are the effective concentration of A and B when administrated. A FICI index of 0.5 or less indicates synergistic effect; between 0.5 and 4 the effect is additive. FICI index greater than 4 denotes antagonism[46,47]. The compounds were tested starting from the higher concentration possible that was 250 µM for the complexes and 125 µM for the ligands due to solubility concerns. Meropenem concentration were chosen following EUCAST 2021 guidelines and breakpoints table. The MIC values for **L3** was set at 250 µM and for **C4** at 500 µM. EDTA served as positive control.

UV-vis spectroscopy

UV-vis spectra were collected using 1 cm quartz cuvette at room temperature. Aliquots of 1 mM or 250 µM were titrated to bismuth complexes solution (50 µM or 25 µM) in PBS (5mM, pH 7.4)/5% DMSO or pure DMSO in a range of 300-600 nm. The UV titration curve were fitted with the program Hypspec2014.[56]

Cytotoxicity

A549 lung carcinoma cells and HuDe human epithelial cells were purchased from the American Type Culture Collection (ATCC, Manassas, VA, USA). Cells were grown in RPMI 1640 medium containing 10% heat inactivated foetal bovine serum, 100 UmL^{-1} penicillin and streptomycin at 37 °C with 5% CO_2. Experiments were conducted with cells in the log phase. Cells (100 000 mL^{-1}) were seeded into 24-well plates 18-24h and then exposed to compoundsThe half maximal inhibitory concentration (IC_{50}) was determined as the concentration resulting in 50% cell growth reduction compared with untreated control cells

2. Chemical space exploration of a second-generation Bi(III), Ga(III), and Sb(III) compounds in the fight against superbugs

This chapter's research involved a collaborative work with Dr Martina Rega from the University of Parma's Department of Veterinary Medicine (Food Inspection Unit). The project was co-supervised by Prof Franco Bisceglie and Prof Cristina Bacci.

Abstract

The exploration of chemical space holds significant promise for advancing drug discovery and development, offering a rich source of novel compounds and insights for future therapeutic agents.

In the initial chapter, one lead compound was identified for its ability to restore carbapenem sensitivity in NDM-1 producing bacterial strains. The identified lead compound served as the focal point for exploring the surrounding chemical space. Alterations were made to the central metal core, substituting it with other p-block metals like gallium(III) and antimony(III). Simultaneously, the ligand was modified, resulting in a limited, but efficient, chemical space around the lead compound, enabling the exploration of their associated biological activities.

After synthesis and characterization, the compounds were tested for their antimicrobial activity. Notably, compounds derived from pyridine with a dimethyl substituent exhibited heightened antibacterial activity. Bismuth-based compounds demonstrated lower MIC values than gallium and antimony compounds, especially against gram-positive bacteria. Synergistic studies against resistant strains shed light on potential combination therapies and identified four new lead compounds. Furthermore, *in vivo* toxicity was evaluated using *Galleria mellonella* larvae.

Chemical space in drug development

Chemical space, a fundamental concept in cheminformatics, encompasses the expansive realm of all conceivable molecules and chemical compounds adhering to specific construction principles and boundary conditions.[57]

One significant facet of chemical space pertains to potential pharmacologically active molecules, estimated to be a number around 10^{60}, although determining its precise size remains a challenge. Estimations are often based on the Lipinski rules, which include criteria such as a molecular weight limit of 500 and the use of carbon, hydrogen, oxygen, nitrogen, and sulfur as constituent elements. This approximation also assumes a maximum of 30 atoms, allowing for branching and up to 4 rings, ultimately arriving at an estimate of 10^{63}.[58] It is important to note that this figure is occasionally misattributed as the size of the entire organic chemistry space, which would be significantly larger when accounting for elements like halogens.

In addition to these theoretical spaces, there are practical subdivisions like the drug-like space and lead-like space, partly defined by Lipinski's rule of five. Another concept, known drug space (KDS), is defined by the molecular descriptors of marketed drugs. KDS serves as a valuable tool for predicting the boundaries of chemical spaces for drug development, aiding in the comparison of designed and synthesized molecules with the molecular descriptor parameters defined by established drug compounds.[59] This comprehensive understanding of chemical space is instrumental in accelerating the discovery and development of novel pharmaceuticals, ultimately advancing healthcare and improving patient well-being.

Metallodrug chemical space

Exploring the chemical space generated by metal-based drugs is of paramount importance in modern drug discovery and development. Metal-based compounds offer unique properties and mechanisms of action not found in traditional organic molecules. This uncharted chemical space presents a wealth of opportunities to design novel therapeutic agents for a wide range of diseases, from cancer to

infectious diseases. Understanding and systematically cataloguing this chemical space through a dedicated metallodrug database could accelerate the discovery of effective treatments, enable the development of predictive models for drug activity, and foster innovation in drug design. Furthermore, by harnessing computational approaches and cheminformatics, researchers can gain insights into the structure-activity relationships of metal-based compounds, leading to the design of more potent and selective metallo-drugs.[60]

Exploration of the chemical space around a lead compound

In the initial chapter, I identified a lead compound named **Bi4**, for its ability to restore carbapenem sensitivity in NDM-1 producing bacterial strains. **Bi4** is characterized by a bismuth metal core and a ligand featuring a thiosemicarbazone moiety. The ligand consists of a quinoline moiety, derived from the corresponding aldehyde, while the thiosemicarbazone included a phenyl ring as a substituent. Another compound, **Bi3**, demonstrated similar activity, albeit with the thiosemicarbazone moiety substituted by two methyl groups instead of a phenyl ring. To investigate the chemical space surrounding these known lead compounds, I opted to alter the central metal core, substituting it with other p-block metals such as gallium(III) and antimony(III). Furthermore, I explored variations in the ligand without introducing additional coordination sites, achieved by simplifying the quinoline to a single pyridine ring while retaining the active structural motifs within the thiosemicarbazone moiety. This strategy led to the synthesis of a limited chemical space around the lead compounds, allowing for the exploration of their connected biological activities (Figure 19).

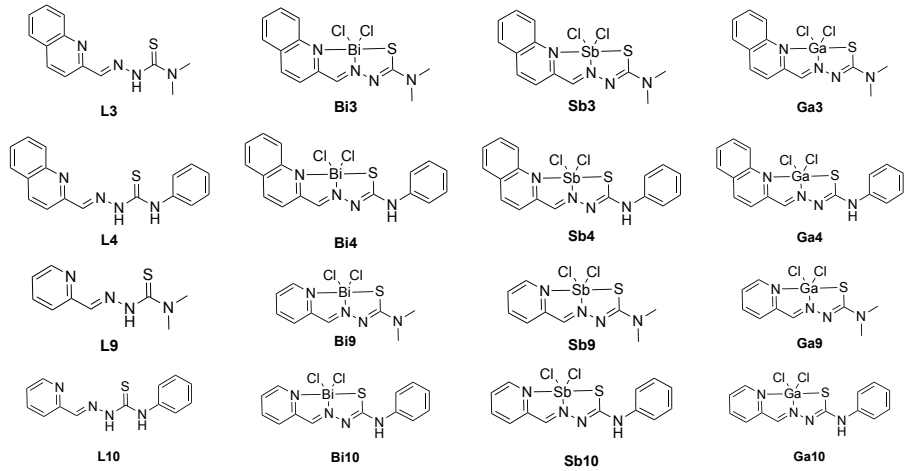

Figure 19. Set of synthesized compounds for chemical space exploration

Synthesis

The ligands were synthesized using the same procedure described in the first chapter, involving a condensation reaction between the respective aldehyde and N^4-substituted thiosemicarbazides (Scheme 4). This reaction was carried out in methanol with acetic acid as a catalyst. Upon refrigeration of the reaction mixture, the ligands precipitated and were subsequently collected. To form the Bi(III) complexes, the ligands were dissolved in a hot mixture of MeOH, and $BiCl_3$ was added in the smallest possible quantity of acetic acid necessary to dissolve it. The Ga(III) and Sb(III) complexes were prepared similarly, dissolving $GaCl_3$ and $SbCl_3$ in MeOH. The compounds were characterized by ^1H NMR, ^{13}C NMR, IR and the purity was confirmed by CHNS element analysis.

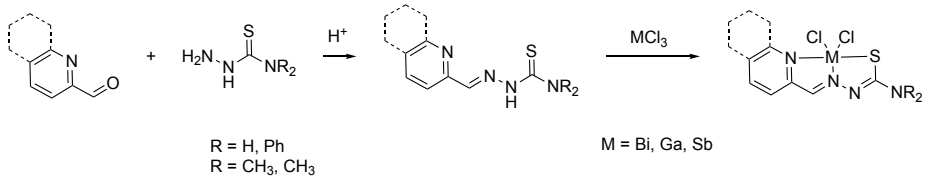

*Scheme 4. Synthetic route of the ligands **L3-4**,**L9-10** and their corresponding Bi(III), Ga(III), Sb(III) complexes.*

Antimicrobial activity of Bi(III), Sb(III), Ga(III) compounds

The antimicrobial activity was assessed by determining the minimum inhibitory concentrations (MIC) of the compounds against distinct bacterial strains, including *E. coli, K. pneumoniae* ESβL, *K. pneumoniae* NDM-1, and Methicillin-resistant *S. aureus* (MRSA) (Table 3). The structural diversity within the compounds allows for a comparison of the various structural motifs:

- Pyridine vs. quinoline: comparing compounds derived from pyridine and quinoline, I observe that pyridine derivatives show 12 times MIC ≤ 25 μM, while quinoline derivatives show only 6 times. This suggests that the use of pyridine as a starting structure contributes to increased antibacterial activity.

- Dimethyl vs. phenyl ring: within each structural group (pyridine or quinoline), compounds with a dimethyl substituent generally exhibit lower MIC values than those with a phenyl ring. This implies that the presence of a dimethyl substituent enhances the antibacterial activity of these compounds.

- Metals comparison: bismuth-based compounds consistently demonstrate lower MIC values than gallium and antimony compounds for most bacterial strains. This suggests that bismuth-based compounds are more active against these bacteria.

- Gram-negative vs. gram-positive: *E.coli* and *K. pneumoniae* (both ESβL and NDM-1) are gram-negative bacteria, while MRSA is a gram-positive bacterium. The compounds appear to have varying degrees of effectiveness but in general the compounds are more active against the gram-positive bacteria

The structural motifs, as expected, of the compounds play a crucial role in determining their antibacterial activity. Compounds derived from pyridine with a dimethyl substituent appear to be the most active against the tested bacterial strains, especially when combined with bismuth.

Table 3. Antibacterial activity displayed as MIC (μM) against different bacteria strain. Color code: White indicates compounds with negligible antibacterial activity, deep blue represents the most active compounds, and light blue signifies those with lower activity.

	Aldehyde	TSC	Ec	Kp ESβL	Kp NDM-1	MRSA	HuDe[a]
L3			> 100	200	200	25	> 100
Bi3			**	50	50	6.25	> 100 (106 ± 16)**
Sb3			> 100	50	50	12.5	> 100
Ga3			> 100	25	12.5	50-25	> 100
L4			> 100	>200	>200	> 100	> 100
Bi4			> 100	>200	>200	12.5	54 ± 10**
Sb4	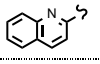		> 100	>200	>200	100	> 100
Ga4	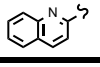		> 100	>200	>200	> 100	> 100
L9			100	25	25	50	> 100
Bi9			25	50	200	12.5	60 ± 2
Sb9			50	12.5	25	25	> 100
Ga9			25	6.25	12.5	50	> 100
L10			> 100	>200	>200	> 100	> 100
Bi10			> 100	>200	>200	6.25	> 100 (110 ± 2)
Sb10			**	100	200	6.25	> 100
Ga10			> 100	50	50	> 100	> 100
AB*			1	8	256	1	nd

*Ec – Escherichia coli, Kp – Klebsiella pneumoniae, MRSA – methicillin resistant S. aureus; CC_{50} – HuDe cells; **refer to Chapter 1; *AB – Antibiotic: MEM – Meropenem for Kp NDM-1, CTX – Cefataxime for Kp ESβL, VAN – Vancomycin for MRSA. PMX – Polymixin B for Ec. * in μg/mL MIC determined with n=4 across two biological replicates.*

Synergic studies against *Klebsiella pneumoniae* NDM-1 and *Klebsiella pneumoniae ESβL*

To gather information regarding a potential combination therapy, *Klebsiella pneumoniae* NDM-1 and *Klebsiella pneumoniae* ESβL that developed resistance due to the expression of beta-lactamase were selected for synergistic studies. *Klebsiella pneumoniae* NDM-1 produces a metallo-β-lactamase capable of hydrolyzing carbapenem β-lactams, and it exhibits a meropenem MIC of 256 μg/mL. On the other hand, *Klebsiella pneumoniae* ESβL produces serine-β-lactamase (SHV-18) and has a cefotaxime MIC of 8 μg/mL.

A subinhibitory concentration of the compounds, designed to ensure they would not affect bacterial growth, was chosen to be MIC/4 and kept constant. Meanwhile, the concentration of the clinical approved antibiotic was reduced to detect any potential decrease in MIC and a potential restoration of antibiotic sensitivity.

Notably, there was no observed increase in sensitivity in *Klebsiella pneumoniae* ESβL, which produces a serine beta-lactamase. However, in the strain producing the metallo-beta-lactamase NDM-1, I detect a series of compounds capable of reducing the MIC of meropenem (Table 4). I confirmed that the compounds previously studied in the first chapter, **L3** and **Bi4**, indeed exhibited antibacterial activity in a combination therapy. Additionally, I identified four more active compounds: **Sb4**, **Ga4**, **Bi9**, and **Bi10**. These compounds represent close modifications of the lead compound **Bi4**, with **Sb4** and **Ga4** being its analogs with the different metal center, while **Bi9** and **Bi10** maintain the bismuth core with newly designed ligands.

Table 4. Minimum inhibitory concentration of the antibiotic against resistant strains of K. pneumoniae in combination therapy with a sub inhibitory concentration of the compounds (MIC/4). Color code: White indicates compounds with negligible antibacterial activity, deep blue represents the most active compounds, and light blue signifies those with lower activity. The structure of the compounds with promising activity is highlighted in grey.*

	Aldehyde	TSC	Kp NDM-1		Kp ESβL	
			Effective concentration (MIC/4) [μM	*MIC meropenem [μgmL^{-1}]*	*Effective concentration (MIC/4) [μM*	*MIC cefotaxime [μgmL^{-1}]*
L3			50	8	50	>8
Bi3			12.5	64	12.5	>8/8
Sb3			12.5	64	12.5	>8
Ga3			3.1	>64	6.2	>8
L4			50	64	50	>8/8
Bi4			50	32	50	>8/8
Sb4			50	8	50	>8
Ga4			50	16	50	>8
L9			6.2	>64	6.2	>8/8
Bi9			50	4	12.5	>8/8
Sb9			6.2	>64/64	3.1	>8
Ga9			3.1	>64	1.5	>8
L10			50	>64	50	>8
Bi10			50	32	50	>8
Sb10			50	>64	25	>8/8
Ga10			12.5	>64	12.5	>8

Cytotoxicity assessment in eukaryotic cells

To assess the cytotoxicity of these compounds on eukaryotic cells, we employed HuDe human epithelial cells. In general, the compounds exhibited no significant cytotoxic effects. However, when HuDe cells were exposed to the highest concentration of bismuth compounds **Bi9** and **Bi10**, noticeable morphological alterations compared to the control group were observed, along with a slight decrease in cell proliferation.

Given the promising adjuvant potential of **Bi9**, **Bi10**, **Sb4**, and **Ga4**, we will proceed to evaluate their *in vivo* toxicity using the *Galleria mellonella* model.

In vivo toxicity evaluation using *Galleria mellonella* larvae

In the realm of antibiotic discovery, novel and reliable models are essential for assessing in vivo toxicity and efficacy. One such model, *Galleria mellonella*, often referred to as the greater wax moth larva, has gained prominence for its remarkable utility in this context.[61] This model offers several advantages, including ease of use, cost-effectiveness, and the ability to provide insights into the potential toxicity and therapeutic efficacy of compounds. Importantly, previous research has demonstrated a strong correlation between the toxicity data obtained from this animal model and higher organisms, such as murine models.[62]

Larvae were injected with a 10 µL water solution containing a maximum of 10% of the initial stock solution in DMSO for compound injection. A 10% DMSO solution served as the control. The solutions were prepared to have an *in vivo* concentration of 40 µM, 20 µM or 10 µM based on the compound solubility.[61] The larvae were incubated at 37 °C and monitored every 24h for one week. Larval performance was assessed according to the *G. mellonella* Health Index Scoring System.[63]

Remarkably, **Sb4, Ga4** and **Bi10** exhibited no signs of toxicity even at the highest concentration tested, which was 40 µM (equivalent to 19.9 mg/kg) for **Sb4**, 20 µM (equivalent to 28.9 mg/kg) for **Ga4** and 40 µM (equivalent to 11.4 mg/kg) for **Bi10** (Figure 20). On the other hand **Bi9** demonstrated toxicity when compared to

untreated and control groups, when the internal concentration of the compounds reached 40 µM (equivalent to 19.5 mg/kg).

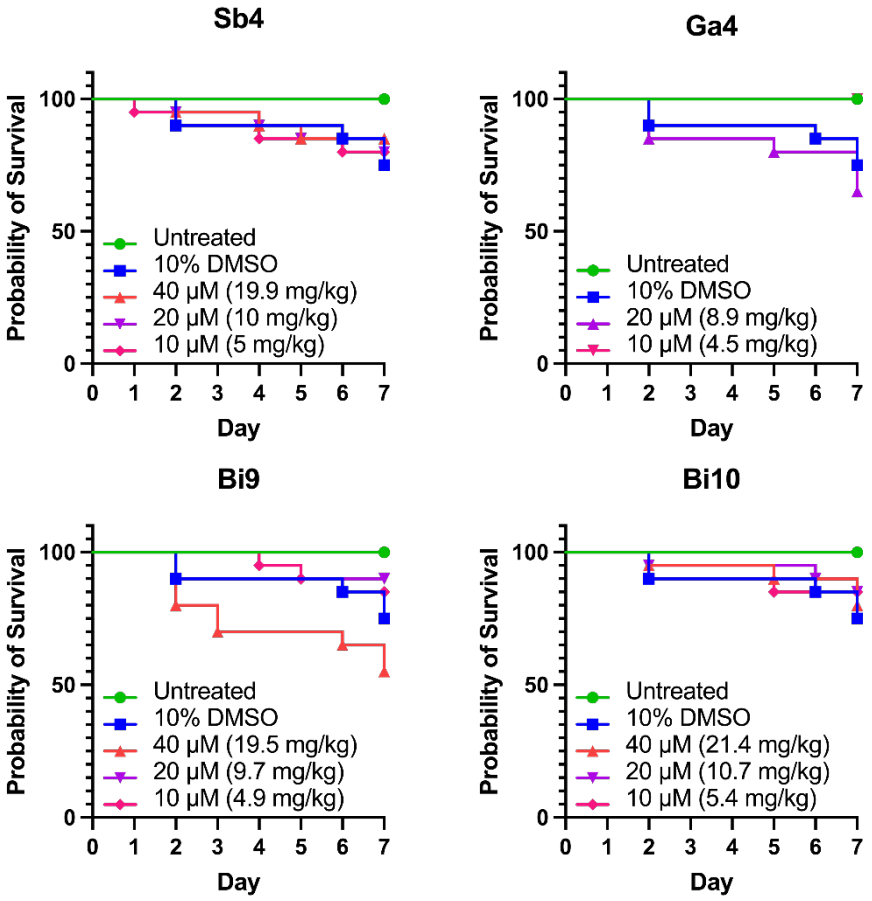

*Figure 20. Survival of G. mellonella (n = 20) recorded over a 7-Day period post-injection of **Sb4**, **Ga4**, **Bi9**, **Bi10.***

Conclusion

Through systematic modifications to both the central metal core and the ligand structures, I synthesized a set of compounds with antimicrobial activity. Notably, the findings underscore the advantages of compounds derived from pyridine with dimethyl substituents, suggesting a significant role for this structural motif in enhancing antibacterial properties. Furthermore, bismuth-based compounds emerged as potent contenders, particularly against gram-positive bacteria.

Synergistic studies showed the potential of combination therapies, revealing four novel lead compounds that could be helpful in restoring antibiotic sensitivity in resistant strains. Notably, these compounds exhibited no significant *in vitro* cytotoxicity. The *in vivo* toxicity was evaluated using *Galleria mellonella* larvae. Three compounds were considered safe and now are undergoing further biological characterization and *in vivo* efficacy tests.

In this chapter, I have demonstrated that systematic modifications hold promise in the search for a lead metal complex, paving the way to the exploration of the metallodrug chemical space and the discovery of a next generation of therapeutic agents.

Materials

All common laboratory chemicals were purchased from commercial sources and used without further purification: 4,4-dimethyl-3-thiosemicarbazide, 98 % (TCI); 4-phenyl-3-thiosemicarbazide, 99% (Sigma Aldrich); quinoline-2-carboxaldehyde, 97% (Sigma Aldrich); 2-pyridinecarboxaldehyde, 99% (Sigma Aldrich); $BiCl_3$, 98% (Sigma Aldrich); $SbCl_3$, 99% (Sigma Aldrich); $GaCl_3$, 99% (abcr). NMR were recorded on a Bruker Anova spectrometer at 400 MHz, with chemical shift reported in δ units (ppm). NMR spectra were referenced relative to residual NMR solvent peaks. Solvent used in the spectra's acquisitions is DMSO-d_6. The FT-IR measurements were recorded on Perkin Elmer's Spectrum Two in the 4000-400 cm^{-1} range, equipped with the UATR accessory. Elemental analyses were performed using Flashsmart CHNS Elemental Analyzer (Thermofisher Scientific). ESI-MS were recorded on a spectrometer with Single Quadrupole Detector (Sesto San Giovanni, MI, Italy). UV/Vis spectra were collected using a Thermofisher Scientific Evolution 260 Bio Spectrophotometer, using quartz cuvettes of 1 cm path length. **L3**, **L4**, **Bi3** and **Bi4** were synthetized according to our previous published procedure.

Preparation of the ligands.

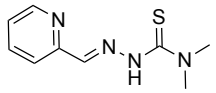

L9. N^4N^4-methyl-3-thiosemicarbazide (200 mg, 1.67 mmol) were dissolved in 10 mL of EtOH and maintained under stirring until complete dissolution of the solid. An equimolar amount of 2-pyridinecarboxaldehyde (0.160 mL, 1.67 mmol) was the added to the solution with 1 mL of acetic acid. The solution turned immediately pale yellow. The reaction was left under stirring for 24 h. Et_2O was then added. A white solid started form and it was isolated via filtration. White solid. Yield 68% ^1H NMR (400 MHz, DMSO-d_6): 11.18 ppm (s, 1H), 8.58 ppm (d, 1H, J=4.8 Hz), 8.23 ppm (s, 1H), 7.88 ppm (d, 1H, J=8.0), 7.83 ppm (m, 1H), 7.36 ppm (m, 1H), 3.31 ppm (s, 6H). ESI-MS (+, m/z, MeOH): 231. CHNS analysis: $C_9H_{12}N_4S$. Calc: C 51.90%, H 5.81%, N 26.90%, S 15.39% Exp: C 51.67%, H 5.92%, N 26.97%, S 15.21%.

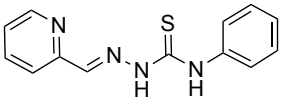

L10. N^4-phenyl-3-thiosemicarbazide (200 mg, 1.2 mmol) were dissolved in 10 mL of EtOH and maintained under stirring at room temperature until complete dissolution of the solid. An equimolar amount of 2-pyridinecarboxaldehyde (0.113 mL, 1.2 mmol) was then added to the solution with 1 mL of acetic acid. The solution turned immediately yellow. The reaction was left under stirring for 24 hours. After 24h the solid was filtered and washed with EtOH. With powder. Yield 79.6 %.^{1}H NMR (400 MHz, DMSO-d_6):12.03 ppm (s, 1H), 10.25 ppm (s, 1H), 8.59 ppm (m, 1H), 8.45 ppm (d, 1H), 8.20 ppm (s, 1H), 7.85 ppm (t, 1H), 7.56 ppm (m, 2H), 7.39 ppm (m, 3H), 7.23 ppm (m, 1H). ESI-MS (+, m/z, MeOH): 279 $[C_{13}H_{12}N_4S+Na]^+$, 257 $[C_{13}H_{12}N_4S+H]^+$. IR (ATR): 3034 cm^{-1} and 3110 cm^{-1} v N-H, 1593 cm^{-1} v C=N, 1108 cm^{-1} and 777 cm^{-1} v C=S. CHNS analysis: $C_9H_{12}N_4S$. Calc: C 60.92%, H 4.72%, N 21.86%, S 12.51% Exp: C 61.12%, H 4.63%, N 22.05%, S 12.23%.

Preparation of the complexes.

The complexes were prepared dissolving the ligands in 5 mL of methanol. $BiCl_3$ were dissolved in 1 mL of acetic acid, while $GaCl_3$ and $SbCl_3$ were dissolved in 1 mL of methanol. The metal then were added dropwise to the ligand solution. The mixture immediately changed color, and a precipitate started to form. The mixture was left stirring for one hour. The solid was then filtered on filter paper, and washed with methanol and dimethyl ether.

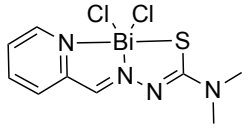

Bi9. Solvent MeOH. Yellow Powder. Yield 65%. ^{1}H NMR (400 MHz, DMSO-d6): 8.79 ppm (m, 2H), 8.09 ppm (m, 1H), 7.91 ppm (m, 1H), 7.60 ppm (m, 1H), 3.37 ppm (s, 6H,). ^{13}C NMR (400 MHz, DMSO): 172.47 ppm, 148.55 ppm, 140.11 ppm, 136.60 ppm, 127.87 ppm, 126.22 ppm, 124.29 ppm, 21.60 ppm. ESI-MS (+, m/z, MeOH): 452 $[C_9H_{11}BiClN_4S]^+$. IR (ATR): 1707 cm^{-1} v C=N. CHNS analysis: $C_9H_{11}BiCl_2N_4S$. Calc: C 22.19%, H 2.28%, N 11.50%, S 6.58%. Exp: C 22.07%, H 2.53%, N 10.35%, S 6.25%.

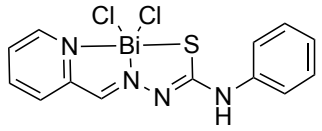

Bi10. Solvent MeOH/CH_3COOH. Yellow powder. Yield 90%. ^1H NMR (400 MHz, DMSO-d_6): 9.88 ppm (d,1H), 9.09 ppm (m, 2H), 8.17 ppm (t, 1H), 7.93 ppm (m, 1H), 7.73 ppm (d, 1H), 7.66 ppm (m, 2H), 7.32 ppm (m, 2H), 7.03 ppm (m, 1H).^{13}C NMR (400 MHz, DMSO) 172.54 ppm, 152.57 ppm, 149.83 ppm, 148.89 ppm, 141.73 ppm, 140.15 ppm, 128.95 ppm, 127.77 ppm, 126.31 ppm, 123.65 ppm, 121.06 ppm. ESI-MS (+, m/z, MeOH): 499 $[C_{13}H_{11}BiClN_4S]^+$. IR (ATR): 3400 cm^{-1} v N-H, 1601 cm^{-1} v C=N, 1095 cm^{-1} and 769 cm^{-1} v C=S. CHNS analysis: $C_{13}H_{11}BiCl_2N_4S$ Calc: C 29.17%, H 2.07%, N 10.47%, S 5.99%. Exp: C 29.22%, H 2.27%, N 10.25%, S 6.00%.

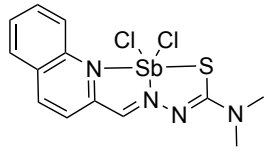

Sb3. Solvent MeOH. Red powder. Yield 69%. ^1H NMR (400 MHz, DMSO-d_6): 9.10 ppm (s, 1H), 8.83 ppm (d, 1H), 8.23 ppm (d, 1H), 8.21 ppm (d, 1H), 8.07 ppm (m, 2H), 7.84 ppm (t, 1H), 3.39 ppm (s, 6H). ^{13}C NMR (400 MHz, DMSO): 174.48 ppm, 147.07 ppm, 144.41 ppm, 141.44 ppm, 133.60 ppm, 129.72 ppm, 129.33 ppm, 128.92 ppm, 123.93 ppm, 123.74 ppm, methyl peaks rely under solvent peak. ESI-MS (+, m/z, MeOH): 413 $[C_{13}H_{13}ClN_4SSb]^+$. IR (ATR): 1590 cm-^{1} v C=N, 1507 cm-^{1} v C=C, 1114 cm^{-1} and 749 cm^{-1} v C=S. CHNS analysis: $C_{13}H_{13}Cl_2N_4SSb$. Calc: C 34.70%, H 2.91%, N 12.45%, S 7.12%. Exp: C 34.81%, H 2.90%, N 12.53%, S 7.35%.

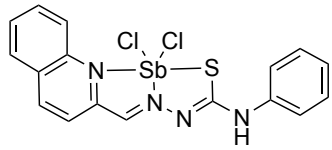

Sb4. Solvent MeOH. Red powder. Yield 58%. ^1H NMR (400 MHz, DMSO-d_6): 12.19 ppm (s, 1H), 10.39 ppm (s, 1H), 8.63 ppm (d, 1H), 8.40 ppm (d, 1H), 8.35 ppm (s, 1H), 8.04 ppm (d, 1H), 8.01 ppm (d, 1H), 7.64 ppm (t, 1H), 7.59 ppm (d, 2H), 7.43 ppm (d, 2H), 7.26 ppm (t, 1H). ^{13}C NMR (400 MHz, DMSO): 177.07 ppm, 154.25 ppm, 147.82 ppm, 143.53 ppm, 139.45 ppm, 136.76 ppm, 130.46 ppm, 129.28 ppm, 128.63 ppm, 128.41 ppm, 127.73 ppm, 126.80 ppm, 126.16 ppm, 121.87 ppm, 118.94 ppm. ESI-MS (+, m/z, MeOH): 461 $[C_{17}H_{13}ClN_4SSb]^+$. IR (ATR): 1599 cm^{-1} v C=N, 1538 cm^{-1} v C=C, 1114 cm^{-1} and 749 cm^{-1} v C=S. CHNS analysis: $C_{13}H_{11}Cl_2N_4SSb$. Calc: C 41.00%, H 2.63%, N 11.25%, S 6.44%. Exp: C 41.01%, H 2.64%, N 11.44%, S 6.62%.

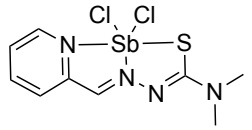

Sb9. Solvent MeOH. Yellow powder. Yield 61%. ^{1}H NMR (400 MHz, DMSO-d_6): 9.01 ppm (m, 1H), 8.91 ppm (s, 1H), 8.27 ppm (td, 1H, J=7.7 Hz), 8.00 ppm, (d, 1H, J=7.8), 7.76 ppm (m, 1H), 3.33 ppm (s, 6H). ^{13}C NMR (400 MHz, DMSO) δ (ppm): 174.44, 145.85, 145.19, 141.97, 141.30, 127.33, 127.13, 30.73. ESI-MS (+, m/z, MeOH): 362 $[C_9H_{11}ClN_4SSb]^+$. IR (ATR): 1601 cm^{-1} v C=N. CHNS analysis: $C_9H_{11}Cl_2N_4SSb$. Calc: C 27.03%, H 2.77%, N 13.85%, 8.02%. Exp: C 27.13%, H 2.81%, N 13.67%, 8.04%.

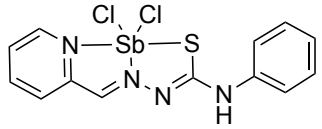

Sb10. Solvent MeOH. Orange powder. Yield 54%. ^{1}H NMR (400 MHz, DMSO-d_6): 10.38 ppm (s, 1H), 9.15 ppm (s, 1H), 9.09 ppm (d, 1H, J=5 Hz), 8.31 ppm (t, 1H, J=7.7 Hz) , 8.10 ppm (d, 1H, J=7.7 Hz), 7.84 ppm (m, 1H), 7.37 ppm (m, 4H), 7.11 ppm (t, 1H).^{13}C NMR. ESI-MS (+, m/z, MeOH): 443 $[C_{13}H_{11}ClN_4SSb\text{-}MeOH]^+$. IR (ATR): 3248 cm^{-1} v N-H, 1599 cm^{-1} v C=N. CHNS analysis: $C_{13}H_{11}Cl_2N_4SSb$. Calc: C 34.85%, H 2.48%, N 12.51%, S 7.16%. Exp: C 34.37%, H 2.61%, N 12.21%, S 6.94%. . ESI-MS (+, m/z, MeOH): 461 $[C_{17}H_{13}ClN_4SSb]^+$.

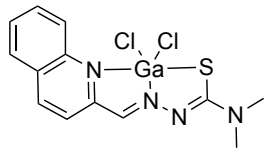

Ga3. Solvent MeOH. Orange powder. Yield 65%. ^{1}H NMR (400 MHz, DMSO-d_6): 9.29 ppm (s, 1H), 8.82 ppm (s, 1H), 9.29 ppm (s, 1H), 8.20 ppm (d, 1H), 8.17 ppm (d, 1H), 8.07 ppm (d, 1H), 7.98 ppm (d, 1H), 7.76 ppm (t, 1H), 7.58 ppm (t, 1H), methyl peaks rely under solvent peak. ^{13}C NMR (400 MHz, DMSO): 178.44 ppm, 143.62 ppm, 136.18 ppm, 134.44 ppm, 132.76 ppm, 130.51 ppm, 129.45 ppm, 128.36 ppm, 123.86 ppm, 122.73 ppm, 122.08 ppm, 41.63 ppm. ESI-MS (+, m/z, MeOH): 361 $[C_{13}H_{13}ClGaN_4S]^+$. IR (ATR): 1590 cm-^{1} v C=N, 1513 cm-^{1} v C=C, 1134 cm^{-1} and 743 cm^{-1} v C=S.CHNS analysis: $C_{13}H_{13}Cl_2GaN_4S$. Calc: C 39.24%, H 3.29%, N 14.08%, S 8.06% Exp: C 39.35%, H 3.35%, N 13.99%, S 8.15%.

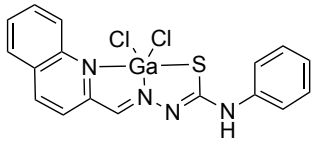

Ga4. Solvent MeOH. Dark orange powder. Yield 50%. Yield 65%. ^{1}H NMR (400 MHz, DMSO-d_6): 12.19 ppm (s, 1H), 10.28 ppm (s, 1H), 8.63 ppm (d, 1H), 8.40 ppm (d, 1H), 8.35 ppm (s, 1H), 8.00 ppm (d, 1H), 7.65 ppm (t, 1H), 7.57 ppm (d, 2H), 7.41 ppm (d, 2H), 7.26 ppm (t, 1H). ^{13}C NMR (400MHz, DMSO) 177.07 ppm, 154.26 ppm, 147.86 ppm, 143.57 ppm, 139.45 ppm, 136.72 ppm, 130.43 ppm, 129.31 ppm, 129.16 ppm, 128.62 ppm, 128.40 ppm, 127.71 ppm, 126.79 ppm, 126.15 ppm, 118.93 ppm. ESI-MS (+, m/z, MeOH): 409 $[C_{17}H_{13}ClGaN_4S]^+$.]$^+$. IR (ATR): 1602 cm^{-1} v C=N, 1541 cm^{-1} v C=C, 1120 cm^{-1} and 740 cm^{-1} v C=S CHNS analysis: $C_{13}H_{13}Cl_2GaN_4S$. Calc: C 45.78%, H 2.94%, N 12.56%, S 7.19% Exp: C 45.91%, H 2.96%, N 12.65%, S 7.39%.

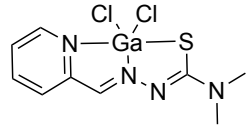

Ga9. Solvent MeOH. Yellow powder. Yield 59%. ^{1}H NMR (400 MHz, DMSO-d_6): 8.83 ppm (d, 1H), 8.50 ppm (s, 1H), 8.27 ppm (m, 1H), 7.90 ppm (m, 1H), 7.77 ppm (m,1H), 3.32 ppm (s, 6H). ^{13}C NMR (400 MHz, DMSO): 177.34 ppm, 146.13 ppm, 144.97 ppm, 142.81 ppm, 138.23 ppm, 126.44 ppm, 125.55 ppm, 31.18 ppm. ESI-MS (+, m/z, MeOH): 312 $[C_9H_{11}ClGaN_4S]^+$. IR (ATR): 1612 cm^{-1} v C=N. CHNS analysis: $C_9H_{11}Cl_2GaN_4S$. Calc: C 31.07%, H 3.19%, N 16.10%, S 9.22% Exp: C 31.27%, H 3.27%, N 15.99%, S 9.33%.

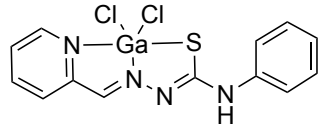

Ga10. Solvent MeOH. Orange powder. Yield 64%. ^{1}H NMR (400 MHz, DMSO-d_6): 10.24 ppm (s, 1H), 8.59 ppm (dt, 1H), 8.43 ppm (d, 1H), 8.20 ppm (s, 1H), 7.85 (m, 2H), 7.55 (m, 2H), 7.24 ppm (m, 1H), 7.11 ppm (m, 2H). ^{13}C NMR (400 MHz, DMSO): 170.05 ppm, 154.51 ppm, 151.49 ppm, 146.43 ppm, 143.54 ppm, 136.98 ppm, 129.13 ppm, 128.59 ppm, 126.59 ppm, 124.74 ppm, 122.21 ppm.
ESI-MS (+, m/z, MeOH): 359 $[C_{13}H_{11}ClGaN_4S]^+$. IR (ATR, cm^{-1}): 3346 cm^{-1} v N-H, 1596 cm^{-1} v C=N.
CHNS analysis: $C_{13}H_{11}Cl_2GaN_4S$. Calc: C 39.44%, H 2.80%, N 14.15%, S 8.10% Exp: C 39.87%, H 2.98%, N 14.11%, S 8.29%.

Microdilution MIC and MBC assay
The samples were tested for their antimicrobial activity against *Escherichia coli* W3110, *Staphylococcus aureus* COL (MRSA), *Klebsiella pneumoniae NDM-1* (NTCT14331) and *Klebsiella pneumoniae* ESβL (NCTC13368).

MIC (Minimum Inhibitory Concentration) values were determined by standard broth micro-dilution method following ISO 20776-1 (2019). Briefly, frozen stock bacteria were put into 5 mL of Buffered Peptone Water (BPW) and incubated for 2 h at 37 °C or until 0.5 McFarland. The bacterial density was adjusted to reach a final concentration of 5×10^5 $CFUmL^{-1}$. Tested antimicrobials were added in triplicate into 96-microwells plates, performing 2-fold serial dilution, followed by the addition of water (for antibacterial screening) or antibiotic (for combination therapy screening) and the prepared bacterial inocula. The plates were incubated at 37 °C for 18-24h. The MIC values were determined by OD reading at 620 nm using a spectrophotometer plate reader. MIC is the lowest concentration of a drug/broth dilution of antimicrobials that results in inhibition of the growth of the tested bacteria.[55]

In vivo tox (moth).
Larvae (400-500 mg) were sterilized by gently rubbing them with a paper towel soaked in an ethanoic solution and then individually injected with 10 µL of solution into one proleg using a 50 µL syringe (Hamilton Ltd). The compound was dissolved in DMSO (18 mM) and diluted to final concentrations of 40 µM, 20 µM and 10 µM with milliQ water. Five larvae were used for each group. Untreated larvae and larvae injected with 10% DMSO / milliQ water were included as negative controls. Following injection, the larvae were incubated at 37 °C and monitored every 24h for 7 days. Larval performance was assessed according to the *G.mellonella* Health Index Scoring System.[63] The experiments were repeated four separate times. The experiment was repeated four times

3. Gallium complexes as growth inhibitors of gram-negative bacteria

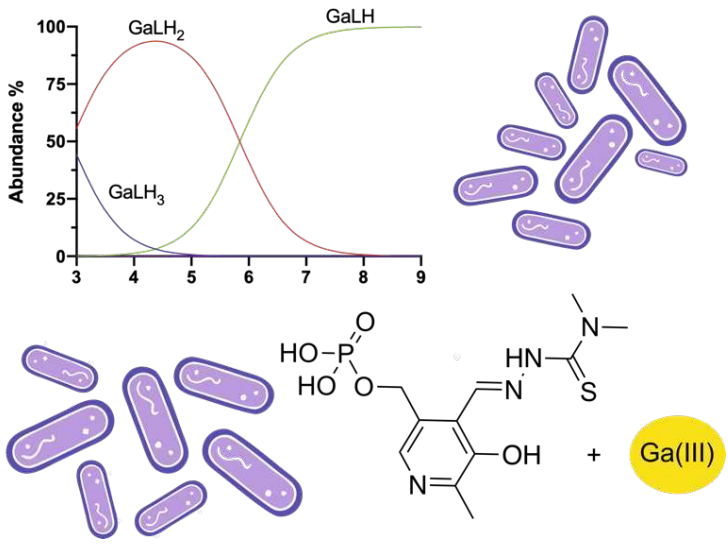

This chapter's research involved a collaborative work with Dr Martina Rega from the University of Parma's Department of Veterinary Medicine (Food Inspection Unit). The project was co-supervised by Professors Franco Bisceglie, Matteo Tegoni and Cristina Bacci.

Abstract

In this chapter, I have chosen to focus on investigating gallium(III) complexes because of their potential antimicrobial properties against various strains of bacteria, including *Klebsiella pneumoniae*, *Escherichia coli*, and *Pseudomonas aeruginosa*. These bacteria have developed diverse resistance mechanisms, such as the expression of β-lactamases (NDM-1, ESβL, or AmpC) and the production of biofilms.

The study centered on a series of thiosemicarbazones derived from pyridoxal, their corresponding Ga(III) complexes, and the speciation of Ga(III)/ligand systems in solution, with a focus on pH-dependent behavior. I determined proton dissociation constants and conditional stability constants of Ga(III) complexes using UV/Vis spectroscopy. This allowed me to identify the most significant species present under physiological pH conditions.

Moreover, I conducted cytotoxicity experiments to assess the safety of these compounds. Encouragingly, my findings indicate that these compounds exhibit potent activity against resistant Gram-negative bacterial strains, with minimal inhibitory concentrations in the micromolar range. Importantly, no cytotoxic effects were observed in eukaryotic cells. This suggests the potential for these gallium(III) complexes to serve as effective and safe candidates for combating antibiotic-resistant infections.

Diverse mechanisms of antibiotic resistance: beyond β-lactamases

Within this chapter, my focus has been on finding new metalloantibiotics against various bacteria which present different mechanisms of antibiotic resistance, extending beyond β-lactamases. The World Health Organization (WHO) has established a list of Critically Important Antimicrobials (CIAs), vital molecules for human medicine that should remain effective. Nevertheless, despite these efforts, instances of Antimicrobial Resistance (AMR) related to these antibiotics have emerged, underscoring the need for vigilant monitoring of their prevalence.[64]

Specifically, I've delved into bacteria exhibiting resistance to 3rd and 4th generation cephalosporins and carbapenems, all belonging to the class of β-lactam antibiotics. These bacteria acquire resistance through the production of β-lactamases, with notable examples being Extended-Spectrum β-lactamases (ESβL), AmpC β-lactamases, and carbapenemases. The genes responsible for these enzyme biosyntheses are often associated with mobile plasmid elements.[65]

Another significant mechanism of antibiotic resistance in Gram-positive bacteria involves a major threat known as *Vancomycin-resistant Enterococci* (VRE). *Enterococcus faecalis* and *Enterococcus faecium* are the predominant species in this group of bacteria. These bacteria have evolved resistance to vancomycin, a critical antibiotic often considered the last line of defense against numerous Gram-positive bacterial infections, including those caused by methicillin-resistant *Staphylococcus aureus* (MRSA).[66]

The spread of AMR can also be linked to the ability of bacteria to form biofilms.[67] These microbial communities reside within a self-produced extracellular polymeric matrix, allowing them to thrive in challenging environmental conditions. Furthermore, biofilm populations can acquire additional antibiotic resistance genes through horizontal gene transfer from other organisms, facilitating the diffusion of AMR.[68]

Given WHO's identification of priority pathogens in 2017,[69] particularly Gram-negative bacteria with developed resistance mechanisms, I decided to assess my compounds against a pool of resistant Gram-negative and Gram-positive

bacteria. This pool includes two distinct strains of *Klebsiella pneumoniae* capable of producing different types of β-lactamases (NDM-1 and ESβL), two different strains of *Escherichia coli* with the ability to produce ESβL or form biofilms, and a strain of *Pseudomonas aeruginosa* capable of producing AmpC. To provide a comprehensive perspective, I also included a clinically isolated Gram-positive strain, *Vancomycin-resistant Enterococcus spp*, another CIA-resistant pathogen.

The antimicrobial potential of gallium(III) salts

Gallium(III) shares chemical similarities with iron(III) and can serve as an iron(III) mimic within both eukaryotic and prokaryotic organisms. It can effectively target iron-dependent proteins. Notably, in physiological conditions, Gallium(III) lacks redox activity and has the potential to disrupt iron metabolism, leading to the generation of oxidative stress.[70]

Furthermore, it is worth mentioning that Gallium nitrate has received FDA approval in the form of the Ganite® formulation, where it acts as a bone resorption inhibitor. Additionally, Gallium(III) salts have been the subject of research regarding their antimicrobial properties across various strains, demonstrating promising activity in this context.[37,70–72]

Exploring gallium(III)-complexes with a pyridoxal moiety: insights into their antimicrobial potential

In this chapter, my focus is directed toward the examination of gallium(III)-complexes, specifically those in which I have integrated the pyridoxal moiety into the ligand design.

Pyridoxal is renowned for its role in metabolic processes within both prokaryotic and eukaryotic cells. Recently, it has also been employed in research on resistant pathogens to identify new bacterial targets.[73] Pyridoxal belongs to the vitamin B6 group, which includes pyridoxine, pyridoxamine, and their respective 5'-phosphates. Pyridoxal phosphate, the active form, predominates in animal tissues. Its absorption is regulated through phosphatase-mediated hydrolysis, enabling the non-phosphorylated form to passively diffuse into cells.[74]

I functionalized pyridoxal 5'-phosphate and pyridoxal with thiosemicarbazide (**L11**, **L12**, **L14**, and **L15**) or semicarbazide (**L13** and **L16**) as illustrated in Figure 21. To explore potential variations in their biological behavior, I chose to utilize the phosphorylated forms (**L11**-**L13**) to enhance the compounds' water solubility. Additionally, I introduced two methyl groups on the terminal nitrogen N^4 of **L12** and **L15** to increase the ligands' hydrophobicity, allowing me to investigate the electron-donating effect of these groups in metal coordination. The synthesis of semicarbazide derivatives **L13** and **L16** provided an opportunity to study the influence of oxygen as a coordinating atom concerning gallium(III). The chemical and antimicrobial properties of the compounds under study allowed us to explore their Structure-Activity Relationship (SAR).

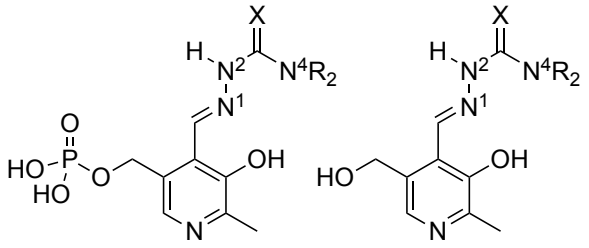

L11 X=S R=H
L12 X=S R=CH_3
L13 X=O R=H

L14 X=S R=H
L15 X=S R=CH_3
L16 X=O R=H

*Figure 21. Structure of the ligands with elucidation of the nitrogen numeration of the thiosemicarbazide (**L11-12**, **L14-15**) and semicarbazide (**L13**, **L16**) moiety.*

Synthesis

The ligands were synthetized according to adapted general procedures previously reported.[75–77]. Briefly, the reaction involves a condensation process between two aldehydes, namely pyridoxal 5'-phosphate and pyridoxal, and various thiosemicarbazides or semicarbazide compounds. This reaction took place in either methanol or water, depending on the solubility of the reactants, with acetic acid serving as the catalyst.

To characterize the resulting compounds, I employed a comprehensive range of analytical techniques including ^{1}H NMR spectroscopy, ^{13}C NMR spectroscopy, ESI-MS, IR spectroscopy, and elemental analysis. Additionally, I prepared the

corresponding Ga(III) complexes, **GaL11**–**GaL16**, in situ and characterized them using UV/Vis spectroscopy and HR-MS.

Exploring pH-dependent species distribution in gallium(III) complexes

The bioactivity of the metal compounds is strongly dependent on the prevalent species at the physiological pH of 7.4. The distribution of these species at various pH levels is intricately tied to their relative stability, which, in turn, is closely connected to the proton dissociation constants of the coordinating donor groups. To determine the speciation of the gallium(III)/ligand systems, I conducted a series of pH-metric UV/Vis titrations. These titrations were performed on solutions containing the ligands both independently and in conjunction with 1 equivalent of Ga(III) nitrate.

The ligands and Ga(III)/L systems in alkaline solutions (approximately pH 11) were progressively titrated with 0.1 M HCl, reducing the pH to around 3. The UV/Vis spectra were collected after each titrant addition. Representative spectra for the titration of **L15** and Ga(III)/**L15** are reported in Figure 22a and Figure 22c. Analyzing the spectral dataset from the ligand titration enabled the determination of proton dissociation constants (K_a), which are reported in in the form of pK_a. In Table 5 the logarithm of the global formation constants of the Ga(III) complexes (log β) are also reported along with the calculated conditional formation constants of the 1:1 **GaL11**-**GaL16** adducts at pH 7.4 (log K_{app}).

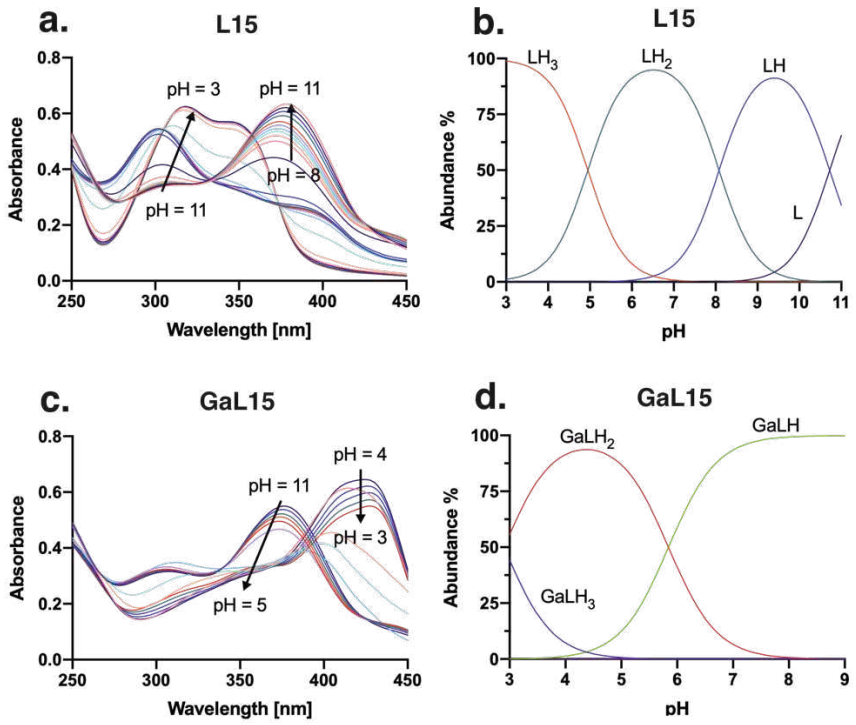

Figure 22. ***a.*** *UV/Vis absorption spectra of* ***L15*** *at different pH (C_{L15} = 50μM).* ***b.*** *Representative species distribution diagram of* ***L15*** *(C_{L15} = 100μM).* ***c.*** *UV/Vis absorption spectra of the Ga^{3+}/**L15** system at different pH (C_{L15} = 50μM; Ga/**L15** = 1:1).* ***d.*** *Representative species distribution diagram of the Ga^{3+}/**L15** system (C_{L15} = 100μM; Ga/**L15** = 1:1). All experiments were performed in aqueous solution, T =298 K, I = 0.1 mol L^{-1} (KCl).*

In their fully protonated forms, the pyridoxal phosphate derivatives **L11**-**L13** possess four functional groups capable of undergoing proton dissociation in aqueous solutions: the phosphate moiety (with potential for two protons), the protonated pyridyl nitrogen, the phenolic OH, and the N^2H group of the (thio)semicarbazone moiety. In the case of **L11** and **L12**, spectrophotometric data allowed us to determine four out of the corresponding five pK_a values. The first pK_a, associated with the phosphate group, was unsurprisingly too low to be observed within the experimental pH range. The data analysis indicated that for all three **L11**-**L13** derivatives, the pK_{a1} is below 2.5.

Conversely, in the semicarbazone derivative **L13**, the NH(C=O) group exhibited negligible dissociation in water, consistently yielding only three pK_a values within the experimental pH range of the titrations. On the other hand, the ligands **L14**-

L16 lack the phosphate group, resulting in an expectation of only three pK_a values.

The determined pK_a values are in good agreement with those reported for similar compounds.[78,79] **L12** undergoes a series of proton dissociations in its deprotonation process (Scheme 5). Initially, the phosphate group loses a proton, but this occurs outside the detectable pH range of the study. The second proton dissociation, with a pK_a range of 4.1-4.9, likely involves the protonated pyridyl nitrogen, a common behavior for pyridines with electron-withdrawing groups.[80] The third proton dissociation happens near a neutral pH (around pK_a 6) and corresponds to the second dissociation at the phosphate group. In contrast, phenol deprotonation typically occurs at a lower pH than the thiosemicarbazide NH group (pH 8 versus 11.5).

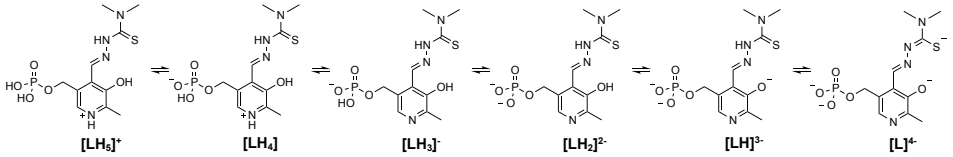

*Scheme 5. Representative proton dissociation equilibria for **L12**.*

The spectral data for the pH titration of the ligands in the presence of Ga(III) exhibit differences compared to those of the ligands alone at acidic and neutral pH levels. However, at alkaline pH (e.g., pH 11), the spectra closely resemble each other, indicating the probable presence of uncomplexed ligand and Ga(III) in the form of hydroxo-species.

To determine the stability constants of the gallium(III) complexes with the ligands, I utilized the pK_a values and the molar absorption spectra of the ligands in their various protonation forms as fixed parameters. Additionally, I included the formation constants of the hydroxo-complexes of Ga(III) in the calculations as fixed parameters for precise data treatment.[81] The spectrophotometric titration and its corresponding species distribution diagram are depicted in Figure 22c and Figure 22d.

The logβ values of the Ga(III)/ligand adducts are detailed in Table 5. The pH range in Table 1 corresponds to the pH range where fitting of the spectral data was feasible, using the molar spectra of the various protonated forms of the ligand as fixed parameters, alongside their associated pK_a values. Within these pH ranges, five out of the six ligands form $[GaLH_3]^{2+}$, $[GaLH_2]^{+}$, and [GaLH] species, with the latter being the predominant species at pH 7.4.

In the absence of X-ray structural data, proposing a coordination mode of the ligands to Ga(III) is challenging. However, when compared to analogous compounds in the literature, it is reasonable to hypothesize that the ligands in the solution coordinate with Ga(III) through the chelating moiety O^N^S/O.[82,83] Moreover, it is expected that the remaining coordination sites are occupied by water molecules, possibly resulting in the formation of hydroxo species, even at approximately neutral pH levels. It is evident from the speciation data that almost all Ga(III) is present in the form of Ga(III) complexes and not of Ga(III) hydroxo-species (with the exception of **L11** for which no precise information at this pH can be obtained from species distribution).

*Table 5. Proton dissociation (pK_a) of the H^+ of the ligands **L11**-**L16** with overall stability (log β)[a] and conditional stability (log K_{cond})[b] constants of Ga(III) complexes formed with the ligands **L11**-**L16**. T = 25.0 °C, I = 0.10 M (KCl) in H_2O. The constant for hydrolytic cleavage for Ga^{3+} are log$\beta_{GaH_{-1}}$ –3.93, log$\beta_{GaH_{-2}}$ –7.73, log$\beta_{GaH_{-3}}$ –12.38, log$\beta_{GaH_{-4}}$ –15.96.*[81]

Species/pK_a	Functional gr.	L11	L12	L13	Functional gr.	L14	L15	L16
pK_a								
$[LH_5]^+$; pK_{a1}	$OP=O(OH)_2$	<2.5	<2.5	<2.5				
$[LH_4]$; pK_{a2}	pyridyl NH^+	4.104(3)	4.82(2)	4.457(4)				
$[LH_3]^-$; pK_{a3}	$OP=O(O^-)(OH)$	6.098(7)	5.93(9)	5.97(2)	Pyridyl NH^+	4.066(2)	4.949(2)	4.551(2)
$[LH_2]^{2-}$; pK_{a4}	phenolic OH	8.06(1)	7.39(7)	9.52(4)	Phenolic OH	8.048(4)	8.034(3)	8.603(8)
$[LH]^{3-}$; pK_{a5}	(C=S)NH	9.21(2)	8.71(1)	-	(C=S)NH	10.914(5)	10.720(8)	-
logβ								
$[GaLH_4]^{3+}$		45.1(3)	44.7(3)	–		–	–	–
$[GaLH_3]^{2+}$		41.1(3)	42.1(2)	44.61(3)		43.85(6)	43.64(9)	42.4(6)
$[GaLH_2]^{+}$		35.5(3)	36.9(2)	41.37(3)		39.72(6)	40.74(3)	38.1(6)
[GaLH]		-	30.9(3)	35.43(3)		34.67(5)	34.90(3)	30.8(6)
log K_{cond} (pH=7.4)		-	8.2(3)	12.27(3)		9.38(5)	9.78(3)	8.8(6)
pH range		3.2-6.3	3.0-7.4	2.8-9.3		3.5-8.5	3.3-8.9	3.3-7.7

[a] For the generic equilibrium pGa + qL + rH = $[Ga_pL_qH_r]$, $\beta = [Ga_pL_qH_r]/([Ga]^p \cdot [L]^q \cdot [H]^r)$; [b] K_{cond} = [Ga(III) bound to L]/([Ga(III) not bound to L]·[L not bound to Ga(III)])

Complex interactions between gallium(III) and ligands enhance antibacterial properties

The minimal inhibitory concentration (MIC) was assessed against various Gram-negative bacteria strains, including:

1. *Klebsiella pneumoniae* (NTCT14331), which harbors the bla_{NDM-1} metallo-carbapenemase gene and was initially isolated from a human blood infection.
2. Klebsiella pneumoniae (NCTC13368), capable of producing Extended-spectrum-β-lactamases (ESβL) encoded by the bla_{SHV-18} gene.
3. *Pseudomonas aeruginosa* clinical isolate (NCTC13713) displaying intrinsic upregulated AmpC β-lactamase activity.
4. Gram-negative *Escherichia coli* strains carrying ESβL genes (bla_{CTXM1}, bla_{CTXM2}, bla_{TEM}, and bla_{SHV}).
5. A non-pathogenic Gram-negative *Escherichia coli* (phylogenetic group A) with biofilm-producing ability.
6. A Gram-positive *Enterococcus spp* resistant to vancomycin (VRE) due to the presence of the VanA gene.

Among the compounds tested, **GaL12** and **GaL15** exhibited the lowest MIC values and demonstrated activity against all the tested Gram-negative bacteria (Table 6). The corresponding ligands, **L12** and **L15**, also displayed activity but with slightly higher MIC values. Interestingly, compounds with the $-OPO_3^{2-}$ moiety, such as **GaL12** and **L12**, showed slightly reduced activity compared to compounds with hydroxyl groups in the same position, suggesting that compounds with higher charges may encounter difficulties penetrating the cells. The active compounds **GaL12**, **L12**, **GaL15**, and **L15** are thiosemicarbazones featuring a doubly methylated N^4. In contrast, the corresponding compounds lacking N^4 substitution were only active at high concentrations, with no enhanced activity observed for gallium(III) compounds. Ligands **L12** and **L15** and their complexes **GaL12** and **GaL15** were more effective against the tested *E. coli* strains compared to *K. pneumoniae* strains. None of the compounds exhibited activity against the tested Gram-positive bacteria, indicating that this group of

compounds may hold promise for the development of selective antibacterial agents targeting Gram-negative species. Additionally, Minimum Bactericidal Concentration (MBC) testing revealed growth inhibition with MBC values exceeding the tested concentrations for all compounds. Notably, the pure $Ga(NO_3)_3$ inorganic salt displayed no activity, underscoring that the observed properties result from complex interactions between the metal and the ligand rather than the simple summation of individual properties.

Table 6. Antibacterial activity displayed as minimum inhibitory concentration (MIC; μM) against a panel of resistant bacteria strains

Bacteria	**Kp NDM-1**	**Kp ESβL**	**Ec ESβL**	**Ec biofilm**	**Pa AmpC**	**Ec VRE**	**HuDe[a]**
L11	1000	500	>1000	500	500	>1000	>100
GaL11	>1000	>1000	>1000	250	>1000	>1000	>100
L12	500	250	500	31.25	125	>1000	>100
GaL12	62.5	62.5-31.25	15.63	15.63	31.25	>1000	>100
L13	>1000	>1000	>1000	>1000	>1000	>1000	>100
GaL13	>1000	>1000	>1000	>1000	>1000	>1000	>100
L14	1000	500	1000	500	500	>1000	>100
GaL14	>1000	500	500	500	500	>1000	>100
L15	250	125	250	31.25	125	>1000	>100
GaL15	31.25	31.25	15.63	15.63	62.5	>1000	>100
L16	>1000	>1000	>1000	>1000	>1000	>1000	>100
GaL16	>1000	>1000	>1000	>1000	>1000	>1000	>100
MEM	256*	-	-	-	-	-	-
CTX	-	8*	16*	2*	32*	-	-
$Ga(NO_3)_3$	>1000	>1000	>1000	>1000	>1000	>1000	-

*[a] Cytotoxicity against HuDe cells as IC_{50} value. * μg/mL. Ec – Escherichia coli, Kp – Klebsiella pneumoniae, Ec – Enterococcus; MEM – Meropenem 1, CTX – Cefataxime. MIC determined with n=4 across two biological replicates*

Enhancing carbapenem sensitivity in *Klebsiella pneumoniae* NDM-1 with gallium(III) complexes

Klebsiella pneumoniae NDM-1 and Klebsiella pneumoniae ESβL were reference type culture (NCTC) and were chosen to test a combination therapy with the compounds and the antibiotics (meropenem and cefotaxime respectively).

Initially, we determined the Minimum Inhibitory Concentrations (MIC) of the antibiotics. Subsequently, we evaluated these MIC values in the presence of a sub-inhibitory concentration (MIC/4) of the synthesized compounds. The *Klebsiella pneumoniae NDM-1* produces a metallo β-lactamase able to hydrolyse the β-lactam of carbapenems and shows a meropenem MIC of 256 μg/mL, while

Klebsiella pneumoniae ESβL, produces serine-β-lactamase (SHV-18) and has a cefotaxime MIC of 8 μg/mL,

Notably, the pure ligands **L11**-**L16** and the Ga(III) semicarbazone derivatives **GaL13** and **GaL16** displayed no activity. However, when Ga(III) was complexed with thiosemicarbazone ligands (**GaL11**, **GaL12**, **GaL14**, and **GaL15**), the meropenem MIC significantly decreased to 64-32 μg/mL. This reduction was accompanied by a Fractional Inhibitory Concentration Index (FICI) of 0.5, indicating a synergistic interaction between meropenem and the gallium complexes of thiosemicarbazone ligands.[46,47] Among these complexes, **GaL12** and **GaL15** exhibited the most potent synergistic effect, requiring lower effective concentrations in the combination therapy compared to other compounds (Table 7). However, it is important to note that the synergism did not fully restore carbapenem sensitivity. Notably, only Ga(III)-complexes displayed synergism with the strain producing metallo-β-lactamase (MBL), suggesting potential inhibitory activity. On the other hand, *Klebsiella pneumoniae* ESβL, which produces a serine-β-lactamase, did not exhibit significant biological activity in response to the combination therapy involving any of the tested compounds.

Table 7. Minimum inhibitory concentration of the antibiotic against resistant strains of K. pneumoniae in combination therapy with a sub inhibitory concentration of the compounds (MIC/4).*

Bacteria	***K. pneumoniae* NDM-1**		***K. pneumoniae* ESβL**	
Compounds	**Effective concentration (MIC/4) [μM]**	**MIC meropenem [μg/mL]**	**Effective concentration (MIC/4) [μM]**	**MIC cefotaxime [μg/mL]**
L1	250	>64	125	>4
GaL1	250	64	250	>4
L2	125	>64	62.5	>4
GaL2	15.63	64	15.63	>4
L3	250	>64	250	>4
GaL3	250	>64	250	>4
L4	250	>64	125	>4
GaL4	250	64	125	>4
L5	62.5	>64	31.25	>4
GaL5	7.81	64-32	7.81	>4
L6	250	>64	250	>4
GaL6	250	>64	250	>4
$Ga(NO_3)_3$	250	>64	250	>4
Antibiotic*	-	256	-	8

**Meropenem for K. pneumoniae NDM-1, cefotaxime for K. pneumoniae ESβL.*

Bacterial selectivity: no toxicity in healthy eukaryotic cells

The selectivity of the compounds against bacterial strains was assessed by studying their cytotoxic effects on human epithelial HuDe cells, which served as a model for eukaryotic cells. Remarkably, all the ligands and complexes demonstrated no cytotoxicity even after a 24-hour treatment, with IC_{50} values exceeding 100 µM. Furthermore, a thorough examination of cell morphology revealed no discernible differences when compared to control lines. This underscores the compounds' notable selectivity for bacterial cells, as they exhibited no adverse effects on the tested healthy human cells.

Conclusion

I synthesized and characterized a series of ligands incorporating thiosemicarbazone or semicarbazone moieties derived from pyridoxal and their respective 5'-phosphates. I elucidated the speciation of Ga(III)/ligand systems through UV/Vis spectrophotometric titrations and calculated the stability of Ga(III)/L adducts. At pH 7.4, Ga(III) exists solely in the form of Ga(III) complexes in all examined gallium(III)/ligand systems.

These compounds underwent testing against various strains of *Klebsiella pneumoniae*, *Escherichia coli*, and *Pseudomonas aeruginosa*, which exhibit diverse resistance mechanisms, including β-lactamase production (NDM-1, ESβL, or AmpC) or biofilm formation. **GaL12** and **GaL15**, gallium(III) complexes of thiosemicarbazone ligands with dimethylated N-terminals, demonstrated antibacterial activity against drug-resistant Gram-negative bacteria, with MIC values ranging from 62.5 to 15.63 μM. The corresponding ligands **L12** and **L15** also exhibited antibacterial activity but with higher MIC values. Conversely, compounds derived from semicarbazide moieties (**L13**, **GaL13**, **L16**, **GaL16**) did not inhibit bacterial growth. These compounds displayed no activity against the Gram-positive *Enterococcus spp*. tested.

Additionally, in the combination therapy studies with NDM-1-producing *Klebsiella pneumoniae*, I observed synergism between meropenem and **GaL11**, **GaL12**, **GaL14**, and **GaL15**. Remarkably, this group of compounds demonstrated no cytotoxicity against eukaryotic cells, suggesting their potential suitability for developing selective antibacterial agents targeting Gram-negative bacteria.

Materials

All common laboratory chemicals were purchased from commercial sources and used without further purification: thiosemicarbazide, 99% (Sigma Aldrich); semicarbazide hydrochloride, 99% (Alpha Aeser); 4,4-dimethyl-3-thiosemicarbazide, 98 % (TCI); pyridoxal-5-phosphate, 98.5 % (Merck); pyridoxal hydrochloride, 99 % (Alfa Aesar); $Ga(NO_3)_3 \cdot H_2O$, 99.9 % (Aldrich); potassium hydroxide, 85% (Sigma Aldrich), Sodium hydroxide pellets (Carlo Erba), Meropenem (Aldrich), Cefotaxime sodium salt (Aldrich). Triptic Soy Agar (TSA; Biolife Italiana, Milan, Italy) and Buffered Peptone Water (BPW; Biolife Italiana, Milan, Italy) were commercially available.

NMR were recorded on a Bruker Anova spectrometer at 400 MHz, with chemical shift reported in δ units (ppm). NMR spectra were referenced relative to residual NMR solvent peaks. Solvent used in the spectra's acquisitions is DMSO-d_6, D_2O. NaOD was made starting from NaOH, with several cycles of dissolution/evaporation in D_2O. The FT-IR measurements were recorded on Perkin Elmer's Spectrum Two in the 4000-400 cm^{-1} range, equipped with the UATR accessory. Elemental analyses were performed using Flashsmart CHNS Elemental Analyzer (Thermofisher Scientific). ESI-MS were recorded on a spectrometer with Single Quadrupole Detector (Sesto San Giovanni, MI, Italy). HR-MS were recorded on a Thermo Scientific Orbitrap LTQ-XL (Rodano, MI, Italy). UV/Vis spectra were collected using a Thermofisher Scientific Evolution 260 Bio Spectrophotometer, using quartz cuvettes of 1 cm path length. Stock solution of the ligands (10 mM) and $Ga(NO_3)_3$ (10 mM) were freshly prepared in NaOH 0.1 M and HCl 0.1 M, respectively. Complexes was prepared in situ by mixing 1:1 the stock solutions of the ligands and the metal. Stock solution of meropenem (2048 μgmL^{-1}) and cefataxime (2560 μgmL^{-1}) was dissolved in sterile water and stored at -18 °C. The 96-wells plates optical density was recorded at 620 nm by Multiskan FC Version 1.00.75 by Thermofisher Scientific. The plates containing selected bacteria strains were incubated in ICN200 Super ArgoLab at 37 °C.

Preparation of the ligands.

The thiosemicarbazones were synthetized from adapted known synthetic procedures.[75–77]

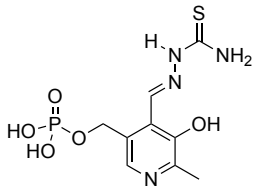

L11: Pyridoxal-5-phosphate (0.8 mmol, 201 mg) was completely dissolved in water (20 mL) under reflux. Thiosemicarbazide (0.8 mmol, 73.5 mg) was added. A bright yellow precipitate started to form. The reaction was stirred at room temperature for 8 more hours. The solid was filtered on filter paper, washed with cold ethanol, diethyl ether and dried under vacuum. Yellow powder. Yield: 80%. CHNS analysis $C_9H_{13}N_4O_5PS$. Calc: C 33.75, H 4.09, N 17.49, S 10.01. Found: C 33.90, H 4.22, N 17.15, S 9.65. ^{1}H NMR (400 MHz, D_2O, pH 13) δ 8.36 (s, 1H, NH-N=), 7.66(s, 1H, CH arom.), 4.86 (m, 2H, CH_2), 2.29 (s, 3H, CH_3). ^{13}C NMR (400 MHz, D_2O, pH 13) δ 176.30 (C=S), 160.38 (C-OH), 146.40 (C arom.), 143.37 (C=N), 133.59 (C arom.), 127.07(C arom.), 126.65(C arom.), 62.32(-CH_2-), 16.26(-CH_3). ^{31}P NMR (400 MHz, D_2O, pH 13) δ 3.76. ESI-MS (+, m/z, MeOH): calc. 343.0, found 343.2 $[M+Na]^+$. IR (ATR, cm^{-1}): 3354 cm^{-1}, 3283 cm^{-1}, 3142 cm^{-1} ν NH and ν OH; 1642 cm^{-1} ν C=N; 1585 cm^{-1} ν C=C, 1040 cm^{-1} ν N-C=S; 852 cm^{-1} ν C=S.

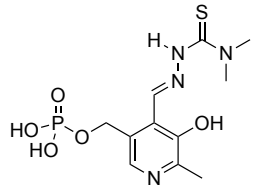

L12: Pyridoxal-5-phosphate (0.25 mmol, 624 mg) was dissolved in hot water (60 mL) with 1 mL of acetic acid. The mixture was kept under stirring and reflux until complete dissolution of the powder. Then 4,4'-dimethyl-3-thiosemicarbazide (301 mg, 0.25 mmol) was added. The formation of a yellow to orange precipitate started shortly after the addition of 4,4'-dimethyl-3-thiosemicarbazide. The reaction mixture was stirred at room temperature for 8 h. The solid was filtered on filter paper, washed with cold ethanol, diethyl ether and dried under vacuum. Yellow powder. Yield: 82 %. CHNS analysis $C_{11}H_{17}N_4O_5PS$. Calc: C 37.93, H 4.92, N 16.09, S 9.20. Found: C 37.66, H 4.90, N 15.82, S 9.36.^{1}H NMR (400 MHz, D_2O, pH 13) δ 8.51(s, 1H, NH-N=), 7.64 (s, 1H, CH arom.), 4.80 (m, 2H, CH_2), 3.16 (s, 6H, N-CH_3), 2.31(s, 3H, CH_3).^{13}C NMR (400 MHz, D_2O, pH 13) δ 181.46 (C=S), 168.36 (C-OH), 150.69 (C arom.), 146.16 (C=N), 134.47(C arom.), 131.99 (C arom.), 129.52 (C arom.), 61.77 (-CH_2-), 40.04 (N-CH_3), 18.20 (-CH_3).^{31}P NMR (400 MHz, D_2O, pH 13) δ 3.68. ESI-MS (+, m/z, MeOH): calc. 349.07, found 349.21 $[M+H]^+$; calc. 371.05, found 371.17 $[M+Na]^+$. IR (ATR, cm-1): 3167 cm^{-1}, 2987 cm^{-1} ν NH and ν OH; 1625 cm^{-1} ν C=N,1555 cm^{-1} ν C=C, 1098 cm^{-1} ν N-C=S, 841 cm^{-1} ν C=S.

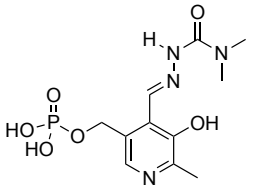

L13: Pyridoxal-5-phosphate (1.43 mmol, 353 mg) were dissolved in hot water (13 mL) under reflux for 30 minutes. Semicarbazide hydrochloride (1.43 mmol, 160 mg) were dissolved in water (2 mL) and then slowly added to the reaction solution. A precipitate starts to form shortly after. The reaction was stirred at room temperature for 4 hours. The solid was filtered on filter paper, washed with cold ethanol, diethyl ether and dried under vacuum. White precipitate. Yield: 88%. CHNS analysis $C_9H_{13}N_4O_6P$. Calc: C 35.54, H 4.31, N 18.42; Found: C 35.28, H 4.44, N 18.39. ^{1}H NMR (400 MHz, D_2O, pH 13) δ 8.20 (s, 1H, NH-N=), 7.69 (s, 1H, CH arom.), 4.79 (m, 2H, CH_2), 2.25 (s, 3H, CH_3). ^{13}C NMR (400 MHz, D_2O, pH 13) δ 196.01 (C=O), 160.22 (C-OH), 158.12 (C arom.), 151.70 (C arom.), 146.25 (C arom.), 141.16 (C=N), 61.95 (-CH_2-), 16.44 (-CH_3). ^{31}P NMR (400 MHz, D_2O, pH 13) δ 3.32.ESI-MS (+, m/z, MeOH): calc. 305.0, found 305.2 $[M+H]^+$. IR (ATR, cm^{-1}): 3376 cm^{-1}, 3160 cm^{-1} ν NH and ν OH; 1742 cm^{-1} ν CO; 1560 cm^{-1} ν C=C.

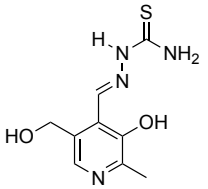

L14: Pyridoxal hydrochloride (0.9 mmol, 200 mg) and KOH (0.9 mmol, 59 mg) were dissolved in 20 mL of water at room temperature. Thiosemicarbazide (0.9 mmol, 82 mg) was then added. A precipitate starts to form shortly after. The reaction was stirred at room temperature for 4 hours and then filtered on paper filter. The solid was filtered on filter paper, washed with cold ethanol, diethyl ether and dried under vacuum. Yellow powder. Yield: 40%. CHNS analysis for $C_9H_{12}N_4O_2S$: C 44.99, H 5.03, N 23.32, S 13.34. Found: C 44.79, H 5.05, N 23.16, S 13.02.^{1}H NMR (400 MHz, DMSO-d_6): δ 11.61 ppm (s broad, 1H, NH=N), 9.67 ppm (s broad, 1H, phenolic OH), 8.58 ppm (s, 1H, CH=N), 8.33 ppm (s broad, 1H, NH_2), 8.10 ppm (s broad, 1H, NH_2), 8.0 ppm (s, 1H, CH arom.), 5.26 ppm (s, 1H, aliphatic OH), 4.59 ppm (s, 2H, CH_2), 2.41 ppm (s, 3H, CH_3).^{13}C NMR (400 MHz, DMSO-d_6): δ 149.56, 147.46, 142.50, 139.44, 133.35, 122.09, 59.40, 31.17, 19.60. ESI-MS (+, m/z, MeOH): calc. 263.3, found 263.1 $[M+Na]^+$. IR (ATR, cm^{-1}): 3440 cm^{-1}, 3374 cm^{-1}, 3260 cm^{-1}, 3160 cm^{-1}, 3090 cm^{-1} ν NH and ν OH, 1620 cm^{-1} ν C=N, 1528 cm^{-1} ν C=C, 1030 cm^{-1} ν N-C=S, 820 cm^{-1} ν C=S.

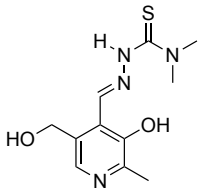

L15: Pyridoxal hydrochloride (3.3 mmol, 682 mg) and KOH (3.3 mmol, 157 mmol) were dissolved in 10 mL of hot MeOH. 4,4'-3-thiosemicarbazide (3.3 mmol, 398 mg) was then added. A precipitate starts to form shortly after. The reaction was stirred at room temperature for 8 hours. The solid was filtered on filter paper, washed with cold ethanol, diethyl ether and dried under vacuum. Yellow powder. Yield: 86 %. CHNS analysis for $C_{11}H_{16}N_4O_2S$: C 49.24, H 6.01, N 20.88, S 11.95. Found: C 49.11, H 6.16, N 20.83, S 12.16; ^{1}H NMR (400 MHz, DMSO-d_6): 12.38 ppm (s, 1 H, NH), 11.67 ppm (s, 1H, phenolic OH), 8.90 ppm (s, 1 H, CH=N), 7.94 ppm (s, 1H, CH arom.), 5.38 ppm (s, 1H, aliphatic OH), 4.60 ppm (s, 2H, CH_2), 2.42 ppm (s, 3H, CH_3), methyl peaks rely under water peak. ^{13}C NMR (400 MHz, DMSO-d_6): δ 181.64, 164.24, 150.36, 145.52, 132.46, 128.90, 127.53, 61.59, 38.84, 20.72. ESI-MS (+, m/z, MeOH): calc. 269.1, found 269.2 $[M+H]^+$; calc. 291.1, found 291.2 $[M+Na]^+$. IR (ATR, cm^{-1}): 3451 cm^{-1}, 3232 cm^{-1} ν NH and ν OH, 1678 cm^{-1} ν C=N, 1514 cm^{-1} ν C=C, 1046 cm^{-1} ν N-C=S, 806 cm^{-1} ν C=S.

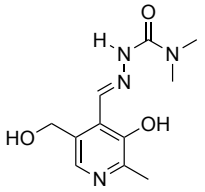

L16: Pyridoxal hydrochloride (0.96 mmol, 196 mg) and KOH (0.96 mmol, 46 mg) were dissolved in 5 mL of water at room temperature. Semicarbazide hydrochloride (0.96 mmol,106 mg) were dissolved apart in water (2 mL) and then slowly added to the pyridoxal solution A precipitate starts to form shortly after. The reaction was stirred at room temperature for 4 hours. The solid was filtered on filter paper, washed with cold ethanol, diethyl ether and dried under vacuum. White powder. Yield: 95%. CHNS analysis for $C_9H_{12}N_4O_p$: C 48.21, H 5.39, N 24.99; Found: C 48.31, H 5.46, N 25.14.^{1}H NMR (400 MHz, DMSO-d_6): 11.08 (s, 1H, NH), 8.40 (s, 1H, CH=N), 8.09 (s, 1H, CH arom.), 6.62 (s, 2H, NH_2), 5.62 (s broad, 1H, OH aliphatic), 4.69 (s, 2H, CH_2), 2.53 (s, 3H, CH_3). ^{13}C NMR (400 MHz, DMSO-d_6): δ 155.28 (C=O), 151.48 (C-OH), 144.15 (C arom.),137.36 (C=N), 135.28 (C arom.), 132.98 (C arom.), 127.05 (C arom.), 59.98 (-CH_2-), 16.58 (-CH_3); ESI-MS (+, m/z, MeOH): calc. 247.1, found 247.2 $[M+Na]^+$. IR (ATR, cm^{-1}): 3461 cm^{-1}, 3350 cm^{-1}, 3278 cm^{-1} , 3134 cm^{-1} ν NH and ν OH, 1699 cm^{-1} ν C=O, 1579 cm^{-1} ν C=C.

Preparation of the complexes
Stock solution of 3 mM Ga^{3+} complexes were freshly prepared in situ by mixing equimolar solution of $Ga(NO_3)_3$ dissolved in HCl 0.1M and the ligands dissolved in NaOH 0.1M. The pH of the resulting stock solution was neutral. Ga(III) complex solution were immediately used for antibacterial and cytotoxicity screening. The stock solutions were diluted 1: 200 with a mixture H_2O/MeOH 1:1 for HR-MS (eluent MeOH with 0.1% formic acid).

GaL11: [GaL11/$C_9H_{11}O_5N_4GaPS]^+$ calculated: 386.94436; found: 386.94381.

GaL12: [GaL12/$C_{11}H_{15}O_5N_4GaPS]^+$ calculated: 414.97566; found: 414.97511.

GaL13: [GaL13/$C_9H_{11}GaN_4O_6P]^+$ calculated: 370.96720; found: 370.96692: [GaL3-HCOOH/$C_{10}H_{13}GaN_4O_8P]^+$ calculated: 416.97268; found: 416.97213; [GaL13-HCOOH-HCOONa-$C_{11}H_{14}GaN_4NaO_{10}P]^+$ calculated: 484.96011; found: 484.95966; found: 416.97213; [GaL13-2HCOONa/$C_{11}H_{13}GaN_4Na_2O_{10}P]^+$ calculated: 506.94205; found: 506.94154. GaL13 has a high affinity for formic acid, and it ionizes with the track of the solvent in the source of ESI.

GaL14: [GaL14-H_2O / $C_9H_{12}GaN_4O_3S]^+$ calculated: 324.98859; found: 324.98804; [GaL4-CH_3OH/$C_{10}H_{14}GaN_4O_3S]^+$ calculated: 339.00424; found: 339.00369; [GaL14-Cl / $C_9H_{11}ClGaN_4O_2S]^+$ calculated: 342.95471; found: 342.95461; [GaL4-HCOOH / $C_{10}H_{12}GaN_4O_4S]^+$ calculated: 352.98351; found: 352.98324. GaL14 has a high affinity for formic acid, and it ionizes with the track of the solvent in the source of ESI.

GaL15: [GaL15-H_2O / $C_{11}H_{16}GaN_4O_3S]^+$ calculated: 353.01989; found: 353.01934; [GaL15-CH_3OH / $C_{12}H_{18}GaN_4O_3S]^+$ calculated: 367.03554; found: 367.03595; [GaL15-Cl / $C_{11}H_{15}ClGaN_4O_2S]^+$ calculated: 370.98601; found: 370.98659; [GaL15-HCOOH / $C_{12}H_{16}GaN_4O_4S]^+$ calculated: 381.01481; found: 381.01426. GaL15 has a high affinity for formic acid, and it ionizes with the track of the solvent in the source of ESI.

GaL16: [GaL16-H_2O / $C_9H_{12}GaN_4O_4]^+$ calculated: 309.01144; found: 309.01124; [GaL16-CH_3OH / $C_{10}H_{14}GaN_4O_4]^+$ calculated: 323.02709; found: 323.02679; [GaL16-Cl / $C_9H_{11}ClGaN_4O_3$]+ calculated: 326.97755; found: 326.97732.

Microdilution MIC and MBC assay
Klebsiella pneumoniae NDM-1 (NTCT14331); *Klebsiella pneumoniae* ESβL (NCTC13368), *Pseudomonas aeruginosa* clinical isolate (NCTC13713) were purchased from Star Ecotronics s.r.l. *Escherichia coli* ESβL, *Escherichia coli* biofilm, *Enterococcus spp*. *VRE* were isolated in the laboratory of Food Inspection of Parma University. The isolates were tested for their AMR profiles both phenotypically, through Kirby Bauer test, and genotypically by end-point PCR and Real time PCR technique. PCR allows the detection of the most common resistance genes in ESβL, AmpC, CRE and VRE bacteria.[84–87]

MIC (Minimum Inhibitory Concentration) and MBC (Minimum Bactericidal Concentration) values were determined by standard broth micro-dilution method following ISO 20776-1 (2019). Briefly, frozen stock bacteria were put into 5 mL of Buffered Peptone Water (BPW) and incubated for 2 h at 37 °C or until 0.5 McFarland. The bacterial density was adjusted to reach a final concentration of 5 $\times$ 10^5 $CFUmL^{-1}$. Tested antimicrobials were added in triplicate into 96-microwells plates, performing 2-fold serial dilution, followed by the addition of water (for antibacterial screening) or antibiotic (for combination therapy screening) and the prepared bacterial inocula. The plates were incubated at 37 °C for 18-24h. The MIC values were determined by OD reading at 620 nm using a spectrophotometer plate reader. The Fractional Inhibitory Concentration Index (FICI) values were determined as follows: $FICI=FIC_A+FIC_B=C_A/MIC_A+C_B/MIC_B$, where MIC_A and MIC_B are the MIC values of compounds A and B alone, and C_A and C_B are the effective concentration of A and B when administrated. A FICI index of 0.5 or less indicates synergistic effect; between 0.5 and 4 the effect is additive. FICI index greater than 4 denotes antagonism.[46,47] The compounds were tested starting from the 1 mM. Meropenem and cefotaxime concentration were chosen following EUCAST 2021 guidelines and breakpoints table (MERO resistance MIC>8 μgmL^{-1} and CTX resistance MIC>2 μgmL^{-1}).[45]

UV/Vis spectroscopy

UV/Vis spectra were collected in the 250-450 nm range at 25 °C using quartz cuvettes of 1 cm path length. Spectrophotometric titrations of the ligands (C_L = 50 µM,) or of the ligands in the presence of Ga(III) (C_L = 50 µM, Ga:L = 1:1) 1:1 stoichiometry over a pH range between 3 and 11 at an ionic strength of 0.1 M KCl in water at 25 °C. The samples were prepared by diluting to 2.0 mL a proper amount of a 10 mM solution of L in 0.1 M NaOH solution, followed by addition of a proper amount of a 10 mM of gallium(III) nitrate in 0.1 M HCl. The pH was corrected to 11 by addition of 0.1 M NaOH. The samples were titrated with a standard HCl 0.1 M solution, registering the UV/Vis spectrum of the solution for each titrant addition. The spectrophotometric titration curves were treated to determine the protonation (ligand titration) and the complex stability constants (Ga(III)/ligand titration). Data treatment was performed using the program Hypspec2014.[88] Speciation diagrams were calculated using the Hyss2009 software.[56]

CytotoxicityHuman dermal fibroblasts HuDe were purchased from the Istituto Zooproflattico Sperimentale della Lombardia e dell'Emila (IZSLE) (Brescia, Italy). Cells were grown in RPMI 1640 medium containing 10% heat inactivated foetal bovine serum, 100 UmL^{-1} penicillin and 100 μgmL^{-1} streptomycin at 37 °C with 5% CO_2. Experiments were conducted with cells in the log phase growth. Cells (100000 mL^{-1}) were seeded into 96-well plates 24h and then exposed to compounds at concentrations between 0.1 µM and 100 µM. After incubation at 37°C for 24h cells were stained with Trypan Blue and counted with hemacytometer. At least three independent experiments were performed for each sample. Cell viability was assessed by the MTT (3-(4,5-dimethylthiazol-2-yl)-2,5-diphenyltetrazolium bromide) test, samples were read by spectrophotometer (Varioskan LUX Multimode Microplate Reader, Thermo Fisher Scientific).

4. Mn(I) tricarbonyl libraries for the discovery of new metalloantibiotics

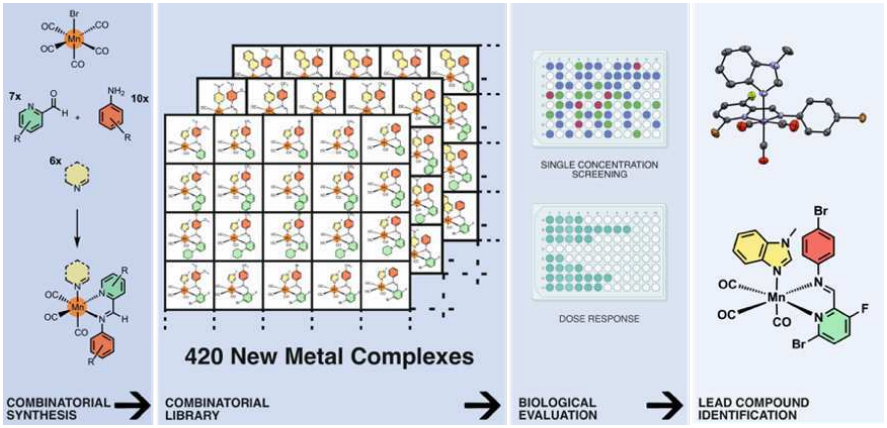

The work presented in this chapter was conducted at the University of Bern, under the co-supervision of Dr. Angelo Frei.

Abstract

Recent advances have highlighted the potential of metal complexes as effective antimicrobial agents. However, the exploration of such compounds remains significantly limited, hampering the ability to identify promising compound classes and establish structure-activity relationships. To expedite discoveries in the realm of metalloantibiotics, I have employed a combinatorial chemistry approach for the synthesis of manganese tricarbonyl complexes.

Through the application of robust Schiff-base chemistry, I combined seven picolinaldehydes with ten aniline derivatives and five axial ligands, resulting in the creation of an extensive library comprising 420 novel manganese complexes. The comprehensive evaluation of these compounds for antibacterial properties led to the identification of ten lead candidates, which were subsequently synthesized and subjected to a complete characterization. Impressively, all ten compounds exhibited robust and broad-spectrum activity against Gram-positive bacteria.

Among these candidates, **MnG9MeBeIm** emerged as the most promising, demonstrating low toxicity to human cells with a therapeutic index exceeding 100. Initial investigations into its mode of action revealed that **MnG9MeBeIm** primarily targets the bacterial membrane without inducing pore formation or depolarization. Instead, it releases its carbon monoxide ligands in proximity to the bacterial membrane, thereby inhibiting the bacterial respiratory chain.

Exploring new metalloantibiotics: the power of combinatorial chemistry

Metal-based compounds have emerged as a promising platform for discovering novel antibacterial agents. However, traditional batch chemistry synthesis methods have proven insufficient for efficiently explore the vast chemical space of potential metalloantibiotics. Combinatorial chemistry is a valuable strategy that expedites synthesis through small-scale procedures that bypass many time-consuming purification and characterization steps. This approach enables extensive exploration of chemical diversity and the establishment of crucial structure-activity relationships. Moreover, the big amount of data generated through combinatorial synthesis can serve as valuable training material for artificial intelligence systems, facilitating the prediction and design of the next generation of compounds with enhanced antibacterial activity.

In the realm of medicinally applied combinatorial metal complex synthesis, a three-component assembly protocol has been pioneered for the synthesis of Schiff-base arene ruthenium(II) complexes (Figure 23A).[89,90] A similar approach, albeit with two components, has been applied to prepare rhenium carbonyl complexes, identifying some with potent anticancer properties (Figure 23B).[91] Additionally, a recent approach has been reported for the preparation of polypyridyl iridium complexes, optimized to obtain photo-cytotoxic compounds with activity against human cancer cells (Figure 23C).[92]

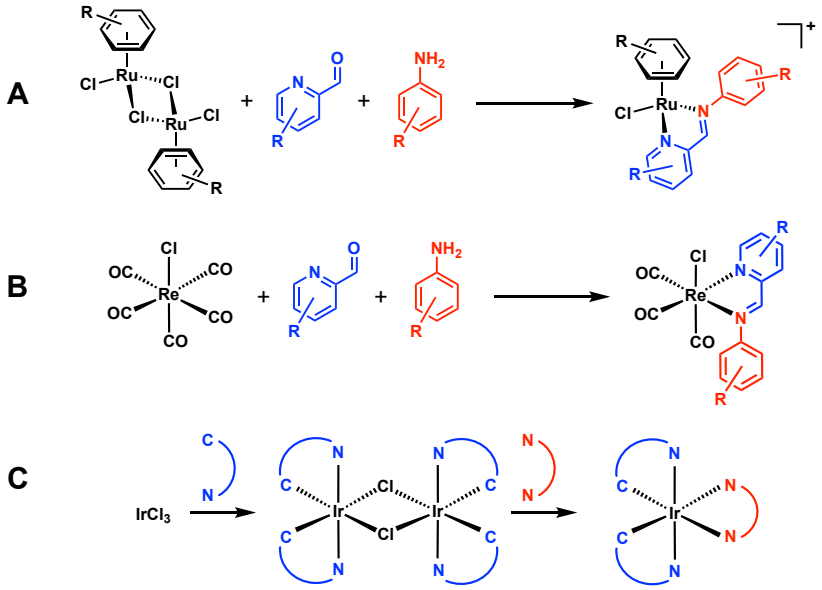

Figure 23. Prior combinatorial reactions for biological applications in combinatorial chemistry.

Tricarbonyl moieties as a scaffold for antibacterial drug development

Among the pool of studied metal compound classes, the metal carbonyl core ($M(CO)_3$) has emerged as a frequently encountered structural motif.[93]

Research into its mode of action has suggested that this compound is associated with adverse effects on bacterial cell membranes, leading to depolarization but without the formation of pores. However, due to challenges related to solubility and cytotoxicity, these compounds were not subjected to *in vivo* evaluation.

More recently, several research efforts have delved into the exploration of additional metal complexes based on the $Re(CO)_3$ scaffold. For instance, bisquinoline rhenium tricarbonyl complexes with a dual mode of action were introduced, demonstrating antibacterial activity that is both light-dependent and independent against drug-resistant Gram-positive and Gram-negative bacteria.[94] Likewise, *fac*-[$Re(CO)_3$] diiamine compounds have exhibited notable effectiveness against Gram-positive bacteria, including drug-resistant strains, with promising results observed in a Zebrafish infection model.[95]

Antimicrobial insights into manganese tricarbonyl complexes

Transition metal manganese, akin to rhenium, has garnered attention for its potential antibacterial properties. Manganese tricarbonyl complexes have been extensively studied due to their role as CO-releasing molecules (CORM), facilitated by the relative instability of its carbonyl ligands. Some studies have synthesized manganese and rhenium tricarbonyl compounds featuring the antifungal drug clotrimazole as an axial ligand, suggesting that their mode of action involves peptidoglycan synthesis inhibition in Gram-positive bacteria.[96] The group of Schatzschneider introduced antimicrobial manganese-based light-activated CORMs (photoCORMs), which have been studied intensively for their antibacterial properties.[97–99] Furthermore, a water-soluble manganese tetracarbonyl-based CORM (CORM-401) was first reported and thoroughly studied for its antimicrobial properties.[100] These investigations revealed that CORM-401 disrupts cytoplasmic ion balance and induces osmotic stress. It is worth noting that the antimicrobial effects of CORM-401 were observed at high compound concentrations and raised concerns about toxicity to eukaryotic cells.[101]

Optimization of $Mn(CO_3)$ combinatorial synthesis and preparation of compound library

A reaction protocol, to be suitable for combinatorial chemistry, must meet two key criteria: a) it should exhibit sufficient robustness to accommodate a wide range of building blocks (BB), and b) it should be adaptable for use in a relatively high-throughput setup. My choice of $MnBr(CO)_5$ as the initial material was based on its commercial availability and its established utility as a precursor for $Mn(CO)_3$-type compounds. The synthesis of Schiff-base type ligands from picolinaldehydes and aniline derivatives has emerged as a promising strategy, primarily because this reaction proceeds under mild conditions and is compatible with various solvents, including water.[89,91] To enhance the diversity of the compounds I synthesized, I introduced an axial ligand to the third available coordination site (Scheme 6).

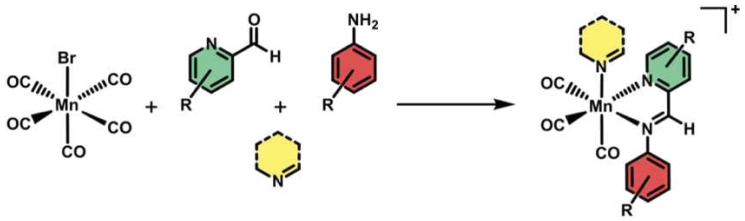

Scheme 6. Reaction scheme for the combinatorial synthesis of manganese Schiff-base complexes.

The selection of picolinaldehyde, aniline, and axial ligand building blocks (BBs) involved several considerations. I compiled a list of reportedly commercially available picolinaldehyde derivatives using the Reaxys platform. These compounds underwent further filtering based on price, and their chemical similarity was assessed using Tanimoto indices.[102] This process led to the identification of seven picolinaldehydes characterized by maximized diversity and reasonable cost (Figure 24).

Regarding anilines, a substantial number of these structures were readily accessible within the Department of Chemistry, Biochemistry and Pharmacy at the University of Bern. From this pool, I selected a set of 10 anilines with maximum diversity, determined based on their Tanimoto similarity, for inclusion in the compound library.

Lastly, I conducted screening tests for various compounds as axial ligands. These tests revealed that, even with optimized conditions, some axial ligands did not achieve sufficiently high conversion rates. Therefore, the final selection of axial ligands (Figure 24) constitutes a subset of ligands that successfully coordinated under the reaction conditions.

Clotrimazole (**clo**), known for its antifungal properties, has been employed as a ligand in previous studies, demonstrating biological activity beyond that of the parent compound.[96,98] Consequently, I included clotrimazole in the investigations to enable comparisons with compounds reported in the existing literature.

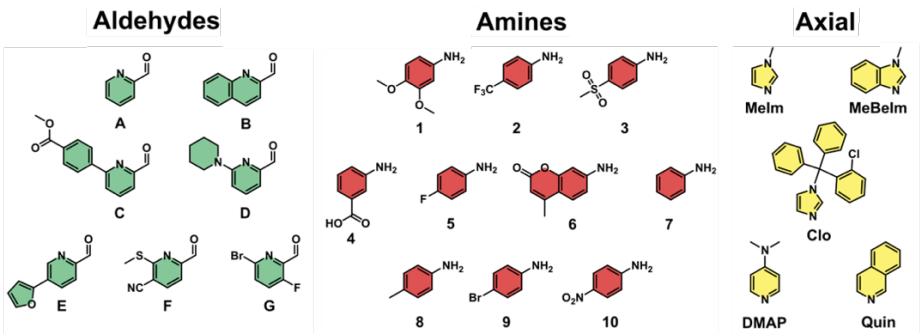

Figure 24. Building Bbocks for the synthesis of 420 Mn-complexes (including 70 compounds without axial ligand).

The initial attempts to initiate the reaction directly from $MnBr(CO)_5$ yielded low conversion rates, demanding prolonged reaction times and elevated temperatures, as confirmed by LC-MS analysis. Following extensive screening of reaction conditions, it was established that pre-activating the $MnBr(CO)_5$ precursor through its reaction with one equivalent of silver triflate under inert atmosphere in dry THF led to a more reactive intermediate. This intermediate could then be directly employed for subsequent reactions with the Schiff-base components and the axial ligand, all conducted in a single reaction vessel. This process required only 90 minutes of heating at 70 °C under standard atmospheric conditions and using readily available synthesis-grade solvents.

With the 10 anilines, 7 picolinaldehydes, and 5 axial ligands in hand, I proceeded to set up the combinatorial syntheses. Briefly, I initiated 70 reactions by combining equimolar amounts of pre-activated manganese carbonyl (20 mM, 100 µL) together with the different BBs from pre-prepared stock solutions in THF (40 mM, 50 µL) in 500 µL polypropylene tubes. I sealed the vessels, placed them within a plastic rack, and heated them in a water bath in the dark at 75 °C for 120 minutes. Subsequently, I removed the solvent in vacuo, and the dried reaction crudes were re-dissolved in 100 µL of DMSO (stock solution 20 mM) and diluted 1:20 in acetonitrile for LC-MS analysis. The LC-MS spectra were then analyzed for both target product formation and conversion percentage (a representative sample of LC-MS spectra is provided in the Figure 25). Altogether, I prepared and characterized 420 novel manganese complexes by LC-MS with minimal use of reagents (less than 1 mg of bromopentacarbonylmanganese per reaction).

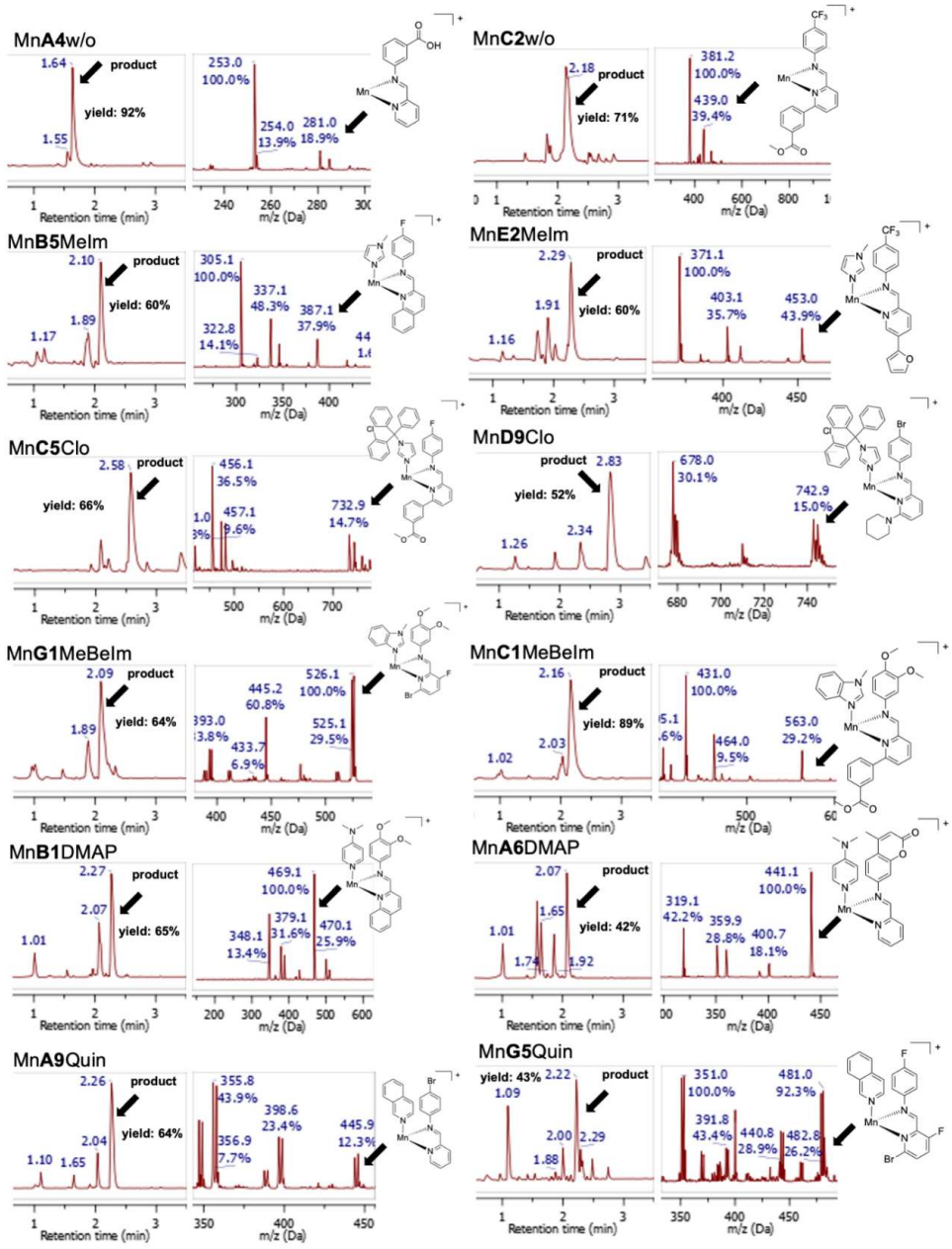

Figure 25. Representative chromatogram depicting the product peak and yield, along with their corresponding MS spectra indicating the molecular fragments within a selected sample from the crude reaction mixture during combinatorial synthesis.

Antimicrobial activity of combinatorial $Mn(CO)_3$ library

To efficiently obtain an overview of the activity profile of all 420 compounds, I performed a single concentration screen of all crude reaction mixtures at 100 µM against the Gram-positive methicillin-resistant *Staphylococcus aureus* (MRSA) and the Gram-negative *Escherichia coli*. For compounds that exhibited complete growth inhibition under these conditions, I proceeded to conduct a microdilution dose-response assay to determine the minimum inhibitory concentration (Figure 26).

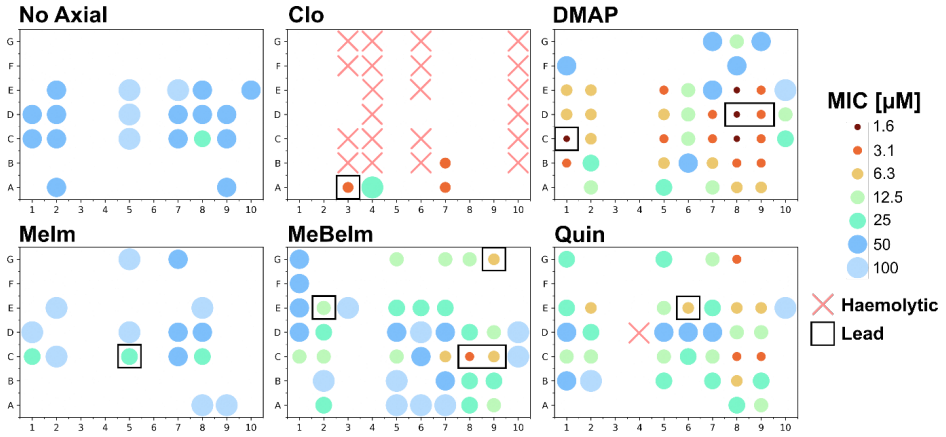

Figure 26. Antibacterial activity of the 420 manganese complexes from combinatorial synthesis against MRSA. Haemolytic compounds are indicated and the 10 lead compounds are highlighted.

In line with the majority of tricarbonyl complexes reported in the literature, I observed minimal activity against the Gram-negative *E. coli*. Although 38 compounds exhibited some inhibition in the single concentration assay at 100 µM, only 5 compounds could be assessed for their minimum inhibitory concentration (MIC). The lowest MIC determined was 50 µM for **MnA7Clo**.

Conversely, significantly higher levels of activity were detected against the Gram-positive MRSA. Among all 420 compound crudes tested, MICs could be determined for 152 of them (36.2%) (Figure 27). Only for 31 compounds where growth inhibition was observed in the single concentration assay at 100 µM, no MIC could be detected at that concentration or lower. Defining active compounds as those with an MIC of 12.5 µM or lower, 64 out of the 420 compounds (15.3%)

met this criterion. Impressively, 39 compounds (9.3%) exhibited an MIC of 6.25 µM or lower, and 4 compounds had an MIC as low as 1.56.

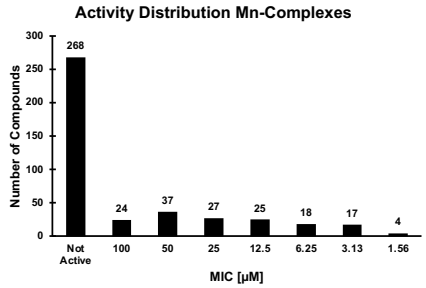

Figure 27. Distribution of the manganese compounds based on their activity against MRSA, represented as MIC [µM].

To ascertain whether the observed activity could be attributed to the building blocks (BB) rather than the complex, I also tested all picolinaldehydes, anilines, and axial ligands. None of the BB showed activity except for **clo** alone, which exhibited an MIC of 12.5 µM against MRSA. This confirmed that, in most cases, the observed activity likely originates from the manganese tricarbonyl complex formation.

The hit rate obtained is impressive, but it aligns with the existing literature on this compound class, which had already hinted at their potential activity. To gain an initial understanding of the synthesized complexes' potential toxicity towards human cells, I conducted hemolytic tests on all 420 crude compounds using human red blood cells. Surprisingly, only 22 compounds exhibited any signs of hemolysis at 20 µM, and notably, 21 of these compounds contained the clo axial ligand (Figure 26). Furthermore, none of the compounds that displayed hemolysis in this assay exhibited antibacterial activity. This initial toxicity screening suggests that the majority of these manganese Schiff-base compounds are non-hemolytic.

It is worth noting that all tested substances thus far were reaction crudes containing the target compound, with average purities of 65 ± 15%. This approach allowed for significantly higher throughput and reduced time consumption compared to purifying and fully characterizing each compound individually. However, the varying purity levels of the crudes raise the possibility that the

observed activity could be attributed to side products or impurities rather than the intended metal complex.

In order to visualize the chemical space generated through the combinatorial synthesis and facilitate the identification of lead compounds, I collaborated with Markus Orsi to develop a TMAP (Topological Map of Chemical Space) for the compounds (Figure 28). TMAP is a powerful tool used in chemistry and drug discovery to visualize and navigate the vast and complex landscape of chemical compounds. It offers a graphical representation of chemical space, where each compound is plotted as a point based on its molecular structure and properties. TMAP helps to organize and analyze large datasets of chemical compounds, facilitating the identification of patterns, clusters, and relationships among molecules.[103]

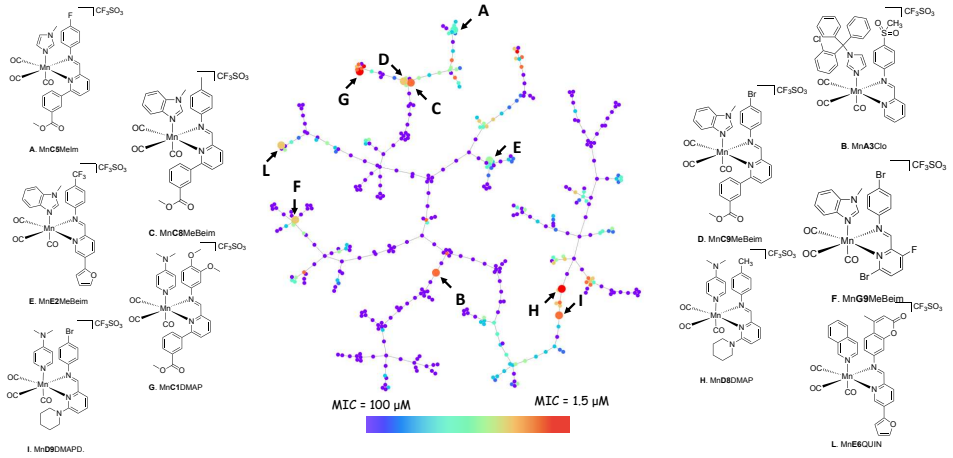

Figure 28. Topological map of chemical space (TMAP) for compounds by combinatorial synthesis. Biological activity is displayed as MIC against MRSA, represented by a color scale. The identified lead compounds are pinpointed with arrows.

Re-synthesis, purification and characterization of lead compounds

After the preliminary biological assessment, I identified ten lead compounds for resynthesis (Figure 29). The selection of these lead compounds was primarily guided by their determined antibacterial activity. Additionally, I aimed to maximize the chemical diversity within the selected leads, striving to include at least one example with each axial ligand (Figure 28). These chosen compounds underwent

resynthesis using conventional batch-style chemistry on a 20 mg/0.072 mmol scale and were subsequently purified via preparative HPLC. Yields from this process ranged from 26% to 99%, and in some instances, the pure compound could be directly isolated by precipitation. The pure metal complexes underwent comprehensive characterization through ^{1}H NMR, ^{13}C NMR, LC-MS, HR-MS, and IR spectroscopy. Notably, single crystals suitable for X-ray diffraction structural elucidation were successfully obtained for compounds **MnD8DMAP**, **MnC1DMAP**, and **MnG9MeBeIm** (Figure 30).

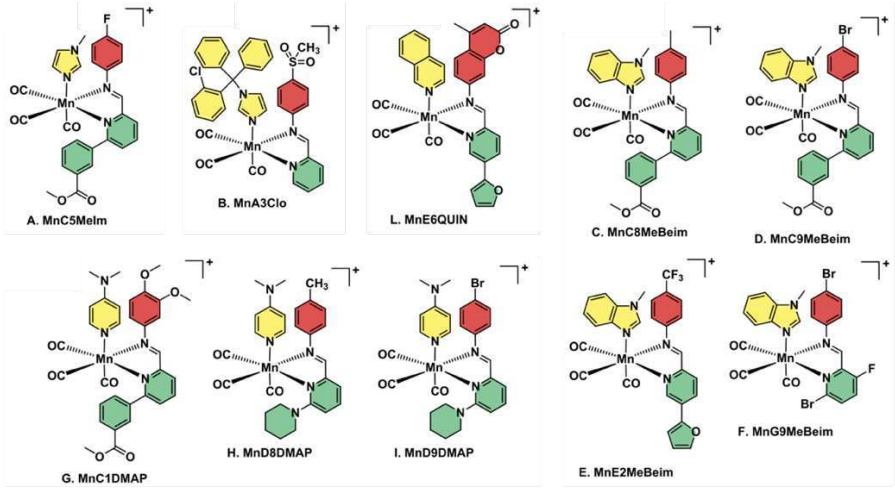

Figure 29. Characterized structures of the ten re-synthesized Mn-lead compounds following the combinatorial screening.

The X-ray structures of these compounds introduce an unexplored category within the CCDC database. This category showcases a Schiff base derived from picolylamide and benzylamine, accompanied by an aromatic axial ligand possessing nitrogen-donating capabilities. Structural analysis reveals that the manganese atom adopts a pentahedral configuration, coordinating with the bidentate Schiff base and the N-donor axial ligand sourced from either imidazole or pyridine. Remarkably, bond distances exhibit minimal disparity across the three structures in this study, aligning with expectations based on the parent compounds.[104] Furthermore, it is intriguing to note that the two rings of the Schiff base deviate from planarity, demonstrating torsion angles spanning between 37° and 46°.

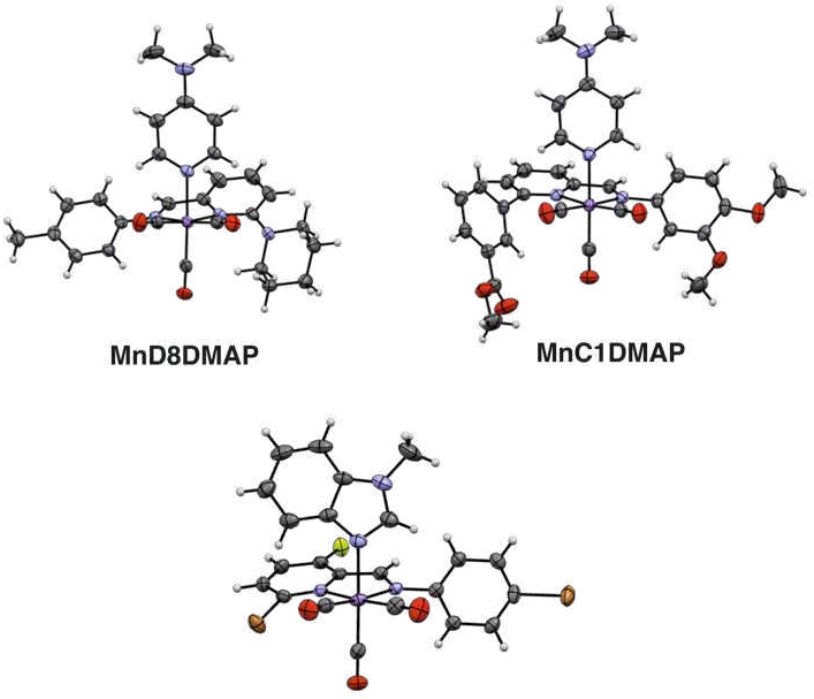

Figure 30. X-ray crystal strucutre of the cations of MnD8DMAP, MnC1DMAP, and MnG9MeBeIm (CCDC No 2280008-10). Triflate counterions and a co-crystallized solvent are not represented for clarity.

Stability of manganese tricarbonyl complexes

As previously mentioned, certain manganese tricarbonyl complexes are recognized for their light-induced carbon monoxide release. In the experiments, we indeed observed rapid decomposition of these compounds when exposed to natural daylight, indicated by the decolorization of stock solutions. However, it is worth noting that no such decolorization occurred under dim-light conditions, ensuring the reproducibility of data across multiple biological replicates. To further investigate the stability of these compounds, we monitored the absorbance of solutions containing all ten lead compounds in various solvents (including water, DMSO, HEPES, PBS and culture media MH) over time (Figure 31). Remarkably, over an 18-hour period, no decomposition was observed in DMSO, while only minor changes in absorbance were detected in water and the buffers.

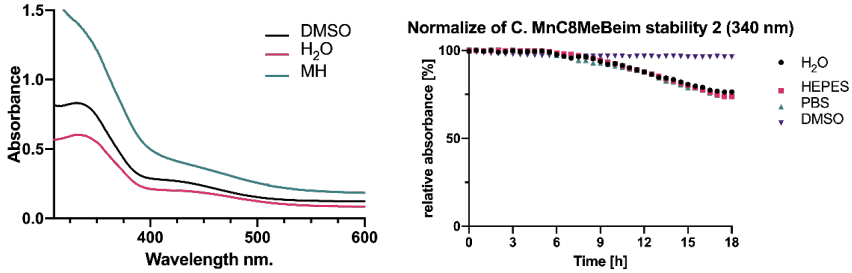

Figure 31. UV-Vis spectra ***for MnC8MeBeim*** *(on the left) at a concentration of 50 μM in varying solvents, along with its stability observed over 18 hours, tracked at the peak absorbance (on the right).*

Biological evaluation of lead manganese compounds

The antibacterial activity of the pure lead compounds was assessed against a selection of Gram-positive and Gram-negative bacteria. (Table 8 and Table 9). The compounds demonstrated generally robust activity against various bacterial strains, including the challenging ESKAPE pathogens (Enterococcus faecium, Staphylococcus aureus, Klebsiella pneumoniae, Acinetobacter baumannii, Pseudomonas aeruginosa e Enterobacter spp.) such as MRSA and clinical isolate of Vancomycin-resistant *Enterococcus*.[105] Additionally, some of the compounds exhibited moderate activity against Gram-negative bacteria like *A. baumannii* and *E. coli*. This observation hints at the potential for structural optimization to yield compounds with broad-spectrum antibacterial efficacy (Table 9). To determine whether the lead compounds exhibit bacteriostatic or bactericidal effects, I assessed the minimum bactericidal concentration (MBC) against MRSA (Table 8). Notably, for all compounds except MnC5MeIm, the MBC closely mirrored the MIC, suggesting that the majority of the tested compounds possess bactericidal properties.

Table 8. Antibacterial activity against a selection of resistant Gram-positive strains, toxicity data in HuDe cells and human red blood cells and therapeutic indices (TI) for the 10 synthesized lead compounds.

	MBC [µM]	MIC [µM]		Toxicity [µM]		
	MRSA	MRSA	*En* VRE	CC_{50}	HC_{50}	TI
MnC5MeIm	50-25	3.13-6.25	25	46.1 ± 0.1	>200	7
MnA3Clo	3.13	1.56	3.13	37.1 ± 0.2	68 ± 15	24
MnC8MeBeim	6.25	3.13-1.56	6.25	18.0 ± 0.2	77 ± 10	6
MnC9MeBeim	6.25	3.13-1.56	12.5	16.8 ± 0.2	95 ± 13	5
MnE2MeBeim	6.25	3.13-1.56	12.5	7.2 ± 0.3	49 ± 12	2
MnG9MeBeim	1.56	0.78	6.25	85.2 ± 0.1	117 ± 12	109
MnC1DMAP	6.25-3.13	3.13-1.56	6.25	37.0 ± 0.2	>200	12
MnD8DMAP	6.25-3.13	1.56	12.5	7.9 ± 0.2	>200	5
MnD9DMAP	6.25-3.13	1.56	6.25	9.4 ± 0.2	>200	6
MnE6Quin	12.5-6.25	6.25-3.13	25	36.3 ± 0.1	>200	6
VAN [µg/mL]	8	1	8			

MRSA – methicillin resistant S. aureus; En VRE – Enterococcus casselliflavus VRE, CC_{50} – HuDe cells; HC_{50} – Human red blood cells; TI – therapeutic index, determined by dividing the lowest value between CC_{50} and HC_{50} with the lowest MIC value for each compound; VAN – Vancomycin.

Table 9. Antibacterial activity against an extended selection of Gram-negative and Gram-positive strains, for the 10 synthesized lead compounds.

	MIC [µM] vs. Gram-negative bacteria				MIC [µM] vs. Gram-positive bacteria			
	Ab	Pa	Kp	Ec	MSSA	Se	Bs	En
MnC5MeIm	> 100	>100	>100	> 100	12.5-6.25	12.5	12.5-6.25	25
MnA3Clo	50	>100	>100	> 100	1.56	3.13	3.13-1.56	6.25
MnC8MeBeim	100-50	>100	>100	> 100	6.25	6.25	6.25	12.5
MnC9MeBeim	25	>100	>100	> 100	3.13	6.25	3.13	12.5
MnE2MeBeim	25	>100	>100	> 100	3.13	6.25-3.13	3.13	12.5
MnG9MeBeim	100	>100	>100	100-50	<0.78	<0.78	3.13-1.56	6.25
MnC1DMAP	100	>100	>100	> 100	3.13-1.56	6.25	6.25-3.13	12.5
MnD8DMAP	25	>100	>100	100-50	1.56-0.78	1.56	3.13-1.56	12.5
MnD9DMAP	>100-50	>100	>100	50-25	1.56	3.13	1.56	12.5
MnE6Quin	>100	>100	>100	> 100	6.25	12.5-6.25	6.25	50
PMX [µg/mL]	0.25	1	2	1	Nd	nd	nd	nd
VAN [µg/mL]	nd	nd	nd	nd	1	1	0.25	1

Ab – Acinetobacter baumannii; Pa – Pseudomonas aeruginosa; Kp – Klebsiella pneumoniae; Ec – Eschericchia coli; MSSA – methicillin susceptible S. aureus; Se – S. epidermidis; Bs – Bacillus subtilis; En – Enterococcus spp PMX – Polymixin B, VAN – Vancomycin.

To further assess the potential toxicity of the lead compounds, haemolysis was re-evaluated by determining HC_{50} values, and cytotoxicity tests were conducted using healthy eukaryotic HuDe human epithelial cells. The activity observed in the crude reaction mixtures consistently translated to activity for the pure compounds, affirming the efficacy of the pursued combinatorial chemistry approach in discovering antibacterial metal complexes within this project. Moreover, haemolysis values obtained with the pure compounds were consistent with those measured for the crude samples, indicating that none of the compounds induced haemolysis at concentrations below 49 µM. However, some of the compounds exhibited relatively high levels of cytotoxicity against HuDe cells. Nevertheless, three of the lead compounds still demonstrated therapeutic indices exceeding 10, with **MnG9MeBeim** achieving an impressive TI exceeding 100. The MICs of **MnG9MeBeim** were comparable to the standard of care for Gram-positive infections, such as vancomycin.

Considering the extensive biological data, compound **MnG9MeBeim**, due to its exceptional antibacterial potency, minimal haemolysis, low cytotoxicity, and robust stability under physiological conditions, emerged as the exclusive lead compound for further investigations.

Analyzing the CO-mediated antibacterial activity

Based on previous studies of manganese tricarbonyl complexes, it is reasonable to consider that the release of carbon monoxide (CO) plays a role in the antibacterial mechanism. To investigate whether CO contributes to the antibacterial properties of the primary compound, we re-evaluated its Minimum Inhibitory Concentration (MIC) against MRSA both in the presence and absence of haemoglobin (Hb), a recognized CO scavenger.[106]

Significantly, we observed a substantial 4-8x rise in the MIC for **MnG9MeBeIm** when 20 µM Hb was present. Subsequently, we conducted a checkerboard assay, varying the concentrations of **MnG9MeBeIm** and Hb (as depicted in Figure 32A). Notably, a distinct antagonistic effect (FICI >> 4)[47] was observed, indicating that Hb adversely impacts the antibacterial activity of **MnG9MeBeIm**, likely due

to its irreversible binding of the CO released by the manganese compound. However, even in the presence of substantial Hb concentrations, **MnG9MeBeIm**'s activity was not entirely suppressed, suggesting the involvement of multiple mechanisms (with the MIC of **MnG9MeBeIm** being 50 µM in the presence of 160 µM Hb).

To confirm CO release, we employed UV/Vis spectroscopy to monitor changes in Hb's absorbance when exposed to **MnG9MeBeIm** over an 8-hour period at 25 °C (as shown in Figure 32B). These findings, in conjunction with the structural similarities and the shared $MnCO_3$ framework among the compound library, imply that CO release plays a role in the antibacterial effects of these compounds. Nevertheless, the varied levels of antibacterial activity within this compound library suggest that the compound's structure significantly influences the characteristics of CO release and potentially bacterial uptake, consequently impacting their efficacy against bacteria.

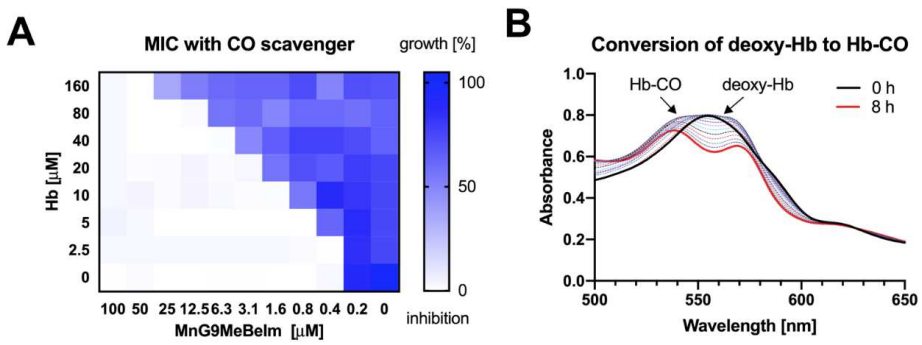

*Figure 32. Evaluation of CO-releasing properties of **MnG9MeBeIm**: (A) Assessment of its biological activity against MRSA through a checkerboard assay, displaying growth percentage over the control, in the presence of varying concentrations of the CO scavenger hemoglobin. (B) Monitoring the conversion of deoxyhemoglobin (80 µM, HEPES pH 7.4, 25 °C) to carboxyhemoglobin in the presence of **MnG9MeBeIm** (20 µM) over an 8-hour duration.*

Bacterial cytological profiling

In order to gain an initial insight into **MnG9MeBeIm**'s impact on bacteria, I performed bacterial cytological profiling (BCP) with *Bacillus subtilis*. BCP is a microscopy-based technique used to study the cellular morphology and subcellular organization of bacterial cells, particularly with *Bacillus subtilis*, a

widely nonpathogenic Gram-positive bacterium. The process involves fluorescently labeling specific cellular components like the nucleoid, cell membrane or specific proteins, and then imaging the cells with fluorescence microscopy.[107,108] To pinpoint the optimal stressor dosage and incubation duration, essential for these experiments, we conducted growth curve experiments involving various compound concentrations. Ultimately, we determined that employing 3 μM of **MnG9MeBeIm** for a 20-minute incubation period yielded the most informative results.

A *B. subtilis* strain, expressing cytosolic GFP from the robust ribosomal PrpsD promoter (referred to as PrpsD-gfp reporter), was subjected to a 15-minute incubation with **MnG9MeBeIm**. Following this incubation, DNA was stained with DAPI, and the bacterial membrane was stained using Nile red. Subsequent examination through fluorescence microscopy unveiled no significant alterations in GFP signals and no significative difference in the DNA localisation from the DAPI images. In contrast, the membrane stained with Nile red presented distinct disparities, manifesting as multiple focal points on the bacterial membrane (as indicated in Figure 33B). Worth noting, these specific locations exhibited a slightly diminished GFP signal, indicating the presence of small invaginations.

Given **MnG9MeBeIm**'s distinctive influence on the bacterial membrane and the knowledge that MinD is involved in cell division regulation, I used a MinD-gfp *Bacillus subtilis* strain to discern any potential effects on membrane polarization.[108] Notably, similar 'blob-like' accumulations, akin to those observed with Nile red, emerged. However, these patterns starkly diverged from the positive control, nisin (as shown in Figure 33B), where complete MinD dispersion was noted. This disparity implies that **MnG9MeBeIm** does not impede membrane polarization but rather triggers invagination, which may disrupt MinD localization.

Lastly, guided by the findings implicating CO release in the compound's mode of action, we exposed *B. subtilis* to both **MnG9MeBeIm** and COP-1, a fluorescent probe designed for intracellular CO detection.[109] Concurrently, I stained the cells with Nile red (refer to Figure 33C). The imagery captured at COP-1's emission wavelength clearly illuminated CO release, evident through the resultant

fluorescence. Furthermore, the membranous 'blobs' observed with Nile red coincided with the peaks in COP-1 fluorescence, affirming that CO preferentially emanates within and around the membrane. This underscores the hypothesis that **MnG9MeBeIm** exerts a unique influence on the bacterial membrane.

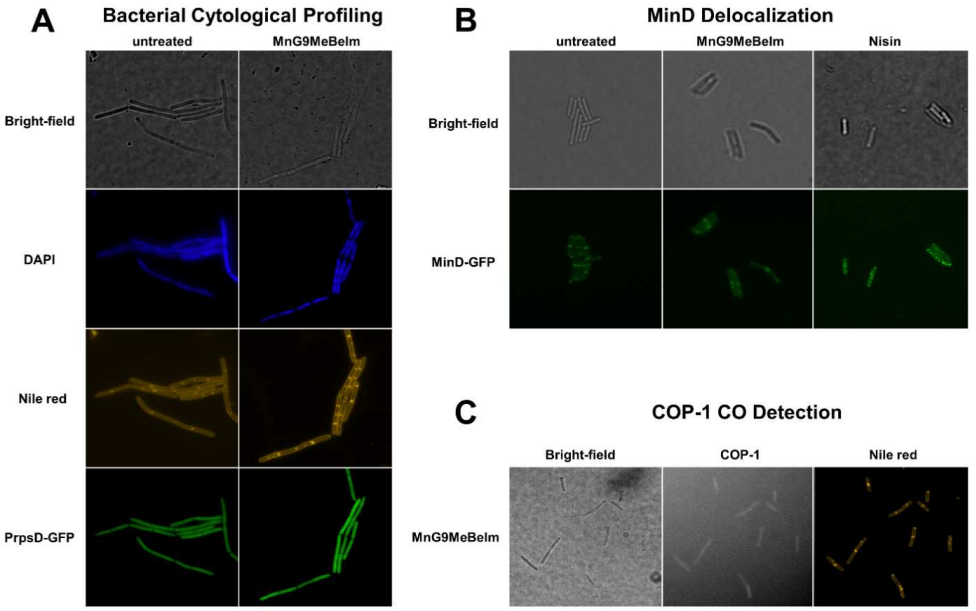

*Figure 33. Fluorescence microscopy images, illustrating: (A) The response of the B. subtilis PrpsD strain to 6.25 µM **MnG9MeBeIm** treatment for 20 minutes, followed by DAPI and Nile red staining, in comparison to an untreated control. (B) The effects of 6.25 µM **MnG9MeBeIm** exposure on B. subtilis carrying a MinD reporter, contrasted with an untreated control. (C) The impact of 6.25 µM **MnG9MeBeIm** treatment for 20 minutes on B. subtilis in the presence of COP-1, with subsequent Nile red staining."*

Influence on bacterial membranes and respiratory chain inhibition

Based on the microscopy findings, it became evident that **MnG9MeBeIm** had an impact on the bacterial membrane. In previous research, certain manganese tricarbonyl compounds were shown to induce pore formation and other detrimental effects on bacterial membranes.[110] To probe the influence of the lead compound on the bacterial membrane, I employed propidium iodide (PI), a fluorescent agent that cannot penetrate intact membranes but accumulates when pores compromise membrane integrity. When compared to sodium dodecyl sulfate (SDS), a known surfactant that forms sizable membrane pores, it became apparent that **MnG9MeBeIm** did not lead to significant PI uptake by the bacteria (as depicted in Figure 34A).

Additionally, I conducted a $DIS_3(5)$ assay to investigate any potential effects on membrane polarization. The absence of a noteworthy increase in fluorescence (Figure 34B), as indicated by the distinct MinD distribution pattern described earlier (Figure 33B), suggests that **MnG9MeBeIm** does not disrupt membrane polarization. Collectively, these experiments, in conjunction with the PI assay, imply that any influence exerted by the lead compound on the bacterial membrane does not involve pore formation or depolarization.

Prior reports have hinted at the respiratory chain's inhibition as a potential target for ruthenium-based CORMs (although questions have arisen regarding whether Ru-CORMs genuinely owe their antibacterial effect to CO release).[111,112] To investigate whether **MnG9MeBeIm** impacts the respiratory chain, I quantified respiratory activity by monitoring resazurin reduction[113], which revealed a dose-dependent decrease in respiratory chain activity (as illustrated in Figure 34C). This suggests that the CO released by the compounds indeed inhibits the electron transport chain, with the effect at the highest concentration tested mirroring that of sodium azide, a well-known electron transport chain inhibitor (as shown in Figure 34C).[114] Notably, the aerobic respiratory chain is located on the bacterial plasma membrane, aligning with the observations of bacterial death resulting from **MnG9MeBeIm**'s inhibition, as highlighted in the earlier fluorescent microscopy data.

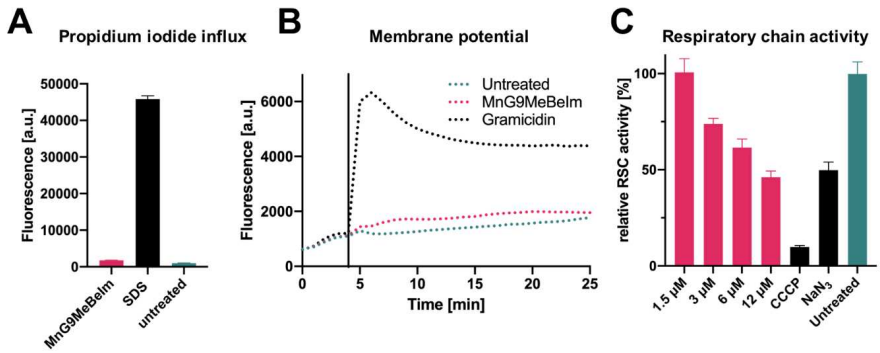

*Figure 34. Mechanism of **MnG9MeBeIm**'s Action: (A) Quantitative assessment of PI fluorescence in bacteria following exposure to compounds (3 µM, 20 min), SDS (positive control, 0.05%, 20 min), or no compound. (B) Evaluation of $DiOC_2$ fluorescence to gauge membrane depolarization after the introduction of **MnG9MeBeIm** (3 µM) and Gramicidin (positive control, 1 µg/mL). The solid black line marks the time of antibiotic addition. (C) Assessment of relative respiratory chain activity via resazurin reduction. **MnG9MeBeIm** was tested at four different concentrations (after a 20-minute incubation) and compared to positive controls CCCP (100 µM, 20 min) and NaN_3 (15 mM, 20 min).*

In vivo toxicity evaluation using *Galleria mellonella* larvae

With the aim of evaluating the in vivo toxicity of **MnG9MeBeIm**, I employed *Galleria mellonella* as a valuable tool to evaluate the compound's safety profile. The compounds were dissolved in DMSO, and subsequently, I administered to the larvae 10 µL of a water solution containing a maximum of 5% of the initial stock solution in DMSO for compound injection. A 5% DMSO solution served as the control. At the highest concentration, 40 µM, which equated to a dose of approximately 31 mg/kg of larval weight, no detectable toxicity was observed, as there were no significant differences between the treated groups and the control group (Figure 35).

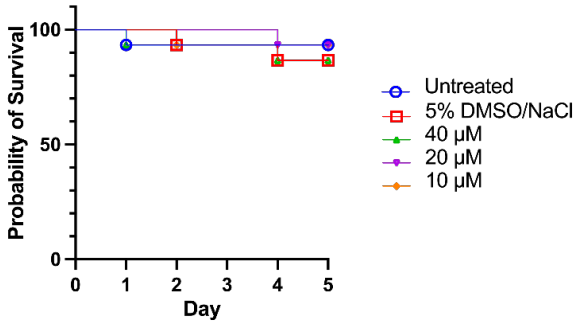

*Figure 35. Survival of G. mellonella (n = 15) recorded over a 5-Day period post-injection of **MnG9MeBeIm**.*

In vivo efficacy test in a *Galleria mellonella* systemic infection

After confirming the favorable tolerance of **MnG9MeBeIm** by *G. mellonella*, we proceeded to initiate preliminary *in vivo* efficacy experiments in collaboration with our partners at the University of Queensland, Sydney, Australia. In a concise outline of the methodology, the *G. mellonella* larvae were initially infected with 10^6 cells of *Staphylococcus aureus* (ATCC 43300). Subsequently, two hours later, **MnG9MeBeIm** was administered at its highest concentration (300 µM) via injection. To provide a robust basis for comparison, we established control groups that received injections of 10 % DMSO and rifampicin. The results are visually summarized in Figure 36.

It is noteworthy to mention that rifampicin, a known effective antibiotic, demonstrated remarkable efficacy, with all larvae surviving the injection. In contrast, the treatment with the manganese compound did not exhibit a statistically significant difference from the group treated with the buffer post-injection, indicating a lack of *in vivo* efficacy.

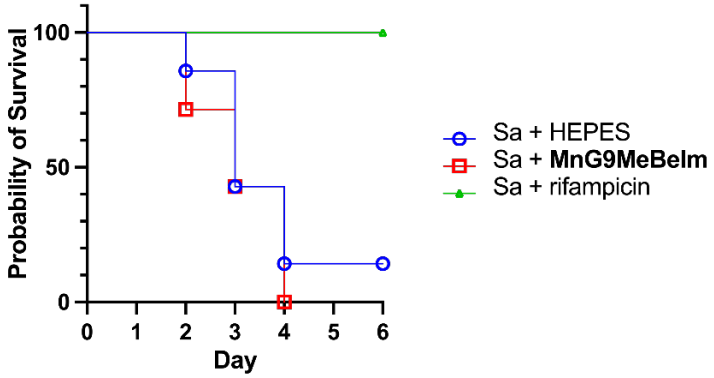

*Figure 36. Survival of G. mellonella (n = 7) infected with S. aureous over a 6-Day period post-infection and treated with **MnG9MeBeIm**. Rifampicin served as control antiobiotic.*

In vivo efficacy test in a *Galleria mellonella* burn wound infection model

The burn wound infection model serves as a vital tool for evaluating the efficacy of antibacterial agents, as burn wound infections stand as a primary cause of mortality in burn patients. Given the intricacies of burn wound trauma and infection, it is imperative to employ an *in vivo* model for the development of novel therapeutic interventions.

In partnership with Dr. Ronan McCarthy from Brunel University London, we embraced this infection model to assess the effectiveness of **MnG9MeBeIm**. Unfortunately, our results did not unveil any notable improvement in **MnG9MeBeIm**'s efficacy within this model, as there was no discernible enhancement in survival rates when compared to the untreated control group (Figure 37).

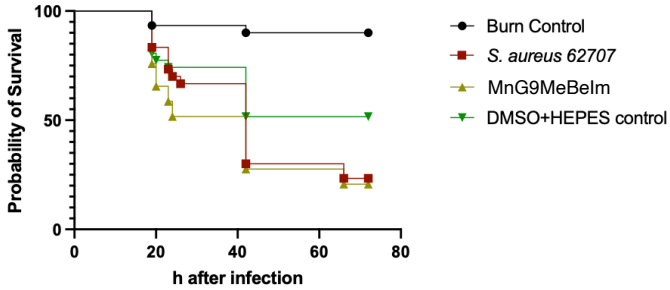

Figure 37. Survival curves of in vivo burn wound infected with S. aureus 62707 and treated with MnG9MeBeIm (3 mM) (n=30).

Conclusion

To accelerate the pace of discovery for novel metalloantibiotics, I employed combinatorial chemistry for the first time to synthesize manganese tricarbonyl compounds. This innovative approach enabled me to prepare and subsequently screen a remarkable 420 new Schiff-base $Mn(CO)_3$ complexes for their antibacterial potential. A substantial portion of these compounds (64 out of 420, accounting for 15.3%) exhibited significant activity against MRSA, with a minimal inhibitory concentration (MIC) of 12.5 μM or lower. Importantly, only those compounds lacking antibacterial activity displayed any evidence of hemolysis against human red blood cells.

Leveraging this initial screening data, I identified 10 lead compounds, maximizing antibacterial activity and structural diversity. These selected compounds underwent meticulous resynthesis, purification, and thorough characterization. Upon re-evaluation of their antibacterial efficacy and assessment of human cell toxicity, one standout emerged: **MnG9MeBeIm**, which boasted an impressive therapeutic index exceeding 100. Its structural identity was unequivocally confirmed through X-ray diffraction.

Further exploration of **MnG9MeBeIm**'s properties led me to investigate its CO-releasing characteristics, unveiling a gradual release of CO. Intriguingly, the presence of hemoglobin (Hb) was found to diminish the lead compound's antibacterial activity, implying a significant role for CO in its bacterial killing mechanism. My mode-of-action investigations, employing bacterial cytological profiling, unveiled a distinct impact of **MnG9MeBeIm** on the bacterial membrane. While conventional modes of membrane interference such as pore formation and membrane depolarization were ruled out, I established that CO is released *in vitro* and colocalizes with apparent membrane invaginations. Lastly, my studies demonstrated that the compound effectively inhibits the aerobic cell respiratory chain, a key feature of which is its location within the bacterial membrane.

Initial *in vivo* assessments indicated that **MnG9MeBeIm** did not exhibit any discernible toxicity when administered on its own, suggesting a favorable safety

profile for this compound. Encouraged by these results, we proceeded with efficacy studies using two distinct infection models: systemic infection and burn wound infection. However, it is with regret that we report that, despite the absence of toxicity concerns, **MnG9MeBeIm** failed to demonstrate any significant improvement in survival rates in either of the infection models employed.

Physical Measurements

Analytical RP-HPLC−MS was performed with an Ultimate 3000 Rapid Separation LC−MS System (DAD-3000RS diode array detector) using an Acclaim RSLC 120 C18 column (2.2 µm, 120 Å, 3 × 50 mm, flow 1.2 mL/min) from Dionex. The HPLC is directly linked to a Thermo Scientific LCQ- Fleet Ion-trap MS. The elution solutions were A: MilliQ deionized water containing 0.05% TFA and D: MilliQ deionized water/acetonitrile (10:90,v/v) containing 0.05% TFA. High resolution mass spectra were recorded from LTQ Orbitrap XL with nano ESI (Thermo) positive mode, samples prepared in acetonitrile. NMR were recorded from AVANCE II 400 MHz (Bruker). The FT-IR measurements were recorded on Jasco FT/IR-4700 in the 2500-400 cm^{-1} range, equipped with the UATR accessory. UV-vis spectra were collected using 1 cm quartz cuvette at room temperature with a Shimadzu UV-1800 UV spectrophotometer.

Materials and Reagents

Reagents were commercially available and they were used without any further purification.

Combinatorial Synthesis

Stock solutions of the amines, aldehydes, and axial ligands where prepared at 40 mM in THF. Manganese(I) was activated according previously reported methods.[115] Briefly, bromopentacarbonylmanganese(I) (100 mg, 0.36 mmol) and silver triflate (93.5 mg, 0.36 mmol) were dried with three cycles of vacuum and argon flux. Then 6 mL of dry THF were added. The suspension then was stirred and refluxed under argon for 45 min. The suspension was then filtered off to get rid of AgBr, and the solution is diluted 1:3 to obtain a 20 mM stock solution in dry THF. The reactants stock solution were combined in a 500 µL Eppendorf vial (50 µL of the amine, 50 µL of the aldehyde, 50 µL of the axial ligand and 100 µL of the Mn(I)), and heated at 75 °C for 2 hours in a water bath.[96] The reaction solution were evaporated under vacuum and dissolved with 100 µL of DMSO to obtained the stock solution at 20 mM. LC-MS was carried out diluting the stock solutions in DMSO in a mixture of ACN:water (50:50).

Batch Synthesis

Manganese pentacarbonyl bromide (100 mg 0.36 mmol) and silver triflate (93.5 mg, 0.36 mmol) were dried under vacuum. Then 5 mL of dry THF are added and reflux under stirring and under argon atmosphere for 45 min. The suspension was then filtered off. The corresponding amines, aldehydes, and axial ligands (0.072 mmol) are dissolved in 1 mL of the solution of manganese(I) (0.072 mmol). The reaction is headed at reflux under argon for 2 hours. The product is precipitate with 5 mL of heptane, the solid collected, washed with diethylether and dry under vacuum. The pure product is obtained after purification of prepHPLC (flux 40mLmin^{-1}; A= H_2O 0.1%TFA, D=90%ACN 10% H_2O, 0.1% TFA; program: time 0 min A/D 100:0, 5 min A/D 70:30, time 45 min A/D 30-70. For DMAP derivatives A= H_2O, D=100% ACN; program: 0 min A/D 100:0, 5 min A/D 75:25, time 60 min A/D 40-60). The fractions are collected, checked by LC-MS ((flux 1.2 mLmin^{-1}; A=

H_2O 0.1%TFA, D=90%ACN 10% H_2O, 0.1% TFA; program: A/D 100:0 to 0:100 in 10.00 min, total absorbance) and lyophilised.

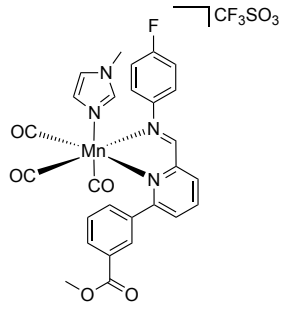

MnC5MeIm. Yield 45%. MW 704.49 gmol^{-1}. HR-MS (+, m/z, [M-TfO]$^+$) [$C_{27}H_{21}FMnN_4O_5$]$^+$ calculated: 555.0876; found: 555.0859. Analytical RP-HPLC: t_R = 4.90 min. ESI-MS (+, m/z, [M-TfO-3CO]$^+$): 470.9 [$C_{24}H_{21}FMnN_4O_2$]$^+$. ^{1}H NMR (300 MHz, CD_3CN) δ 8.87 (1H, s), 8.39-8.19 (4H, br), 7.89 (1H, m), 7.76-7.59 (2H, br), 7.45-7.35 (5H, br), 7.15-7.06 (1H, m), 6.39 (1H, br), 3.93 (3H, s), 3.68 (3H, br). ^{13}C NMR (400 MHz, CD_3CN) 171.8, 166.5, 165.5, 164.4, 163.8, 163.0, 162.5, 161.9, 148.2, 142.0, 140.7, 134.1, 131.7, 131.6, 130.2, 129.9, 124.5, 123.8, 117.3, 117.1, 52.7, 34.8. IR (ATR): 2033 cm^{-1}, 1931 cm^{-1} ν CO.

.

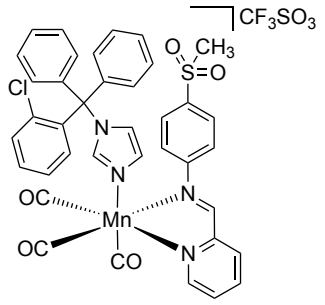

MnA3Clo. Yield 28%. MW 893.18 gmol^{-1}. HR-MS (+, m/z, [M-TfO]$^+$): [$C_{38}H_{29}ClMnN_4O_5S$]$^+$ calculated: 743.0928; found: 743.0909. Analytical RP-HPLC: t_R = 5.54 min. ESI-MS (+, m/z, [M-TfO-3CO]$^+$): 658.8 [$C_{35}H_{29}ClMnN_4O_2S$]$^+$. ^{1}H NMR (400 MHz, DMSO-d_6) δ 8.50 (1H, s), 8.14 (1H, s), 7.50 (1H, m), 7.44 (1H, m) 7.33-7.31 (2H, m), 7.05 (1H, m), 6.68-6.65 (4H, m), 6.69-6.52 (7H, m), 6.28 (1H, s), 6.18-6.18(7H, m), 2.42 (3H, s). ^{13}C NMR (400 MHz, DMSO-d_6) δ 170.6, 153.8, 140.6, 139.8, 139.5, 139.1, 138.7, 137.7, 131.5, 130.3, 130.0, 129.6, 129.2, 129.0, 128.7, 128.5, 128.4, 127.8, 127.8, 127.4, 126.5, 123.2, 121.9, 75.9, 42.0. IR (ATR): 2037 cm^{-1}, 1932 cm^{-1} ν CO.

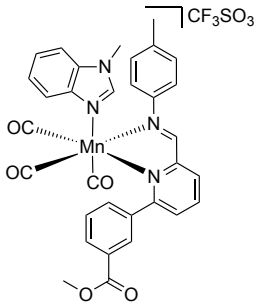

MnC8MeBeim. Yield 30%. MW 750.58 gmol^{-1}. HR-MS (+, m/z, [M-TfO]$^+$): [$C_{32}H_{26}MnN_4O_5$]$^+$ calculated: 601.1284; found: 601.1266. Analytical RP-HPLC: t_R = 5.51 min. ESI-MS (+, m/z, [M-TfO-3CO]$^+$): 517.0 [$C_{29}H_{26}MnN_4O_2$]$^+$. ^{1}H NMR (300 MHz, CD_3CN) δ 9.02 (1H, br), 8.33 (2H, br), 8.08 (1H, br), 7.88-7.85 (1H, d), 7.76-7.65 (3H, m), 7.55 (2H, t), 7.43 (2H, t), 7.35-7.29 (3H, br), 7.12 (2H, br), 3.87 (4.5H, m), 3.41 (1.5H, br), 2.39 (3H, s).. ^{13}C NMR (400 MHz, CD_3CN) δ 171.4, 167.1, 166.2, 165.9, 162.1, 161.1, 159.3, 155.4, 149.6, 146.3, 141.8, 140.8, 140.5, 139.0, 138.8, 131.7, 131.5, 130.7, 130.6, 130.5, 130.1, 125.2, 124.6, 122.1, 121.9, 112.6, 52.6, 32.5, 20.7. IR (ATR): 2029 cm^{-1}, 1918 cm^{-1} ν CO.

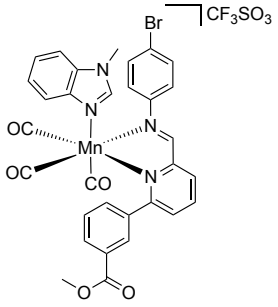

MnC9MeBeim. Yield 28%. MW 815.45 gmol^{-1}. HR-MS (+, m/z, [M-TfO]$^+$): [$C_{31}H_{23}BrMnN_4O_5$]$^+$ calculated: 665.0232; found: 665.0206. Analytical RP-HPLC: t_R = 5.68 min. ESI-MS (+, m/z, [M-TfO-3CO]$^+$): 581.0 [$C_{28}H_{23}BrMnN_4O_2$]$^+$. ^{1}H NMR (300 MHz, CD3CN) δ 9.04 (1H, s), 8.36-8.24 (3H, br), 8.08 (1H, d), 7.88 (1H, d), 7.76-7.53 (7H, m), 7.46-7.35 (2H, m), 7.13 (2H, br), 3.95-3.87 (4.5H, m), 3.41 (1.5H, s). ^{13}C NMR (400 MHz, CD_3CN) δ 172.7, 171.4, 166.0, 151.6, 150.9, 146.3, 142.4, 141.7, 140.9, 134.1, 133.3, 133.2, 132.0, 131.6, 131.5, 130.5, 130.4, 130.1, 128.7, 125.3, 124.6, 124.2, 124.0, 112.6, 52.6, 32.5. IR (ATR): 2031 cm^{-1}, 1923 cm^{-1} ν CO.

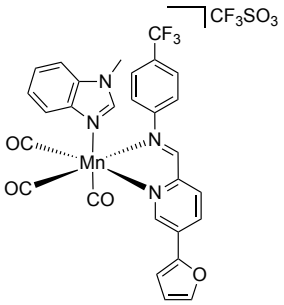

MnE2MeBeim. No prepHPLC needed. Compound pure after precipitation and washing. Yield 99%. MW 686.47 gmol^{-1}. HR-MS (+, m/z, [M-TfO]$^+$) $[C_{28}H_{19}F_3MnN_4O_4]^+$ calculated: 587.0739; found: 587.0718. Analytical RP-HPLC: t_R = 5.74 min. ESI-MS (+, m/z, [M-TfO-3CO]$^+$): 503.1 $[C_{25}H_{19}F_3MnN_4O_1]^+$. ^{1}H NMR (300 MHz, CD_3CN) δ 9.42 (1H, s), 8.85 (1H, s), 8.47-8.44 (1H, d), 8.31-8.28 (1H, d), 7.84-7.79 (4H, m), 7.63-7.60 (1H, m), 7.48-7.45 (1H, m), 7.39 (1H, m), 7.32 (1H, d), 7.29 (1H, s), 6.73 (1H, s), 3.73 (3H, s). ^{13}C NMR (400 MHz, CD_3CN) δ 171.5, 154.7, 152.7, 150.7, 149.1, 146.9, 146.1, 142.8, 135.5, 133.7, 132.5, 131.6, 127.6, 127.6, 125.1, 124.4, 123.5, 118.6, 113.8, 113.1, 112.3, 32.3. IR (ATR): 2033 cm^{-1}, 1934 cm^{-1} ν CO.

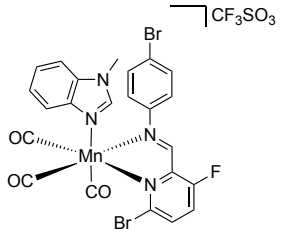

MnG9MeBeim. Yield 26%. MW 778.21 gmol^{-1}. HR-MS (+, m/z, [M-TfO]$^+$): $[C_{23}H_{15}Br_2FMnN_4O_3]^+$ calculated: 626.8875; found: 626.8860. Analytical RP-HPLC: t_R = 5.42 min. ESI-MS (+, m/z, [M-TfO-3CO]$^+$): 544.1 $[C_{20}H_{15}Br_2FMnN_4]^+$. ^{1}H NMR (300 MHz, CD_3CN) δ 8.92 (1H, s), 8.15 (1H, br), 7.90 (1H, br), 7.77-7.75 (2H, d), 7.70-7.65 (2H, t), 7.52-7.47 (2H, t), 7.43-7.41 (1H, d), 7.38-7.32 (2H, m), 3.81 (3H, s). ^{13}C NMR (400 MHz, CD_3CN) δ 166.8, 150.7, 147.0, 142.5, 138.0, 137.9, 135.4, 133.5, 133.2, 132.9, 125.2, 124.7, 124.6, 124.5, 124.0, 123.7, 112.5, 32.4. IR (ATR): 2034 cm^{-1}, 1923 cm^{-1} ν CO. XRD: CCDC No 2280008.

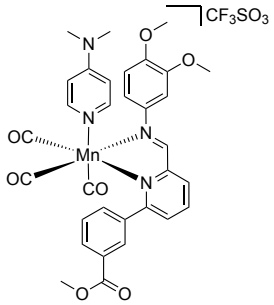

MnC1DMAP. Yield 29%. MW 740.59 gmol^{-1}. HR-MS (+, m/z, [M-TfO]$^+$) [$C_{32}H_{30}MnN_4O_7$]$^+$ calculated: 637.1495; found: 637.1478. Analytical RP-HPLC: t_R = 5.35 min. ESI-MS (+, m/z, [M-TfO-3CO]$^+$): 553.1 [$C_{29}H_{30}MnN_4O_4$]$^+$. ^{1}H NMR (300 MHz, CD_3CN) δ 8.85 (1H,br), 8.24-7.76 (9H, m and br), 7.34 (2H. br), 7.10 (2H, br), 6.50 (2H, br), 3.89 (6H, br), 2.96 (3H, br), 1.94 (6H, br). ^{13}C NMR (400 MHz, CD_3CN) δ 169.7, 166.5, 158.2, 155.8, 151.6, 150.9, 150.3, 145.1, 144.8, 141.8, 140.7, 131.9, 131.7, 131.1, 130.3, 129.3, 112.3, 109.0, 106.7, 56.3, 52.7, 39.0. IR (ATR): 2027 cm^{-1}, 1916 cm^{-1} ν CO. XRD: CCDC No 2280009.

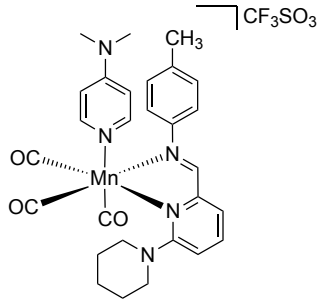

MnD8DMAP. No prepHPLC needed. Yield 64%. MW 689.59 gmol^{-1}. HR-MS (+, m/z, [M-TfO]$^+$) [$C_{28}H_{31}MnN_5O_3$]$^+$ calculated: 540.1807; found: 540.1790. Analytical RP-HPLC: t_R = 6.30 min. ESI-MS (+, m/z, [M-TfO-3CO]$^+$): 456.1 [$C_{28}H_{31}MnN_5O_3$]$^+$. ^{1}H NMR (300 MHz, CD_3CN) δ 8.70 (1H, s), 8.06 (1H, m), 7.66-7.59 (2H, m), 7.48 (m, 4H), 7.33 (2H, m), 6.46 (2H, m), 3.50 (2H, br), 3.21-3.05 (4H, br), 2.95 (6H, s), 2.49 (3H, s), 1.88 (2H, br),1.75 (2H, br). ^{13}C NMR (400 MHz, CD_3CN) δ 170.6, 169.8, 155.0, 153.0, 151.4, 149.2, 141.7, 140.6, 131.0, 125.0, 122.7, 121.7, 108.7, 39.1, 39.0, 24.6, 24.0, 20.7. IR (ATR): 2024 cm^{-1}, 1924 cm^{-1} ν CO. XRD: CCDC No 2280010.

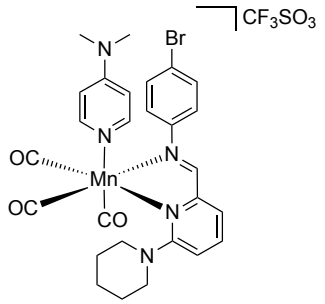

MnD9DMAP. Yield 29%. MW 754.46 gmol^{-1}. HR-MS (+, m/z, [M-TfO]$^+$) [$C_{27}H_{28}BrMnN_5O_3$]$^+$ calculated: 604.0756; found: 604.0740. Analytical RP-HPLC: t_R = 6.38 min. ESI-MS (+, m/z, [M-TfO-3CO]$^+$): 522.0 [$C_{24}H_{28}BrMnN_5$]$^+$. ^{1}H NMR (300 MHz, CD_3CN) δ 8.71 (1H, s), 8.08 (1H, t), 7.82 (2H, d), 7.69-7.62 (2H, m), 7.49 (2H, d), 7.32 (2H, d), 6.45 (2H, d), 3.64-3.22 (5H, br), 2.95 (6H, s),1.87-1.65 (5H, br). ^{13}C NMR (400 MHz, CD_3CN) δ 171.9, 169.9, 155.3, 154.8, 151.4, 150.5, 141.8, 137.9, 133.7, 125.5, 124.8, 123.2, 122.2, 108.8, 39.0, 24.6, 24.0. IR (ATR): 2028 cm^{-1}, 1919 cm^{-1} ν CO.

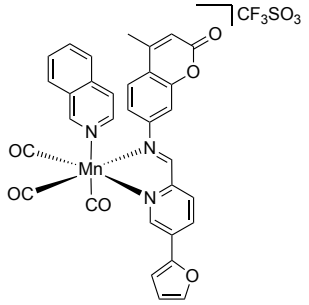

MnE6Quin. Yield 34%. MW 747.53 gmol^{-1}. HR-MS (+, m/z): [M-TfO]$^+$/ [$C_{32}H_{21}MnN_3O_6$]$^+$ calculated: 598.0811; found: 598.0800; [M-TfO-3CO+MeOH]$^+$/ [$C_{30}H_{25}MnN_3O_4$]$^+$ calculated: 546.1226; found: 598.0848. Analytical RP-HPLC: t_R = 5.35 min. ESI-MS (+, m/z, [M-TfO-3CO]$^+$): 514.1 [$C_{29}H_{21}MnN_3O_3$]$^+$. ^{1}H NMR (300 MHz, CD_3CN) δ 9.56 (1H, s), 8.76 (1H, s), 8.61 (1H, s), 8.32 (1H, d), 8.00 (1H, d), 7.92 -7.84 (4H, m), 7.78-7.75 (2H, m), 7.67-7.61(2H, m), 7.41 (1H, d), 7.32 (1H, d), 7.25 (1H, s), 6.69 (1H, s), 6.34 (1H), 2.44 (3H, s). ^{13}C NMR (400 MHz, CD_3CN) δ 171.4, 157.5, 154.9, 153.4, 153.2, 152.8, 150.7, 149.1, 147.0, 145.0, 136.6, 134.0, 133.9, 132.8, 131.2, 129.8, 129.7, 128.7, 127.6, 127.0, 123.8, 121.4, 119.6, 116.2, 114.0, 113.5, 111.1, 18.4. IR (ATR): 2037 cm^{-1}, 1941 cm^{-1} ν CO.

Crystallographic data collection and crystal structure determination
Single crystal X-ray diffraction analyses were carried out with a Bruker D8Venture diffractometer equipped with a kappa goniometer and an Oxford cryosystem. Microfocused MoKα radiation (λ = 0.71073) was used and Lorentz polarization and absorption correction were applied by the SADABS[49] procedure. The phase problem was solved by direct methods and the structures were refined by full-matrix least-squares on all F2 using SHELXL[50,51], as implemented in the OLEX2 suite of programs. Analytical expressions of neutral atom scattering factors were taken from the International Tables for X-Ray Crystallography[52]. The structure drawings were obtained using ORTEPIII[53] and Mercury[54]. CCDC 2280008-2280010 contain the supplementary crystallographic data. These data can be obtained free of charge via http://www.ccdc.cam.ac.uk/conts/retrieving.html. X-Ray structure determination analysis were performed on crystals grown by recrystallization from the solvent (EtOH for MnD8DMAP, MeOH for MnC1DMAP, THF in diffusion with heptane for MnG9MeBeIm).

UV-vis spectroscopy
UV-vis spectra were collected using 1 cm quartz cuvette at room temperature. Stock solution of the complexes were 5 mM in DMSO and were diluted in DMSO or PBS to 50 μM finial concentration. Stability was checked by following the maximum of absorption during 18 hours of incubation with a plate reader (Tecan instrument Infinite M1000).

The release of carbon monoxide (CO) from metal carbonyl complexes was assessed spectrophotometrically by measuring the conversion of hemoglobin (Hb) to carboxyhemoglobin (Hb-CO) adapting a previously published procedure.[116] Briefly, fresh solutions of hemoglobin with a final concentration of 80 μM were prepared by dissolving the protein in HEPES pH 7.4. Prior to each reading, a freshly prepared solution of sodium dithionite (0.1%) was added to convert hemoblogin to deoxyhemoglobin. After preparing the myoglobin solutions, a stock solution of MnG9MeBeIm was added to achieve a final concentration of 20 μM. The absorbance was then measured from 500 nm to 650 nm at 30-minute intervals over a duration of 8 hours.

Identification of active compounds and MIC and MBC determination.
The samples were tested for their antimicrobial activity against Escherichia coli W3110, Staphylococcus aureus COL (MRSA), Pseudomonas aeruginosa PAO1, Acinetobacter baumannii ATCC19606, Klebsiella pneumoniae NCTC418, and methicillin-resistant Staphylococcus aureus COL, clinical isolate Staphylococcus epidermidis, clinical isolate methicillin susceptible Staphylococcus aureus, Bacillus subtilis 168 CA (wild type), Enterococcus spp S342, Enterococcus casselliflavus S9. Enterococcus clinical isolate strains isolated in the laboratory of Food Inspection Unit of Parma University from pig food chain. Resistance to vancomycin was carried by VanA detected by PCR. A colony of bacteria was grown in Luria-Bertani (LB) medium overnight at 37 °C. Stock solutions of 2 mM of the samples were prepared in DMSO and diluted to a starting concentration of 100 μM in Mueller Hinton (MH) medium. For the identification of the active compound only one concentration (100 μM) was used, for the MIC determination the samples were two folds diluted. The bacteria concentration was measured by

measuring the optical density at 600 nm and diluted to OD_{600} of 0.022 in MH medium. 5 µL of the diluted bacterial solution was used to inoculate 150 µL of the sample solutions, resulting in a final inoculation of about 5×10^5 CFU/mL. The plates were then incubated at 37 °C for 18 hours. For each assay, a control of broth only and a growth control of broth with bacterial inoculum without antibiotics were included in two columns of the plate. Polymyxin B and Vancomycin were used as control antibiotic for E. coli and MRSA respectively. The growth was measured by analysing the absorbance of the bacterial suspension at 600 nm using a plate reader (Tecan instrument Infinite M1000). The MBC values were determined by resuspending 10 µL of the suspension from the MIC plate in fresh LB agar. After 18 hours, the agar plates were checked and the MBC was chosen as the concentration that could prevent the growth of any bacteria.

A competitive assay with hemoglobin was conducted by preparing different MH media (with 160, 80, 40, 20, 10, 5, 2.5 µM). This was achieved by adding a stock solution of hemoglobin in PBS, which was sterilized through filtration. The FICI values were determined as follows: $FICI=FIC_A+FIC_B=C_A/MIC_A+C_B/MIC_B$, where MIC_A and MIC_B are the MIC values of compounds A and B alone, and C_A and C_B are the effective concentration of A and B when administrated. A FICI index of 0.5 or less indicates synergistic effect; between 0.5 and 4 the effect is additive. FICI index greater than 4 denotes antagonism.[46,47]

Haemolysis assay

The compounds were tested on human red blood cells (hRBCs) using a haemolysis assay as previously reported.[117] Blood was obtained from Interregionale Blutspende SRK AG in Bern, Switzerland. 1.5 mL of whole blood was centrifuged at 3000 rpm for 15 minutes at 4 °C, and the plasma was discarded. The hRBC pellet was washed three times with PBS (pH 7.4) and then resuspended to a final volume of 10 mL in PBS. For the identification of the not haemolytic compound only one concentration (20 µM) was used, for the determination of HC_{50} of the lead compounds, the samples were two folds diluted starting from 200 µM. Samples stock solution was 20 mM in DMSO. Each plate included a blank medium control (PBS) and a haemolytic activity control (0.1% Triton TM X-100). hRBC suspension was incubated with the samples in PBS in a V-shaped 96-well plate for 4 hours at 20 °C. After the incubation, 100 µL of supernatant was carefully pipetted to a flat bottom, clear 96-wells plate. Haemolysis was measured by analysing the absorbance of free haemoglobin in the supernatants at 540 nm using a plate reader (Tecan instrument Infinite M1000). The percentage of haemolysis at each concentration was determined and the HC_{50} was calculated. The growth was measured by analysing the absorbance of free hemoglobin in the supernatants at 540 nm using a plate reader (Tecan instrument Infinite M1000).

Cytotoxicity.
The HuDe human epithelial cells were purchased from the American Type Culture Collection (ATCC, Manassas, VA, USA). The cells were cultivated in RPMI 1640 medium supplemented with 10% heat-inactivated fetal bovine serum, 100 UmL^{-1} of penicillin and streptomycin, and maintained at a temperature of 37 °C with 5% CO_2. All experiments were carried out using cells that were in the log phase. Initially, 100 000 mL^{-1} of cells were seeded into 96-well plates and incubated for 18-24 hours before being exposed to compounds at concentrations ranging from 0.1 µM to 100 µM. Following a 24 hour incubation period at 37 °C, the cells were stained with Trypan Blue and counted using a haemocytometer. The control for the experiments was DMSO. Each sample was tested in at least three independent experiments. The concentration of a compound required to reduce cell growth by 50% compared to untreated control cells was determined as the half maximal inhibitory concentration (IC_{50}).

Fluorescence light microscopy
Protocols were adapted from previous reported papers.[118] Fluorescence light microscopy was performed using a Nikon Ti-2 Eclipse,Nikon Europe BV, Amsterdam, Netherlands with a CFI Plan Fluor 40× oil immersion objective (CFI Plan Fluor 40×/1.30 W.D. 0.24, Nikon Europe BV). Brightfield and fluorescence images were recorded by an Andor Zyla 4.2 Plus USB3 camera in Widefield and using LED light excitation. Images were analyzed using ImageJ (Fiji) Version: 2.0.0-rc-69/1.52p. Bacillus subtilis PrpsD (MW54) expressing cytosolic GFP from the strong ribosomal PrpsD promoter was grown in LB at 37 °C under steady agitation in the presence of 100 µg/mL Spectinomycin. Bacillus subtilis MinD (KS69) was grown in LB at 37 °C under steady agitation in the presence of 50 µg/mL Spectinomycin. Overnight cultures of B. subtilis were regrown in LB (for MinD, 0.1% Xylose as an inducer is needed for the second culture). MnG9MeBeIm and controls were added at an OD_{600} of 0.3 and images were taken after 20 min of antibiotic treatment. Cells were immobilized on pre warmed 1.2% agarose-covered slides in HEPES buffer (50 mM pH 7.4)[119]. Membranes were stained with 0.5 µg/mL Nile red for 5 min. Nucleoids were stained with 1 µg/mL DAPI for 5 min. Carbon monoxide release was measured using BioTracker Carbon Monoxide Probe 1 Live Cell Dye (Sigma, SCT051) with the addition of $PdCl_2$ at 5 µM for 20 minutes.

Propidium iodide assay
Permeability for the large fluorescent molecule propidium iodide as a reporter for the presence of large membrane pores or severe membrane disruption was quantified using a Tecan Infinite M1000 plate reader, following the previously described protocol[113,120]. Cells were grown until an OD_{600} of 0.3 and antibiotics were added simultaneously with 13.3 µg/mL propidium iodide (1 mg/mL stock in DMSO). After 15 min, cells were centrifugated and the pallet washed twice with HEPES buffer (pH 7.4) and fluorescence was measured using 535 nm excitation and 617 nm emission wavelengths. SDS 0.05% served as positive control. Each experiment was performed in triplicate.

$DIS_3(5)$ assay

Membrane potential measurements were conducted using the potentiometric fluorescent probe 3,3'-dipropylthiadicarbocyanine iodide (DiSC3(5)) on a Tecan Infinite M1000 plate reader, following the previously described protocol.[113,120] Briefly, 1 µM $DiSC_3(5)$ was added to exponentially growing *B. subtilis* 168 cultures at 37 °C, and the baseline was recorded for 5 minutes using an excitation wavelength of 651 nm and an emission wavelength of 675 nm. MnG9MeBeIm (3 µM), gramicidin (1 µg/mL, positive control) were then added, and samples were measured for an additional 20 minutes at 37 °C. Each experiment was performed in triplicate.

Resazurin assay

Respiratory chain activity was measured following the reduction of resazurin to resofurin by fluorescence, following the previously described protocol[113,120]. B. subtilis 168 was cultivated in LB medium at 37 °C until reaching an optical density (OD_{600}) of 0.3. Following that, the cells were treated with different concentrations of MnG9MeBeIm (1.5, 3, 6, 12 µM), 100 µM CCCP, or 15 mM sodium azide. After 15 minutes, samples were collected and adjusted to an OD_{600} of 0.15 through dilution with medium. Subsequently, the samples were incubated for 5 minutes with 100 µg/mL of resazurin under steady agitation at 37 °C. Fluorescence measurements were taken using an excitation wavelength of 545 nm, and the emitted light was recorded at 630 nm. The reported percentages represent the relative values compared to the untreated control. Each experiment was performed with two biological replicates and three technical replicates.

In vivo tox (moth).

Larvae (200-300 mg) were sterilized by gently rubbing them with a paper towel soaked in an ethanoic solution and then individually injected with 10 µL of solution into one proleg using a 50 µL syringe (Hamilton Ltd). The compound was dissolved in DMSO (28 mM) and diluted to final concentrations of 40 µM, 20 µM and 10 µM with physiological solution (0.9% NaCl, maximum 5% DMSO). Five larvae were used for each group. Untreated larvae and larvae injected with 5% DMSO / physiological solution (0.9% NaCl) were included as negative controls. Following injection, the larvae were incubated at 37 °C and monitored every 24h for 5 days. Larval performance was assessed according to the *G. mellonella* Health Index Scoring System.[63] The experiments were repeated three separate times.

In vivo efficacy (moth).

Galleria larvae, with a weight range of 200-250 mg, were intentionally infected with 10 cells of Staphylococcus aureus (ATCC 43300) and subsequently incubated at 37 °C. Two hours following the infection, a precisely measured volume of 10 µL containing MnG9MeBeIm (at a concentration of 300 µM) was administered via injection into the larvae. For comparative analysis, control groups were established, which included larvae injected with a vehicle solution composed of DMSO and HEPES, as well as another group treated with Rifampicin (at a concentration of 0.4 mg/mL). Each treatment group consisted of seven larvae, ensuring statistical reliability

***In vivo* burn wound infection model**

In vivo burn wound infection model was conducted following the previously described protocol.[121] To ensure aseptic conditions, we employed 70% ethanol to sterilize the larval body surfaces. This involved thoroughly spraying the entire larval body with the ethanol solution. Following sterilization, Petri dishes were left uncovered in a sterile environment to facilitate ethanol evaporation.To induce burns, a *G. mellonella* larva was positioned on its ventral side, enabling access to the back segment. It was securely immobilized by holding down its head and thorax segments. The burn instrument, a steel nail with a head size of 2 mm^2 embedded in cork, was heated in the middle flame of a Bunsen burner until it reached a red/white-hot state. This burn instrument was then applied to the middle segment of the *G. mellonella* back for a duration of 4 seconds. Any larvae displaying significant haemolymph loss or protruding fat body after the procedure were promptly euthanized by placing them at -20°C for a minimum of 20 minutes to minimize suffering. Following the burn induction, 10 µL of an overnight *S. aureus* 62707 culture was carefully pipetted onto the wound site. Subsequently, the larvae were given a 45-minute resting period before any additional treatments were introduced. To further the experiment, a 10 µL solution of MnG9MeBeIm 3 mM (90% 50 mM HEPES Buffer, pH = 7.4 + 10% DMSO) were applied to the infected burn. The control groups did not receive any treatment after the burn induction. These larvae were incubated at a temperature of 37°C for a total duration of 72 hours, with mortality rates being recorded hourly throughout this period.

5. Targeting lung cancer cells with gold(III) complexes

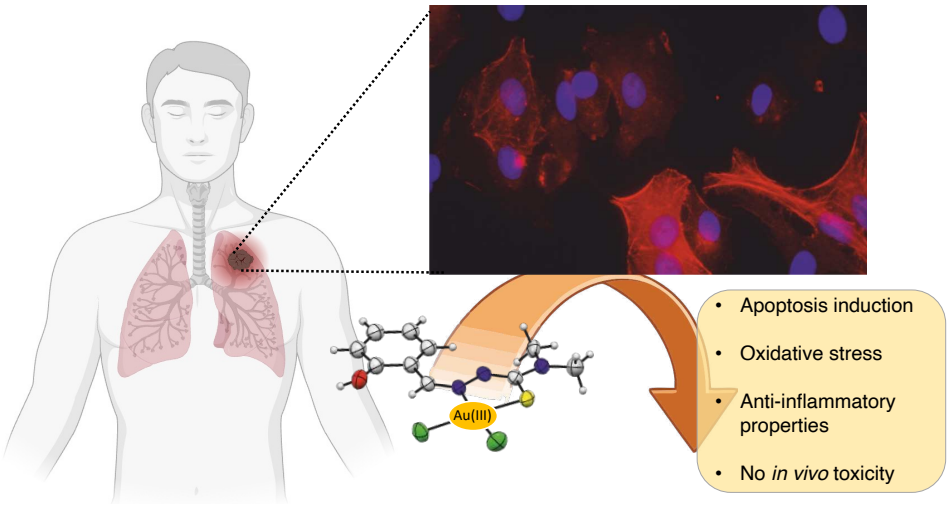

This chapter's research involved a collaborative work with Silvana Pinelli from the University of Parma's Department of Medicine and part of the work was carried out at Otto-von-Guericke Universität Magdeburg. The project was co-supervised from Prof. Franco Bisceglie and Prof. Nora Kulak.

Abstract

Cancer continues to pose a global threat, underscoring the urgent need for more effective and safer treatment options. Recent developments have highlighted gold-based compounds as promising candidates, thanks to their wide array of biological activities. This chapter presents the synthesis of three gold(III) complexes, derived from thiosemicarbazone ligands, with comprehensive characterizations that encompass their X-ray crystal structures.

The investigation started with preliminary mode-of-action studies on DNA and BSA and leading to an extensive exploration of the cytotoxic impact of these novel gold(III) complexes on lung cancer cells (A549, H2052, and H28). The findings unveil a concentration-dependent cytotoxic response, with H28 cells displaying the highest sensitivity to the treatment. Furthermore, an in-depth analysis of the cell cycle showcases that these compounds induce cell cycle arrest and stimulate apoptosis as a response to treatment. Morphological changes and increased oxidative stress have been observed, contributing significantly to cell death. One notable aspect is the complexes' ability to effectively suppress interleukin-6 production in mesothelioma cell lines, thus highlighting their anti-inflammatory potential.

To gain an initial understanding of their cytotoxicity on healty cells, hemolysis tests were conducted against human blood cells, yielding no evidence of hemolysis even at higher concentrations. Furthermore, an in-depth toxicity assessment through the *in vivo Galleria mellonella* model underscores the absence of detectable toxicity. These findings provide invaluable insights into the cytotoxic effects of gold(III) complexes and further proves that these complexes are promising novel therapeutic agents for lung cancer.

Cancer as a global challenge

Cancer, a persistent global threat, continues to pose a steadfast challenge to the medical and scientific communities, driving them to explore innovative approaches and pave the way for more effective treatments.[122] Despite remarkable progress in the field of oncology, the persistence of therapy-resistant solid tumors, particularly in response to platinum-based treatments like cisplatin, underscores the urgency of this endeavor. These treatments, while effective to some extent, frequently exact a heavy toll on patients in the form of debilitating side effects, such as nephron and neurotoxicity.[123]

"Golden" innovations in cancer therapy: the potential of gold-based compounds

In recent years, there has been a growing interest in exploring gold-based compounds for their potential in combating cancer. This interest was ignited by the successful development of auranofin, a gold-based compound originally used to treat rheumatoid arthritis.[124] Researchers have increasingly recognized the diverse biological activities of gold derivatives, which extend beyond their anti-rheumatic properties. These compounds have demonstrated antiviral, antimicrobial, and antiproliferative effects, offering a multifaceted approach to addressing various medical challenges.[38,125,126]

Gold(I) complexes represent a promising pool in which to look for new metal-based compounds. These compounds have emerged for the treatment of carcinomas as therapeutics with reduced side effects. This is particularly significant given the limitations and adverse effects associated with platinum-based therapies. Gold(I) complexes exhibit a unique set of chemical properties and biological activities, making them attractive candidates for further exploration.[124,127,128] While gold(I) has garnered considerable attention, gold(III) is also gaining recognition in the realm of cancer research. Gold(III) compounds are intriguing due to their electronic configuration, which is isoelectronic with Pt(II).[129] This similarity enables them to form square planar geometries and engage in

ligand exchange reactions, akin to platinum-based compounds. Consequently, gold(III) compounds are being investigated as potential candidates for the development of anticancer metallodrugs. In physiological conditions, gold(I) remains the stable form of gold, whereas gold(III) is often observed to be more reactive or less stable.[129,130] However, their reactivity and stability under biological conditions necessitate meticulous ligand design (e.g. cyclometalated gold(III) complexes) to prevent premature reduction in the presence of thiols.[131]

Gold(III)-thiosemicarbazone complexes as cytotoxic agents against lung cancer

In this chapter, my focus centers on the N^S moiety present in thiosemicarbazone (TSC) ligands. The extensive biological activity of TSC and their metal complexes has been widely investigated, with reported antibacterial and anticancer properties.[132–136] For instance, gold(III)-thiosemicarbazones have been found, for instance, to inhibit the proliferation of glioma cells.[137] Here, we extend the studies to variously N^4-substitued thiosemicarbazones derived from salicylaldehyde with an O^N^S chelating system. The gold(III) complexes were then tested for their cytotoxicity against different lung cancer cells, with particular attention to their candidacy to be used as drug to treat mesothelioma. Malignant pleural mesothelioma (MPM) is a rare cancer that affects pleura mesothelial cells, usually associated with the exposure to asbestos fibres.[138] Affected people have low life-expectancy due to its aggressive nature, and because it has been found to be therapy-resistant. The therapy used for this kind of tumor is still a combined administration of platinum (in the form of *cisplatin* or *carboplatin*) with antifolates.[139]

Synthesis

The complexes **Au17**, **Au18** and **Au19** were obtained from the corresponding ligands **L17**, **L18** and **L19** by reacting them with $[AuCl_4]^-$ (Scheme 7) and the reactions were optimized to have a single and pure product, changing the reaction solvent (MeOH or THF) and the form of Au(III) ($HAuCl_4$ or $NaAuCl_4$). The compounds were characterized by ^1H NMR, ^{13}C NMR, IR, and ESI and the purity was confirmed by CHNS elemental analysis.

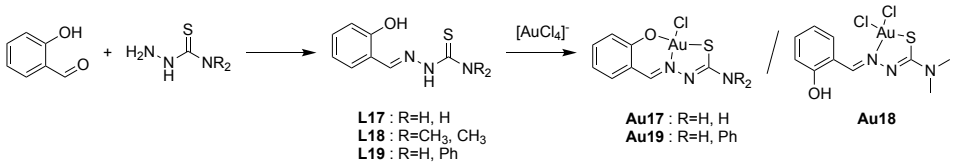

Scheme 7. General synthetic route of gold(III) complexes Au17, Au18 and Au19.

Crystallographic structural analysis of gold(III) complexes

The structural analysis of these compounds was further substantiated through X-ray diffraction of single crystals, which were obtained by refrigerating the reaction mixtures. The crystallographic data unequivocally reveal that all the complexes adopt a planar geometry, as illustrated in Figure 38.

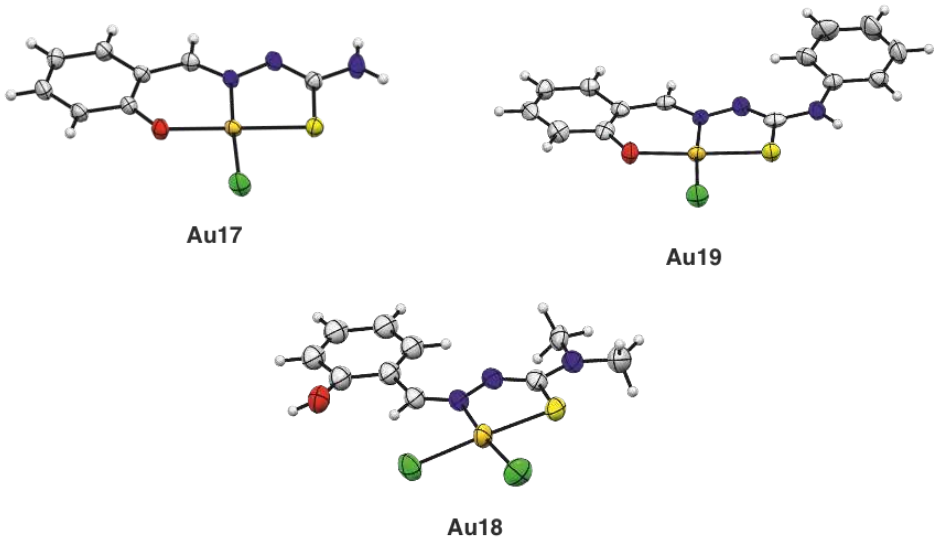

Figure 38. X-ray crystallographic structures of the gold(III) complex moieties (CCDC No 2193027-2193029)

In the cases of **Au17** and **Au19**, the Au(III) ions coordinate the tridentate ligand, with the unique feature that the ligand also binds through the hydroxyl oxygen atom. A chloride ion completes the coordination sphere. Conversely, in **Au18**, the Au(III) ion coordinates with the ligand in a bidentate manner, forming bonds solely through the immine nitrogen and sulfur atoms. In this instance, two chloride ions complete the coordination sphere. Notably, within the asymmetric unit, two complex moieties coexist, with one of them exhibiting disorder on two positions.

Stability assessment of gold(III) complexes

To assess the stability of the gold(III) complexes under physiological conditions, we subjected them to a 24-hour examination at 37 °C, employing UV-Vis spectroscopy in RPMI cell culture medium (Figure 39). Remarkably, the absorption profile displayed no notable variations, affirming the aptitude of the ligands in effectively stabilizing gold(III) in a physiologically mimicked environment.

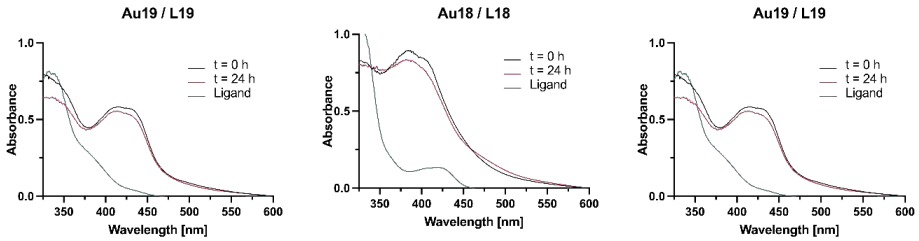

*Figure 39. UV-Vis spectra of the Au(III) complexes' stability (**Au17-Au19**) at 100 µM in 0.5% DMSO in RPMI medium freshly made (t=0 h) and after incubation at 37 °C for 24 h (t=24 h) plus comparison with the free ligand at 100 µM under the same condition.*

Gold(III) stability through cyclic voltammetry

Cyclic voltammograms were recorded to study the redox behavior of these complexes at a pH of 7.4, as depicted in Figure 40. This analytical technique plays a pivotal role in assessing the stability of gold(III) in its intended form and determining whether it has a propensity to convert into different forms of gold. Intriguingly, the complexes exhibited a conspicuous absence of any significant peaks within the explored potential range, highlighting their remarkable redox inertness. The strong resistance to redox reactions stands as compelling evidence of the complexes' ability to preserve their structural integrity and stability over time.

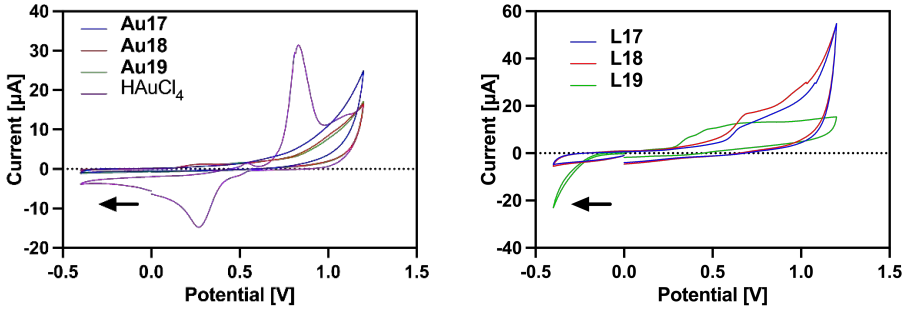

Figure 40. Cyclic voltammograms obtained for 0.2 mM of complexes and ligands at pH 7.4 recorded in 96 mM KNO3/4 mM HNO3 with 10% DMSO. The starting point was at 0 V and the arrow indicates the direction of the potential. The scan rate was 50 mV/s.

For comparative purposes, I employed $HAuCl_4$ as a control, and it demonstrated a reversible peak, attributed to the Au(III)/Au(0) redox pair.[140] This observation further emphasizes the distinctive redox behavior of the complexes. Moreover, we extended the investigation to the CV analysis of the ligands alone, which, like the complexes, displayed negligible redox activity within the applied potential window. This corroborates the earlier conclusion that the ligands in the complexes effectively stabilize gold(III).

Based on these findings, it is possible to posit that gold(III) remains in the biologically active form within these complexes, underscoring their potential as stable candidates for therapies.

Computational electronic potential surface calculation

The atomic coordinates found in the crystal structure served as the basis for computational optimization, utilizing Gaussian16 to generate the electrostatic potential (ESP) surface (Figure 41). Notably, the complexes exhibit a localized partial negative charge proximate to the chlorine atoms, while conversely, a partial positive charge is evident surrounding the acidic protons (-NH_2 for **C17**, -OH for **C18**, -NRH for **C19**).

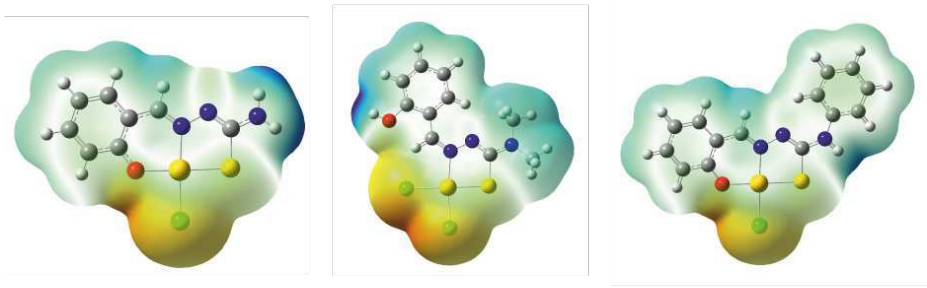

Au17 **Au18** **Au19**

Figure 41. Electrostatic potential surface. Blue indicates a positive charge while orange indicates a negative charge.

DNA interaction studies

Gold compounds are expected to exhibit distinct mechanisms of action. They can function as prodrugs, acquiring the capacity to interact with biomolecules upon activation, often accompanied by the loss of labile ligands and subsequent aquation. When positively charged, they have the ability to directly bind to biomolecules like proteins and DNA. Alternatively, they may possess redox activity, leading to the generation of reactive oxygen species capable of inflicting damage upon biomolecules.[141]

In collaboration with Prof Nora Kulak during my stay funded by the Erasmus SMT at the Otto von Guericke Universität Magdeburg, we studied different biological targets to gain a first insight into the possible mode of action of this class of compounds. The first target that we considered was DNA. Preliminary studies with calf thymus (CT) DNA showed a moderate interaction with DNA, but consistent within different techniques. $HAuCl_4$ was used as a reference compounds for gold(III). **Au17** and **Au19** showed only a minor increase (<0.5 °C) in the melting temperature (T_m) of CT-DNA, indicating the groove and/or electrostatic binding nature of the interaction.[142] **Au18** and $HAuCl_4$ showed an higher increase of the T_m (2-5 °C), indicating a stronger affinity for DNA (Figure 42, Table 11).

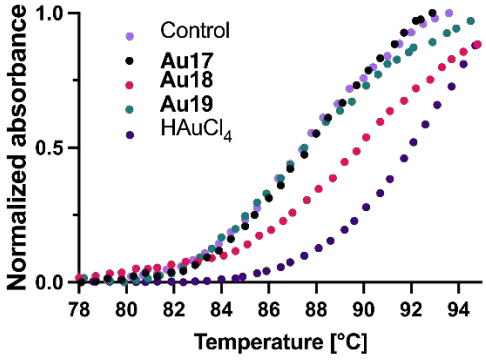

*Figure 42. Normalized DNA melting curves in the presence of **Au17**, **Au18**, **Au19** and $HAuCl_4$ (50 µM, 0.5% DMSO) in PBS buffer (10 mM, pH 7.4), CT-DNA (100 µM).*

The ethidium bromide (EtBr) displacement assay was used to determine a K_{app} towards DNA (Figure 43). The calculated K_{app} showed the same trend found in the DNA melting experiments. The fluorescence of the intercalated EtBr was quenched the most in the presence of **Au18** and $HAuCl_4$ (Figure 44, Table 11).

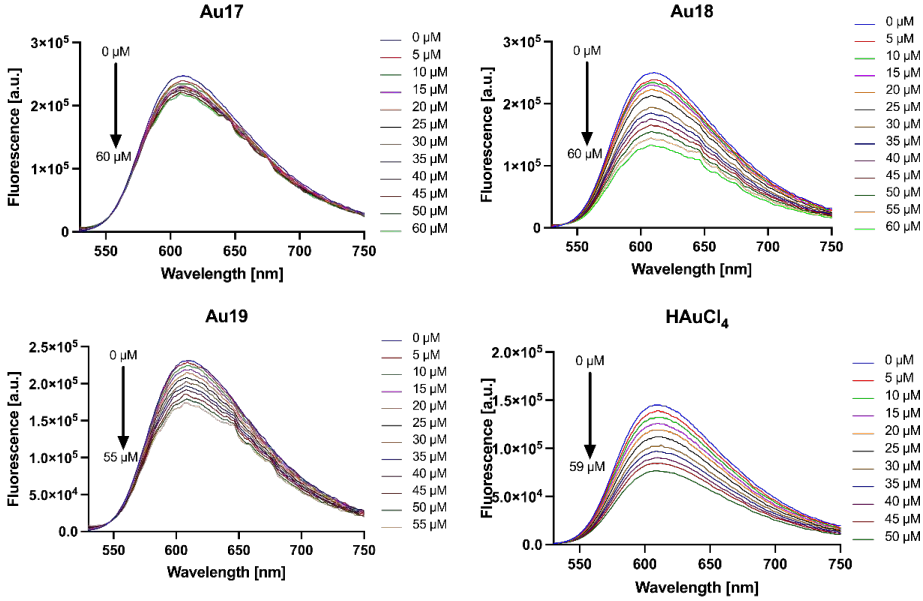

*Figure 43. EtBr displacement of the EtBr-CT-DNA system in PBS buffer (10 mM, pH 7.4) 0.5% DMSO by titration of **Au17**, **Au18**, **Au19** and $HAuCl_4$.*

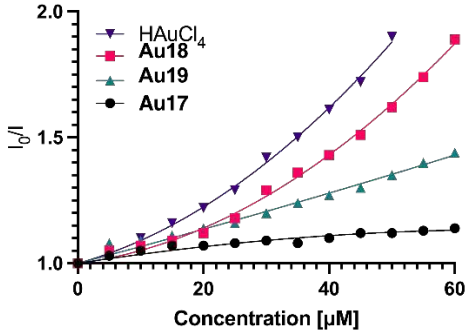

*Figure 44. Plot of I_0/I over concentration of **Au17**, **Au18**, **Au19** and $HAuCl_4$ to calculate K_{app}.*

Circular dichroism was used to distinguish between the electrostatic interaction and grove binding/intercalation (Figure 45). $HAuCl_4$ presents a significant alternation of the positive band, indicating intercalation as the principal interaction.[143–145] For **Au18** we observed minor changes in the negative band due to changes in helicity of the DNA, which hints to groove binding, and in the positive band due to interferences of the base pair stacking.

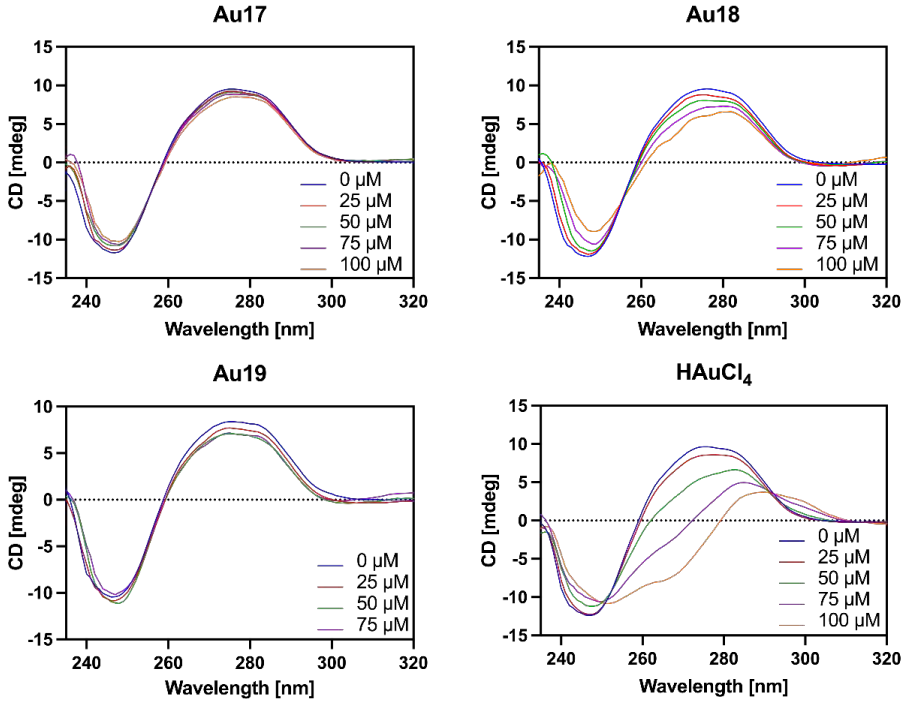

*Figure 45. CD spectra of CT-DNA (100 µM) in HEPES buffer (50 mM, pH 7.4) 10% DMSO with increasing concentrations of the **Au17**, **Au18**, **Au19** and $HAuCl_4$.*

Gel electrophoreses in the presence of the gold(III) compounds and plasmid DNA were conducted to investigate the possible DNA cleavage activity. **Au17**, **Au18**, **Au19** and $HAuCl_4$ did not show any relevant cleaving activity on DNA (Figure 46). The ratio between the plasmid forms I and II is not significantly different from the reference (DNA without complex).

Based on these data, we can exclude DNA cleavage as a mechanism of action. However, the above described intercalation might be a reason for their cytotoxicity, which will be discussed in the next paragraph, and DNA remains one of the possible targets.

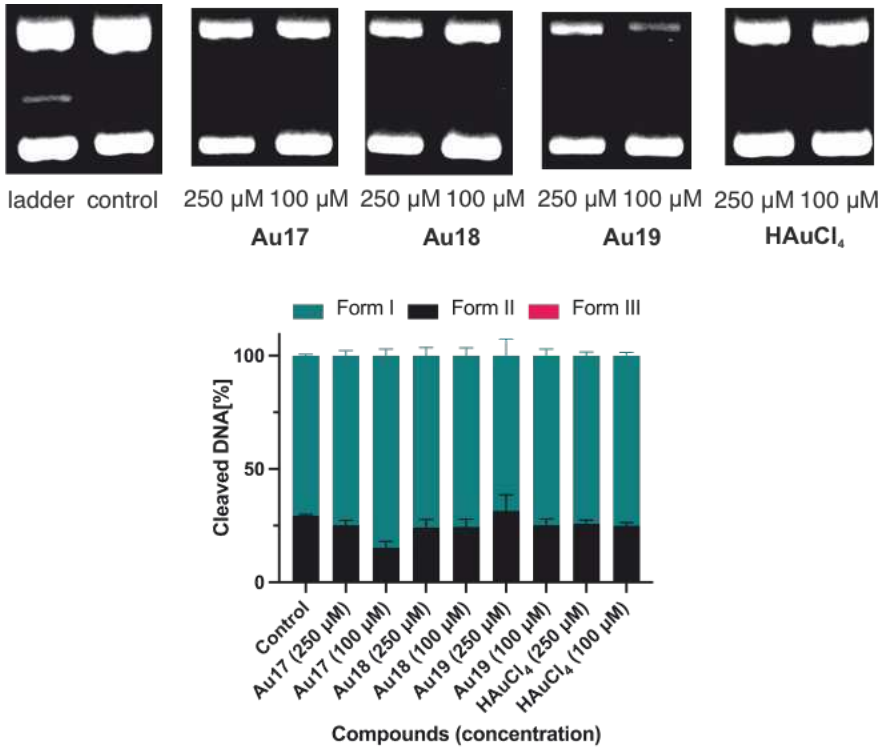

*Figure 46. (Above) Nuclease activity towards plasmid DNA pBR322 (0.025 mg/mL) of **Au17**, **Au18**, **Au19** and $HAuCl_4$ at 250 µM and 100 µM in HEPES buffer (50 mM, pH 7.4) with 10% DMSO in the presence of ascorbate (1 mM) as reducing agent after incubation for 2 h at 37 °C. (Below) Visualization of the extent of DNA cleavage in percent.*

*Table 10. Interaction between **C1**, **C2**, **C3** and $HAuCl_4$ with CT-DNA*

	DNA binding		
	T_m [°C]	ΔT_m [°C]	K_{app} [M^{-1}]
control	87.74	-	-
Au17	88.11	0.37	$< 10^5$
Au18	90.17	2.43	4.01×10^5
Au19	88.08	0.34	2.03×10^5
$HAuCl_4$	92.62	4.88	4.80×10^5

CT-DNA melting temperature (T_m), difference of CT-DNA melting temperature between compounds and the control (ΔT_m),

Serum protein interaction studies

Serum proteins, being abundant constituents in the bloodstream, play a pivotal role in the transport of various metal-based compounds. Understanding how these compounds interact with serum proteins is essential not only for comprehending their pharmacokinetics but also for delineating potential mechanisms of action and the overall fate of these compounds within the biological environment [146]

Fluorescent quenching of the bovine serum albumin (BSA) was monitored during the titration of **Au17**, **Au18**, **Au19** and $HAuCl_4$ (Figure 47). This study has unveiled the remarkable affinity of these gold(III) compounds for serum proteins, with affinity evident in the micromolar concentration range. Particularly noteworthy is **Au17**, which emerges as the standout compound, demonstrating the highest affinity for BSA. The calculated binding constant (K_b) for **Au17** surpasses that of the other compounds under study by a margin ranging from four to two orders of magnitude, as detailed in Table 11.

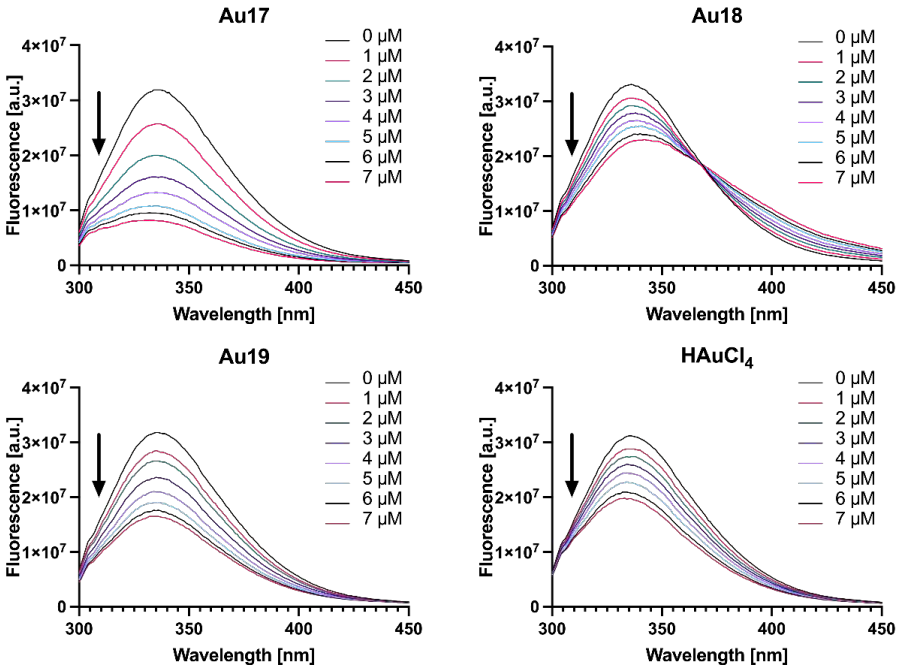

*Figure 47. The emission spectrum of bovine serum albumin (BSA) (2.5 μM; λ_{ex} = 280 nm) with increasing concentrations of **Au17**, **Au18**, **Au19** and $HAuCl_4$.*

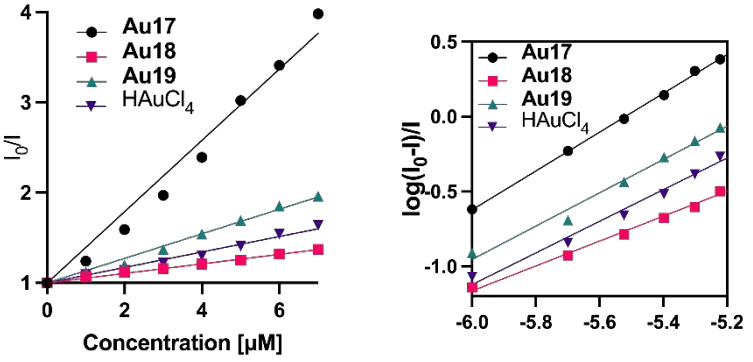

*Figure 48. (left) Plot of I_0/I over concentration of **Au17**, **Au18**, **Au19** and $HAuCl_4$ to calculate K_{SV}. (right). Stern–Volmer plot of BSA quenched by the of **Au17**, **Au18**, **Au19** and $HAuCl_4$ to calculate K_b and n.*

*Table 11. Interaction between **Au17**, **Au18**, **Au19** and $HAuCl_4$ with BSA protein.*

	Protein binding		
	K_{SV} [M^{-1}]	K_b [M^{-1}]	n
control	-	-	-
Au17	3.95×10^5	1.43×10^7	1.296
Au18	5.28×10^4	6.67×10^3	0.831
Au19	1.36×10^5	5.25×10^5	1.112
$HAuCl_4$	8.57×10^4	1.65×10^5	1.056

Stern–Volmer constant (K_{SV}), binding constant towards BSA (K_b), number of average binding sites in BSA (n).

Cytotoxicity evaluation of gold(III) complexes on lung cancer cells

The impact of ligands and complexes on the growth and viability of A549, H2052, and H28 cells was evaluated using the MTT assay, along with cell count analysis (employing Trypan blue to exclude non-viable cells) after 24 h of compound exposure. The results from both methods consistently demonstrated that treatments with **Au17**, **Au18**, and **Au19** significantly inhibited cell growth and affected cell viability in a concentration-dependent manner. Notably, no cytotoxic effects were observed in all examined cell lines up to 100 μM, even at the highest concentrations of the ligands (**L17**, **L18**, and **19**) and of the gold(III) salt. This shows a selectivity in the cytotoxicity of the complexes in comparison to their components. The H28 cell line exhibited the highest sensitivity to the gold compounds, with the lowest IC_{50} values around 2-6 μM (Table 12).

To further elucidate potential toxicity towards healthy cells, I subjected human red blood cells (hRBC) to the compounds, aiming to discern the concentration at which these compounds might induce the rupture of red blood cells (hemolysis). This assessment is crucial in drug development because a new therapeutic agent's hemolytic properties can have profound implications for its safety and effectiveness.[117] Remarkably, none of the compounds exhibited any significant hemolytic behavior, even at concentrations as high as 200 μM.

*Table 12. Antiproliferative activity display as IC_{50} [μM] value within 24 h or *HC_{50} for hRBD.*

	A549	H28	H2052	hRBC*
L17	> 100	> 100	> 100	nd
L18	> 100	> 100	> 100	nd
L19	> 100	> 100	> 100	nd
Au17	14 ± 1	2.2 ± 0.5	9.5 ± 0.9	>200
Au18	32 ± 1	2 ± 1	14 ± 1	>200
Au19	19 ± 1	6.4 ± 0.8	9.3 ± 0.8	>200
$HAuCl_4$	> 100 (114.1 ± 0.7)	> 100 (122.8 ± 0.6)	91.5 ± 0.9	nd

A549 – human lung carcinoma: H28 – human lung mesothelioma (epithelioid), H2052– human lung mesothelioma (sarcomatoid): hRBC – human red blood cells

Morphological analysis

The morphological analysis, conducted under the microscope, revealed that when we exposed A549, H2052, and H28 cells to ligands or complexes, we observed a clear loss of cell specializations, including cell elongations, and a decrease in cell volume (Figure 49). These changes were evident in all cell lines after treatment, indicating a consistent effect. The impact on cell morphology was much more noticeable and significant, compared to the ligands, when cells were treated with the complexes (Figure 49).

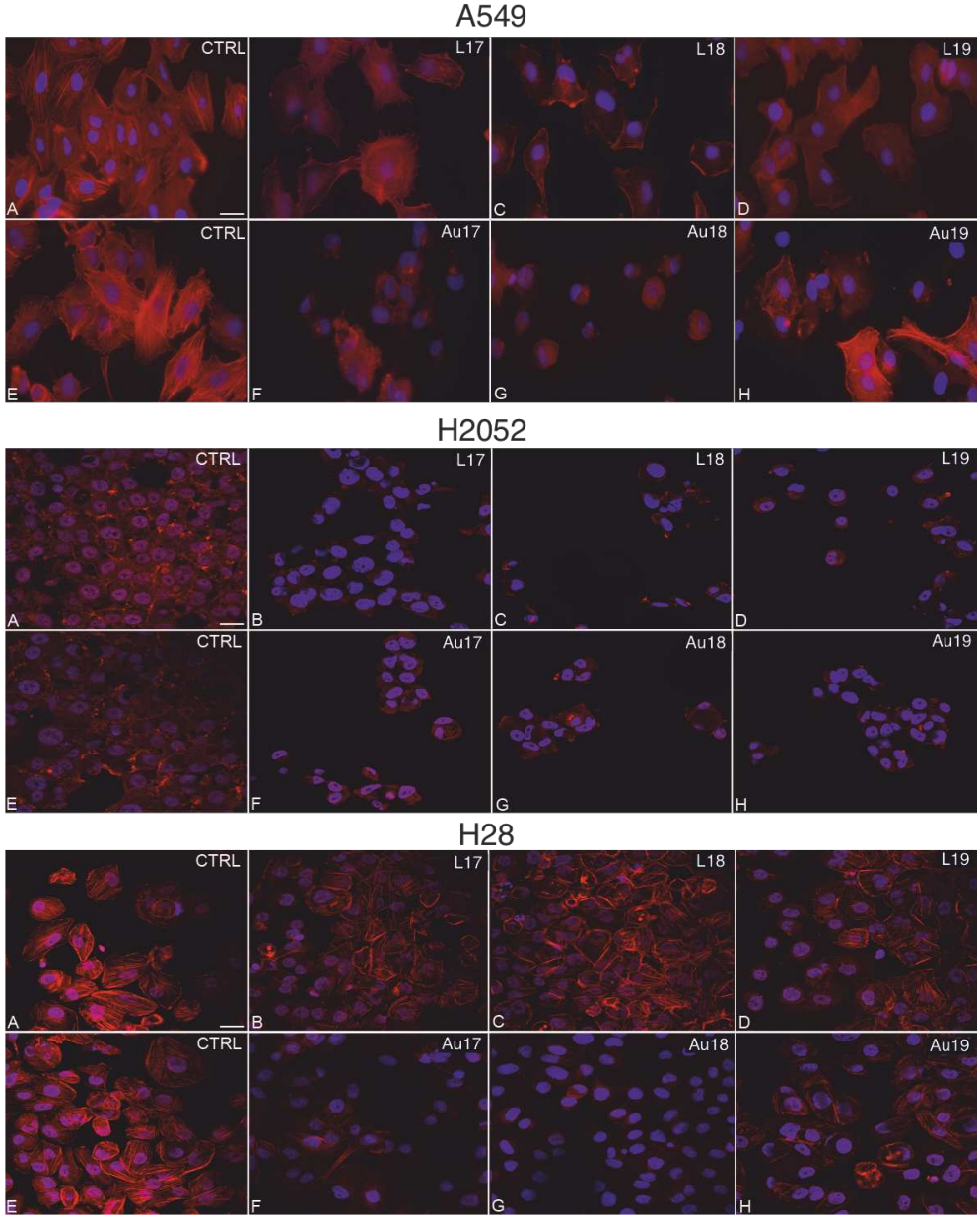

*Figure 49. Confocal microscopy of **A549**, **H2052**, **H28** cell lines treated with IC_{50} concentration of the complexes **Au17**, **Au18**, **Au19,** . Nuclei are stained with DAPI (depicted in purple).*

Cell cycle progression and apoptosis

Cell cycle progression and apoptosis were further investigated for each cell line after treatment with all the compounds. In A549 cells, treatment with **L19** led to a blockage in the G0/G1 phase of the cell cycle. However, when treated with **Au17** and **Au18**, as well as all respective ligands, a significant increase in cells in the subG0/G1 phase was observed, indicating the presence of apoptotic cells (Figure 50). To validate the induction of apoptosis, we evaluated caspase-3 activity, which confirmed the occurrence of apoptosis in response to the treatments (Figure 51). In H2052 cells, treatment with the compounds resulted in a notable decrease in the percentage of cells in the S phase, particularly evident after treatment with **Au18**. Additionally, the subG0/G1 peak was pronounced with all three complexes after treatment (Figure 50). Similar to A549 cells, caspase-3 activity also supported the occurrence of apoptosis in H2052 cells (Figure 51). Notably, cells treated with the **Au19** complex exhibited an increase in the G2/M phase, suggesting an inability to undergo cell division. Morphological analysis further confirmed this finding, with the nucleus observed to be blocked in the cell division phase (Figure 49). In H28 cells, a comparable trend to H2052 cells was observed, with the presence of a subG0/G1 peak in each treatment, except for cells treated with **L19**. Additionally, an increase in the G2/M phase was observed following treatment with **Au18** and **Au19** compounds.

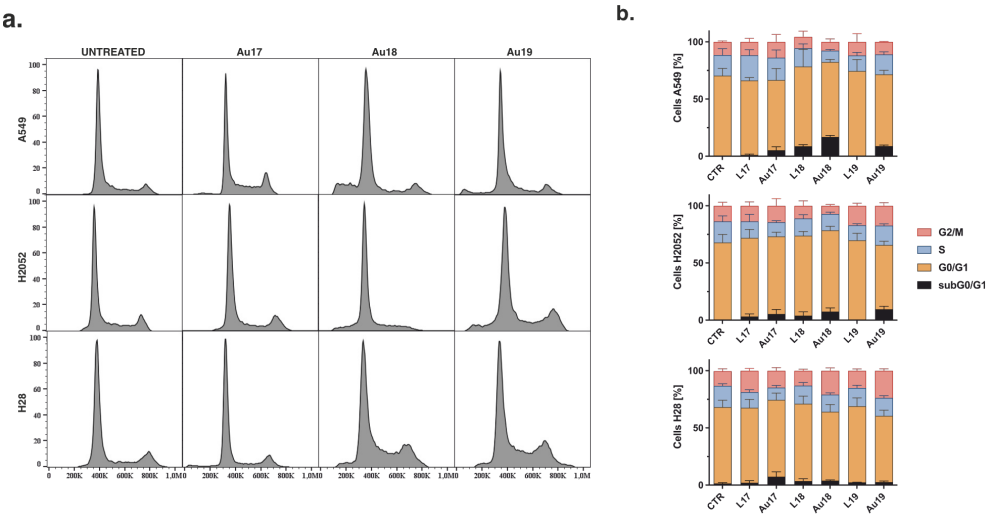

Figure 50. ***a.*** *Flow cytometry histograms of the* ***A549***, ***H2052*** *and* ***H28*** *cell cycle following 24 h of treatment with IC_{50} values of complexes* ***Au17***, ***Au18*** *and* ***Au19***. *By monoparametric DNA analysis four distinct phases could be recognized: the G2/M, S, G0/G1, S and subG0/G1 phase.* ***b.*** *Cell cycle distribution of A549, H2052, and H28 cells after 24 h of treatment with* ***L17***, ***Au18***, ***L18***, ***Au18***, ***L19***, *and* ***Au19***.

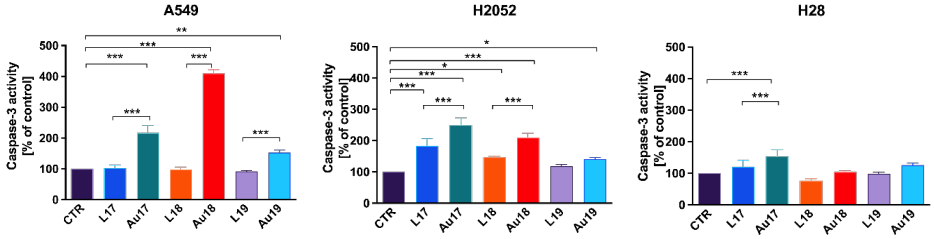

*Figure 51. Caspase-3 expression in A549, H2052, and H28 cells after treatment at the IC50 concentration. Gene expression levels were measured by real-time PCR using the RPL13 gene as a housekeeping gene. Significant differences from untreated cells (unless otherwise indicated): * = p < 0.05; ** = p < 0.01; *** = p < 0.001, ns = not significant*

Compounds' influence on cyclins and cyclin-dependent kinases

To gain further insight into the molecular mechanisms involved in the cell cycle regulation, we conducted the analysis of the expression levels of some key regulators, specifically cyclins and cyclin-dependent kinases (CDKs). Cyclins are a family of proteins that play a critical role in controlling the progression of the cell cycle. They function by forming complexes with specific CDKs, which are enzymes responsible for driving the cell through its various phases. Different

cyclins are expressed at specific stages of the cell cycle and bind to corresponding CDKs, activating them to trigger the necessary events for cell cycle advancement. The expression levels of cyclin E (CCNE1) and cyclin D1 (CCND1), which are critical for the transition from G1 to S phase, were found to be affected by the treatments with the compounds (Figure 52). This suggests that the compounds may exert their effects by modulating the activities of these cyclins, leading to cell cycle arrest and apoptosis induction. Furthermore, the levels of CDK6, CDK1, and CDK4 were also influenced by the compound treatments. These CDKs are essential for the progression through G1 and G2 phases, and their dysregulation can disrupt the cell cycle and promote cell death. Those findings provided additional evidence that the compounds interfere with the activities of these key CDKs, contributing to the observed effects on cell cycle progression and apoptosis in the three cell lines.

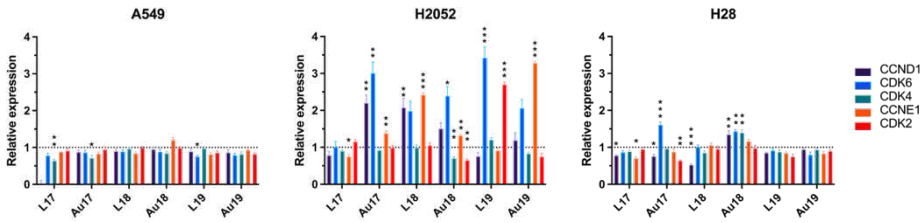

*Figure 52. Cyclins and cyclin-dependent kinase (CDK): CCND1, CDK6, CDK4, CCNE1, and CDK2; expression in A549, H2052, and H28 cells after treatment at the IC_{50} concentration. Gene expression levels were measured by real-time PCR using the RPL13 gene as a housekeeping gene. Significant differences from untreated cells (unless otherwise indicated): * = p < 0.05; ** = p < 0.01; *** = p < 0.001, ns = not significant.*

Oxidative stress evaluation

Oxidative stress, which refers to an imbalance between the production of reactive oxygen species (ROS) and the body's ability to eliminate them, was assessed using the TBARS (Thiobarbituric Acid Reactive Substances) assay. This assay is commonly employed to measure the levels of lipid peroxidation, a process where ROS attack lipids in cell membranes, leading to the formation of lipid peroxides. We used the TBARS assay to evaluate the extent of lipid peroxidation in the cell membranes of A549, H2052, and H28 cells after treatment with ligands or

complexes (Figure 53). In A549 cells, no significant lipid peroxidation of the cell membranes was observed following treatment with the compounds. This suggests that A549 cells possess a robust endogenous antioxidant defense system[147], as evidenced by the unaltered expression of the antioxidant genes superoxide dismutase -1 and -2 (SOD-1 and SOD-2), and heme oxygenase-1 HO-1. These genes encode for important antioxidant enzymes that neutralize ROS and protect cells from oxidative damage. In contrast, the other cell lines, H2052 and H28, exhibited a notable increase in TBARS levels after treatment with the complexes, indicating an elevation in lipid peroxidation and oxidative stress. This increase was further supported by the upregulation of HO-1, SOD-1, and SOD-2 gene expressions in these cells. The upregulation of these genes suggests that H2052 and H28 cells respond to the increased oxidative stress by activating their antioxidant defense mechanisms.

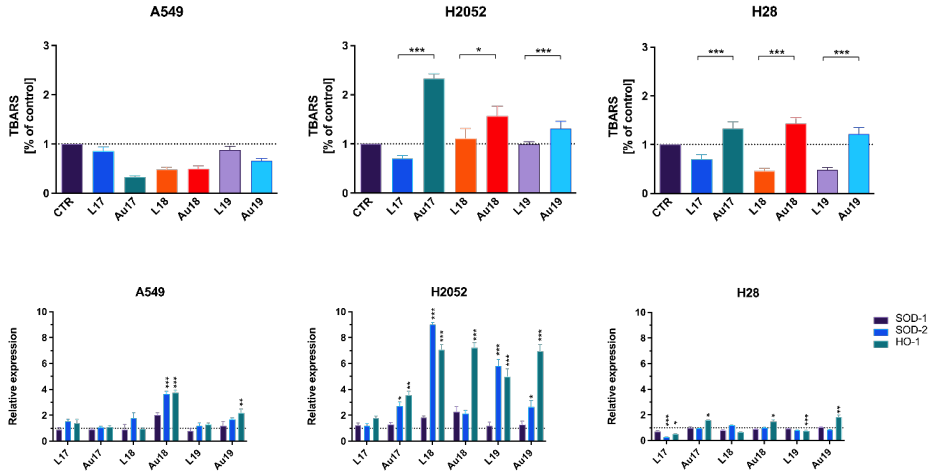

*Figure 53. Oxidative stress as TBARS levels (above) and protein expression of SOD-1, SOD-2, HO-1 expression (below) in A549, H2052, and H28 cells after treatment at the IC50 concentration. Gene expression levels were measured by real-time PCR using the RPL13 gene as a housekeeping gene. Significant differences from untreated cells (unless otherwise indicated): * = p < 0.05; ** = p < 0.01; *** = p < 0.001, ns = not significant.*

Interleukin-6 as a biomarker of inflammation

The quantification of Interleukin-6 (IL-6) provides a valuable insight into the inflammatory response of the cells to the treatments. The complexes effectively inhibited the production of IL-6 in the mesothelioma cell lines H2052 and H28, which indicates a suppression of the chronic inflammatory state in these cells (Figure 54). Conversely, in A549 cells, the production of IL-6 was comparable to that of the control (untreated cells). This finding suggests that the complexes' impact on IL-6 production may be cell-type-specific, and the response to treatment in A549 cells might differ from that in the mesothelioma cell lines.

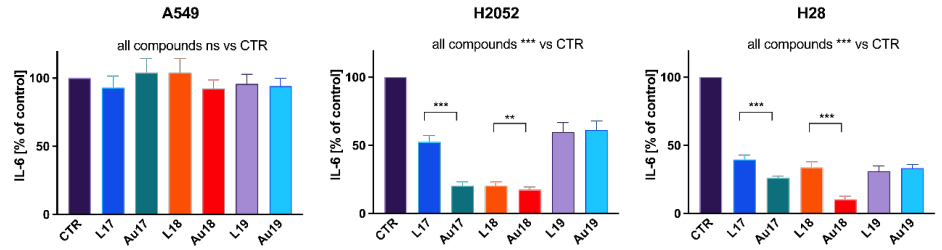

*Figure 54. Inflammatory response as expression of IL-6 in A549, H2052, and H28 cells after treatment at the IC_{50} concentration. Gene expression levels were measured by real-time PCR using the RPL13 gene as a housekeeping gene. Significant differences from untreated cells (unless otherwise indicated): * = p < 0.05; ** = p < 0.01; *** = p < 0.001, ns = not significant.*

In vivo toxicity evaluation using *Galleria mellonella* larvae

To gain initial insights into the toxicity profile of these compounds, we administered the gold complexes to *Galleria mellonella* larvae at varying concentrations, depending on their solubility (Figure 55). Notably, both **Au17** and **Au18** exhibited an absence of toxicity even at the highest concentration tested, which was 30 μM (equivalent to 12.8 mg/kg) for **Au17** and 60 μM (equivalent to 29.4 mg/kg) for **Au18**. Similarly, **Au19** demonstrated no significant toxicity when compared to untreated and control groups. However, it did exhibit a slight increase in population risk, approximately 30%, at the highest concentration tested, which was 60 μM (equivalent to 30.2 mg/kg).

These findings, combined with the absence of hemolytic behavior, position these compounds as promising candidates for further in vivo studies, potentially paving the way for future clinical applications.

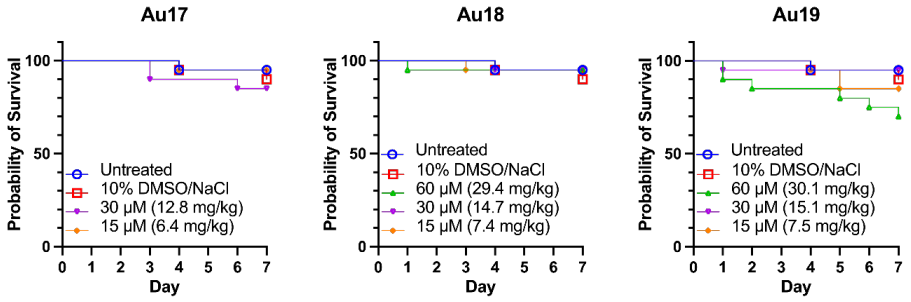

*Figure 55. Survival of G. mellonella (n = 20) recorded over a 7-Day period post-injection of **Au17**, **Au18**, **Au19**.*

Conclusion

In this chapter, I synthesized stable gold(III) complexes derived from thiosemicarbazone ligands, and their structures were confirmed through X-ray crystallography. Studies on the interaction with biomolecules suggest that direct cleavage of DNA is not among the primary actions of the compounds. However, the observed intercalation might contribute to their cytotoxicity. In fact, the compounds exhibited potent inhibition of proliferation in three different lung cancer cell lines, namely A549, H2052, and H28. Cell cycle analysis revealed cell cycle arrest and the induction of apoptosis as the underlying mechanisms of cell death. Furthermore, the cytotoxic effects of the complexes included morphological changes and increased oxidative stress. The suppression of IL-6 production in mesothelioma cells suggests a potential anti-inflammatory property of the complexes, which may play a role in attenuating the inflammatory response associated with cancer progression. These findings, coupled with the absence of hemolysis and in vivo toxicity, establish these compounds as promising candidates for the development of novel and effective anticancer therapeutics. Further investigations are warranted to validate the complexes' anticancer efficacy in *in vivo* models.

Materials

All common laboratory chemicals were purchased from commercial sources and used without further purification: thiosemicarbazide, 99% (Sigma Aldrich); 4,4-dimethyl-3-thiosemicarbazide, 98 % (TCI); 4-phenyl-3-thiosemicarbazide, 99% (Sigma Aldrich), hydrogen tetrachloridoaurate hydrate, 99.99% (Acros Organics). NMR spectra were recorded on a Bruker Anova spectrometer at 400 MHz, with chemical shift reported in δ units (ppm). NMR spectra were referenced relative to residual NMR solvent peaks. Solvent used in the spectra acquisitions is DMSO-d_6. The FT-IR spectra were recorded on Perkin Elmer's Spectrum Two in the 4000-400 cm^{-1} range, equipped with the UATR accessory. Elemental analyses were performed using Flashsmart CHNS Elemental Analyzer (Thermo Fisher Scientific). ESI-MS were recorded on a spectrometer with Single Quadrupole Detector (Sesto San Giovanni, MI, Italy). HR-MS were recorded on a Thermo Scientific Orbitrap LTQ-XL (Rodano, MI, Italy). UV/Vis spectra were collected using a Thermo Fisher Scientific Evolution 260 Bio Spectrophotometer, using quartz cuvettes of 1 cm path length. Circular dichroism spectra were collected with a Chirascan V100 spectrophotometer.

Preparation of the ligands.

Variously N^4-substituted thiosemicarbazides were dissolved in 10 mL of water and maintained under stirring at 25 °C until complete dissolution. An equimolar amount of salicylaldehyde was then added to the solution together with 1 mL of glacial acetic acid. A precipitate started to form shortly after combining. The reaction was stirred at room temperature for 8 hours. The solid was filtered on filter paper, washed with H_2O, and dried under vacuum.

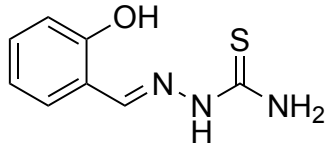

L17: Thiosemicarbazide (150 mg, 1.65 mmol), salicylaldehyde (0.173 mL, 1.65 mmol). White powder. Yield: 91 %.^{1}H NMR (400 MHz, DMSO-d_6): 11.37 ppm (s, 1H), 9.83 ppm (s, 1H), 8.37 ppm (s, 1H), 8.10 ppm (s, 1H), 7.90 ppm (d, 2H). 7,21 ppm (td, 1H), 6.87 ppm (d, 1H), 6.81 ppm (t, 1H). ESI-MS (+, m/z, MeOH): 218 $[M+Na]^+$, 196 $[M+H]^+$, IR (ATR, cm^{-1}): 3439 cm^{-1} , 3307 cm^{-1} and 3165 cm^{-1} ν N-H, 3129 cm^{-1} ν O-H, 1599 cm^{-1} ν C=N, 1059 cm^{-1} and 772 cm^{-1} ν C=S.

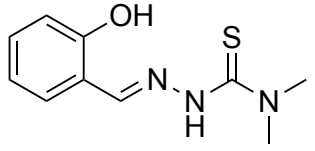

L18: 4,4-dimethyl-3-thiosemicarbazide (150 mg, 1.25 mmol), salicylaldehyde (0.132 mL, 1.25 mmol). White powder. Yield 82%. ^{1}H NMR (400 MHz, DMSO-d_6): 11.72 ppm (s, 1H), 11,23 ppm (s, 1H), 8.50 ppm (s, 1H), 7.38 ppm (dd, 1H), 7,27 ppm (m, 1H), 6.90 ppm (m, 2H), 3,37 ppm (s, 6H). ESI-MS (+, m/z, MeOH):

246 $[M+Na]^+$ IR (ATR, cm^{-1}): 3309 cm^{-1} v N-H, 3276 cm^{-1} v O-H, 1617 cm^{-1} v C=N, 1146 cm^{-1} and 785 cm^{-1} v C=S.

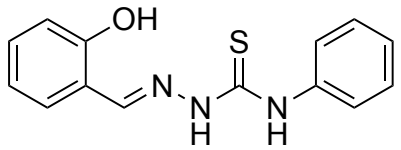

L19: 4,4-dimethyl-3-thiosemicarbazide (150 mg, 1.25 mmol), salicylaldehyde (0.132 mL, 1.25 mmol). White powder. Yield 82%. ^1H NMR (400 MHz, DMSO-d_6): 11.72 ppm (s, 1H), 11,23 ppm (s, 1H), 8.50 ppm (s, 1H), 7.38 ppm (dd, 1H), 7,27 ppm (m, 1H), 6.90 ppm (m, 2H), 3,37 ppm (s, 6H). ESI-MS (+, m/z, MeOH): 246 $[M+Na]^+$ IR (ATR, cm^{-1}): 3309 cm^{-1} v N-H, 3276 cm^{-1} v O-H, 1617 cm^{-1} v C=N, 1146 cm^{-1} and 785 cm^{-1} v C=S.

Preparation of the complexes

The complexes were synthesised by dissolving the ligand in an appropriate solvent at room temperature. $HAuCl_4$ was dissolved in an appropriate solvent, and added dropwise to the ligand solution. The reactions were often fast, with a sudden change in colour (typically from colourless to dark green-brown). A precipitate started to form shortly after combining. The reactions were left under stirring for one hour, then filtered using paper filters, washed with diethyl ether, and dried under vacuum.

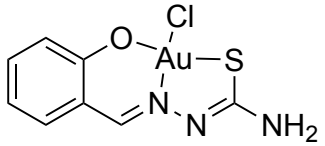

Au17: **L17** (50 mg, 0.254 mmol); $HAuCl_4 \cdot 3H_2O$ (100 mg, 0.254 mmol). $HAuCl_4$ was neutralized with 200 µL of NaOH 5M. Solvent: MeOH (5 mL). Brown powder. Yield 18%. MW 425.64 g/mol. ^1H NMR (400 MHz, DMSO-d_6): 8.86 ppm (s,1H), 7.75 ppm (m, 3H), 7.57 ppm (m, 1H), 7.03 ppm (d, 1H), 6.89 ppm (t, 1H). ^{13}C NMR 400 MHz, DMSO): 167.5 ppm, 157.9 ppm, 146.4 ppm, 137.1 ppm, 135.4 ppm, 118.4 ppm (two carbons from ^1H-^{13}C HSQC), 116.8 ppm. IR (ATR, cm^{-1}): 3459 cm^{-1} v , 3286 cm^{-1} v, 3175 cm^{-1} v, 1617 cm^{-1} v C=N, 1040 and 748 cm^{-1} v C=S. Elemental Analysis: $C_8H_7AuClN_3OS$ Calc: C 22.57%, H 1.66%, N 9.87%, S 7.53%. Exp: C 22.32%, H 1.99%, N 9.34%, S 7.34%. ESI-MS (+, m/z, MeOH): 390.0 $[C_8H_7AuClN_3OS]^+$. XRD: CCDC No 2193027.

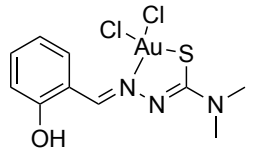

Au18: **L18** (20 mg, 0.09 mmol); $HAuCl_4 \cdot 3H_2O$ (35 mg, 0.09 mmol). Solvent: THF (5 mL). Brown powder. Yield 52%. MW 454.70 g/mol. ^1H NMR (400 MHz, DMSO-d_6): 10.95 ppm (s, 1H), 9.13 ppm (s, 1H), 8.45 ppm (d, 1H), 7.47 ppm (t, 1H), 7.01

ppm (m, 2H), 3.22 ppm (s, 6H). ^{13}C NMR (400 MHz, DMSO): 170.9 ppm, 161.3 ppm, 153.8 ppm, 147.6 ppm, 136.3 ppm, 132.9 ppm, 120.0 ppm, 116.7 ppm, 40.7 ppm (signal close to solvent peak, see ^{1}H-^{13}C HSQC for a better separation of the signals). IR (ATR, cm^{-1}): 3431 cm^{-1} ν O-H, 1539 cm^{-1} ν C=N, 1152 cm^{-1} and 841 cm^{-1} ν C=S. Elemental Analysis: $C_{10}H_{12}AuCl_2N_3OS$ Calc: C 24.50%, H 2.47%, N 8.57%, S 6.54%. Exp: C 8.42%, H 2.28%, N 8.42%, S 6.44%. ESI-MS (+, m/z, MeOH): 418.0 $[C_{10}H_{12}AuCl_2N_3OS]^+$, 450.0 $[C_{10}H_{12}AuCl_2N_3OS\text{-}MeOH]^+$. XRD: CCDC No 2193028.

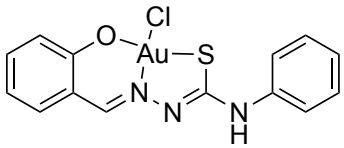

Au19: **L19** (63 mg, 0.232 mmol); $HAuCl_4 \cdot 3H_2O$ (91 mg, 0.232 mmol). Solvent: MeOH (5 mL). Brown powder. Yield 10%. MW 501.74 g/mol. ^{1}H NMR (400 MHz, DMSO-d_6):10.31 ppm (s, 1H, Ha), 9.27 ppm (s, 1H, Hb), 7.84 ppm (d, 1H, Hc), 7.64 ppm (m, 3H, Hd, He and Hf), 7.37 ppm (m, 2H, Hg and Hf), 7.09 ppm (m, 2H, Hi and Hl), 6.94 ppm (t, 1H, Hl).^{13}C NMR (400 MHz, DMSO): 161.93 ppm, 158.44 ppm, 149.44 ppm, 140.75 ppm, 137.81 ppm, 135.69 ppm, 129.38 ppm, 123.71 ppm, 119.77 ppm, 118.67 ppm, 118.62 ppm, 116.73 ppm. Elemental Analysis: $C_{14}H_{11}AuClN_3OS$ Calc: C 33.51%, H 2.21%, N 8.38%, S 6.39%. Exp: C 32.42%, H 2.23%, N 7.74%, S 6.90%. IR (ATR, cm^{-1}): 3338 cm^{-1} ν N-H, 1593 cm^{-1} ν C=N, 1188 cm^{-1} and 849 cm^{-1} ν C=S. ESI-MS (+, m/z, ACN): 523.6 $[C_{14}H_{11}AuClN_3OS\text{-}Na]^+$, 506.9 $[C_{14}H_{11}AuClN_3OS\text{-}ACN]^+$. XRD: CCDC No 2193029.

Crystallographic data collection and crystal structure determination

Single crystal X-ray diffraction analysis were carried out with a Bruker D8Venture diffractometer equipped with a kappa goniometer and an Oxford cryosystem. Microfocused MoKα radiation (λ = 0.71073) was used as the X-ray source and Lorentz polarization and absorption correction were applied through the SADABS[49] procedure. The phase problem was solved by direct methods and the structures were refined by full-matrix least-squares on all F2 using SHELXL[50,51], as implemented in the OLEX2 suite of programs[52]. Analytical expressions of neutral atom scattering factors were taken from the International Tables for X-Ray Crystallography[52]. The structure drawings were obtained using ORTEPIII[53] and Mercury[54]. CCDC 2193027-2193029 contain the supplementary crystallographic data.

Cyclic voltammetry

Cyclic voltammograms were recorded with a μStat 400 Bipotentiostat/Galvanostat (Metrohm DropSens) by working in a 96 mM KNO_3/4 mM HNO_3 aqueous solution with 10%DMSO. The pH was adjusted to 7.4 with 0.1 M KOH and 0.1 M HNO_3. Concentrations of **Au17**, **Au18**, **Au19** and $HAuCl_4$ were 0.2 mM prepared from 10 mM stock solutions in DMSO. A Screen-Printed Carbon electrode (Metrohm DropSens) was used where the electrochemical cell consists of carbon working and auxiliary electrodes and silver as the reference

electrode on a ceramic substrate. The scan rate was 50 mV/s. The Metrohm DropView 8400 software was used for measurements, graph plots and data analysis.

DFT calculations

All calculations were carried out with Gaussian 16[148] and GaussView 6.1.1[149] programs within the density functional theory (DFT) framework. The structures of the gold(III) complexes were optimized starting from the coordinates obtained from XRD. Hybrid functional (B3LYP) correlation functional[150] was employed with a SDD basis set that considers the effective core potential, suitable for heavy atoms like gold (ECP). The Electrostatic potential (ESP) surface was calculated from GaussView. The colour scale was set equal for all the complexes for a better comparison.

DNA melting curves

DNA melting curves of calf thymus (CT) DNA (100 µM) in PBS buffer (10 mM, pH 7.4) in the presence of **Au17**, **Au18**, **Au19** and $HAuCl_4$ were measured at 260 nm using a heating rate of 0.5 °C/min. The experiment was performed in triplicate. Normalization of melting curves was utilized for better visualization. T_m was evaluated as the point where 50% of the double-stranded DNA is split into two single strands. ΔT_m is referred to the control DNA which was treated with DMSO only.

Ethidium bromide displacement assay

A mixture of CT-DNA (60 µM) and ethidium bromide (EtBr) (2.6 µM) in PBS buffer (10 mM, pH 7.4) was prepared in a 2 mL fluorescence cuvette. The solution was treated with increasing amounts of **Au17**, **Au18**, **Au19** and $HAuCl_4$. The fluorescence spectra were collected after each addition, mixing and a waiting time of 2 min in a range of 530–650 nm using an excitation wavelength of 518 nm. The magnitude of decrease of the fluorescence emission is usually described by the Stern-Volmer equation $I_0/I = 1 + K_{SV}[Q]$.[143] The Stern–Volmer plot shown in Figure 2b exhibits an upward curvature, indicating that both static and dynamic quenching processes contributed to the overall quenching of the system.[151] The non-linearity of the Stern–Volmer plot, already detected with other metals,[152] was plotted with a modified equation: $I_0/I = 1 + a[Q] + b[Q]^2$.[153] [Q] is the concentration of the competitive binder, where the fluorescence emission of EtBr is quenched by 50%, which was further used to evaluate K_{app} from: $K_{EtBr}[EtBr]=K_{app}[Q]$. ($K_{EtBr} = 10^7\ M^{-1}$).[154]

Circular dichroism spectroscopy

Circular dichroism (CD) spectra of CT-DNA (100 µM) in HEPES buffer (50 mM, pH 7.4) in the presence of 10% DMSO were recorded in a range of 235 to 320 nm with a scan rate of 100 nm/min and a data point interval of 0.1 nm. **Au17**, **Au18**, **Au19** and $HAuCl_4$ (stock solution 2.5 mM, 50% DMSO) were added stepwise (10 µL) to investigate their modes of interaction with DNA. The initial volume of all samples was 1 mL, containing already 10% DMSO.

DNA cleavage studies
Plasmid DNA pBR322 was purchased from Carl Roth. All DNA cleavage experiments were performed at least in triplicate to ensure reproducibility. The standard deviations are represented as the error bars.
The complexes and $HAuCl_4$ were incubated with plasmid DNA pBR322 (0.025 µg/µL) buffered in HEPES (50 mM, pH 7.4) with 10% DMSO in the presence of ascorbate (1 mM ascorbic acid) as reducing agent for 2 h at 37 °C. Gel electrophoresis was carried out for 2 h at 40 V using a 1% agarose gel in 0.5X TBE buffer containing ethidium bromide (EtBr) (0.2 µg/mL). The bands of supercoiled (form I), open-circular/nicked (form II), and linear (form III) DNA were visualized by fluorescence imaging of intercalating EtBr on a Bio-Rad GelDoc EZ Imager. Data analysis was performed with Bio-Rad's Image Lab Software (Version 6.1). Due to the decreased affinity of EtBr to supercoiled DNA a correction factor of 1.22 was used.[143,155]

Bovine Serum Albumin binding studies
A protein-binding study was performed by tryptophan fluorescence quenching experiments using Bovine Serum Albumin (BSA, PBS 10 mM, pH 7.4, 2.5 µM). The excitation wavelength of BSA at 280 nm and the quenching of the emission intensity of tryptophan residues of BSA at 345 nm were monitored using **Au17**, **Au18**, **Au19** and $HAuCl_4$ (stock solution 10 mM in DMSO) as quenchers with increasing concentrations (0-7 µM). The linear Stern–Volmer equations (cf. Ethidium bromide displacement assay) were used to quantify the interaction of the quencher with serum albumins.[156 157]

Cell culture and treatments
A549 (human lung adenocarcinoma cells), H2052 (human mesothelioma epithelial cells), and H28 (human pleural sarcomatoid mesothelioma cells) were obtained from the American Type Culture Collection (Manassas, VA) and cultured in RPMI 1640 supplemented with 10% fetal bovine serum and antibiotics (100 U/ml penicillin and 100 µg/ml streptomycin, respectively). The cells were routinely maintained at 37 °C in a humidified atmosphere of 5% CO_2.

Cell viability assay
Cells were used in log-phase growth after a minimum of 24 h of adherence to culture flasks. Cells for each treatment were incubated for 24 h at different drug concentrations (0.1-100µM). An untreated sample was used as a control. The cells were seeded into 96-well plates and incubated for 24 h, then treated with ligands and gold complexes for another 24 h. All treatments were performed in triplicate. At the fixed time-point, the MTT (3-(4,5-dimethylthiazole)-2, 5-diphenyltetrazoliumbromide) reagent was added into each well and incubated at 37 °C for 3 h. The absorbance was detected with a Varioskan™ LUX multimode microplate reader (Thermo Fisher Scientific™, Helsinki, Finland) at a wavelength of 560 nm (wavelength reference: 655 nm). MTT assay results were confirmed by counting viable cells (impermeable to Trypan Blue) in a haemocytometer.

Haemolysis assay
The compounds were tested on human red blood cells (hRBCs) using a haemolysis assay as previously reported.[117] Blood was obtained from

Interregionale Blutspende SRK AG in Bern, Switzerland. 1.5 mL of whole blood was centrifuged at 3000 rpm for 15 minutes at 4 °C, and the plasma was discarded. The hRBC pellet was washed three times with PBS (pH 7.4) and then resuspended to a final volume of 10 mL in PBS. For the determination of HC_{50} of gold compounds, the samples were two folds diluted starting from 200 µM. Samples stock solution was 20 mM in DMSO. Each plate included a blank medium control (PBS) and a haemolytic activity control (0.1% Triton TM X-100). hRBC suspension was incubated with the samples in PBS in a V-shaped 96-well plate for 4 hours at 20 °C. After the incubation, 100 µL of supernatant was carefully pipetted to a flat bottom, clear 96-wells plate. Haemolysis was measured by analysing the absorbance of free haemoglobin in the supernatants at 540 nm using a plate reader (Tecan instrument Infinite M1000).

Cell morphology

A549, H2052, and H28 cells were cultured on slides for 24 h and exposed to compounds at IC_{50} concentrations for another 24 h. Slides with adhered untreated cells were used as controls. The cells were washed thoroughly three times in PBS, fixed with 4% (w/v) formaldehyde for 15 min, and permeabilized using 0.1% Triton X-100 for 5 min at room temperature. Nonspecific antigenic sites were blocked with 10% bovine serum albumin (Sigma-Aldrich, Saint Louis, MO) and 3% Normal Goat Serum (Sigma-Aldrich, Saint Louis, MO) for 90 min. Subsequently, slides were incubated with TRITC-Conjugated Phalloidin primary antibody (Cat. 90228, Merk Millipore, Burlington MA USA) at a dilution of 1:100 for 60 min. Then, cells were washed twice with PBS and stained with DAPI (Cat. 90229, Merck Millipore, Burlington MA USA) for nuclei detection. The immunofluorescence samples were observed using a Confocal Laser Scanning Microscope (Stellaris 5, Leica Microsystems, Germany).

Cell cycle analysis

The quantification of DNA content by flow cytometry is the most used method for the identification of the cell distribution during the phases of the cell cycle. Nuclear DNA content was labeled with propidium iodide (PI). Briefly, about 1×10^6 cells were harvested, resuspended in PBS (Ca^{2+} and Mg^{2+} free and supplemented with EDTA 0.5 mM), and fixed adding 96% cold ethanol. After overnight incubation at 4 °C, samples were washed and incubated with 1 mL of PBS containing 20 µg/mL PI and 12.5 µL RNase (1 mg/mL in water), then stained cells were sorted by a FC500™ flow cytometer (Instrumentation Laboratory, Bedford, MA, USA). At least 20,000 events were counted. The percentages of cells occupying the different phases of the cell cycle were calculated by FlowJo Software (Tree Star Inc, Ashland, OR, U.S.A.).

Apoptosis

Caspase-3 activity was measured by Caspase-Glo® 3/7 Assay System (Promega Madison, WI, USA) adding a proluminescent DEVD-aminoluciferin substrate. Luminescence was measured by means of a Varioskan™ LUX (Thermo Fisher Scientific™, Helsinki, Finland) microplate reader.

Thiobarbituric acid reactive substance (TBARS) detection
Cellular TBARS were measured according to a previously described method adapted for cultured cells[158]. Briefly, 10^6 cells were seeded in 25 cm^2 flasks. Cells in log-phase growth were treated with the tested compounds for 24 h, then collected and centrifuged. After three cycles of freezing and thawing (−80 °C to +37 °C), control and treated cells were centrifuged at 3000g for 5 min, and lipid peroxidation products were detected in the supernatants by the TBARS method, based on the condensation of malondialdehyde (MDA), derived from polyunsaturated fatty acids, with two equivalents of thiobarbituric acid to give a fluorescent red derivative. The fluorescence was measured using a Cary Eclipse fluorescence spectrophotometer (Varian, Inc., Palo Alto, CA, USA) (excitation 515 nm, emission 545 nm). TBARS concentrations were normalized to total protein concentration in each sample.

Protein Determination
Protein concentrations were measured using a bicinchoninic acid (BCA Protein Assay (Thermo Fisher Scientific, Rockford, IL, USA). The protein assay was carried out in accordance with the manufacturer's microwell plate protocol: bovine serum albumin dilutions were included as standard curves. Absorbances were read at 550 nm in a Multiskan Ascent microwell plate reader (Thermo Labsystems, Helsinki, Finland).

RNA Extraction and Gene Expressions Quantification
RNA isolation from cultured cells involved the use of TRIzol reagent (Thermo Fisher Scientific), following the manufacturer's instructions. Subsequently, DNase I (DNA-free kit; Thermo Fisher Scientific, Waltham, MA) was used to digest the RNA samples and eliminate any genomic DNA contamination. The RNA concentration was determined using a NanoDrop spectrophotometer (Thermo Scientific). For gene expression analysis, cDNA was synthesized with a commercial kit and subjected to quantitative real-time PCR amplification using specific primers that included exon-exon junctions, designed specifically for SOD-1, SOD-2, HO-1, CDK6, CDK2, CDK4, CCND1, and CCNE1 (Table S1). The expression levels of each mRNA were normalized to the RPL13 housekeeping gene expression. To determine changes in mRNA expression relative to untreated controls, the equation $2^{-\Delta\Delta Ct}$ was employed[159].

Interleukin-6 quantification
After incubating A549, H2052, and H28 cell lines with their respective compounds at IC50 concentration for 24 h, the culture supernatants were collected and centrifuged at 16,000 g for 5 min to remove cell debris and particles. The concentrations of interleukin-6 (IL-6) were measured using a commercially available ELISA Kit (Human IL-6 ELISA Kit Invitrogen, Thermo Fisher Scientific, Waltham, MA, USA) following the manufacturer's instructions. The results were normalized to the number of cells, and IL-6 concentrations of the treated cells were compared to the concentrations of untreated cells.

In vivo tox (moth).
Larvae (400-500 mg) were sterilized by gently rubbing them with a paper towel soaked in an ethanoic solution and then individually injected with 10 µL of solution into one proleg using a 50 µL syringe (Hamilton Ltd). The compound was dissolved in DMSO (27 mM) and diluted to final concentrations of 60 µM, 30 µM and 15 µM with milliQ water. Five larvae were used for each group. Untreated larvae and larvae injected with 10% DMSO / milliQ water were included as negative controls. Following injection, the larvae were incubated at 37 °C and monitored every 24h for 7 days. Larval performance was assessed according to the *G. mellonella* Health Index Scoring System.[63] The experiments were repeated four separate times.

Statistical analyses
All experiments were performed in triplicate. The data are expressed as the mean±standard deviation (SD). The comparisons were analyzed using one-way analysis of variance (ANOVA) with Dunnett's or Turkey's post hoc tests employing SPSS software. $P<0.05$ values were considered statistically significant

6. Targeting *Toxoplasma gondii* infections with gold(III) complexes

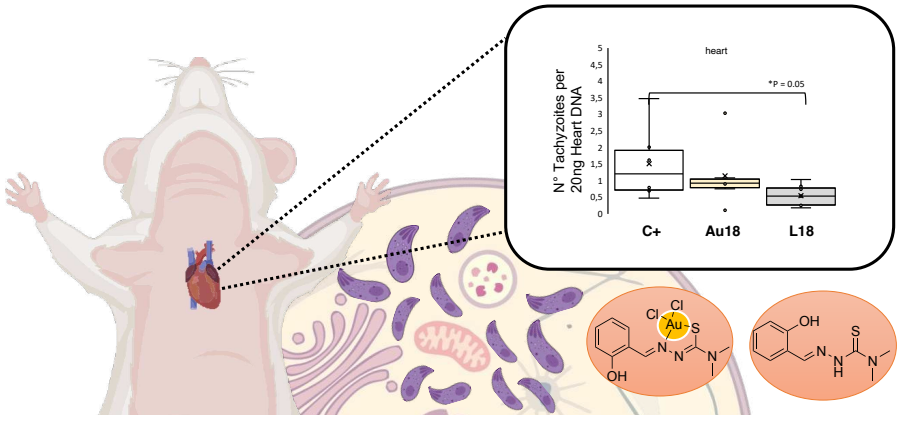

This chapter's research involved a collaborative effort with Manuela Semeraro from the University of Parma's Department of Veterinary Medicine (Parasitology Operative Unit). Some aspects of the research were conducted at the University of Bern, and the project was co-supervised by Dr Ghalia Boubaker and Professors Franco Bisceglie, Laura Helen Kramer, Alice Vismarra, and Andrew Hemphill.

Abstract

Toxoplasma gondii, an obligate intracellular protozoan parasite, is the causative agent of toxoplasmosis, a pervasive infectious disease affecting both humans and animals. This chapter delves into the exploration of metal-based drugs, specifically gold complexes derived from thiosemicarbazone ligands, as potential antiparasitic agents against *T. gondii.* The in vitro screening of a diverse range of compounds reveals their significant efficacy against *T. gondii*, with two standout compounds demonstrating remarkable selectivity.

The comprehensive *in vitro* characterization encompasses an examination of the compounds' interactions with the immune system and their mode of action - whether they exhibit parasitostatic or parasiticidal properties. These investigations unveil their parasitostatic nature, effectively inhibiting parasite growth without achieving complete eradication.

Furthermore, the evaluation extends to *in vivo* models, employing zebrafish and murine models, to assess potential toxicity and efficacy. While the compounds exhibited adverse effects on zebrafish embryonic development, leading to the exclusion of the murine model of congenital toxoplasmosis, they demonstrated safety and effectiveness in the murine model by reducing the parasite load in the heart.

This chapter introduces the promising potential of gold-based compounds as antiparasitic agents and underscores the imperative need for further research to refine these compounds, enhancing their safety and efficacy. This endeavor offers a ray of hope for pioneering therapeutic solutions against this insidious parasite.

Toxoplasma gondii and toxoplasmosis: insights into its life cycle and impact on human health

Toxoplasma gondii, classified as an obligate intracellular protozoan parasite, is responsible for the insidious infectious disease toxoplasmosis. This adaptable parasite has an indirect life cycle, characterized by a definitive host and one or more intermediate hosts. Intermediate hosts of *T. gondii* include warm-blooded mammals, including humans, reptiles, and birds, whereas felids (typically cats) serve as its definitive hosts.[160] Within intermediate hosts, *Toxoplasma gondii* reproduces asexually, whereas it can complete its life cycle and reproduce sexually within definitive hosts, involving the production of male microgametes and female macrogametes in the feline intestine, leading to the formation of oocysts. Cats shed a significant number of unsporulated oocysts in their feces for 1-3 weeks after initial contact with the parasite. These oocysts subsequently sporulate, becoming mature and infectious, within 1-5 days in the environment.[161]

In intermediate hosts, *Toxoplasma gondii* can exist in two main infective stages: tachyzoites (acute phase) and as tissue cysts containing bradyzoites (chronic phase). In immunocompetent individuals, tachyzoites, under immune system pressure, convert into slowly dividing bradyzoites, forming tissue cysts primarily in various tissues, with a predilection for the central nervous system and cardiac tissues. These cysts can remain latent within the host for extended periods.[161]

Conversely, in individuals with weakened or compromised immune systems due to comorbidities, the parasite may reactivate, resulting in cyst rupture and the release of bradyzoites that convert back to tachyzoites. These actively invade cells, leading to tissue necrosis and acute disease, particularly affecting the eyes and central nervous system.[162]

In humans, infection with *T. gondii* primarily occurs through the ingestion of undercooked or raw meat containing tissue cysts or via the consumption of water or vegetables contaminated with soil containing sporulated oocysts. Additionally, infection can occur through blood transfusion, organ transplantation, and vertical transmission from mother to fetus.[161]

In humans, *T. gondii* infection can lead to toxoplasmosis, which manifests with flu-like symptoms in healthy individuals but can cause significant damage and lesions in immunocompromised individuals or if contracted for the first time during pregnancy. In immunocompromised individuals, the disease can worsen and result in severe consequences, sometimes leading to death. The most affected organs are the brain and eyes, where active parasite replication induces tissue necrosis.[162]

In pregnant women who become infected during gestation, the parasite can cause various effects depending on the timing of exposure. If acquired in the first trimester, it can lead to spontaneous abortion, stillbirth, or severe fetal abnormalities. In the second trimester, the infection can result in hydrocephalus and late-onset chorioretinitis, an inflammation affecting the back of the eye, even years after initial infection. In the later stages of pregnancy, symptoms may be absent or less severe, including neonatal jaundice, a yellowing of the skin and sclera caused by excess bilirubin in the blood.[163]

The treatment of toxoplasmosis necessitates effective solutions for various forms of the parasite, both tachyzoites responsible for tissue necrosis and host cell destruction, and especially the bradyzoite form, which, being encysted, is the most challenging to reach. Currently, conventional therapy includes antibiotics and molecules such as spiramycin, pyrimethamine, sulfadiazine, and clindamycin but most of them cause side effects in the host. Furthemore, there is currently no effective treatment against bradyzoites that can penetrate the blood-brain barrier or cyst walls.[164] Consequently, there is an urgent need for new therapeutic solutions against this pathogen.

Gold complexes from thiosemicarbazone ligands against *Toxoplasma*

In recent times, there has been growing interest in the exploration of metal-based drugs as potential candidates for combating *Toxoplasma gondii* infections. Among these, a noteworthy example is the ferrocenylvinyl derivative of decoquinate, which has exhibited promising in vitro activity against the parasite (Figure 56). Specifically, this compound demonstrated a remarkable 84%

reduction in the proliferation activity of *T. gondii* at a concentration of 1 µM.[160] Additionally, ruthenium compounds have emerged as compelling contenders in the realm of antiparasitic agents, exemplified by polinuclear ruthenium(II)-arene (Figure 56).[165,166] Intriguingly, while metal-based compounds like organometallic iron or ruthenium have been explored for their antiparasitic potential, there remains a gap in the assessment of gold compounds against this particular parasite. Building upon the promising safety profile that we previously identified in the preceding chapter for compounds **Au17**, **Au18** and **Au19**, we embarked on a quest to screen these gold-based compounds for their potential antiparasitic activity.

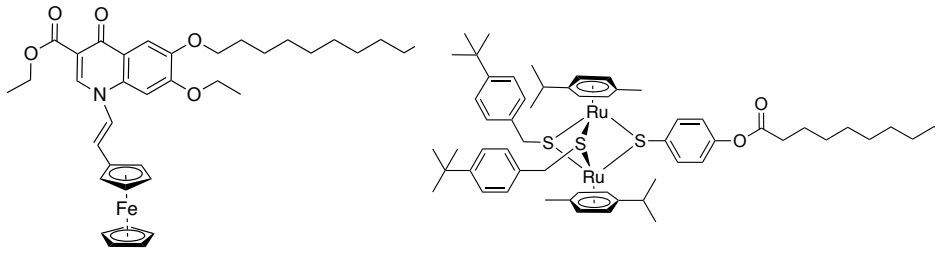

Figure 56. Two illustrative compounds of metal-based compounds demonstrating anti-Toxoplasma activity.

In vitro screening

For the evaluation of the gold compounds, an *in vitro* screening was conducted against *T. gondii* using the transgenic strain *T. gondii* β-gal, which consistently expresses β-galactosidase. These parasites were cultured within human foreskin fibroblast (HFF) monolayers. It was essential to assess both the impact on parasitic activity and potential effects on uninfected HFF host cells, ensuring safety.

The evaluation of the compounds involved the Alamar Blue assay to measure HFF culture viability post-drug treatments. Concurrently, the quantification of *T. gondii* proliferation was performed through the measurement of β-galactosidase activity. This dual approach facilitated a comprehensive assessment of compound efficacy against the parasite, while maintaining an objective perspective on their potential as antiparasitic agents. In the case of **Au17** and

Au19, we observed a similar level of activity against both the parasite and the host cells, with no discernible selectivity. Conversely, for **Au18**, we observed a potent antiparasitic effect at a nanomolar concentration (103 nM), while its cytotoxicity towards healthy cells was significantly higher, surpassing it by two orders of magnitude. This resulted in a remarkable selectivity index exceeding 200 μM (Table 13).

Table 13. Antiproliferative activity display as IC_{50} [μM] value within 24 h

		***T. gondii* β-gal** [μM]	**HFF** [μM]	**SI**
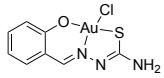	**Au17**	11 ± 1	13 ± 7	1
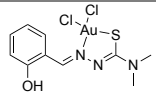	**Au18**	0.103 ± 0.03	24 ± 7	>200
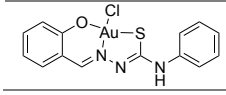	**Au19**	7 ± 2	8 ± 3	1

HFF – human foreskin fibroblast monolayers; S – selectivity index (IC_{50} against HFF/ IC_{50} against T. gondii)

To ascertain whether the activity of **Au18** stemmed from the entire compound or a specific component, we conducted further investigations involving the inhibition of *T. gondii* proliferation. This evaluation extended to the ligand **L18** and its individual constituents: salicylaldehyde, 4,4-dimethylthiosemicarbazide, and $HAuCl_4$. Intriguingly, while the individual components did not exhibit any significant activity, the ligand **L18** demonstrated an IC_{50} value of 30 nM against *T. gondii*. Remarkably, **L18** also displayed negligible toxicity to host cells, with no detectable adverse effects observed up to a concentration of 25 μM. This compelling outcome led us to the decision to advance the studies exclusively with **Au18** and its corresponding ligand **L18**, recognizing their potential as candidate compounds to treat toxoplasmosis.

Mode of action: parasitostatic versus parasiticidal effect

To gain insights into the mode of action of these compounds, we conducted an experiment aimed at determining whether they exhibit parasitostatic properties (slowing the parasite proliferation), parasiticidal properties (killing the parasite),

or have a sustained effect in the long-term treatment of cells infected with the parasite.

In this experimental setup, infected cells were exposed to low concentrations of the compounds, typically at 0.5 μM, over a period of 21 days. At three-day intervals, the compounds were removed from each flask, and subsequent observations by light microscopy were made to assess whether the parasite was capable of resuming its proliferation.

Notably, the findings from this experiment, conducted with both **Au18** and **L18**, revealed that after 5 days from the removal of the drug, the parasite exhibited renewed proliferation. This observation strongly suggests that the compounds act as parasitostatic agents, effectively inhibiting parasite growth, rather than as parasiticidal agents that would lead to the complete eradication of the parasite.

In vitro interaction with the immune system: viability of splenocytes

A very important step, before planning any in vivo experiments, is to assess the safety of the compounds in correlation with the host immune system, to avoid any toxic effect on T and B lymphocytes.

The immune system's resting state is represented by splenocytes, which transform into specialized cells, known as lymphocytes, upon exposure to external immune stimuli. In the experimental protocol, these splenocytes are activated using ConA (a T cell stimulant) and LPS (a B cell stimulant) (Figure 57).[167]

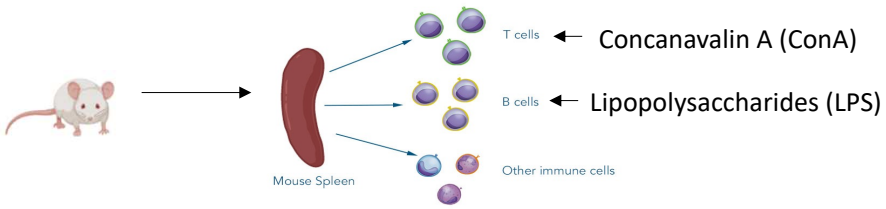

Figure 57. Splenocytes are isolated from mice and subjected to LPS and ConA stimulation for T and B cell activation studies

If the splenocytes exhibit compromised viability and a reduced capacity to transform into their respective lymphocyte forms when exposed to the

compounds, it indicates that these compounds interfere with the host's immune defenses, thereby weakening the host's ability to recover from the infection.

In the in vitro experimental approach, we subjected splenocytes from mouse spleens to treatment with **Au18** and **L18**, followed by the addition of the corresponding stimulant. As illustrated in Figure 58, the presence of these compounds had no discernible impact on the immune system, except for a specific instance involving **Au18** at 2 µM, where a reduced activity against the B cells was observed.

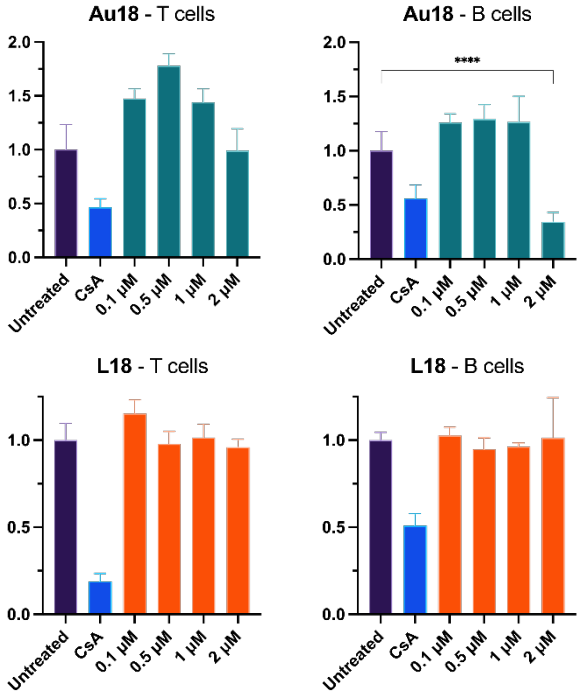

Figure 58. Normalized relative response of ConA- and LPS-stimulated T- and B lymphocytes compared to untreated compounds. CsA is a known inhibitor of the immune system.

In vivo toxicity in zebrafish model

The zebrafish (*Danio rerio*) stands as a widely embraced model organism in scientific research. Its appeal lies in several key attributes: firstly, zebrafish shares a substantial portion of its genetic makeup with humans, providing biological relevance for a range of studies. Secondly, the transparency of zebrafish embryos

is a remarkable feature, permitting real-time observation of critical processes, including organ development and responses to various treatments or compounds. Furthermore, these embryos undergo rapid development, unfolding within a matter of days, making them particularly suitable for time-sensitive experiments.[168] Beyond these advantages, zebrafish are regarded as an ethically responsible choice for early-stage toxicity assessments, owing to their lower complexity and smaller size in comparison to mammals.

In the realm of *T. gondii* infection research, zebrafish emerge as invaluable models. Their value becomes apparent when assessing reproductive toxicity, with a particular emphasis on understanding how compounds affect the intricate stages of embryonic development and obtaining insights into possible teratogenic effects. This involves a close examination of the formation of birth defects. Adverse effects observed in zebrafish embryos serve as early indicators of possible developmental and reproductive toxicity, prompting further investigation.[169] Since *T. gondii* causes disease during pregnancy, the effects of interesting candidate compounds on zebrafish embryo development can be assessed. This approach not only helps us understand the potential teratogenic risks but also provides insights into how these compounds might influence the embryonic development of hosts and the consequences of exposure during pregnancy, mirroring some aspects of toxoplasma infection in humans.[170]

In this context, **Au18** and **L18** were evaluated using this model, but regrettably, they demonstrated adverse effects on embryonic development. At higher concentrations, particularly in the case of the gold compound, eggs were observed to perish within 24 hours (Figure 59). Additionally, the ligand **L18** exhibited a detrimental impact on embryos, resulting in both egg mortality at higher concentrations and malformations at lower concentrations (Figure 60). Due to these concerning findings, the decision has been made to refrain from subjecting the compounds to a murine model of congenital toxoplasmosis.

Day 0	Day 1	Day 2	Day 3
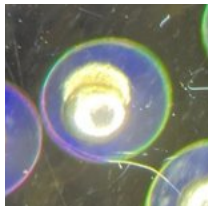 *Fertilized eggs*	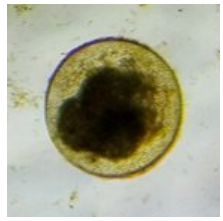 *20 µM: dead eggs* 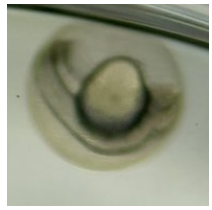 *0.2 µM: viable eggs*	 *0.2 µM: viable eggs*	 *0.2 µM: viable eggs*

*Figure 59. Timeline with pictures depicting the embryonic development of zebrafish at various concentrations of **Au18**.*

Day 0	Day 1	Day 3
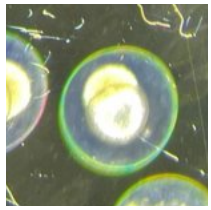 *Fertilized eggs*	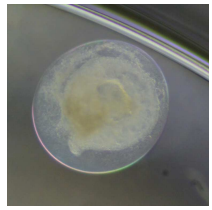 *20 µM: dead eggs*	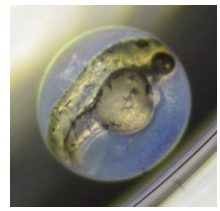 *10 µM: malformation* 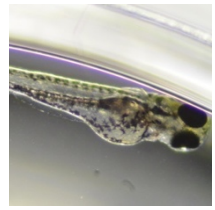 *1 µM: malformation*  *0.2 µM: malformation*

*Figure 60. Timeline with pictures depicting the embryonic development of zebrafish at various concentrations of **L18**.*

In vivo efficacy on infection in murine cerebral toxoplasmosis model

Building upon the promising in vitro efficacy results, **Au18** and **L18** underwent further assessment for their *in vivo* efficacy using a murine model of cerebral toxoplasmosis. A total of 48 mice were divided into infected and non-infected groups, with each group subjected to treatments involving DMSO, **Au18**, or **L18** (Figure 61). To induce infection, the mice were administered 100 TgShSp1 oocysts of *Toxoplasma gondii*. The compounds were orally administered, suspended in corn oil, at a dose of 10 mg/kg/day for a duration of 5 days. Subsequently, the mice were monitored for a period of 30 days. After this timeframe, the mice were euthanized, and DNA from their internal organs was extracted to subject a real-time PCR to quantify the parasite burden.

	untreated	DMSO	**Au18**	**L18**
infected		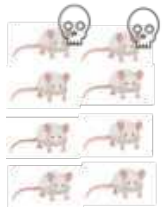	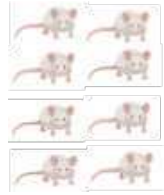	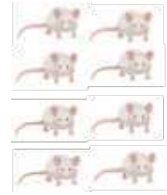
not infected			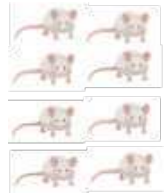	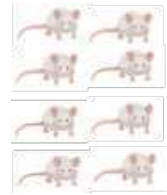

Figure 61. Illustration depicting the various groups of mice utilized in the efficacy trial of Au18 and L18 compounds against T. gondii infection

Throughout the course of the experiment, all mice managed to survive the treatment, except for two mice within the infected and DMSO-treated group. This observation underscores the safety profile of these compounds at the administered dosage and within the designated timeframe for this particular model. Subsequently, DNA from the brains and the hearts of the mice underwent real-time PCR analysis (Figure 62). Unfortunately, there was no significant

difference detected in the parasite load within the brain. This lack of efficacy in reducing the infection in the brain is likely attributed to the compounds' inability to traverse the blood-brain barrier (BBB). However, a notable and statistically significant difference was observed in the parasite load within the heart, suggesting the compounds' effectiveness in treatment (Figure 62).

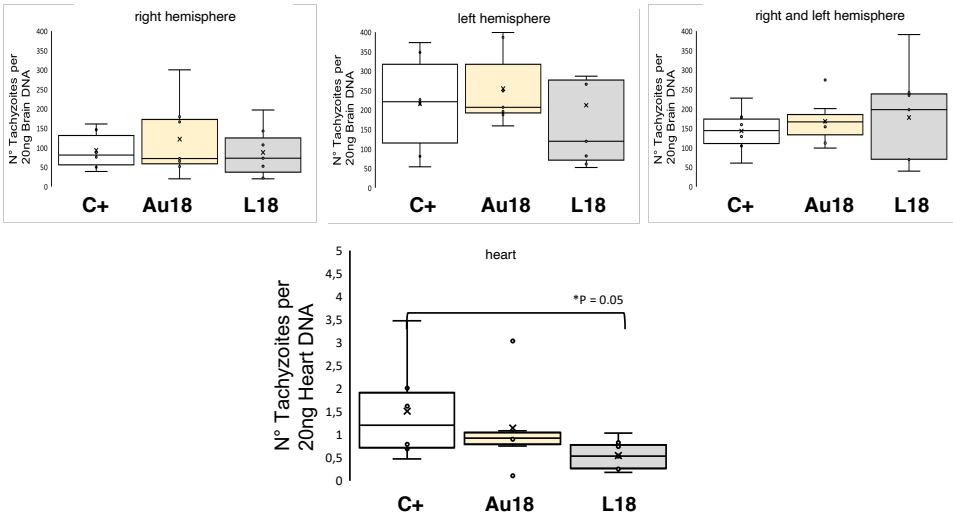

Figure 62. Quantification of the T. gondii load in various mouse organs using real-time PCR, conducted 30 days post-infection.

In vivo interaction with the immune system

To gain insights into potential interactions of the compounds with the immune system and validate the *in vitro* findings, we collected splenocytes from the treatment groups of mice, including both infected and uninfected mice. The splenocytes were then externally stimulated with LPS to activate B cells and with ConA to activate T cells (Figure 63).

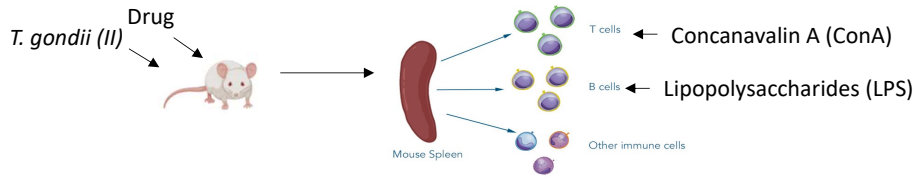

*Figure 63. Splenocytes are isolated from mice treated with **Au18** and **L18** and subjected to LPS and ConA stimulation for T and B cell activation studies*

As depicted in Figure 64, it is evident that the immune system responded similarly in both healthy or infected mice. This unequivocally confirms that lymphocytes from infected and treated mice (with **Au18** and **L18**) exhibited responses to LPS and ConA stimulation that mirrored those of solely infected mice. Importantly, this rules out any immunosuppressive effects of the treatment on immune cells.

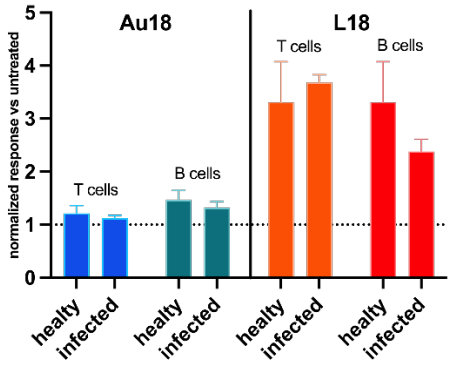

Figure 64. Normalized response of the immune cells collected from the mice after stimulation with ConA for T cells, and LPS for B cells.

Conclusion

In summary, our investigation into metal-based drugs, specifically gold complexes derived from thiosemicarbazone ligands, has unveiled the potential of two lead compounds, **Au18** and **L18**, as promising antiparasitic agents against *Toxoplasma gondii*.

Au18 exhibited an IC_{50} value of 103 nM, highlighting its strong antiparasitic activity against *T. gondii*. Furthermore, **Au18** demonstrated exceptional selectivity, with a selectivity index (SI) exceeding 200, underlining its potential as a lead compound for further development. Notably its corresponding ligand, **L18** also displayed noteworthy antiparasitic activity, with an IC_{50} value of 30 nM against *T. gondii*. Importantly, **L18** exhibited negligible toxicity to host cells, with no detectable adverse effects observed up to a concentration of 25 µM, emphasizing its safety profile.

The comprehensive *in vitro* characterization unveiled the parasitostatic properties of these compounds, indicating that they inhibit parasite growth without achieving

complete eradication. Additionally, we conducted assessments to determine the interaction of these compounds with the immune system. Our findings indicated that these compounds had no discernible impact on the immune system's ability to respond to immune stimuli, effectively ruling out any immunosuppressive effects.

Moving to the *in vivo* models, we observed adverse effects on zebrafish embryonic development, including mortality at higher concentrations and malformations at lower concentrations. These findings precluded the compounds from being tested in a murine model of congenital toxoplasmosis. It is essential to note these teratogenic effects, as they provide insight into potential developmental and reproductive toxicity.

In contrast, the murine model demonstrated the compounds' safety and effectiveness. While the compounds did not significantly reduce the parasite burden within the brain at a dose of 10mg/kg/day for five days, this observation can be attributed to their inability to traverse the blood-brain barrier (BBB). However, a noteworthy and statistically significant reduction in parasite burden was observed within the heart, indicating the compounds' efficacy against heart infection.

Cytotoxicity and efficacy assessment anti-T. gondii activity in vitro

HFF cytotoxicity assessments and IC_{50} determinations using cultures of Tg-β-gal tachyzoites grown in HFF were performed as previously described.[171] IC_{50} values were calculated with the logit-log-transformation of the relative growth and following regression analysis was done with the corresponding software tool contained in Microsoft Excel software package (Microsoft, Seattle, WA).

Long-term drug treatment in vitro: parasitostatic versus parasiticidal activity

For the long-term treatments, HFF grown in T25 culture flasks were infected with 2×10^5 TgMe49 tachyzoites and treated after 3.5 h with 0.5 μM **Au18** and **L18**. Proper controls were prepared using infected cultures treated with the highest corresponding concentration of DMSO of the drugs stocks (0.0025%). Prolonged treatments until 20 days were carried out, refreshing medium containing the respective drug every 3–4 days. On days 3, 6, 9, 13, 16 and 20, the drugs were removed, and parasites were maintained without drug pressure until host cell lysis (plaque formation) was evident. Cultures were checked by light microscopy daily.

In vitro interaction with the immune system: viability of splenocytes

To perform this in vitro assay, spleens were aseptically collected from mice under the hood after the euthanasia. Spleenocytes were isolated from the spleens and seeded in 96-well plates ($5x10^4$ cells/well). Compounds and different stimulants were added to the plates, ConA to stimulate the T- cells and LPS to stimulate the B- cells. Untreated cells were used as proper controls. After 48h spleenocytes viability was assessed using AlamarBlue assay.[167]

Zebrafish embryo development assay

At 3 hours post-fertilization (hpf), zebrafish eggs were placed into a Petri dish filled with osmosis water containing the tested drug concentrations (20, 10, 1, and 0.2 μM). Subsequently, viable eggs were transferred to individual wells of a 24-well plate, with each well containing one egg in 1 mL of the same solution. For each concentration, a separate 24-well plate was employed, consisting of 20 wells with the respective test solution concentration and 4 wells serving as internal controls (iC) without the drug. A negative control plate included 20 wells filled with 1 mL of osmosis water, while a solvent control plate contained 20 wells with 1 mL of osmosis water containing 0.01% DMSO. All plates were sealed with foil, and the embryos were maintained at 28 °C. The test solution was refreshed every 24 hours. Embryos were examined for malformations or changes in viability at 24, 48, 72, and 96 hpf using a Nikon Eclipse TS100 light microscope at 10× magnification. The plates were placed on a heating pad at 26 °C during observations and medium changes. At 96 hpf, all embryos were euthanized by immersing them in a pre-cooled solution of 3-aminobenzoic acid ethyl ester (100 μg/L; MS222; Argent Chemical Laboratories, Redmond, WA, USA) and storing them at -20 °C for 24 hours.

Drugs stock preparation for the in vivo treatment in mice

L18 was dissolved in DMSO and then diluted 1:10 in corn oil before oral administration.

Au18 was dissolved in DMSO and then diluted 1:10 in H_2O 15% DMSO before oral administration.

Corn oil at 25% DMSO was used as control.

Parasite load quantification by real-time PCR

Quantification of parasite load was carried out by real-time PCR method to detect T. gondi DNA.[172]

The NucleoSpin DNA RapidLyse Kit (Macherey-Nagel, Oensingen, Switzerland) was used for DNA purification according to standard protocols and DNA concentrations were quantified using the QuantiFluor double-stranded DNA (dsDNA) system (Promega, Madison, WI, USA). Quantitative real-time PCR was performed with the Light Cycler (Roche, Basel, Switzerland), and parasite loads were calculated with a standard curve of DNA samples from 1'0000, 1′000, 100, 10, 1 T. gondii tachyzoites included in each run.

***In vivo* interaction with the immune system: viability of spleenocytes**

To perform this in assay, spleens were aseptically collected under the hood after the euthanasia, from mice treated with the compounds. Spleenocytes were isolated from the spleens and seeded in 96-well plates (5×10^4 cells/well). Different stimulants were added to the plates, ConA to stimulate the T- cells and LPS to stimulate the B- cells. Untreated cells were used as proper controls. After 48h spleenocytes viability was assessed using AlamarBlue assay.[167]

Conclusions

During my doctoral period, I synthesized a diverse array of compounds that demonstrated promising potential in tackling critical healthcare challenges. For instance, the bismuth complexes featured in Chapter 1 showcased their capacity to reinstate antibiotic sensitivity in carbapenem-resistant bacteria, marking a substantial advancement in the ongoing battle against antimicrobial resistance. Moreover, the exploration of the chemical space initiated from the lead compounds identified in Chapter 1, as detailed in Chapter 2, culminated in the discovery of novel lead compounds characterized by enhanced activity.

Chapter 3 focused instead on gallium(III) complexes, demonstrating their potential as safe and effective candidates for combating antibiotic-resistant infections, with minimal cytotoxic effects on eukaryotic cells.

The application of combinatorial chemistry, in Chapter 4, led to the identification of ten lead candidates with broad-spectrum antibacterial activity, with one, in particular, showing low toxicity to human cells. Moreover, the exhaustive mode-of-action investigation not only revealed the efficacy of these compounds but also unearthed a novel biological target within the bacterial respiratory chain, offering exciting possibilities for the development of new antibacterial agents.

Chapter 5 investigated the potential of gold(III) complexes as lung cancer therapeutics, emphasizing their cytotoxic effects on cancer cells, including apoptosis induction, without any *in vivo* toxicity.

In Chapter 6, gold complexes were evaluated as antiparasitic agents against *T. gondii*, demonstrating efficacy, selectivity, and safety in *in vivo* murine models.

The key issues achieved in this thesis are:

Synthesis of new metal complexes: I achieved the synthesis of diverse metal complexes, encompassing bismuth(III), gallium(III), antimony(III), manganese(I), and gold(III) complexes, by employing robust ligands such as Schiff bases and thiosemicarbazones. The characterization of these compounds was conducted with a comprehensive array of techniques, including X-ray crystallography, NMR, IR, elemental analysis, and UV-vis spectroscopy, which are fundamental tools in inorganic chemistry. Furthermore, this endeavour incorporated innovative approaches to synthesis, notably the application of combinatorial chemistry, a crucial technique in medicinal chemistry.

Biological methods: among the various phases of my work, assessing biological activity proved to be the most challenging. As a chemist, I had to immerse myself in the intricacies of biological techniques, such as cell culture, cell viability assays, MIC assays, and fluorescent microscopy. These skills were crucial in my role, where I assessed the efficacy of synthesized compounds against medically important targets, including antibiotic-resistant bacteria, lung cancer cells, and the parasite responsible for toxoplasmosis. Gaining an understanding of these compounds' behavior was crucial for drug design and the development of next-generation molecules.

This thesis provides a comprehensive overview of the potential of metal-based compounds in various biomedical applications. By advancing our understanding of their properties, and biological activity, this research contributes to the fields of antibacterial drug discovery, cancer therapeutics, and antiparasitic agents. While challenges remain, these promising results offer hope for the development of new and effective treatments for pressing healthcare issues.

List of publications

1. Pioli, M., Orsoni, N., **Scaccaglia, M.**, Alinovi, R., Pinelli, S., Pelosi, G., & Bisceglie, F. (2021).
   A new photoactivatable ruthenium (II) complex with an asymmetric bis-thiocarbohydrazone: chemical and biological investigations.
   Molecules, *26*(4), 939.

2. Montalbano, S., Degola, F., Bartoli, J., Bisceglie, F., Buschini, A., Carcelli, M., Feretti, D., Galati, S., Marchi, L., Orsoni, N., Pelosi, G., Pioli, M., Restivo, F., Rogolino, D., **Scaccaglia, M.**, Serra, O., Spadola, G., Viola, G., Zerbini, I., Zani, C. (2021).
   The AFLATOX® Project: Approaching the Development of New Generation, Natural-Based Compounds for the Containment of the Mycotoxigenic Phytopathogen Aspergillus flavus and Aflatoxin Contamination.
   International Journal of Molecular Sciences, *22*(9), 4520.

3. **Scaccaglia, M.,** Rega, M., Bacci, C., Giovanardi, D., Pinelli, S., Pelosi, G., & Bisceglie, F. (2022).
   Bismuth complex of quinoline thiosemicarbazone restores carbapenem sensitivity in NDM-1-positive Klebsiella pneumoniae.
   Journal of Inorganic Biochemistry, *234*, 111887.

4. **Scaccaglia, M.,** Rega, M., Vescovi, M., Pinelli, S., Tegoni, M., Bacci, C., Pelosi, G., & Bisceglie, F. (2022).
   Gallium (III)-pyridoxal thiosemicarbazone derivatives as nontoxic agents against Gram-negative bacteria.
   Metallomics, *14*(10), mfac070.

5. Riboni, N., Bianchi, F., **Scaccaglia, M.,** Bisceglie, F., Secchi, A., Massera, C., Luches, P., & Careri, M. (2023).
   A novel multiwalled carbon nanotube–cyclodextrin nanocomposite for solid-phase microextraction–gas chromatography–mass spectrometry determination of polycyclic aromatic hydrocarbons in snow samples.
   Microchimica Acta, 190(6), 1-10.

Poster contributions

XX Giornata della Chimica dell'Emilia Romagna (17th December 2021, Ferrara, Italy).

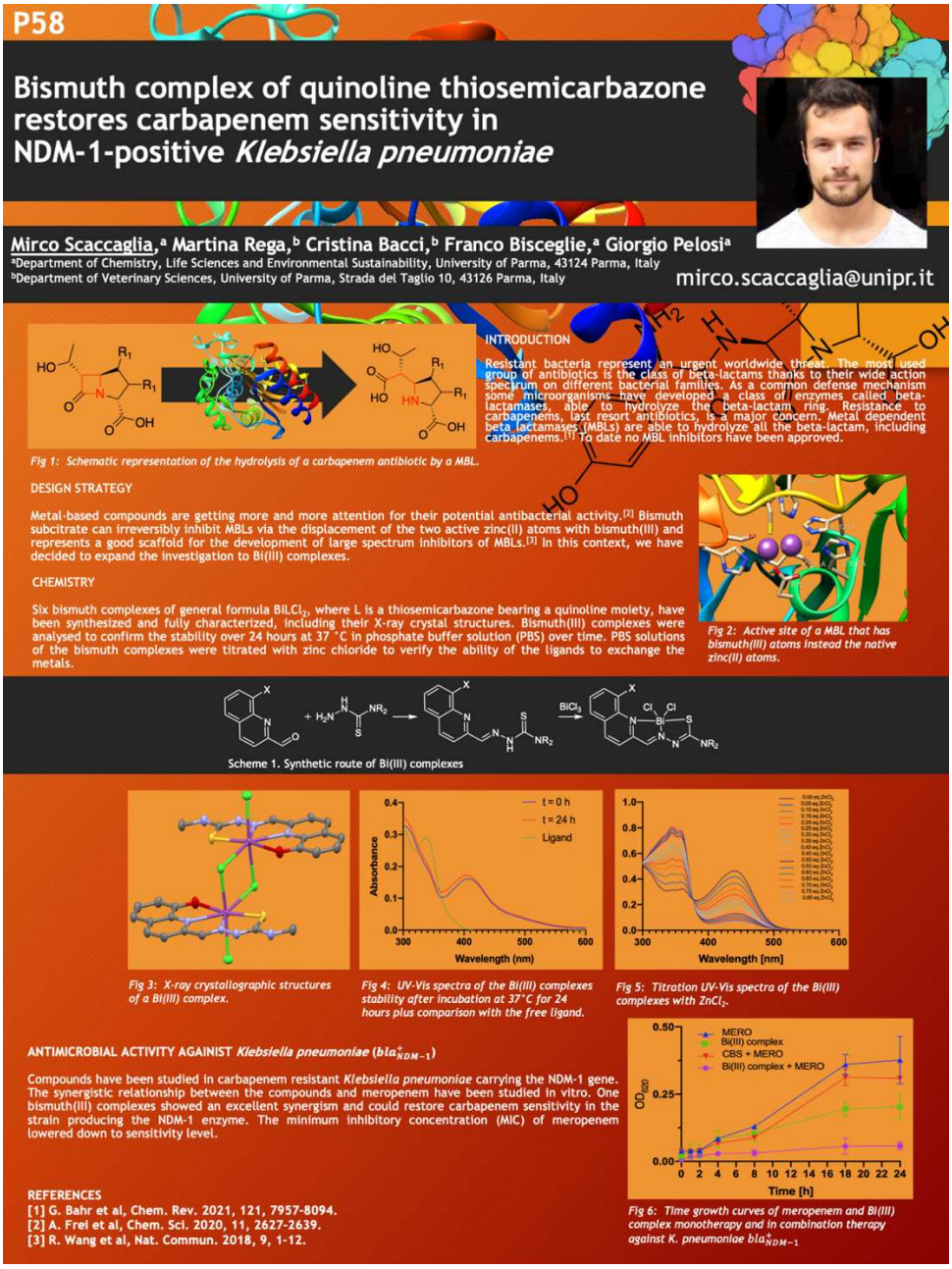

16th International Symposium on Applied Bioinorganic Chemistry (11-14th June 2023, Ioannina, Greece)

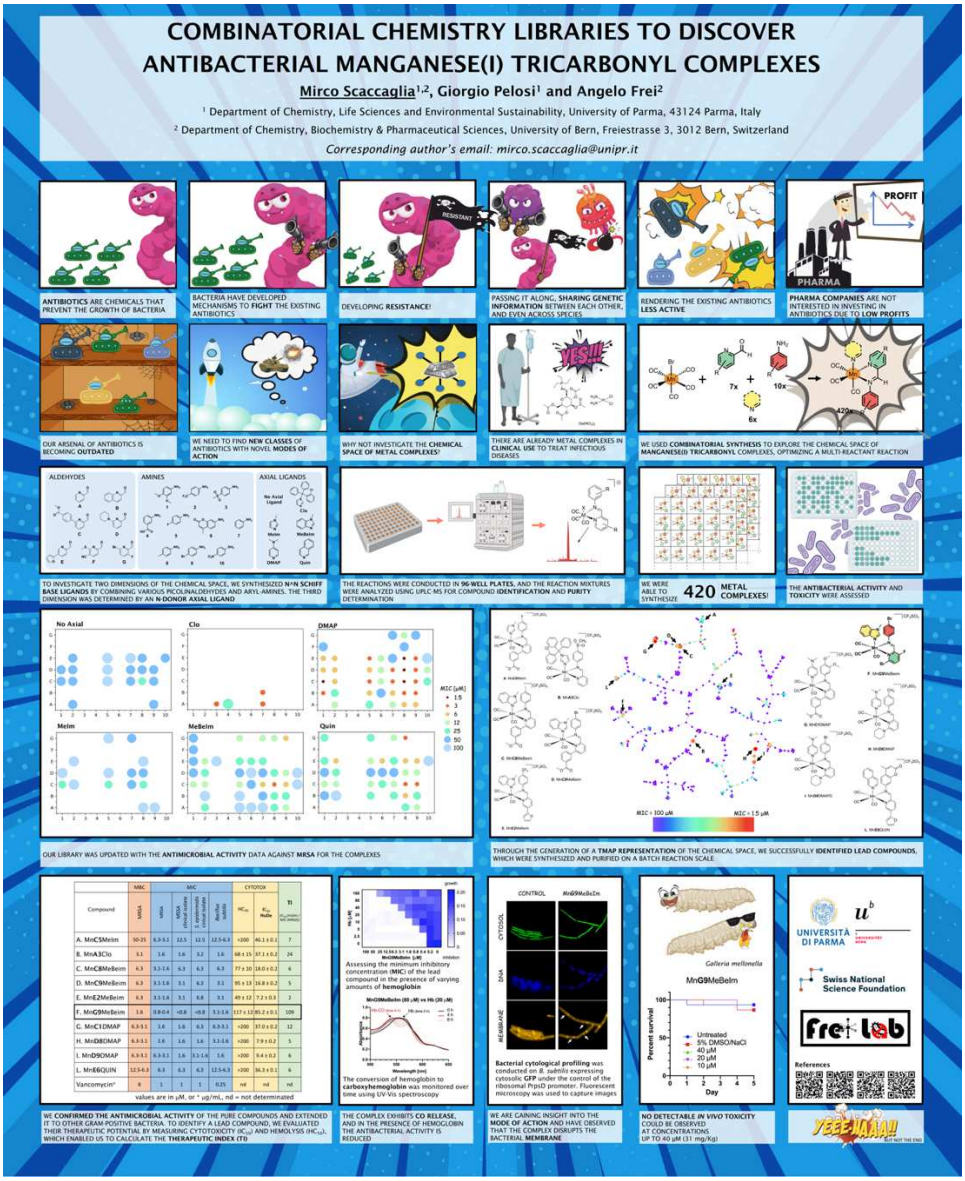

Bibliography

(1) Orvig, C.; Abrams, M. J. Medicinal Inorganic Chemistry: Introduction. *Chem. Rev.* **1999**, *99* (9), 2201–2204.

(2) Holm, R. H.; Solomon, E. I. Preface: Biomimetic Inorganic Chemistry. *Chem. Rev.* **2004**, *104* (2), 347–348.

(3) Sadler, P. J. Inorganic Chemistry and Drug Design. In *Advances in inorganic chemistry*; Elsevier, 1991; Vol. 36, pp 1–48.

(4) Grass, G.; Rensing, C.; Solioz, M. Metallic Copper as an Antimicrobial Surface. *Appl. Environ. Microbiol.* **2011**, *77* (5), 1541–1547.

(5) Goodwin, F. K.; Murphy, D. L.; Bunney, W. E. Lithium-Carbonate Treatment in Depression and Mania: A Longitudinal Double-Blind Study. *Arch. Gen. Psychiatry* **1969**, *21* (4), 486–496.

(6) Dupont, H. L.; Sanchez, J. F.; Ericcson, C. D.; Gomez, J. M.; Dupont, M. W.; Luna, A. C.; Mathewson, J. J. Comparative Efficacy of Loperamide Hydrocholoride and Bismuth Subsalicylate in the Management of Acute Diarrhea. *Am. J. Med.* **1990**, *88* (6), S15–S19.

(7) Muggia, F. Platinum Compounds 30 Years after the Introduction of Cisplatin: Implications for the Treatment of Ovarian Cancer. *Gynecol. Oncol.* **2009**, *112* (1), 275–281.

(8) Nardon, C.; Boscutti, G.; Fregona, D. Beyond Platinums: Gold Complexes as Anticancer Agents. *Anticancer Res.* **2014**, *34* (1), 487–492.

(9) Vock, C. A.; Ang, W. H.; Scolaro, C.; Phillips, A. D.; Lagopoulos, L.; Juillerat-Jeanneret, L.; Sava, G.; Scopelliti, R.; Dyson, P. J. Development of Ruthenium Antitumor Drugs That Overcome Multidrug Resistance Mechanisms. *J. Med. Chem.* **2007**, *50* (9), 2166–2175.

(10) Lemire, J. A.; Harrison, J. J.; Turner, R. J. Antimicrobial Activity of Metals: Mechanisms, Molecular Targets and Applications. *Nat. Rev. Microbiol.* **2013**, *11* (6), 371–384. https://doi.org/10.1038/nrmicro3028.

(11) Cirri, D.; Fabbrini, M. G.; Pratesi, A.; Ciofi, L.; Massai, L.; Marzo, T.; Messori, L. The Leading Established Metal-Based Drugs: A Revisitation of Their Relevant Physico-Chemical Data. *BioMetals* **2019**, *32*, 813–817.

(12) Briand, G. G.; Burford, N. Bismuth Compounds and Preparations with Biological or Medicinal Relevance. *Chem. Rev.* **1999**, *99* (9), 2601–2658.

(13) Abraham, E. P.; Chain, E.; Fletcher, C. M.; Gardner, A. D.; Heatley, N. G.; Jennings, M. A.; Florey, H. W. Further Observations on Penicillin. *Lancet* **1941**, *238* (6155), 177–189.

(14) Hodgkin, D. C. The X-Ray Analysis of the Structure of Penicillin. *Adv. Sci.* **1949**, *6* (22), 85–89.

(15) Fleming, A. On the Antibacterial Action of Cultures of a Penicillium, with Special Reference to Their Use in the Isolation of B. Influenzae. *Br. J. Exp. Pathol.* **1929**, *10* (3), 226.

(16) Hutchings, M. I.; Truman, A. W.; Wilkinson, B. Antibiotics: Past, Present and Future. *Curr. Opin. Microbiol.* **2019**, *51*, 72–80.

(17) Weng, C.; Tan, Y. L. K.; Koh, W. G.; Ang, W. H. Harnessing Transition Metal Scaffolds for Targeted Antibacterial Therapy. *Angew. Chemie Int. Ed.* **2023**, e202310040.

(18) Frei, A.; Verderosa, A. D.; Elliott, A. G.; Zuegg, J.; Blaskovich, M. A. T. Metals to Combat Antimicrobial Resistance. *Nat. Rev. Chem.* **2023**, *7* (3), 202–224.

(19) Pelosi, G. Thiosemicarbazone Metal Complexes: From Structure to Activity. *Open Crystallogr. J.* **2010**, *3* (1).

(20) Bisceglie, F.; Bacci, C.; Vismarra, A.; Barilli, E.; Pioli, M.; Orsoni, N.; Pelosi, G. Antibacterial Activity of Metal Complexes Based on Cinnamaldehyde Thiosemicarbazone Analogues. *J. Inorg. Biochem.* **2020**, *203* (October 2019).

(21) Li, J.-Q.; Gao, H.; Zhai, L.; Sun, L.-Y.; Chen, C.; Chigan, J.-Z.; Ding, H.-H.; Yang, K.-W.

Dipyridyl-Substituted Thiosemicarbazone as a Potent Broad-Spectrum Inhibitor of Metallo-β-Lactamases. *Bioorg. Med. Chem.* **2021**, *38*, 116128.

(22) Beraldo, H.; Gambino, D. The Wide Pharmacological Versatility of Semicarbazones, Thiosemicarba-Zones and Their Metal Complexes. *Mini Rev. Med. Chem.* **2004**, *4* (1), 31–39.

(23) Kwon, J. H.; Powderly, W. G. The Post-Antibiotic Era Is Here. *Science (80-.).* **2021**, *373*, 471. https://doi.org/10.1126/science.abl5997.

(24) Antimicrobial Resistance Collaborators. Global Burden of Bacterial Antimicrobial Resistance in 2019: A Systematic Analysis. *The Lancet*. 2022, pp 629–655. https://doi.org/10.1016/S0140-6736(21)02724-0.

(25) S. Carli, P. Ormas, G. R. *Farmacologia Veterinaria*; Idelson-Gnocchi, Ed.; 2008.

(26) Tooke, C. L.; Hinchliffe, P.; Bragginton, E. C.; Colenso, C. K.; Hirvonen, V. H. A.; Takebayashi, Y.; Spencer, J. β-Lactamases and β-Lactamase Inhibitors in the 21st Century. *J. Mol. Biol.* **2019**, *431* (18), 3472–3500. https://doi.org/10.1016/j.jmb.2019.04.002.

(27) Sengupta, S.; Chattopadhyay, M. K.; Grossart, H. P. The Multifaceted Roles of Antibiotics and Antibiotic Resistance in Nature. *Front. Microbiol.* **2013**, *4* (MAR), 1–13. https://doi.org/10.3389/fmicb.2013.00047.

(28) Bush, K. Past and Present Perspective on B-Lactamase Inhibitors. *Antimicrob. Agents Chemother.* **2018**, *62* (e01076–18), 1–20.

(29) Tilahun, M.; kassa, Y.; Gedefie, A.; Belete, M. A. Emerging Carbapenem-Resistant Enterobacteriaceae Infection, Its Epidemiology and Novel Treatment Options: A Review. *Infect. Drug Resist.* **2021**, *Volume 14* (October), 4363–4374. https://doi.org/10.2147/idr.s337611.

(30) Hamrick, J. C.; Docquier, J.-D.; Uehara, T.; Myers, C. L.; Six, D. A.; Chatwin, C. L.; John, K. J.; Vernacchio, S. F.; Cusick, S. M.; Trout, R. E. L.; et al. VNRX-5133 (Taniborbactam), a Broad-Spectrum Inhibitor of Serine- and Metallo-Beta-Lactamases, Restores Activity of Cefepime in Enterobacterales and Pseudomonas Aeruginosa Jodie. *Antimicrob. Agents Chemother.* **2020**, *5133* (October 2019), 1–19.

(31) Gavara, L.; Sevaille, L.; De Luca, F.; Mercuri, P.; Bebrone, C.; Feller, G.; Legru, A.; Cerboni, G.; Tanfoni, S.; Baud, D.; et al. 4-Amino-1,2,4-Triazole-3-Thione-Derived Schiff Bases as Metallo-β-Lactamase Inhibitors. *Eur. J. Med. Chem.* **2020**, *208*.

(32) Fast, W.; Sutton, L. D. Metallo-β-Lactamase: Inhibitors and Reporter Substrates. *Biochim. Biophys. Acta - Proteins Proteomics* **2013**, *1834* (8), 1648–1659. https://doi.org/10.1016/j.bbapap.2013.04.024.

(33) Tehrani, K. H. M. E.; Martin, N. I. Thiol-Containing Metallo-β-Lactamase Inhibitors Resensitize Resistant Gram-Negative Bacteria to Meropenem. *ACS Infect. Dis.* **2017**, *3* (10), 711–717. https://doi.org/10.1021/acsinfecdis.7b00094.

(34) Zhao, B.; Zhang, X.; Yu, T.; Liu, Y.; Zhang, X.; Yao, Y.; Feng, X.; Liu, H.; Yu, D.; Ma, L.; et al. Discovery of Thiosemicarbazone Derivatives as Effective New Delhi Metallo-β-Lactamase-1 (NDM-1) Inhibitors against NDM-1 Producing Clinical Isolates. *Acta Pharm. Sin. B* **2021**, *11* (1), 203–221. https://doi.org/10.1016/j.apsb.2020.07.005.

(35) Ge, Y.; Kang, P.-W.; Li, J.-Q.; Gao, H.; Zhai, L.; Sun, L.-Y.; Chen, C.; Yang, K.-W. Thiosemicarbazones Exhibit Inhibitory Efficacy against New Delhi Metallo-β-Lactamase-1 (NDM-1). *J. Antibiot. (Tokyo).* **2021**, *74* (9), 574–579. https://doi.org/10.1038/s41429-021-00440-3 CO - JANTAJ.

(36) Frei, A.; Zuegg, J.; Elliott, A. G.; Baker, M.; Braese, S.; Brown, C.; Chen, F.; G. Dowson, C.; Dujardin, G.; Jung, N.; et al. Metal Complexes as a Promising Source for New Antibiotics. *Chem. Sci.* **2020**, *11* (10), 2627–2639. https://doi.org/10.1039/c9sc06460e.

(37) Frei, A. Metal Complexes, an Untapped Source of Antibiotic Potential? *Antibiotics* **2020**, *9* (2).

(38) Buessing, R.; Karge, B.; Lippmann, P.; Jones, P. G.; Bronstrup, M.; Ott, I. Gold(I) and Gold(III) N-Heterocyclic Carbene Complexes as Antibacterial Agents and Inhibitors of

Bacterial Thioredoxin Reductase. *ChemMedChem* **2021**, *16* (22), 3402–3409. https://doi.org/10.1002/cmdc.202100381 CO - CHEMGX.

(39) Frei, A.; Ramu, S.; Lowe, G. J.; Dinh, H.; Semenec, L.; Elliott, A. G.; Zuegg, J.; Deckers, A.; Jung, N.; Bräse, S.; et al. Platinum Cyclooctadiene Complexes with Activity against Gram-Positive Bacteria. *ChemMedChem* **2021**, *16* (20), 3165–3171. https://doi.org/10.1002/cmdc.202100157.

(40) Chey, W. D.; Leontiadis, G. I.; Howden, C. W.; Moss, S. F. ACG Clinical Guideline: Treatment of Helicobacter Pylori Infection. *Am. J. Gastroenterol.* **2017**, *112* (2), 212–238. https://doi.org/10.1038/ajg.2016.563.

(41) Wang, R.; Lai, T. P.; Gao, P.; Zhang, H.; Ho, P. L.; Woo, P. C. Y.; Ma, G.; Kao, R. Y. T.; Li, H.; Sun, H. Bismuth Antimicrobial Drugs Serve as Broad-Spectrum Metallo-β-Lactamase Inhibitors. *Nat. Commun.* **2018**, *9* (1), 1–12. https://doi.org/10.1038/s41467-018-02828-6.

(42) Chen, A. Y.; Thomas, P. W.; Stewart, A. C.; Bergstrom, A.; Cheng, Z.; Miller, C.; Bethel, C. R.; Marshall, S. H.; Credille, C. V.; Riley, C. L.; et al. Dipicolinic Acid Derivatives as Inhibitors of New Delhi Metallo-β-Lactamase-1. *J. Med. Chem.* **2017**, *60* (17), 7267–7283. https://doi.org/10.1021/acs.jmedchem.7b00407.

(43) Lambert, J. R.; Midolo, P. The Actions of Bismuth in the Treatment of Helicobacter Pylori Infection. *Aliment Pharmacol Ther* **1997**, *11*, 27–33.

(44) Damit, N. S. H. H.; Hamid, M. H. S. A.; Rahman, N. S. R. H. A.; Ilias, S. N. H. H.; Keasberry, N. A. Synthesis, Structural Characterisation and Antibacterial Activities of Lead (II) and Some Transition Metal Complexes Derived from Quinoline-2-Carboxaldehyde 4-Methyl-3-Thiosemicarbazone. *Inorganica Chim. Acta* **2021**, *527*, 120557.

(45) www.eucast.org/clinical_breakpoints.

(46) Langeveld, W. T.; Veldhuizen, E. J. A.; Burt, S. A. Synergy between Essential Oil Components and Antibiotics: A Review. *Crit. Rev. Microbiol.* **2013**, *40* (1), 76–94. https://doi.org/10.3109/1040841X.2013.763219.

(47) Huang, R. Y.; Pei, L.; Liu, Q.; Chen, S.; Dou, H.; Shu, G.; Yuan, Z. X.; Lin, J.; Peng, G.; Zhang, W.; et al. Isobologram Analysis: A Comprehensive Review of Methodology and Current Research. *Front. Pharmacol.* **2019**, *10* (OCT), 1–12. https://doi.org/10.3389/fphar.2019.01222.

(48) Asato, E.; Katsura, K.; Mikuriya, M.; Turpeinen, U.; Mutikainen, I.; Reedijk, J. Synthesis, Structure, and Spectroscopic Properties of Bismuth Citrate Compounds and the Bismuth-Containing Ulcer-Healing Agent Colloidal Bismuth Subcitrate (CBS). 4.1 Crystal Structure and Solution Behavior of a Unique Dodecanuclear Cluster (NH4)12[Bi12O8. *Inorg. Chem.* **1995**, *34* (9), 2447–2454. https://doi.org/10.1021/ic00113a028.

(49) Bruker. SAINT and SADABS. Bruker AXS. *APEX3, SAINT SADABS. Bruker AXS Inc., Madison, Wisconsin, USA.* **2016**.

(50) Sheldrick, G. M. Crystal Structure Refinement with SHELXL. *Acta Crystallogr. Sect. C Struct. Chem.* **2015**, *71* (1), 3–8.

(51) Sheldrick, G. M. A Short History of SHELX. *Acta Crystallogr. Sect. A Found. Crystallogr.* **2008**, *64* (1), 112–122.

(52) Dolomanov, O. V; Bourhis, L. J.; Gildea, R. J.; Howard, J. A. K.; Puschmann, H. OLEX2: A Complete Structure Solution, Refinement and Analysis Program. *J. Appl. Crystallogr.* **2009**, *42* (2), 339–341.

(53) Burnett, M. N.; Johnson, C. K. *ORTEP-III: Oak Ridge Thermal Ellipsoid Plot Program for Crystal Structure Illustrations*; Citeseer, 1996.

(54) Macrae, C. F.; Sovago, I.; Cottrell, S. J.; Galek, P. T. A.; McCabe, P.; Pidcock, E.; Platings, M.; Shields, G. P.; Stevens, J. S.; Towler, M. Mercury 4.0: From Visualization to Analysis, Design and Prediction. *J. Appl. Crystallogr.* **2020**, *53* (1), 226–235.

(55) Andrews, J. M. Determination of Minimum Inhibitory Concentrations. *J. Antimicrob. Chemother.* **2001**, *48*, 5–16.

(56) www.hyperquad.co.uk.

(57) Reymond, J.-L.; Awale, M. Exploring Chemical Space for Drug Discovery Using the Chemical Universe Database. *ACS Chem. Neurosci.* **2012**, *3* (9), 649–657.

(58) Bohacek, R. S.; McMartin, C.; Guida, W. C. The Art and Practice of Structure-based Drug Design: A Molecular Modeling Perspective. *Med. Res. Rev.* **1996**, *16* (1), 3–50.

(59) Mirza, A.; Desai, R.; Reynisson, J. Known Drug Space as a Metric in Exploring the Boundaries of Drug-like Chemical Space. *Eur. J. Med. Chem.* **2009**, *44* (12), 5006–5011.

(60) Medina-Franco, J. L.; López-López, E.; Andrade, E.; Ruiz-Azuara, L.; Frei, A.; Guan, D.; Zuegg, J.; Blaskovich, M. A. T. Bridging Informatics and Medicinal Inorganic Chemistry: Toward a Database of Metallodrugs and Metallodrug Candidates. *Drug Discov. Today* **2022**, *xxx* (xx), 1–11. https://doi.org/10.1016/j.drudis.2022.02.021.

(61) Andrea, A.; Krogfelt, K. A.; Jenssen, H. Che. *Microorganisms* **2019**, *7* (3), 85.

(62) Ignasiak, K.; Maxwell, A. Galleria Mellonella (Greater Wax Moth) Larvae as a Model for Antibiotic Susceptibility Testing and Acute Toxicity Trials. *BMC Res. Notes* **2017**, *10*, 1–8.

(63) Tsai, C. J.-Y.; Loh, J. M. S.; Proft, T. Galleria Mellonella Infection Models for the Study of Bacterial Diseases and for Antimicrobial Drug Testing. *Virulence* **2016**, *7* (3), 214–229.

(64) *Critically Important Antimicrobials for Human Medicine: Categorization for the Development of Risk Management Strategies to Contain Antimicrobial Resistance Due to Non-Human Antimicrobial Use: Report of the Second WHO Expert Meeting, Copenhagen, 29-31 May*; World Health Organization, 2007.

(65) Rega, M.; Carmosino, I.; Bonilauri, P.; Frascolla, V.; Vismarra, A.; Bacci, C. Prevalence of EsβL, AmpC and Colistin-Resistant E. Coli in Meat: A Comparison between Pork and Wild Boar. *Microorganisms* **2021**, *9* (2), 214.

(66) Arias, C. A.; Murray, B. E. The Rise of the Enterococcus: Beyond Vancomycin Resistance. *Nat. Rev. Microbiol.* **2012**, *10* (4), 266–278.

(67) Hoelzer, K.; Wong, N.; Thomas, J.; Talkington, K.; Jungman, E.; Coukell, A. Antimicrobial Drug Use in Food-Producing Animals and Associated Human Health Risks: What, and How Strong, Is the Evidence? *BMC Vet. Res.* **2017**, *13* (1), 1–38.

(68) Barilli, E.; Vismarra, A.; Frascolla, V.; Rega, M.; Bacci, C. Escherichia Coli Strains Isolated from Retail Meat Products: Evaluation of Biofilm Formation Ability, Antibiotic Resistance, and Phylogenetic Group Analysis. *J. Food Prot.* **2020**, *83* (2), 233–240.

(69) WHO. Global priority list of antibiotic-resistant bacteria to guide research, discovery, and development of new antibiotics. www.who.int/news/item/27-02-2017-who-publishes-list-of-bacteria-for-which-new-antibiotics-are-urgently-needed.

(70) Minandri, F.; Bonchi, C.; Frangipani, E.; Imperi, F.; Visca, P. Promises and Failures of Gallium as an Antibacterial Agent. *Future Microbiol.* **2014**, *9* (3), 379–397. https://doi.org/10.2217/fmb.14.3.

(71) Lessa, J. A.; Parrilha, G. L.; Beraldo, H. Gallium Complexes as New Promising Metallodrug Candidates. *Inorganica Chim. Acta* **2012**, *393*, 53–63.

(72) Wang, Y.; Han, B.; Xie, Y.; Wang, H.; Wang, R.; Xia, W.; Li, H.; Sun, H. Combination of Gallium (Iii) with Acetate for Combating Antibiotic Resistant Pseudomonas Aeruginosa. *Chem. Sci.* **2019**, *10* (24), 6099–6106.

(73) Pfanzelt, M.; Maher, T. E.; Absmeier, R. M.; Schwarz, M.; Sieber, S. A. Tailored Pyridoxal Probes Unravel Novel Cofactor-Dependent Targets and Antibiotic Hits in Critical Bacterial Pathogens. *Angew. Chemie - Int. Ed.* **2022**, *202117724*, 1–11. https://doi.org/10.1002/anie.202117724.

(74) Acid, P. *Dietary Reference Intakes for Thiamin, Riboflavin, Niacin, Vitamin B6, Folate, Vitamin B12, Pantothenic Acid, Biotin, and Choline*; 1998. https://doi.org/10.17226/6015.

(75) Belicchi-Ferrari, M.; Bisceglie, F.; Casoli, C.; Durot, S.; Morgenstern-Badarau, I.; Pelosi, G.; Pilotti, E.; Pinelli, S.; Tarasconi, P. Copper (II) and Cobalt (III) Pyridoxal Thiosemicarbazone Complexes with Nitroprusside as Counterion: Syntheses, Electronic Properties, and

Antileukemic Activity. *J. Med. Chem.* **2005**, *48* (5), 1671–1675.

(76) Ferrari, M. B.; Bisceglie, F.; Leporati, E.; Pelosi, G.; Tarasconi, P. Synthesis, Solution Chemistry, X-Ray Structure and Biological Activity of Novel Pyridoxal Thiosemicarbazone Derivatives. *Bull. Chem. Soc. Jpn.* **2002**, *75* (4), 781–788.

(77) Ferrari, M. B.; Bisceglie, F.; Pelosi, G.; Tarasconi, P.; Albertini, R.; Dall'Aglio, P. P.; Pinelli, S.; Bergamo, A.; Sava, G. Synthesis, Characterization and Biological Activity of Copper Complexes with Pyridoxal Thiosemicarbazone Derivatives. X-Ray Crystal Structure of Three Dimeric Complexes. *J. Inorg. Biochem.* **2004**, *98* (2), 301–312.

(78) Jakusch, T.; Kozma, K.; Enyedy, É. A.; May, N. V; Roller, A.; Kowol, C. R.; Keppler, B. K.; Kiss, T. Complexes of Pyridoxal Thiosemicarbazones Formed with Vanadium (IV/V) and Copper (II): Solution Equilibrium and Structure. *Inorganica Chim. Acta* **2018**, *472*, 243–253.

(79) Enyedy, E. A.; Bognár, G. M.; Nagy, N. V.; Jakusch, T.; Kiss, T.; Gambino, D. Solution Speciation of Potential Anticancer Metal Complexes of Salicylaldehyde Semicarbazone and Its Bromo Derivative. *Polyhedron* **2014**, *67*, 242–252. https://doi.org/10.1016/j.poly.2013.08.053.

(80) R.M. Smith, A.E. Martell, R.J. Motekaitis. *NIST Critically Selected Stability Constants of Metal Complexes Database*; 2007.

(81) Persson, P.; Zivkovic, K.; Sjöberg, S. Quantitative Adsorption and Local Structures of Gallium(III) at the Water-α-FeOOH Interface. *Langmuir* **2006**, *22* (5), 2096–2104. https://doi.org/10.1021/la052555j.

(82) Hakobyan, S.; Boily, J.-F.; Ramstedt, M. Proton and Gallium (III) Binding Properties of a Biologically Active Salicylidene Acylhydrazide. *J. Inorg. Biochem.* **2014**, *138*, 9–15.

(83) Enyedy, É. A.; Zsigó, É.; Nagy, N. V; Kowol, C. R.; Roller, A.; Keppler, B. K.; Kiss, T. Complex-formation Ability of Salicylaldehyde Thiosemicarbazone towards ZnII, CuII, FeII, FeIII and GaIII Ions. *Eur. J. Inorg. Chem.* **2012**, *2012* (25), 4036–4047.

(84) Doyle, D.; Peirano, G.; Lascols, C.; Lloyd, T.; Church, D. L.; Pitout, J. D. D. Laboratory Detection of Enterobacteriaceae That Produce Carbapenemases. *J. Clin. Microbiol.* **2012**, *50* (12), 3877–3880.

(85) Roschanski, N.; Fischer, J.; Guerra, B.; Roesler, U. Development of a Multiplex Real-Time PCR for the Rapid Detection of the Predominant Beta-Lactamase Genes CTX-M, SHV, TEM and CIT-Type AmpCs in Enterobacteriaceae. *PLoS One* **2014**, *9* (7), e100956.

(86) Pérez-Pérez, F. J.; Hanson, N. D. Detection of Plasmid-Mediated AmpC β-Lactamase Genes in Clinical Isolates by Using Multiplex PCR. *J. Clin. Microbiol.* **2002**, *40* (6), 2153–2162.

(87) Tatsing Foka, F. E.; Ateba, C. N. Detection of Virulence Genes in Multidrug Resistant Enterococci Isolated from Feedlots Dairy and Beef Cattle: Implications for Human Health and Food Safety. *Biomed Res. Int.* **2019**, *2019*.

(88) Gans, P.; Sabatini, A.; Vacca, A. Investigation of Equilibria in Solution. Determination of Equilibrium Constants with the HYPERQUAD Suite of Programs. *Talanta* **1996**, *43* (10), 1739–1753.

(89) Chow, M. J.; Licona, C.; Yuan Qiang Wong, D.; Pastorin, G.; Gaiddon, C.; Ang, W. H. Discovery and Investigation of Anticancer Ruthenium–Arene Schiff-Base Complexes via Water-Promoted Combinatorial Three-Component Assembly. *J. Med. Chem.* **2014**, *57* (14), 6043–6059.

(90) Chow, M. J.; Alfiean, M.; Pastorin, G.; Gaiddon, C.; Ang, W. H. Apoptosis-Independent Organoruthenium Anticancer Complexes That Overcome Multidrug Resistance: Self-Assembly and Phenotypic Screening Strategies. *Chem. Sci.* **2017**, *8* (5), 3641–3649.

(91) Konkankit, C. C.; Vaughn, B. A.; MacMillan, S. N.; Boros, E.; Wilson, J. J. Combinatorial Synthesis to Identify a Potent, Necrosis-Inducing Rhenium Anticancer Agent. *Inorg. Chem.* **2019**, *58* (6), 3895–3909.

(92) Vilar, R.; Kench, T.; Rahardjo, A.; Bellamkonda, A.; Maher, T. E.; Storch, M. A Semi-Automated, High-Throughput Approach for the Synthesis and Identification of Highly Photo-

Cytotoxic Iridium Complexes. **2023**.

(93) Patra, M.; Wenzel, M.; Prochnow, P.; Pierroz, V.; Gasser, G.; Bandow, J. E.; Metzler-Nolte, N. An Organometallic Structure-Activity Relationship Study Reveals the Essential Role of a Re (CO) 3 Moiety in the Activity against Gram-Positive Pathogens Including MRSA. *Chem. Sci.* **2015**, *6* (1), 214–224.

(94) Frei, A.; Amado, M.; Cooper, M. A.; Blaskovich, M. A. T. Light-Activated Rhenium Complexes with Dual Mode of Action against Bacteria. *Chem. Eur. J.* **2020**, *26* (13), 2852–2858.

(95) Sovari, S. N.; Vojnovic, S.; Bogojevic, S. S.; Crochet, A.; Pavic, A.; Nikodinovic-Runic, J.; Zobi, F. Design, Synthesis and in Vivo Evaluation of 3-Arylcoumarin Derivatives of Rhenium (I) Tricarbonyl Complexes as Potent Antibacterial Agents against Methicillin-Resistant Staphylococcus Aureus (MRSA). *Eur. J. Med. Chem.* **2020**, *205*, 112533.

(96) Mendes, S. S.; Marques, J.; Mesterházy, E.; Straetener, J.; Arts, M.; Pissarro, T.; Reginold, J.; Berscheid, A.; Bornikoel, J.; Kluj, R. M. Synergetic Antimicrobial Activity and Mechanism of Clotrimazole-Linked CO-Releasing Molecules. *ACS Bio Med Chem Au* **2022**.

(97) Nagel, C.; McLean, S.; Poole, R. K.; Braunschweig, H.; Kramer, T.; Schatzschneider, U. Introducing [Mn (CO) 3 (Tpa-κ 3 N)]+ as a Novel Photoactivatable CO-Releasing Molecule with Well-Defined ICORM Intermediates–Synthesis, Spectroscopy, and Antibacterial Activity. *Dalt. Trans.* **2014**, *43* (26), 9986–9997.

(98) Simpson, P. V; Nagel, C.; Bruhn, H.; Schatzschneider, U. Antibacterial and Antiparasitic Activity of Manganese (I) Tricarbonyl Complexes with Ketoconazole, Miconazole, and Clotrimazole Ligands. *Organometallics* **2015**, *34* (15), 3809–3815.

(99) Betts, J. W.; Cawthraw, S.; Smyth, J. A.; Poole, R. K.; Roth, P.; Schatzschneider, U.; La Ragione, R. M. The Manganese Carbonyl Complex [Mn (CO) 3 (Tqa-K3N)] Br: A Novel Antimicrobial Agent with the Potential to Treat Avian Pathogenic Escherichia Coli (APEC) Infections. *Vet. Microbiol.* **2023**, 109819.

(100) Crook, S. H.; Mann, B. E.; Meijer, A. J. H. M.; Adams, H.; Sawle, P.; Scapens, D.; Motterlini, R. [Mn (CO) 4 {S 2 CNMe (CH 2 CO 2 H)}], a New Water-Soluble CO-Releasing Molecule. *Dalt. Trans.* **2011**, *40* (16), 4230–4235.

(101) Wareham, L. K.; McLean, S.; Begg, R.; Rana, N.; Ali, S.; Kendall, J. J.; Sanguinetti, G.; Mann, B. E.; Poole, R. K. The Broad-Spectrum Antimicrobial Potential of [Mn (CO) 4 (S2CNMe (CH2CO2H))], a Water-Soluble CO-Releasing Molecule (CORM-401): Intracellular Accumulation, Transcriptomic and Statistical Analyses, and Membrane Polarization. *Antioxid. Redox Signal.* **2018**, *28* (14), 1286–1308.

(102) Bajusz, D.; Rácz, A.; Héberger, K. Why Is Tanimoto Index an Appropriate Choice for Fingerprint-Based Similarity Calculations? *J. Cheminform.* **2015**, *7* (1), 1–13.

(103) Probst, D.; Reymond, J.-L. Visualization of Very Large High-Dimensional Data Sets as Minimum Spanning Trees. *J. Cheminform.* **2020**, *12* (1), 1–13.

(104) Orpen, A. G.; Brammer, L.; Allen, F. H.; Kennard, O.; Watson, D. G.; Taylor, R. Supplement. Tables of Bond Lengths Determined by X-Ray and Neutron Diffraction. Part 2. Organometallic Compounds and Co-Ordination Complexes of the d- and f-Block Metals. *J. Chem. Soc.{,} Dalt. Trans.* **1989**, No. 12, S1–S83. https://doi.org/10.1039/DT98900000S1.

(105) De Oliveira, D. M. P.; Forde, B. M.; Kidd, T. J.; Harris, P. N. A.; Schembri, M. A.; Beatson, S. A.; Paterson, D. L.; Walker, M. J. Antimicrobial Resistance in ESKAPE Pathogens. *Clin. Microbiol. Rev.* **2020**, *33* (3), 10–1128.

(106) Atkin, A. J.; Lynam, J. M.; Moulton, B. E.; Sawle, P.; Motterlini, R.; Boyle, N. M.; Pryce, M. T.; Fairlamb, I. J. S. Modification of the Deoxy-Myoglobin/Carbonmonoxy-Myoglobin UV-Vis Assay for Reliable Determination of CO-Release Rates from Organometallic Carbonyl Complexes. *Dalt. Trans.* **2011**, *40* (21), 5755–5761.

(107) Nonejuie, P.; Burkart, M.; Pogliano, K.; Pogliano, J. Bacterial Cytological Profiling Rapidly Identifies the Cellular Pathways Targeted by Antibacterial Molecules. *Proc. Natl. Acad. Sci.* **2013**, *110* (40), 16169–16174.

(108) Schäfer, A.-B.; Wenzel, M. A How-to Guide for Mode of Action Analysis of Antimicrobial

Peptides. *Front. Cell. Infect. Microbiol.* **2020**, *10*, 540898.

(109) Michel, B. W.; Lippert, A. R.; Chang, C. J. A Reaction-Based Fluorescent Probe for Selective Imaging of Carbon Monoxide in Living Cells Using a Palladium-Mediated Carbonylation. *J. Am. Chem. Soc.* **2012**, *134* (38), 15668–15671.

(110) Güntzel, P.; Nagel, C.; Weigelt, J.; Betts, J. W.; Pattrick, C. A.; Southam, H. M.; La Ragione, R. M.; Poole, R. K.; Schatzschneider, U. Biological Activity of Manganese (i) Tricarbonyl Complexes on Multidrug-Resistant Gram-Negative Bacteria: From Functional Studies to in Vivo Activity in Galleria Mellonella. *Metallomics* **2019**, *11* (12), 2033–2042.

(111) Nielsen, V. G. Ruthenium, Not Carbon Monoxide, Inhibits the Procoagulant Activity of Atheris, Echis, and Pseudonaja Venoms. *Int. J. Mol. Sci.* **2020**, *21* (8), 2970.

(112) Mansour, A. M.; Khaled, R. M.; Khaled, E.; Ahmed, S. K.; Ismael, O. S.; Zeinhom, A.; Magdy, H.; Ibrahim, S. S.; Abdelfatah, M. Ruthenium (II) Carbon Monoxide Releasing Molecules: Structural Perspective, Antimicrobial and Anti-Inflammatory Properties. *Biochem. Pharmacol.* **2022**, *199*, 114991.

(113) Saeloh, D.; Tipmanee, V.; Jim, K. K.; Dekker, M. P.; Bitter, W.; Voravuthikunchai, S. P.; Wenzel, M.; Hamoen, L. W. The Novel Antibiotic Rhodomyrtone Traps Membrane Proteins in Vesicles with Increased Fluidity. *PLoS Pathog.* **2018**, *14* (2), e1006876. https://doi.org/10.1371/journal.ppat.1006876.

(114) Tsubaki, M.; Yoshikawa, S. Fourier-Transform Infrared Study of Azide Binding to the Fea3-CuB Binuclear Site of Bovine Heart Cytochrome c Oxidase: New Evidence for a Redox-Linked Conformational Change at the Binuclear Site. *Biochemistry* **1993**, *32* (1), 174–182.

(115) Usón, R.; Riera, V.; Gimeno, J.; Laguna, M.; Gamasa, M. P. Synthesis of Cationic Pentacarbonyl, Fac-and Mer-Tricarbonyl, and Cis-and Trans-Dicarbonyl Complexes of Manganese (I). *J. Chem. Soc. Dalt. Trans.* **1979**, No. 6, 996–1002.

(116) Motterlini, R.; Clark, J. E.; Foresti, R.; Sarathchandra, P.; Mann, B. E.; Green, C. J. Carbon Monoxide-Releasing Molecules: Characterization of Biochemical and Vascular Activities. *Circ. Res.* **2002**, *90* (2), e17–e24.

(117) Zakharova, E.; Orsi, M.; Capecchi, A.; Reymond, J. Machine Learning Guided Discovery of Non-Hemolytic Membrane Disruptive Anticancer Peptides. *ChemMedChem* **2022**, *17* (17), e202200291.

(118) Wenzel, M.; Rautenbach, M.; Vosloo, J. A.; Siersma, T.; Aisenbrey, C. H. M.; Zaitseva, E.; Laubscher, W. E.; Van Rensburg, W.; Behrends, J. C.; Bechinger, B. The Multifaceted Antibacterial Mechanisms of the Pioneering Peptide Antibiotics Tyrocidine and Gramicidin S. *MBio* **2018**, *9* (5), e00802-18.

(119) te Winkel, J. D.; Gray, D. A.; Seistrup, K. H.; Hamoen, L. W.; Strahl, H. Analysis of Antimicrobial-Triggered Membrane Depolarisation Using Voltage Sensitive Dyes. *Front. Cell Dev. Biol.* **2016**, *4*, 29. https://doi.org/10.3389/fcell.2016.00029.

(120) Müller, A.; Wenzel, M.; Strahl, H.; Grein, F.; Saaki, T. N. V; Kohl, B.; Siersma, T.; Bandow, J. E.; Sahl, H.-G.; Schneider, T.; et al. Daptomycin Inhibits Cell Envelope Synthesis by Interfering with Fluid Membrane Microdomains. *Proc. Natl. Acad. Sci. USA* **2016**, *113*, E7077–E7086. https://doi.org/10.1073/pnas.1611173113.

(121) Maslova, E.; Osman, S.; McCarthy, R. R. Using the Galleria Mellonella Burn Wound and Infection Model to Identify and Characterize Potential Wound Probiotics. *Microbiology* **2023**, *169* (6), 1350.

(122) Ferlay, J.; Colombet, M.; Soerjomataram, I.; Parkin, D. M.; Piñeros, M.; Znaor, A.; Bray, F. Cancer Statistics for the Year 2020: An Overview. *Int. J. cancer* **2021**, *149* (4), 778–789.

(123) Dasari, S.; Tchounwou, P. B. Cisplatin in Cancer Therapy: Molecular Mechanisms of Action. *Eur. J. Pharmacol.* **2014**, *740*, 364–378.

(124) Casini, A.; Thomas, S. R. The Beauty of Gold: Knowledge of Mechanisms Leads to Different Applications of Organogold Compounds in Medicine and Catalysis. *Chem. Lett.* **2021**, *50* (8), 1516–1522.

(125) Li, H.; Yuan, S.; Wei, X.; Sun, H. Metal-Based Strategies for the Fight against COVID-19.

Chem. Commun. **2022**.

(126) Chakraborty, P.; Oosterhuis, D.; Bonsignore, R.; Casini, A.; Olinga, P.; Scheffers, D. An Organogold Compound as Potential Antimicrobial Agent against Drug-Resistant Bacteria: Initial Mechanistic Insights. *ChemMedChem* **2021**, *16* (19), 3060–3070.

(127) Rubbiani, R.; Can, S.; Kitanovic, I.; Alborzinia, H.; Stefanopoulou, M.; Kokoschka, M.; Mönchgesang, S.; Sheldrick, W. S.; Wölfl, S.; Ott, I. Comparative in Vitro Evaluation of N-Heterocyclic Carbene Gold (I) Complexes of the Benzimidazolylidene Type. *J. Med. Chem.* **2011**, *54* (24), 8646–8657.

(128) Schlagintweit, J. F.; Jakob, C. H. G.; Wilke, N. L.; Ahrweiler, M.; Frias, C.; Frias, J.; König, M.; Esslinger, E.-M. H. J.; Marques, F.; Machado, J. F. Gold (I) Bis (1, 2, 3-Triazol-5-Ylidene) Complexes as Promising Selective Anticancer Compounds. *J. Med. Chem.* **2021**, *64* (21), 15747–15757.

(129) Rocchigiani, L.; Bochmann, M. Recent Advances in Gold (III) Chemistry: Structure, Bonding, Reactivity, and Role in Homogeneous Catalysis. *Chem. Rev.* **2020**, *121* (14), 8364–8451.

(130) Zhang, J.; Zhang, Z.; Jiang, M.; Li, S.; Yuan, H.; Sun, H.; Yang, F.; Liang, H. Developing a Novel Gold(III) Agent to Treat Glioma Based on the Unique Properties of Apoferritin Nanoparticles: Inducing Lethal Autophagy and Apoptosis. *J. Med. Chem.* **2020**, *63* (22), 13695–13708. https://doi.org/10.1021/acs.jmedchem.0c01257.

(131) Huang, K.-B.; Wang, F.-Y.; Tang, X.-M.; Feng, H.-W.; Chen, Z.-F.; Liu, Y.-C.; Liu, Y.-N.; Liang, H. Organometallic Gold (III) Complexes Similar to Tetrahydroisoquinoline Induce ER-Stress-Mediated Apoptosis and pro-Death Autophagy in A549 Cancer Cells. *J. Med. Chem.* **2018**, *61* (8), 3478–3490.

(132) Pioli, M.; Orsoni, N.; Scaccaglia, M.; Alinovi, R.; Pinelli, S.; Pelosi, G.; Bisceglie, F. A New Photoactivatable Ruthenium(II) Complex with an Asymmetric Bis-Thiocarbohydrazone: Chemical and Biological Investigations. *Molecules* **2021**, *26* (4).

(133) Scaccaglia, M.; Rega, M.; Bacci, C.; Giovanardi, D.; Pinelli, S.; Pelosi, G.; Bisceglie, F. Bismuth Complex of Quinoline Thiosemicarbazone Restores Carbapenem Sensitivity in NDM-1-Positive Klebsiella Pneumoniae. *J. Inorg. Biochem.* **2022**. https://doi.org/https://doi.org/10.1016/j.jinorgbio.2022.111887.

(134) Scaccaglia, M.; Rega, M.; Vescovi, M.; Pinelli, S.; Tegoni, M.; Bacci, C.; Pelosi, G.; Bisceglie, F. Gallium (III)-Pyridoxal Thiosemicarbazone Derivatives as Nontoxic Agents against Gram-Negative Bacteria. *Metallomics* **2022**, *14* (10), mfac070.

(135) Ritacca, A. G.; Falcone, E.; Doumi, I.; Vileno, B.; Faller, P.; Sicilia, E. Dual Role of Glutathione as a Reducing Agent and Cu-Ligand Governs the ROS Production by Anticancer Cu-Thiosemicarbazone Complexes. *Inorg. Chem.* **2023**, *62* (9), 3957–3964.

(136) Schaier, M.; Falcone, E.; Prstek, T.; Vileno, B.; Hager, S.; Keppler, B. K.; Heffeter, P.; Koellensperger, G.; Faller, P.; Kowol, C. R. Human Serum Albumin as a Copper Source for Anticancer Thiosemicarbazones. *Metallomics* **2023**, *15* (8), mfad046.

(137) Zhang, J.; Zhang, Z.; Jiang, M.; Li, S.; Yuan, H.; Sun, H.; Yang, F.; Liang, H. Developing a Novel Gold (III) Agent to Treat Glioma Based on the Unique Properties of Apoferritin Nanoparticles: Inducing Lethal Autophagy and Apoptosis. *J. Med. Chem.* **2020**, *63* (22), 13695–13708.

(138) Schillebeeckx, E.; van Meerbeeck, J. P.; Lamote, K. Clinical Utility of Diagnostic Biomarkers in Malignant Pleural Mesothelioma: A Systematic Review and Meta-Analysis. *Eur. Respir. Rev.* **2021**, *30* (162).

(139) Sinn, K.; Mosleh, B.; Hoda, M. A. Malignant Pleural Mesothelioma: Recent Developments. *Curr. Opin. Oncol.* **2021**, *33* (1), 80–86.

(140) Messori, L.; Abbate, F.; Marcon, G.; Orioli, P.; Fontani, M.; Mini, E.; Mazzei, T.; Carotti, S.; O'Connell, T.; Zanello, P. Gold(III) Complexes as Potential Antitumor Agents: Solution Chemistry and Cytotoxic Properties of Some Selected Gold(III) Compounds. *J. Med. Chem.* **2000**, *43* (19), 3541–3548. https://doi.org/10.1021/jm990492u.

(141) Nobili, S.; Mini, E.; Landini, I.; Gabbiani, C.; Casini, A.; Messori, L. Gold Compounds as

Anticancer Agents: Chemistry, Cellular Pharmacology, and Preclinical Studies. *Med. Res. Rev.* **2010**, *30* (3), 550–580.

(142) Roy, S.; Patra, A. K.; Dhar, S.; Chakravarty, A. R. Photosensitizer in a Molecular Bowl and Its Effect on the DNA-Binding and-Cleavage Activity of 3d-Metal Scorpionates. *Inorg. Chem.* **2008**, *47* (13), 5625–5633.

(143) Heinrich, J.; Bossak-Ahmad, K.; Riisom, M.; Haeri, H. H.; Steel, T. R.; Hergl, V.; Langhans, A.; Schattschneider, C.; Barrera, J.; Jamieson, S. M. F.; et al. Incorporation of β-Alanine in Cu(II) ATCUN Peptide Complexes Increases ROS Levels, DNA Cleavage and Antiproliferative Activity**. *Chem. - A Eur. J.* **2021**, *27* (72), 18093–18102. https://doi.org/10.1002/chem.202102601.

(144) Heinrich, J.; Stubbe, J.; Kulak, N. Cu (II) Complexes with Hydrazone-Functionalized Phenanthrolines as Self-Activating Metallonucleases. *Inorganica Chim. Acta* **2018**, *481*, 79–86.

(145) Heinrich, J.; König, N. F.; Sobottka, S.; Sarkar, B.; Kulak, N. Flexible vs. Rigid Bis(2-Benzimidazolyl) Ligands in Cu(II) Complexes: Impact on Redox Chemistry and Oxidative DNA Cleavage Activity. *J. Inorg. Biochem.* **2019**, *194* (August 2018), 223–232. https://doi.org/10.1016/j.jinorgbio.2019.01.016.

(146) Binacchi, F.; Guarra, F.; Cirri, D.; Marzo, T.; Pratesi, A.; Messori, L.; Gabbiani, C.; Biver, T. On the Different Mode of Action of Au (I)/Ag (I)-NHC Bis-Anthracenyl Complexes Towards Selected Target Biomolecules. *Molecules* **2020**, *25* (22), 5446.

(147) Järvinen, K.; Pietarinen-Runtti, P.; Linnainmaa, K.; Raivio, K. O.; Krejsa, C. M.; Kavanagh, T.; Kinnula, V. L. Antioxidant Defense Mechanisms of Human Mesothelioma and Lung Adenocarcinoma Cells. *Am. J. Physiol. Cell. Mol. Physiol.* **2000**, *278* (4), L696–L702.

(148) Frisch, M. J.; Trucks, G. W.; Schlegel, H. B.; Scuseria, G. E.; Robb, M. a.; Cheeseman, J. R.; Scalmani, G.; Barone, V.; Petersson, G. a.; Nakatsuji, H.; et al. Gaussian 16, Revision G.09. 2016.

(149) oy Dennington, Todd A. Keith, and John M. Millam, Semichem Inc., S. M. GaussView, Version 6.1. KS 2016.

(150) Becke, A. D. A New Mixing of Hartree–Fock and Local Density-functional Theories. *J. Chem. Phys.* **1993**, *98* (2), 1372–1377.

(151) Mondal, A.; Paira, P. Hypoxia Efficient and Glutathione-Resistant Cytoselective Ruthenium (II)-p-Cymene-Arylimidazophenanthroline Complexes: Biomolecular Interaction and Live Cell Imaging. *Dalt. Trans.* **2020**, *49* (36), 12865–12878.

(152) Atherton, S. J.; Beaumont, P. C. Quenching of the Fluorescence of DNA-Intercalated Ethidium Bromide by Some Transition-Metal Ions. *J. Phys. Chem.* **1986**, *90* (10), 2252–2259.

(153) Gehlen, M. H. The Centenary of the Stern-Volmer Equation of Fluorescence Quenching: From the Single Line Plot to the SV Quenching Map. *J. Photochem. Photobiol. C Photochem. Rev.* **2020**, *42*, 100338.

(154) Morgan, A. R.; Lee, J. S.; Pulleyblank, D. E.; Murray, N. L.; Evans, D. H. Ethidium Fluorescence Assays. Part 1. Physicochemical Studies. *Nucleic Acids Res.* **1979**, *7* (3), 547–565.

(155) Hertzberg, R. P.; Dervan, P. B. Cleavage of DNA with Methidiumpropyl-EDTA-Iron (II): Reaction Conditions and Product Analyses. *Biochemistry* **1984**, *23* (17), 3934–3945.

(156) Alagesan, M.; Sathyadevi, P.; Krishnamoorthy, P.; Bhuvanesh, N. S. P.; Dharmaraj, N. DMSO Containing Ruthenium(Ii) Hydrazone Complexes: In Vitro Evaluation of Biomolecular Interaction and Anticancer Activity. *Dalt. Trans.* **2014**, *43* (42), 15829–15840. https://doi.org/10.1039/c4dt01032a.

(157) Bai, H.; Shi, J.; Guo, Q.; Wang, W.; Zhang, Z.; Li, Y.; Vennampalli, M.; Zhao, X.; Wang, H. Spectroscopy, Structure, Biomacromolecular Interactions, and Antiproliferation Activity of a Fe (II) Complex With DPA-Bpy as Pentadentate Ligand. *Front. Chem.* **2022**, *10*.

(158) Jentzsch, A. M.; Bachmann, H.; Fürst, P.; Biesalski, H. K. Improved Analysis of Malondialdehyde in Human Body Fluids. *Free Radic. Biol. Med.* **1996**, *20* (2), 251–256.

(159) Livak, K. J.; Schmittgen, T. D. Analysis of Relative Gene Expression Data Using Real-Time Quantitative PCR and the 2− ΔΔCT Method. *methods* **2001**, *25* (4), 402–408.

(160) Betts, H. D.; Ong, Y. C.; Anghel, N.; Keller, S.; Karges, J.; Voutsara, N.; Muller, J.; Manoury, E.; Blacque, O.; Cariou, K. Organometallic Derivatives of Decoquinate Targeted toward Toxoplasma Gondii. *Organometallics* **2022**, *41* (15), 2035–2041.

(161) Dubey, J. P. *Toxoplasmosis of Animals and Humans*; CRC press, 2016.

(162) Konstantinovic, N.; Guegan, H.; Stäjner, T.; Belaz, S.; Robert-Gangneux, F. Treatment of Toxoplasmosis: Current Options and Future Perspectives. *Food waterborne Parasitol.* **2019**, *15*, e00036.

(163) Attias, M.; Teixeira, D. E.; Benchimol, M.; Vommaro, R. C.; Crepaldi, P. H.; De Souza, W. The Life-Cycle of Toxoplasma Gondii Reviewed Using Animations. *Parasit. Vectors* **2020**, *13*, 1–13.

(164) Alday, P. H.; Doggett, J. S. Drugs in Development for Toxoplasmosis: Advances, Challenges, and Current Status. *Drug Des. Devel. Ther.* **2017**, 273–293.

(165) Holzer, I.; Desiatkina, O.; Anghel, N.; Johns, S. K.; Boubaker, G.; Hemphill, A.; Furrer, J.; Păunescu, E. Synthesis and Antiparasitic Activity of New Trithiolato-Bridged Dinuclear Ruthenium (II)-Arene-Carbohydrate Conjugates. *Molecules* **2023**, *28* (2), 902.

(166) Desiatkina, O.; Anghel, N.; Boubaker, G.; Amdouni, Y.; Hemphill, A.; Furrer, J.; Păunescu, E. Trithiolato-Bridged Dinuclear Ruthenium (II)-Arene Conjugates Tethered with Lipophilic Units: Synthesis and Toxoplasma Gondii Antiparasitic Activity. *J. Organomet. Chem.* **2023**, *986*, 122624.

(167) Desiatkina, O.; Păunescu, E.; Mösching, M.; Anghel, N.; Boubaker, G.; Amdouni, Y.; Hemphill, A.; Furrer, J. Coumarin-Tagged Dinuclear Trithiolato-Bridged Ruthenium (II)· Arene Complexes: Photophysical Properties and Antiparasitic Activity. *ChemBioChem* **2020**, *21* (19), 2818–2835.

(168) Hill, A. J.; Teraoka, H.; Heideman, W.; Peterson, R. E. Zebrafish as a Model Vertebrate for Investigating Chemical Toxicity. *Toxicol. Sci.* **2005**, *86* (1), 6–19.

(169) Anghel, N.; Winzer, P. A.; Imhof, D.; Müller, J.; Langa, X.; Rieder, J.; Barrett, L. K.; Vidadala, R. S. R.; Huang, W.; Choi, R. Comparative Assessment of the Effects of Bumped Kinase Inhibitors on Early Zebrafish Embryo Development and Pregnancy in Mice. *Int. J. Antimicrob. Agents* **2020**, *56* (3), 106099.

(170) Păunescu, E.; Boubaker, G.; Desiatkina, O.; Anghel, N.; Amdouni, Y.; Hemphill, A.; Furrer, J. The Quest of the Best–A SAR Study of Trithiolato-Bridged Dinuclear Ruthenium (II)-Arene Compounds Presenting Antiparasitic Properties. *Eur. J. Med. Chem.* **2021**, *222*, 113610.

(171) Desiatkina, O.; Mösching, M.; Anghel, N.; Boubaker, G.; Amdouni, Y.; Hemphill, A.; Furrer, J.; Păunescu, E. New Nucleic Base-Tethered Trithiolato-Bridged Dinuclear Ruthenium (II)-Arene Compounds: Synthesis and Antiparasitic Activity. *Molecules* **2022**, *27* (23), 8173.

(172) Costa, J.-M.; Pautas, C.; Ernault, P.; Foulet, F.; Cordonnier, C.; Bretagne, S. Real-Time PCR for Diagnosis and Follow-up of Toxoplasma Reactivation after Allogeneic Stem Cell Transplantation Using Fluorescence Resonance Energy Transfer Hybridization Probes. *J. Clin. Microbiol.* **2000**, *38* (8), 2929–2932.